CONTROLLED SYNTHESIS TO PRODUCE UPCONVERSION MATERIALS WITH MULTICOLOUR LUMINESCENCE

By

Ming Guan

Institute for Biomedical Materials & Devices

School of Mathematical and Physical Sciences, Faculty of Science

Supervisors:

Dr. Jiajia Zhou & Prof. Dayong Jin

This thesis is presented for the degree of Doctor of Philosophy

April 2019

Certificate of Original Authorship

I, Ming Guan, declare that this thesis, is submitted in fulfilment of the requirements for the award of Doctor of Philosophy, in the School of Mathematical and Physical Sciences, Faculty of Science, at the University of Technology Sydney.

This thesis is wholly my own work unless otherwise reference or acknowledged.

In addition, I certify that all information sources and literature used are indicated in the thesis.

I certify that the work in this thesis has not previously been submitted for a degree nor has it been submitted as part of the requirements for a degree except as fully acknowledged within the text.

This thesis is the result of a research candidature jointly delivered with China University of Geosciences (Beijing) as part of a Collaborative Doctoral Research Degree.

This research is supported by the Australian Government Research Training Program.

Signature: Production Note: Signature removed prior to publication.

Date: 27. April. 2019

Acknowledgements

As a cotutelle PhD student at the University of Technology Sydney (UTS) and China University of Geosciences Beijing (CUGB), I have been assisted by many people over my doctoral period. I really appreciate all of them.

Firstly, I would like to thank my principal supervisor at UTS, Dr Jiajia Zhou, for her precious supervision and guidance through all the years I studied at UTS. I learned how to undertake a research project logically, solve problems and overcome challenges. She is my idol. Her tender care and warm encouragement were of vital importance to my growth.

Simultaneously, I am so grateful to my co-supervisor at UTS, distinguished Professor Dayong Jin. It is Professor Jin who provided me the opportunity to be a PhD candidate at UTS. He gave the greatest support to my research over my years at UTS. Professor Jin set an excellent example for me by never giving up, staying enthusiastic, enjoying science, loving life, learning and giving. I count myself so lucky to have been his student.

Next, I would like to thank my principal supervisor at CUGB (Professor Hong Zheng) and my co-supervisor at CUGB (Associate Professor Lefu Mei), as well as Professor Zhaohui Huang. Without them, I cannot imagine how I could have completed this undertaking. All of them are respected teachers and my friends. They provided me so much help in research, working and living. They supported and encouraged me to optimistically meet the challenges in my life. All the things they taught me are precious gifts to my life.

Thanks also to my dear friends and colleagues that I met at IBMD, who not only gave me academic help but also gave my life colour. These include Dr Xiaoxue Xu, Dr Fan Wang, Dr Shihui Wen, Dr Zhiguang Zhou, Dr Yinghui Chen, Dr Hien Dong, Mr Christian Clark, Dr Olga Shimoni, Dr Qian Peter Su, Mr Chaohao Chen, Mr Yong Tao Liu, Ms Du Li, and Dr Wenjing Zhang. Thanks to our international collaborators, Dr Li Wang and Dr Yi Du, and the staff of the XPS lab at the Australian Synchrotron. I sincerely appreciate the generous help from all these nice people. Furthermore, special acknowledgement is also given to all

the staff of our MAPS school and MAU lab. All of them provided me with much guidance and help. In addition, thanks to Mr John who helped revising the thesis.

Deep appreciation should be given to Dr Wei Ren, Mr Hao He, Mr Chao Mi and Ms Jiayan Liao. Words can't express how much I appreciate you. Thanks also to my parents and my girlfriend, I love you all.

Finally, thanks to the China Scholarship Council and the Faculty of Science, UTS, who supported my tuition fees and my living expenses. I appreciate the support I received from both China and Australia. I hope that the friendship between these two great countries will last forever.

Format of the Thesis

This thesis follows the conventional format of six chapters. The relationship between these chapters is illustrated in the flowchart below.

Chapter 1 is the introductory chapter, which is composed of six sections. These sections describe the motivation and background knowledge relevant to developing multicolour luminescent upconversion (UC) materials, including the concepts of multicolour UC luminescence, the mechanism of UC luminescence, the compositions of UC materials, ways of synthesizing UC materials, and current progress on how to fine-tune multicolour UC luminescence. These sections provide the research inspiration and specific aims of this thesis, which were to study the controlled synthesis of UC materials with multicolour luminescence, high-throughput production and wide gamut.

Chapter 2 is the first research chapter, which investigates the distribution and multicolour luminescence of RE^{3+} (RE=Er^{3+}, Ho^{3+}, Tm^{3+}) in alkaline indium oxide UC materials. It indicates that the strategy of doping various RE^{3+} ions is a simple and feasible route to achieving multicolour UC emission.

Chapter 3 is a parallel research chapter that investigates the distribution of RE^{3+} (RE=Tm^{3+}, Yb^{3+}) in fluoride UC nanoparticles. After that, multicolour luminescence was realized via the addition of new activators such as Tb^{3+} and Eu^{3+} by cation exchange.

Chapter 4 presents a novel method of direct cation exchange in surface ligand capped UC nanoparticles. This allows efficient, high-throughput production of strong, multi-coloured, luminescent nanoparticles.

Chapter 5 further applies the knowledge obtained in Chapter 4. Using the current cation exchange strategy, hybridization of UC nanoparticles and lead halide perovskite quantum dots (PQDs) is attempted to fine-tune the multicolour, wide gamut luminescence.

Finally, the key research outcomes of this thesis are summarized in Chapter 6. Potential future developments and prospects of multicolour luminescent UC materials are discussed.

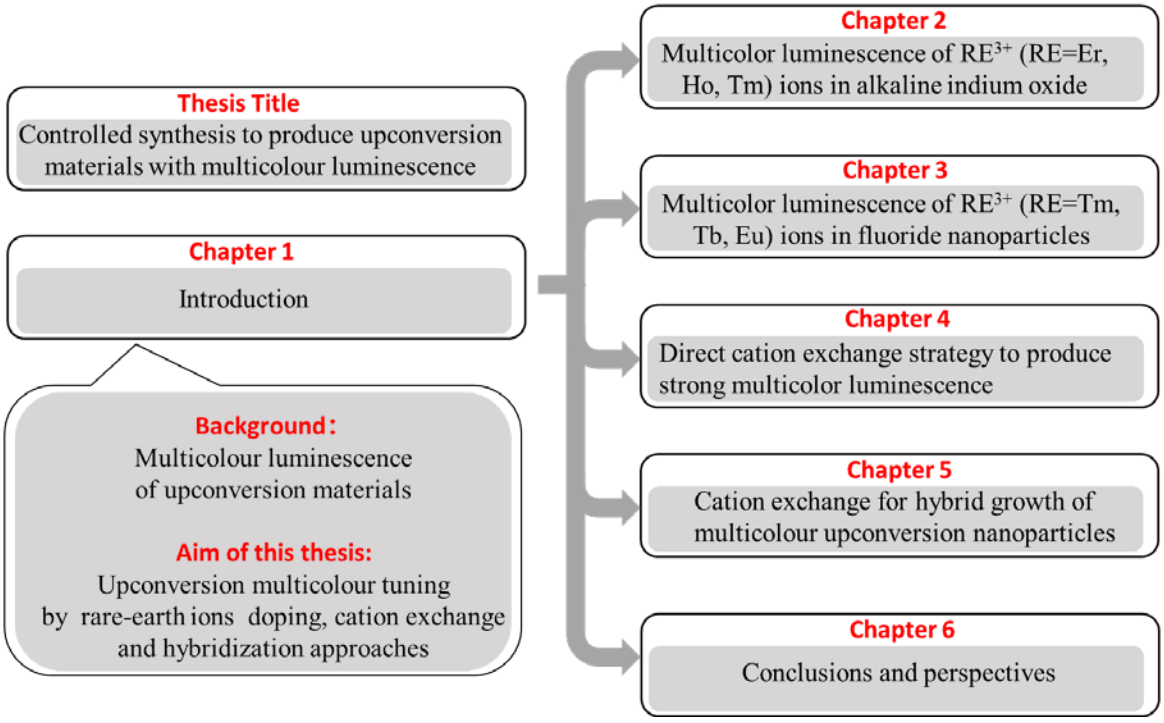
Thesis Title
Controlled synthesis to produce upconversion materials with multicolour luminescence
Chapter 1
Introduction
Background:
Multicolour luminescence of upconversion materials
Aim of this thesis:
Upconversion multicolour tuning by rare-earth ions doping, cation exchange and hybridization approaches
Chapter 2
Multicolor luminescence of RE3+ (RE=Er, Ho, Tm) ions in alkaline indium oxide
Chapter 3
Multicolor luminescence of RE3+ (RE=Tm, Tb, Eu) ions in fluoride nanoparticles
Chapter 4
Direct cation exchange strategy to produce strong multicolor luminescence
Chapter 5
Cation exchange for hybrid growth of multicolour upconversion nanoparticles
Chapter 6
Conclusions and perspectives

List of Publications

Research Papers:

[1] **Ming Guan**, Zhiguang Zhou, Lefu Mei, Hong Zheng, Wei Ren, Li Wang, Yi Du, Dayong Jin and Jiajia Zhou, Direct cation exchange of surface ligand capped upconversion nanocrystals to produce strong luminescence, *Chemical Communications*, 2018, 54: 9587-9590.

[2] Xiaoxue Xu, Christian Clarke, Chenshuo Ma, Gilberto Casillas, Minakshi Das, **Ming Guan**, Deming Liu, Li Wang, Anton Tadich, Yi Du, Cuong Ton-That and Dayong Jin, Depth-Profiling of Yb^{3+} Sensitizer Ions in $NaYF_4$ Upconversion Nanoparticles, *Nanoscale*, 2017, 9: 7719-7726.

[3] **Ming Guan**, Hong Zheng, Lefu Mei, Maxim S. Molokeev, Jing Xie, Tao Yang, Xiaowen Wu, Saifang Huang, Zhaohui Huang, and A. Setlur, Preparation, Structure, and Up-conversion Luminescence of Yb^{3+}/Er^{3+} Codoped $SrIn_2O_4$ Phosphors, *Journal of the American Ceramic Society*, 2015, 98: 1182-87.

[4] **Ming Guan**, Hong Zheng, Zhaohui Huang, Bin Ma, Maxim S. Molokeev, Saifang Huang, and Lefu Mei, Ca/Sr Ratio Dependent Structure and Up-conversion Luminescence of $(Ca_{1-x}Sr_x)In_2O_4 : Yb^{3+}/Ho^{3+}$ Phosphors, *RSC Advances*, 2015, 5: 59403-07.

List of Acronyms

(in alphabetical order)

DMF	N,N-dimethylformamide
DMSO	Dimethylsulfoxide
EDS	Energy-dispersive X-ray spectroscopy
EMU	Energy migration mediated upconversion
ETU	Energy transfer upconversion
FRET	Fluorescence resonance energy transfer
FT-IR	Fourier transform infrared spectroscopy spectra
HCl	Hydrochloric acid
HRTEM	High-transmission electron microscopy
LRR	Luminescence radiative reabsorption
NIR(IR)	Near-infrared
OA	Oleic acid
ODE	1-octadecene
OM	Oleylamine
OSCE	Organic solvent allowing cation exchange
PQDs	Lead halide perovskite quantum dots
QDs	Quantum dots
RE	Rare earth

RGB	Red green blue
SEM	Scanning electron microscopy
STEM	Scanning transition electron microscopy
TEM	Transmission electron microscopy
TFA	Trifluoroacetate
THF	Tetrahydrofuran
UC	Upconversion
UCL	Upconversion luminescence
UCNPs	Upconversion nanoparticles
UV	Ultraviolet
WACE	Cation exchange in water
XPS	X-ray photoelectron spectroscopy
XRD	X-ray diffraction

Abstract

Significant development has been done in rare earth (RE^{3+}) ion-doped upconversion (UC) materials over the past few years, however one challenge remaining lies in the controlled synthesis of UC materials with tunable, wide-gamut, multicolour luminescence and high-throughput production. This thesis focuses on exploring the distribution of RE^{3+} ions, understanding the network of energy transfer systems within interior UC materials, and developing resource- and time-saving methods for fine-tuning UC materials with multicolour luminescence, high performance and wide colour gamuts.

Chapter 1 summarizes the motivations for the thesis and background knowledge relevant to the development of multicolour luminescent UC materials, as well as the specific aims of this thesis: controlled synthesis of multicolour luminescent UC materials and distribution study of RE^{3+} ions within them.

In Chapter 2, Rietveld refinement of X-ray powder diffraction (XRD) was employed to characterize the distribution of RE^{3+} ions in bulk UC materials. Different RE^{3+} ions produced distinct emission peaks. Therefore, multicolour luminescence of activators, such as Er^{3+}, Tm^{3+} and Ho^{3+}, was achieved in alkaline indium oxide UC materials.

In Chapter 3, synchrotron-based X-ray photoelectron spectroscopy (XPS) measurements were used to investigate the depth-resolved distribution of RE^{3+} within fluoride upconversion nanoparticles (UCNPs). The author proposed a natural Gd^{3+}-rich shell in Yb^{3+}/Tm^{3+} doped $NaGdF_4$ UCNPs, which can effectively bridge the gap of energy transfer between sensitizers and activators to realized multicolour luminescence via cation exchange.

Chapter 4 reports on a novel direct cation exchange method for UCNPs without removing surface ligands in organic solvent. It avoids the tedious pre-treatment of synthesized UCNPs, and the luminescent intensities using the new method are much stronger than those using conventional cation exchange in water. This facile and rapid cation exchange strategy opens a new path to the synthesis of multicolour-emitting nanoparticles expeditiously with high performance and high-throughput.

Chapter 5 further applies the knowledge obtained from Chapter 4. We attempted to develop hybrid heterostructures of UCNPs and lead halide perovskite quantum dots (PQDs), and to produce and fine-tune multicolour luminescence. The cation-exchanged ions were expected to bridge these two kinds of nanomaterials. However, it remains a great challenge.

Conclusions and perspectives are given in Chapter 6, which also summarizes the key achievements of the thesis. Controlled synthesis and fine-tuning of the spectral UC emission properties of UCNPs may open a path to more complex applications.

Keywords: Rare-earth ions, upconversion, cation exchange, multicolour luminescence

Table of Contents

CHAPTER 1

Introduction

1.1 Multicolour upconversion luminescence

Multicolour luminescence is composed of a broad spectrum of colours. Multicolour luminescent materials, including organic dyes[1-3], semiconducting quantum dots[4-10], downconversion and upconversion (UC) materials[11-16] and so on, have always been at the forefront of materials science. To enrich the fluorescence colour, nano semiconductors rely on the tuning of bandgap[17-20]20, while the doped nano-insulators require elaborate control of the dopants[21-24]. Controlled synthesis plays a fundamental role in producing multicolour luminescence in rare earth (RE^{3+})-doped UC materials.

Upconversion materials are particularly suitable for such multicolour luminescent emissions because RE^{3+} activators that feature ladder-like-arranged energy levels can produce an individual red-green-blue (RGB) emission band that spans the wavelength range from ultraviolet to near-infrared (NIR). To realize multicolour luminescence in UC materials, one method is the homogeneous mixing of certain amounts of monochromatic RGB materials in a solution or solid-state substrate to produce superimposed colour images in the mixed materials (Figure 1.1a)[25]. Alternatively, by doping of various RE^{3+} activators simultaneously, the blending of various RGB elements in individual materials enables the construction of full-colour luminescence from materials of fixed composition (Figure 1.1b). Therefore, an appealing feature of these UC materials is that the emission colour can be controlled under near-infrared excitation by tailoring the intensity ratio of the different emission peaks.

Apart from their multicolour luminescent properties, UC materials exhibit other unique luminescent properties including large Stokes shifts, high resistance to optical blinking and photobleaching, as well as the unique ability to convert long-wavelength stimulation into short-wavelength emission[26-28]. In addition, due to weak autofluorescence

background as well as the high penetration depth into biological tissue generated by NIR excitation[29-33], multicolour luminescent UC materials rival conventional luminescent materials in challenging tasks, leading to many revolutionary applications in a wide array of research fields[34-40], such as multiplexed biological labelling[41-43], anti-counterfeiting[44-46], as well as graphics imaging and display[47-49] (Figure 1.1 c-e).

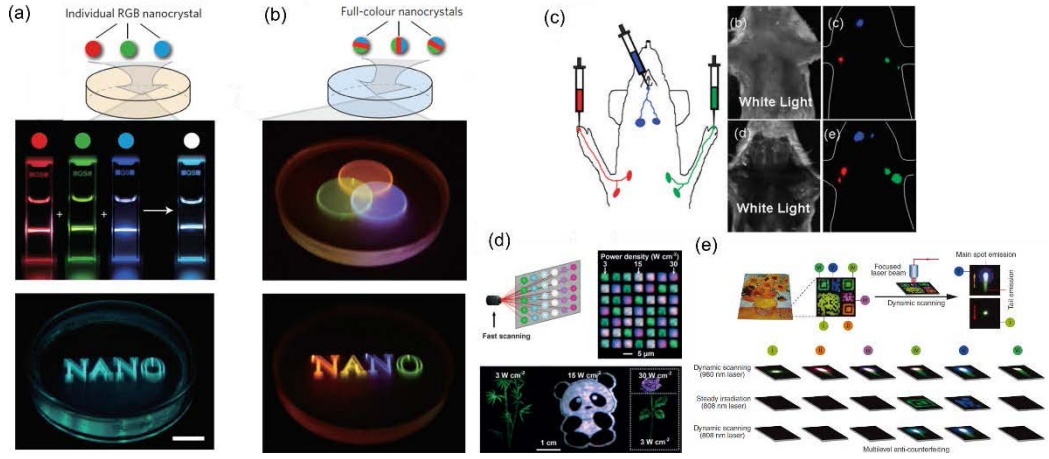

Figure 1.1 Demonstration of volumetric three-dimensional display generated by combining upconversion nanoparticles featuring monochromatic RGB emissions. Note that the mixing of upconversion nanocrystals with differently-coloured emission results in a white colour (a); full-colour volumetric three-dimensional display in composite materials through use of the multilayer upconversion nanocrystals (b)[25]; multicolour upconversion nanoparticles linked to biological applications (c), graphics imaging and display (d)[47], and anti-counterfeiting applications (e)[50]

1.2 Mechanism of UC luminescence

Upconversion luminescence is a nonlinear optical phenomenon known as anti-Stokes emission, in which the sequential absorption of two or more low-energy photons is followed by the luminescent emission of a high-energy photon[51]. Auzel first reported on upconverted visible emission based on energy transfer by using Yb^{3+} to sensitize Er^{3+} and Tm^{3+} ions[52]. Shortly afterwards, upconverted green emission was achieved from a Yb^{3+}-Ho^{3+} coupling. After that, it was Auzel who first described the concept of "UC" and summarized its mechanism. After several decades of development, photon UC involving RE^{3+} ions can be mainly categorized into four classes of mechanisms: excited-state absorption (ESA), energy transfer UC (ETU), photon avalanche (PA) and energy migration-mediated UC (EMU)[53], as shown in Figure 1.2.

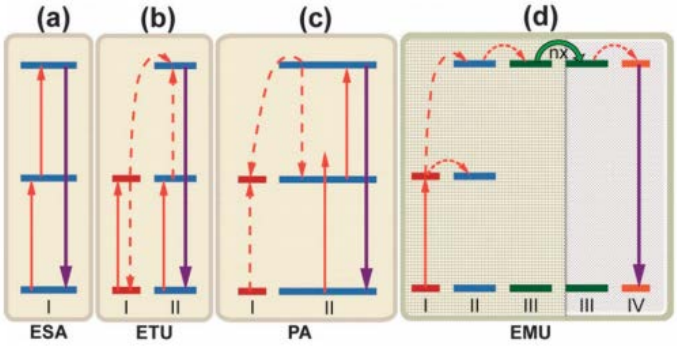

Figure 1.2 Four typical kinds of UC luminescence mechanisms: excited state absorption (a); energy transfer UC (b); photon avalanche (c) and energy migration-mediated UC (EMU)[34]

1.2.1 Excited-state absorption

Excited-state absorption (ESA) is a process in which a single ion in the ground state continuously absorbs two or more pump photons. A schematic diagram of the ESA process is shown in Figure 1.2a for a simple three-level system. In the process of ESA, the ion absorbs the first photon and populates an excited metastable level from ground level, which is called *ground state absorption* (GSA). After that, the ion absorbs the second photon and is promoted from the excited metastable level to a higher state. Finally, the excited ions fall back from the higher-lying state to the ground state to produce upconversion luminescence. ESA is the most fundamental process of UC luminescence.

1.2.2 Energy transfer upconversion

Energy transfer upconversion (ETU) occurs in sensitizer-doped UC materials and is the dominant mechanism of UC luminescence. In this process, a sensitizer is excited and then relaxes back to the ground state; however, the energy is transferred to the neighbouring activator ions to produce UC luminescence, as shown in Figure 1.2b. According to the different energy transfer methods, the ETU can be approximately divided into three styles: successive energy transfer (SET), cross relaxation (CR) and cooperative upconversion (CU). SET occurs between two different types of ions and is the most important energy transfer style. When the energy levels of the sensitizer and activator are matched well, the activator can be excited by continuous energy transfer from the sensitizer, causing a transition to a higher energy level in the activator and resulting in high-energy photon luminescent emission. In contrast, CR occurs between two different or the same ions, one of which transfers energy to another ion, causing it to leap to an upper emitting state, while it returns a lower energy level through non-radiative relaxation. The concentration

of dopants used has a strong influence on the CR process. The higher the dopant concentration, the greater the probability of cross-relaxation, and the upconversion luminescence may exhibit concentration quenching because of the large cross-relaxation. CU is a process that occurs between three kinds of ions. Two ions of the same type in an excited state simultaneously transfer energy to another ion in the ground state, causing it to populate a higher energy level. In sum, ETU is instantaneous and pump power independent, and thus it has been widely studied to provide highly efficient UC luminescence over the past decade.

1.2.3 Photon avalanche

Photon avalanche (PA) is a combination of GSA and ESA and is the process that can produce the highest luminous efficiency. The PA process begins with the population of the metastable level by non-resonant weak GSA, followed by resonant ESA to populate upper emitting levels (Figure 1.2c). Generally, the sensitizer absorbing the incident photon populates the first excited state and another absorption pumps it to the second excited state. The sensitizer in the second excited state will cross-relax with adjacent ground state ions to generate two sensitizers in the first excited state. These two sensitizers may absorb photons and repeat the process, thereby causing snowball-like accumulation and generation of a large amount of sensitized ions, producing strong UC emission as an avalanche. PA usually occurs when the absorption of the excitation light from the excited state is weak, while the ground state absorption of the excitation light and the interaction between the ions in the system are strong.

1.2.4 Energy migration-mediated UC

In 2011, Wang et al. proposed a new UC mechanism named *energy migration-mediated UC* (EMU)[54]. The mechanism of EMU is essentially a type of energy transfer UC. However, it opens the door to solving the problem of energy mismatch between sensitized ions and the activated ion, and realizes UC luminescence of activators without long-lived intermediate energy states. In the process of EMU, sensitizer ions absorb photon energy and transfer it to nearby activator ions. Some of the activator ions at very high energy levels do not generate radiation relaxation via their own transition, but pass energy through the intermediate medium to other optical centres, resulting in a radiation transition that produces upconverted luminescence by new activators. In general, the

upper emitting state of the new activator ion should be slightly lower than the corresponding excited state of the intermediate medium. A schematic of the mechanism of EMU is shown in Figure 1.2d.

1.3 Compositions of upconversion materials

Upconversion materials are luminescent materials that convert NIR excitation into a visible emission by RE^{3+} doping[55]. Compared to commonly used organic fluorophores and quantum dots, UC materials are always composed of an inorganic crystal host and various RE^{3+} dopants embedded in the host lattice[56]. The host material, having a crystalline structure, provides a doping and luminescent lattice for the dopants, while the dopants of RE^{3+} ions provide luminescent centres[52].

1.3.1 Host materials

Selection of appropriate host materials is critical in the synthesis of RE^{3+}-doped nanocrystals with favourable optical properties such as high UC efficiency and a controllable emission profile. Firstly, the host material should not have a large absorption of the excitation power. Secondly, the phonon energy of the host should be low, which is a requirement to minimize the energy loss caused by non-radiative relaxation, thereby maximizing the radiative emission of UC materials. Furthermore, the crystal structure should have low variation. In this thesis, the compounds used for UC host materials are discussed in terms of alkaline indium oxide and fluoride.

Oxides have relatively high phonon energies due to the stretching vibration of the host lattice, but they always exhibit very good chemical stability. Some oxide-based UC phosphors that have relatively low phonon energy, such as Y_2O_3 and Gd_2O_3 (Figures 1.3a and b), are also widely studied[57-64]. Li reported that the oxide of $CaIn_2O_4$ has low phonon energy (~475 cm^{-1}) (Figure 1.3c), which is much lower than those of other typical oxide hosts such as ZrO_2 (~500 cm^{-1}), Y_2O_3 (~550 cm^{-1}), and silicate (~1100 cm^{-1}) [65-68]. In addition, due to the differences in cation valance and radius, the substitution of RE^{3+} ions always leads to a change in the lattice parameters and the formation of lattice distortion, which can significantly influence the energy transfer and optical properties of UC materials. Alkaline earth ions (Ca^{2+}, Sr^{2+}, and Ba^{2+}) have similar ionic sizes to RE^{3+} ions[69]; therefore, alkaline indium oxides are always ideal host materials for RE^{3+} doping[53, 70-76].

Doing research on alkaline indium oxide helps researchers to explore new excellent host materials for multicolour UC luminescence.

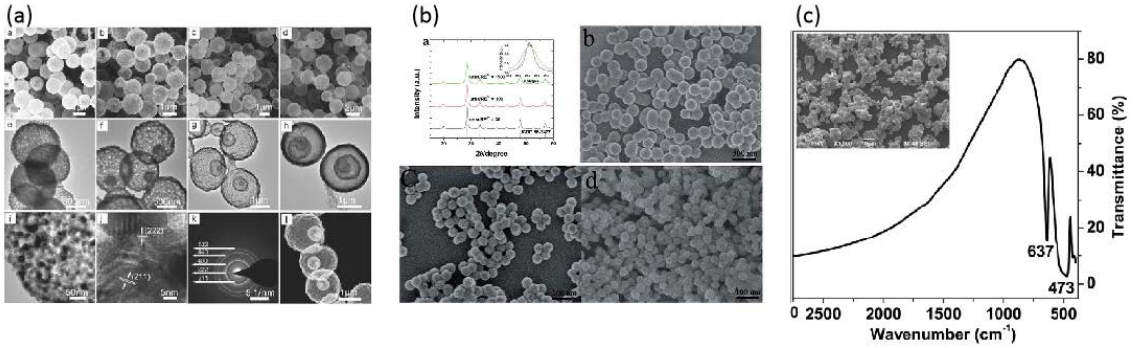

Figure 1.3 Oxide host materials for UC luminescence: SEM and TEM images of Y_2O_3 upconverted materials (a)[64]; SEM images of Gd_2O_3 upconverted materials (b)[63]; FT-IR spectra of $CaIn_2O_4$ showing its low phonon energy, with an inset showing an SEM photograph of $CaIn_2O_4$ upconverted materials (c)[66]

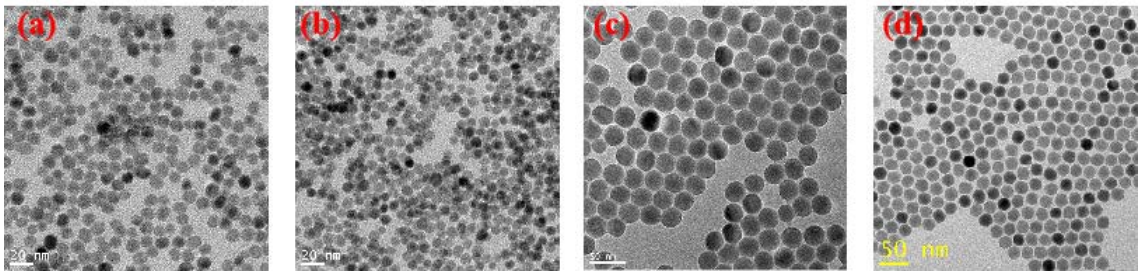

Figure 1.4 Synthesized UC host materials of α-$NaYF_4$ (a), α-$NaGdF_4$ (b), β-$NaYF_4$ (c) and β-$NaGdF_4$ (d)

Fluoride has low phonon energy, a high refractive index, and good thermal stability[9, 77]. Therefore, it has been proposed to be the most promising host for UC luminescence. Fluorides of CaF_2, $LiGdF_4$, YF_3, $NaYF_4$ and $KMnF_3$ have been synthesized and studied widely as UC host materials[78-83]. Among the fluorides, the hexagonal-phase $NaYF_4$, having a phonon energy of about 350 cm^{-1}, is acknowledged to be one of the most efficient UC hosts[84-87]. $NaGdF_4$ is another promising and efficient host material for UC luminescence[88-89]. In the NaY(Gd)F_4 host, Na^+ and Y^{3+} (Gd^{3+}) are used as host cations because their ionic radii are close to the ionic radius of RE^{3+} activators[69]. Therefore, crystal defects and lattice stress can be prevented during the synthesis of nanoscale particles with excellent UC luminescent properties. Gd^{3+} ions in a $NaGdF_4$ structure can also effectively bridge the gap in energy transfer from sensitizer/accumulator to activators through long-range energy migration in the sub-lattice. Furthermore, Gd^{3+} is a common T1-weighted MRI contrast agent. Direct doping of a high concentration of Gd^{3+} ions into

the host can yield magnetic/upconverting UCNP probes, which can be used in bioimaging[41-42].

It should be noted that typical $NaYF_4$ or $NaGdF_4$ host materials have two kinds of crystal structure (cubic phase of α-$NaREF_4$ and hexagonal phase of β-$NaREF_4$, as shown in Figure 1.4) and the UC emission intensity is much higher in the hexagonal than the cubic phase. Therefore, β-$NaREF_4$ (including β-$NaYF_4$ and β-$NaGdF_4$) are presently considered to be the most efficient host materials for UC luminescence.

1.3.2 Dopants of RE^{3+} Ions

Characterized by the progressive filling of the 4f orbitals, RE^{3+} ions always have considerable energy levels and, thus, exhibit fascinating optical properties.

Activator. In the case of sensitized UC, the luminescence emitter is the *activator*. Specifically, the activator is the dopant ions that accumulate sufficient energy from the non-radiative transfer of another dopant ion and reach a corresponding upper-emitting state, which then induces emission of high-energy photons. In order to produce a practically useful UC emission, the energy difference between each excitation level and its lower intermediate level (or ground state) should be close enough to facilitate the photon absorption and energy transfer steps involved in UC processes. Er^{3+}, Tm^{3+}, and Ho^{3+} typically feature such ladder-like-arranged energy levels and are, thus, frequently-used activators[90-93]. Usually, the doping concentrations of Tm^{3+} (or Er^{3+}) activators are determined as 0.3%~2% (when Yb^{3+} sensitizers are determined as 10~25%)[94-98]. Under these concentrations, the synthesized UC materials always can generate brighter emissions under mild excitation.

Sensitizer. A sensitizer is a donator of energy in the UC process. A sensitizer with a sufficient absorption cross-section in the near-infrared (NIR) region is usually co-doped along with the activator, taking advantage of the efficient ETU process between the sensitizer and activator to enhance UC luminescence efficiency. Currently, almost all UC materials are based on the co-doping of trivalent Yb^{3+} ions due to their very simple energy levels with only one excited 4f level of $^2F_{5/2}$ [99-103]. The energy level interval between the ground state of $^2F_{7/2}$ and the excited state of the $^2F_{5/2}$ level is well matched with the 980 nm NIR semiconductor laser, and the absorption cross-section of Yb^{3+} ions is much larger than that of other RE^{3+} ions. In addition, the $^2F_{7/2}$-$^2F_{5/2}$ transition of Yb^{3+} is highly resonant

with many f-f transitions of typical upconverting RE^{3+} ions such as Er^{3+}, Tm^{3+}, and Ho^{3+}, thus facilitating efficient energy transfer from Yb^{3+} to other ions. These optical characteristics make Yb^{3+} ions by far the most ideal UC sensitizer ions. The sensitizer content is normally kept no higher than 20 mol% in doubly (or triply) doped UC materials to minimize the energy loss of cross-relaxation. However, Ma et al. reported that ion doping with high concentrations of Yb^{3+} (up to 60%) can also greatly enhance the luminescent intensity in UC nanoparticles[104-105].

1.4 Synthesis and modification of upconversion materials

Development of facile synthesis strategies for making high-quality RE^{3+}-doped UC materials with controlled stoichiometric compositions, crystal structures, and morphologies is crucial for producing materials with desired chemical and optical properties. Since Auzel observed upconverted visible emissions, the practical use of UC materials has been primarily focused on bulk materials. To synthesize bulk UC materials such as oxide UC materials, high-temperature solid-state synthesis is a common method[106-108]. In recent years, with the rapid development of nanoscale materials, high-quality UC fluoride nanoparticles can now be prepared by a range of synthetic approaches such as coprecipitation, thermal decomposition, hydro-(solvo)thermal synthesis, sol-gel processing[109-115]. In addition, cation exchange methods can be used to modify the properties of the as-synthesized UC nanoparticles[116-119].

1.4.1 Solid-state methods

Solid-state reaction is a common method for synthesizing oxide matrix UC bulk materials due to its simplicity, large yield, low cost, and the ease with which raw materials can be obtained. In a general procedure, the raw materials required for synthesis are weighed, mixed and ground thoroughly according to stoichiometric ratios. After that, the mixtures are packed into alumina crucibles and placed in a muffle furnace or electric resistance furnace to conduct a sintering process at a suitable temperature and holding time. The matrix material and the RE^{3+} ions pass through a solid-state chemical reaction, and the RE^{3+} ions diffuse into the lattice of the matrix during the process of recrystallization at high temperature. Notably, thorough mixing of the raw materials is the key to preparing high-quality UC bulk materials by solid-state reaction. When the total amount of raw

materials is small, raw materials can be manually ground using an agate mortar. Alternatively, machine ball milling is used to uniformly mix large amounts of raw materials. Mixing also can be completed by wet blending; that is, the raw materials are first mixed with water, ethanol or another volatile solvent to form a uniform slurry, and then the blocks in the slurry are crushed by ball milling. Depending on the desired bulk materials, the mixed raw materials are sintered under a given atmosphere. For example, oxide bulk UC materials are usually sintered under an oxidizing atmosphere (air, oxygen), an inert atmosphere (N_2, Ar), or a reducing atmosphere (CO, H_2, NH_3)[120-123]. Some unnecessary residues may be removed through washing by a solvent such as water or ethanol, and the prepared bulk UC materials may need to be ground again to obtain ultrasmall powder for testing and use. In this thesis, the solid-state method was used for synthesizing oxide bulk UC materials.

1.4.2 Coprecipitation and thermal decomposition methods

Coprecipitation methods are perhaps one of the most common techniques for producing UCNPs with a uniform size distribution[21, 124]. This thesis mainly used coprecipitation and thermal decomposition techniques to synthesize β-$NaREF_4$ UCNPs.

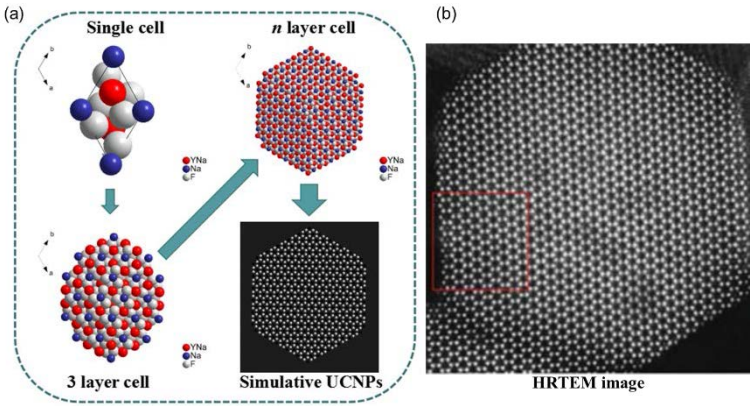

Figure 1.5 Simulated crystal growth of β-$NaREF_4$ UCNPs (a) and HRTEM photos of real UCNPs (b)

Coprecipitation of $NaREF_4$ UCNPs occurs in long-chain hydrocarbon solvents (e.g., 1-octadecene) and unsaturated fatty acids such as oleic acid (OA). Given insight into the growth process, $NaREF_4$ UCNPs are a solid material whose constituents (such as atoms or ions) are arranged in a highly ordered microscopic structure, forming a crystal lattice that extends in all directions. The smallest group of particles that constitutes the highly ordered microscopic structure is the unit cell. When growing into nanoparticles, symmetrical arrangements of a large number of constituent β-$NaYF_4$ unit cells leads to

the formation of a large crystalline UCNP nanoparticle. From simulations of UCNP growth, one can see that the atomic arrangements of the final particles match well with the HRTEM photos of real UCNPs (Figure 1.5).

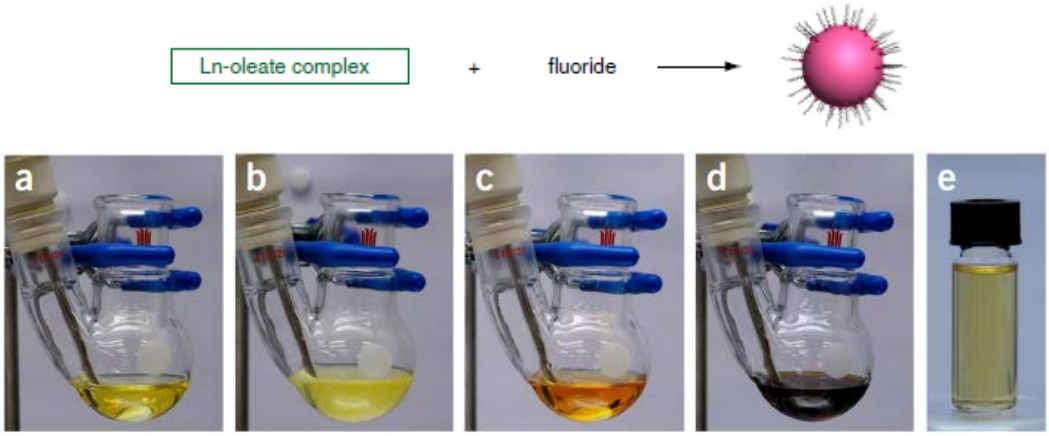

Figure 1.6 Schematic illustration of the co-precipitation strategy used for the synthesis of RE^{3+}-doped UCNPs and photographs of the reaction mixture at various stages of the co-precipitation method. The RE^{3+} oleate precursors are dissolved in oleic acid and 1-octadecene (a); precursor solution upon addition of NaOH and NH_4F (b); precursor solution before nucleation (c); solution after nucleation by heating (d); and colloid of re-dispersed nanoparticles in cyclohexane after purification (e)[124]

For the synthesis of monodispersed nanoparticles, an inorganic salt containing RE^{3+} ions is first transferred into a flask containing 1-octadecene and oleic acid. The unsaturated fatty acid is used as a surface ligand to control particle growth and subsequently stabilize the resulting nanoparticles against agglomeration. The mixture is then heated to 150 °C, resulting in the formation of RE^{3+}-oleate coordination complexes. After that, injection of a methanol solution of NaOH and NH_4F leads to the nucleation and growth of nanocrystals. A schematic illustration of the co-precipitation strategy involved in the synthesis of RE^{3+}-doped UCNPs and photographs of the reaction mixture at various stages of co-precipitation are shown in Figure 1.6. In this process, RE^{3+}-based acetates and chlorides provide RE^{3+} cations, while NaOH and NH_4F provide anions. The process should occur under an anhydrous and oxygen-free environment. Temperature, reaction time and the amount of solvent are important in controlling the synthesis. β-phase nanoparticles of $NaGdF_4$, $NaLuF_4$, $NaDyF_4$ and $NaYbF_4$ NCs were also made using this method. The core-shell structure of $NaREF_4$ UCNPs is obtained via a two-step reaction using the as-synthesized core particles as templates. A shell layer is then epitaxially grown onto the cores. The shell layer is grown by following a similar procedure to that

just described, except that the presynthesized core particles are added to the solution before the injection of the $NaOH/NH_4F$ solution. The hot-injection method also is an alternative method for epitaxial growth of the shell layer. As a result of the core-shell structure, the surface properties of the UCNPs can be modified, and the shape and size uniformity of the nanoparticles can be controlled well.

The thermal decomposition method is another important technique for the production of UCNPs. It uses organometallic compounds as precursors for decomposition to form uniform UCNPs. Oleic acid and 1-octadecene are also frequently employed as high-boiling-point organic solvents and passivating ligands that prevent the nanocrystals agglomerating. Nanoparticles made with this approach are monodispersed and uniform in their morphology and size. When oleylamine (OM) is employed as a polar capping reagent, the thermal decomposition method is ideal for synthesizing α-$NaREF_4$ UCNPs[125]. In this thesis, the α-$NaREF_4$ UCNPs that were tested were synthesized via this thermal decomposition method.

It should be noted that no matter whether they are synthesized by coprecipitation or thermal decomposition, UCNPs are covered with organic surfactant molecules, making them dispersible in nonpolar solvents. To make them dispersible in an aqueous phase, many surface modification strategies have been reported, such as surfactant ligand removal[126-127], amphiphilic molecule interaction[128-130], and direct ligand exchange[131-132]. Removal of surfactant ligands provides a simple way to disperse UCNPs into an aqueous phase[133]. The oleic acid molecules weakly bind to the surfaces of UCNPs via coordinate covalent bonds, which make their removal by hydrochloric acid (HCl) easy under sonication. After HCl treatment, the abundant RE^{3+} ions exposed on the surface of UCNPs have a strong coordination capacity, allowing direct cation exchange via an aqueous phase reaction to further tune their luminescence.

1.4.3 Cation exchange modification approach

Currently, the main approaches for preparing UC nanoparticles are co-precipitation, thermal decomposition and hydrothermal reaction. Alternatively, cation exchange allows high-throughput production of multicolour-emitting nanoparticles[134]. The capability to modulate emission colours in RE^{3+}-doped nanoparticles allows rapid access to a myriad of different colour spaces with minimum sample processing time. Furthermore,

preservation of the morphology of the initial nanoparticle template upon exchange enables the formation of nanoparticles with compositions, morphologies, and crystal phases that are not readily accessible by conventional synthesis methods.

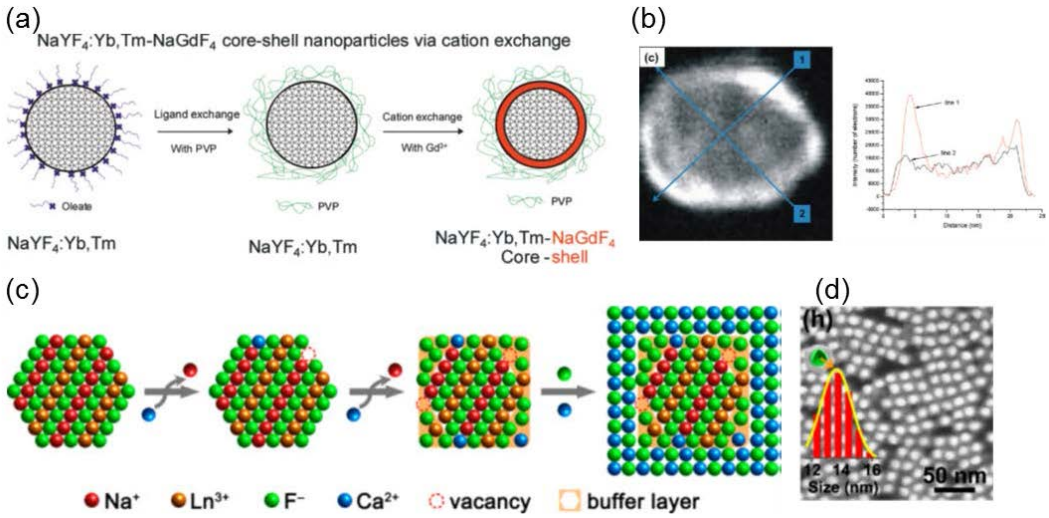

Figure 1.7 Schematic illustration of Gd^{3+}-exchange on $NaYF_4$:Yb,Tm UCNPs (a), and EELS 2D elemental maps and line profiles showing $NaYF_4$:Yb,Tm-$NaGdF_4$ core-shell nanoparticles prepared by cation exchange (b)[135]; selective cation exchange for the growth of β-$NaREF_4$@CaF_2 nanoparticles (c), and HRTEM image showing synthesized hybrid β-$NaREF_4$@CaF_2 nanoparticles after cation exchange (d)[136]

Van Veggel et al. reported cation exchange of $NaYF_4$:Yb,Tm nanoparticles with Gd^{3+} ions in aqueous media after the as-prepared oleate-stabilized $NaYF_4$:Yb,Tm nanoparticles were made water-dispersible by ligand exchange with PVP (Figures 1.7a, b)[135]. A thin, tuneable and uniform $NaGdF_4$ shell of $NaYF_4$:Yb,Tm-$NaGdF_4$ core-shell nanoparticles has been achieved via the cation exchange process. These core-shell nanoparticles have enhanced upconversion properties. Wang et al. also reported the development of a facile in situ Gd^{3+}-exchange strategy that greatly enhances the UC luminescence of hexagonal-phase $NaYF_4$ UCNPs while maintaining their shape and small particle size[117]. After Gd^{3+}-exchange, the naked-eye visible UC emission of the NPs was enhanced about 29 times under 980 nm near-infrared (NIR) excitation with unchanged particle size. Yan et al. discovered a selective cation exchange strategy to construct hybrid RE^{3+}-doped core/shell $NaREF_4$ nanoparticles with dissimilar structures[136]. In that work, preferential cation exchange between Ca^{2+} and Na^+ triggered surface hexagonal-to-cubic structure evolution, which remediated the large barrier for heteroepitaxy of monocrystalline CaF_2 shell (Figure 1.7c, d). The new heterostructured CaF_2 shell leads to greatly enhanced UC luminescence of $NaREF_4$ nanoparticles.

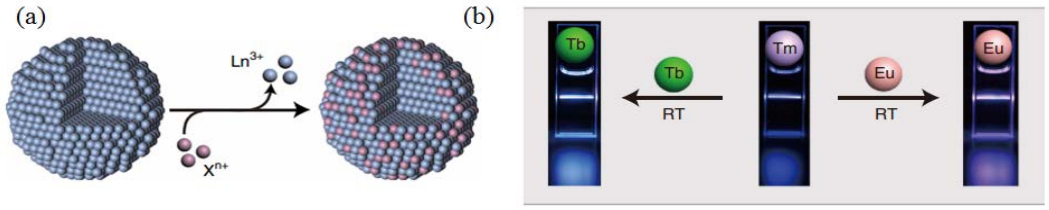

Figure 1.8 Cation exchange in water strategy of UCNPs: Schematic representation of the cation exchange process (a); UC luminescence images showing the change in the emission colour of $NaGdF_4$:Yb^{3+}/Tm^{3+}@$NaGdF_4$ colloidal solutions upon addition of Tb^{3+} or Eu^{3+} ions (b)[133].

Particularly, Liu et al. reported a cation exchange in water strategy to achieve multicolour synthesis in $NaGdF_4$: Yb^{3+}/Tm^{3+}@$NaGdF_4$ core-shell nanoparticles under room temperature[133]. With core-shell structure containing $NaGdF_4$ long-range energy migration layer, the luminescence properties of the nanoparticles can be easily tuned through adding different kinds of new activators ions such as Tb^{3+}, Eu^{3+}, Ce^{3+} and Mn^{2+} ions (Figure 1.8). However, without oleic acid protecting layer, the naked particles would show low UC emission intensities because of strong quenching effect from water. In addition, lacking of the coverage of surface ligands may lead the nanoparticles to produce aggregation and degradation, which recently has been observed in water circumstance.

1.5 Current progress on multicolour upconversion luminescence

Multicolour luminescence of UC materials is of particular importance to the development of more complex and multiplexed applications. The various strategies that can fine-tune multicolour UC luminescence mainly focus on: (1) doping with various RE^{3+} ions (a combination of different activator/sensitizers, or control of their concentrations); (2) utilization of energy migration-mediated upconversion (EMU) pathways; (3) utilization of an appropriate core/shell design; (4) control of nanosize and shape; (5) control of relaxation processes induced by the surrounding ligands; and (6) utilization of luminescence radiative reabsorption (LRR) or Forster resonance energy transfer (FRET) between the UCNPs and other luminescent materials[22, 68, 137-140]. In this thesis, the strategies adopted to produce multicolour luminescence are described as the following subsections.

1.5.1 Doping with various RE^{3+} ions

Each RE^{3+} ion has its own set of energy level structures. Different RE^{3+} ions can produce

distinct emission peaks, thus collectively covering a broad spectrum from the UV to NIR range. Therefore, a range of colour outputs can be selected by doping various RE^{3+} ions or using combinations of them. The most common activator ions used in UCNPs so far have mainly been Er^{3+}, Tm^{3+}, and Ho^{3+} ions, due to their ladder-like energy levels (Figure 1.9) [141-143]. The Er^{3+} ions have three main UC emission bands. Two green emission bands are located at around 525 nm and 540 nm, which correspond to the transitions of $^2H_{11/2} \rightarrow {}^4I_{15/2}$ and $^4S_{3/2} \rightarrow {}^4I_{15/2}$, respectively. One red emission band centred at around 650 nm is associated with the transition of $^4F_{9/2} \rightarrow {}^4I_{15/2}$. The Tm^{3+} ions have two main visible UC emission bands located at around 475 nm and 450nm, which originate from the transitions of $^1G_4 \rightarrow {}^3H_6$ and $^1D_2 \rightarrow {}^3F_4$, respectively. The Ho^{3+} ions have three UC bands of green to red emission, centred at 485, 540 and 650 nm in the visible region, which come from the transitions of $^5F_3 \rightarrow {}^5I_8$, $^5S_2/{}^5F_4 \rightarrow {}^5I_8$ and $^5F_5 \rightarrow {}^5I_8$, respectively. Notably, all of the Er^{3+}, Tm^{3+}, and Ho^{3+} activator ions matched well with the 975 nm absorption for the $^2F_{7/2} \rightarrow {}^2F_{5/2}$ transition of Yb^{3+} ions. Thereby, these activator ions can be efficiently sensitized by Yb^{3+} ions via energy transfer, enabling these RE^{3+} ions or their various combinations to produce multicolour UC emissions with extremely high efficiency.

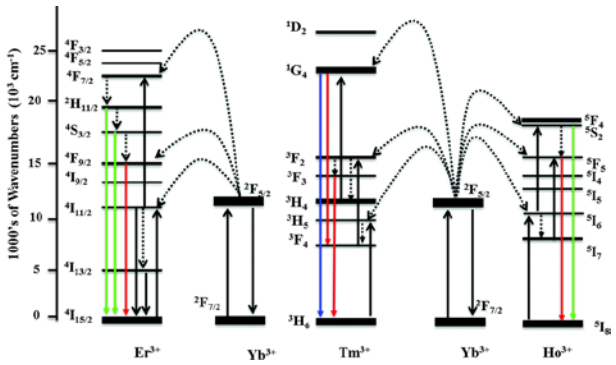

Figure 1.9 The ladder-like energy levels of Er^{3+}, Tm^{3+}, Ho^{3+} and Yb^{3+} ions, as well as the general emissions bands of Er^{3+}, Tm^{3+} and Ho^{3+} ions, showing they are common activators ions for multicolour UC luminescence[144]

The selection of single RE^{3+} activators (combined with a sensitizer) in an individual host is a straightforward approach to producing multicolour UC emissions. In 2004, Haase et al. first reported efficient multicolour UC emission in colloidal RE^{3+}-doped nanoparticles by codoping Yb^{3+}/Er^{3+} and Yb^{3+}/Tm^{3+} pairs into $NaYF_4$ nanoparticles[145]. Upon the sensitization of Yb^{3+} ions, Er^{3+} produced strong yellow emissions, while Tm^{3+} yielded strong blue emissions (Figure 1.10a). Later, Capobianco et al. observed similar results in $NaYF_4$ nanoparticles[146]. The Yb^{3+}/Er^{3+} and Yb^{3+}/Tm^{3+} doped particles exhibited

green/red and blue upconversion luminescence, respectively, under 977 nm laser excitation with low power densities (Figure 1.10b).

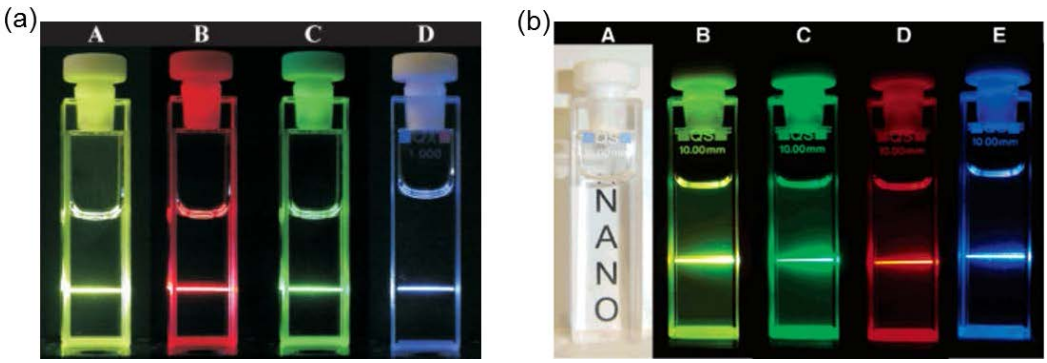

Figure 1.10 Photographs of the UC luminescence of the $NaYF_4$:20 %Yb^{3+},2 %Er^{3+} sample (A), with the same luminescence seen through red (B) and green (C) colour filters, and the UC luminescence of $NaYF_4$:20 %Yb^{3+},2 %Tm^{3+} (D) (a)[145]. Photographs of transparent $NaYF_4$:2% Er^{3+}, 20% Yb^{3+} solution (A), the total upconversion luminescence of $NaYF_4$:2%Er^{3+}, 20%Yb^{3+}(B), the same luminescence viewed through green (C) and red (D) filters, and the upconversion luminescence of $NaYF_4$:2%Tm^{3+}, 20% Yb^{3+} (E) (b)[146]

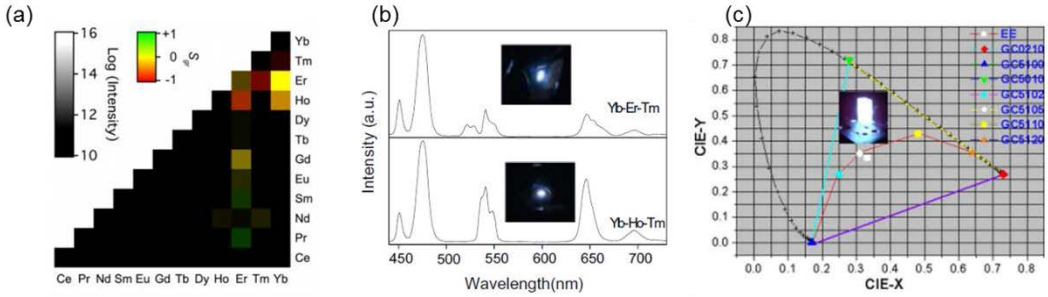

Figure 1.11 Color map depicting the integrated UC luminescent intensity and green/red spectral purity of 78 binary combinations of 12 lanthanide dopants (a)[147]; UC spectra and white emissions of $Yb^{3+}/Er^{3+}/Tm^{3+}$ and $Yb^{3+}/Ho^{3+}/Tm^{3+}$ triply-doped $NaYF_4$ nanorods (b)[148]; and white emission of $Tm^{3+}/Er^{3+}/Yb^{3+}$ co-doped YF_3 nanocrystals (c)[149]

Co-doping of two or more kinds of RE^{3+} activators (also combined with sensitizers) into an individual host can produce a broad range of emission wavelengths through colour overlay. In particular, the simultaneous use of green and red colour from Er^{3+} or Ho^{3+}, and the blue emission of Tm^{3+}, can yield white UC emission in UC materials. Milliron et al. reported a combinatorial nanoparticle screening approach of multiply-doped $NaYF_4$ nanoparticles to identify a series of doubly- and triply-doped upconverting nanoparticles that exhibit narrow and pure emission spectra at various visible wavelengths (Figure 1.11a)[147]. Chu et al. reported bright white UC emission consisting of blue UC radiation at 450 nm and 475 nm, a green band at 545 nm, and red bands at 650 nm and 695 nm. These were observed in Yb^{3+}-Ho^{3+}-Tm^{3+} and Yb^{3+}-Er^{3+}-Tm^{3+} triply-

doped $NaYF_4$ nanorods under 980 nm laser excitation (Figure 1.11b)[148]. Many other studies have also produced white UC emissions through doping with two or more RE^{3+} activators (Figure 1.11c)[149-150]. Since blue, green, and red are the three primary colours that can be combined to produce other colours, the appropriate co-doping of different RE^{3+} activator combinations can generate a large range of emission spectra in the NIR-UV spectral.

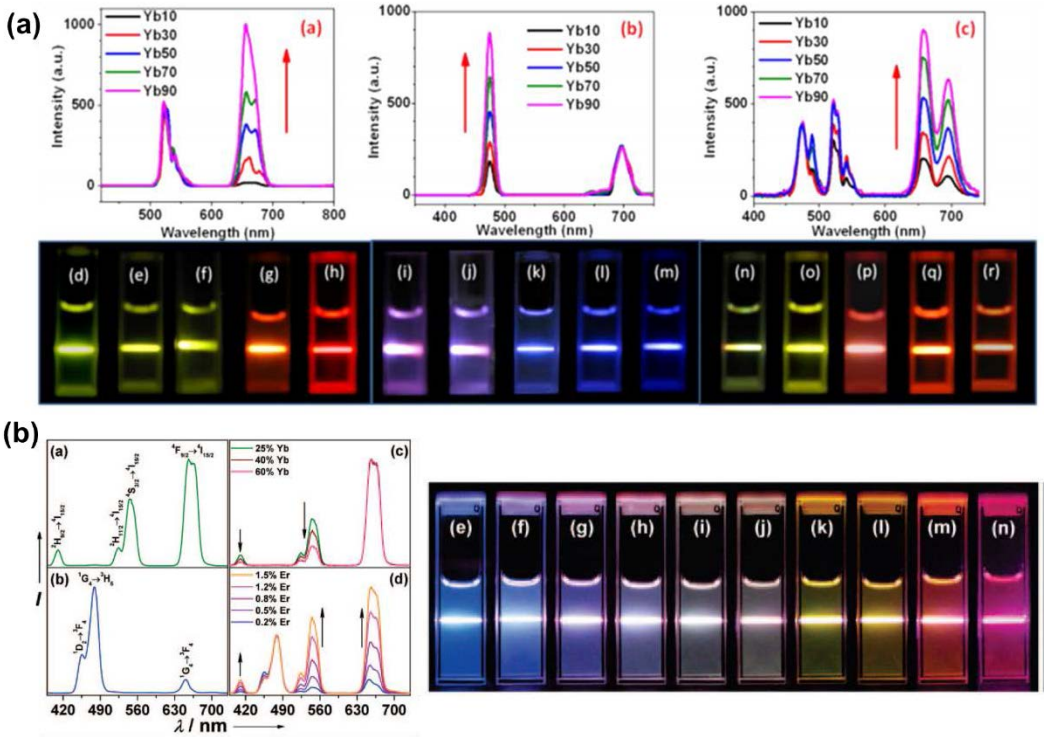

Figure 1.12 Tuneable luminescence emission by precise control of the emission intensity balance through control of different combinations of RE^{3+} dopants and dopant concentrations (a) [151]; A number of colour outputs in ultra-small YF_3 nanocrystals produced by varying the concentration of Yb^{3+} ions (b) [152]

Multicolour UC emissions can be produced not only by using different single activators or combinations of dopants but also by tuning the doping level to modulate the colour of the emission and the relative emission intensities. For example, Liu et al. reported a general and versatile approach to fine-tune UC emission colours based upon a single host source of $NaYF_4$ nanoparticles doped with Yb^{3+}, Tm^{3+}, and Er^{3+} [151]. By precise control of the emission intensity balance through the use of different combinations of RE^{3+} dopants and dopant concentrations, the luminescence emission could be deliberately tuned from visible to NIR under single-wavelength excitation (Figure 1.12a). Han et al. varied the concentration of Yb^{3+} ions to modulate the interaction between the sensitizer and the activator, which generated a number of colour outputs in ultra-small YF_3 nanocrystals

doped with Yb^{3+}/Er^{3+}, Yb^{3+}/Tm^{3+} and $Yb^{3+}/Er^{3+}/Tm^{3+}$ under single-wavelength excitation of 980 nm (Figure 1.12b)[152].

Some transition metal ions, such as Mn^{2+}, also can be doped in UC materials to tune the UC emission colour. Zhao et al. presented a facile strategy for the rational manipulation of green and red UC emissions, and the pure dark red emission of $NaYF_4:Yb^{3+}/Er^{3+}$ UCNPs by manganese-ion (Mn^{2+}) doping[153]. The existence of Mn^{2+} ions disturbs the transition possibilities between the green and red emissions of Er^{3+} and facilitates red emission, resulting in a range of emission colours (from green to red) by variation of the Mn^{2+}-doping level (Figure 1.13).

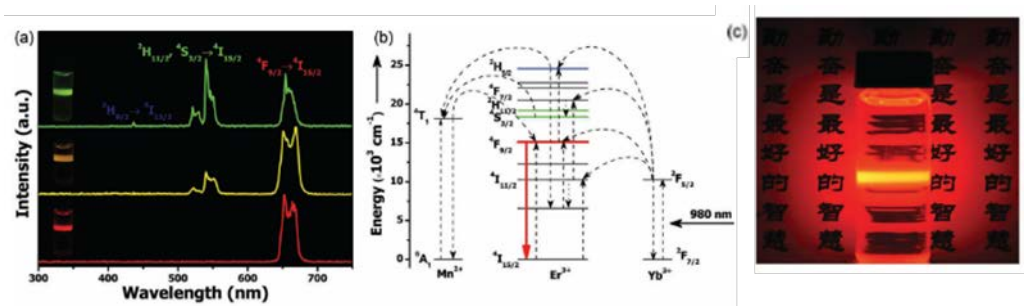

Figure 1.13 Photoluminescence studies of $NaYF_4:Yb^{3+}/Er^{3+}$ nanoparticles with various Mn^{2+} dopant concentrations: room temperature UC emission spectra of $NaYF_4:Yb^{3+}/Er^{3+}$ nanocrystals with 0, 5 and 30 mol% Mn^{2+} dopant ions, respectively (a); schematic energy level diagram showing the possible UC mechanism of Mn^{2+}-doped $NaYF_4:Yb^{3+}/Er^{3+}$ nanocrystals (b); luminescent photograph of 30 mol% Mn^{2+}-doped UCNPs dispersed in cyclohexane (c) [153]

1.5.2 Energy migration-mediated upconversion pathways

Efficient UC emission is generally limited to RE^{3+} activators of Er^{3+}, Tm^{3+}, and Ho^{3+} ions. However, with the new UC mechanism of energy migration-mediated UC (EMU), efficient multicolour UC emission is also possible for RE^{3+} activators without long-lived intermediate energy states[154-158]. Liu et al. reported that through the use of Gd-mediated energy migration and core-shell engineering, efficient multicolour luminescence can be achieved in $NaGdF_4:Yb^{3+}$, Tm^{3+}@$NaGdF_4:X^{3+}$ (X = Eu, Tb, Dy, or Sm) core-shell nanoparticles with RE^{3+} ions separately incorporated into the cores and shell layers of the nanoparticles (Figures 1.14a-c)[54]. In the case of the energy migration approach, Tm^{3+} is used as a ladder to assist energy transfer from a sensitizer ion to a migratory ion and then to an activator ion, while Gd^{3+} ions effectively bridge the energy transfer gap from sensitizer/accumulator to activators through long-range energy migration in the sub-lattice. The ability to accomplish UC PL with a rather wide range of activators expands

the applications of RE^{3+}-doped nanoparticles. Importantly, a $NaYF_4$ shell-coating on $NaGdF_4:Yb^{3+}$, Tm^{3+}@$NaGdF_4:X^{3+}$ (X = Eu, Tb, Dy, or Sm) nanoparticles allows tuneable upconversion emissions with a variety of activators (Dy^{3+}, Sm^{3+}, Tb^{3+}, and Eu^{3+}) doped at very low concentrations. Zhang et al. designed an integrated full-spectrum upconversion nanostructure by optimizing the pathways of photon transitions from a set of selected RE^{3+} ions[47]. The $NaGdF_4$: Yb^{3+}/Tm^{3+}/Er@$NaGdF_4$: Eu@$NaYF_4$ nanostructure accommodates six kinds of RE^{3+} ions that produce tuneable light (Figures 1.14d and e). Note that the emission of Eu^{3+} ions here comes from energy transfer through the EMU route. The RGB emitters exhibit different spectral sensitivities to the excitation laser's power density and, thus, allow the modulation of a wide range of emission colours.

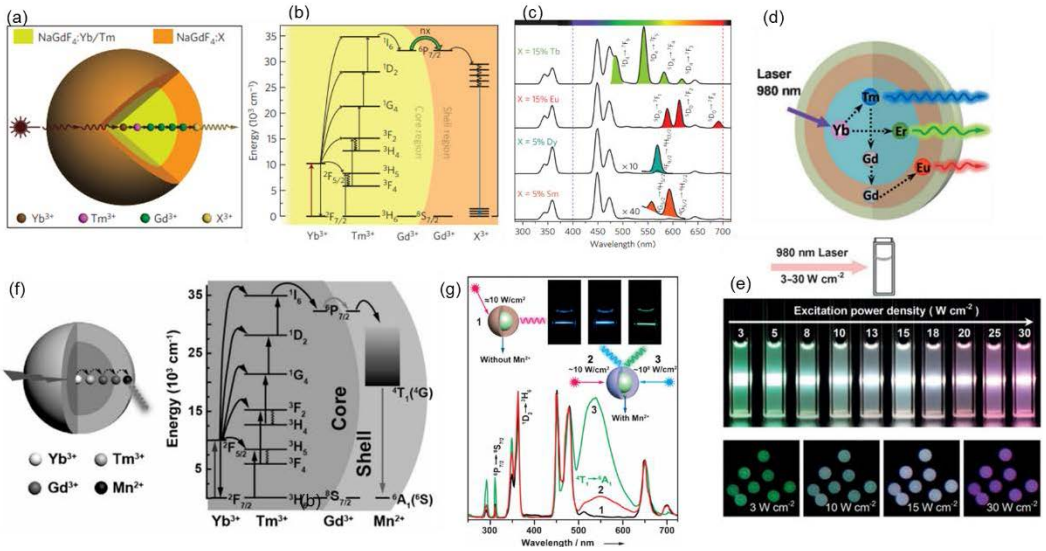

Figure 1.14 Tuning UC through energy migration in UCNPs (a-c): (a) Schematic illustration of a RE^{3+}-doped $NaGdF_4$@$NaGdF_4$ core-shell nanoparticles for energy migration-mediated UC; (b) proposed energy transfer mechanisms; (c) UC fluorescence spectra of the as-prepared UC nanoparticles[54]. Full-spectral upconversion prepared by optimizing the pathways of photon transitions (d and e): (d) white-light-emitting nanostructure; (e) multicolour luminescence of nanocrystals[47]. UC emissions of Mn^{2+} ions through EMU (f and g): (f) schematic illustration of migration-mediated UC mechanism; (g) UC spectra of Mn^{2+} showing broad 550 nm emission peak[159]

Through this EMU process, some transition metal ions, which do not readily exhibit UC luminescence in single-doping systems, also show colour-tuneable UC emissions[159]. Mn^{2+} ions act as an excellent UC luminescence activator, showing very long lifetime green UC luminescence by taking advantage of energy transfer through Yb→Tm→Gd→Mn in $NaGdF_4$: Yb^{3+}/Tm^{3+}@$NaGdF_4$: Mn core-shell nanoparticles (Figures 1.4f and g). Liu et al. have also demonstrated that the integration of long-lived

Mn^{2+} UC emission and relatively short-lived RE^{3+} UC emission in a particulate platform allows the generation of binary temporal codes for efficient data encoding[50].

1.5.3 Utilization of luminescence radiative reabsorption or Forster resonance energy transfer

Luminescence radiative reabsorption (LRR) or Forster resonance energy transfer (FRET) always occurs in a composite system of different kinds of luminescent materials. One of the materials is an energy donor and the another is an acceptor. When utilizing UCNPs as an energy donor and dye or quantum dots (QDs) as an energy acceptor, a wider range of multicolour UC emission wavelengths is possible than when merely using RE^{3+} ions[160-162].

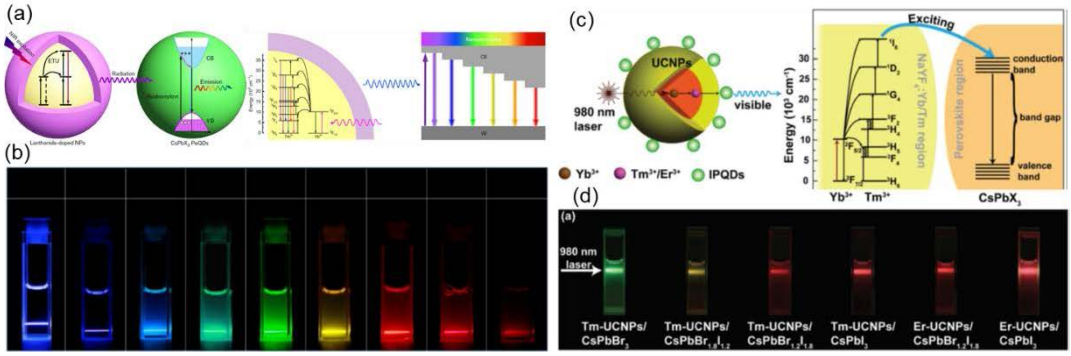

Figure 1.15 Full-colour upconversion tuning in $CsPbX_3$ PQDs through LRR sensitization by $LiYbF_4$:0.5%Tm^{3+}@$LiYF_4$ core/shell NPs, and schematic illustration of full-colour upconversion tuning in $CsPbX_3$ PeQDs through sensitization (a); photographs of samples under 980 nm showing colour tuning through bandgap tailoring of PQDs (b)[163]. Schematic representation of the LRR processes in $CsPbX_3$ perovskite quantum dots (PQDs) through sensitization by RE^{3+}-doped $NaYF_4$: Yb^{3+}/Tm^{3+}@$NaYF_4$ and $NaYF_4$: Yb^{3+}/Er^{3+}@$NaYF_4$ nanoparticles (c); photographs of samples under 980 nm illumination showing multicoloured emissions from green to red (d)[164].

Luminescence radiative reabsorption (LRR) is a radiative process where the light emitted by a donor is absorbed by an acceptor. Chen et al. reported an approach to fine-tuning the UC luminescence of $CsPbX_3$ PQDs through LRR sensitization by RE^{3+}-doped $LiYbF_4$:Tm^{3+}@$LiYF_4$ UCNPs (Figures 1.15a and b)[163]. Their experimental results showed that the emissions of the UCNPs could be efficiently absorbed by the PQDs, enabling single-band emissions under invisible NIR illumination at 980 nm. They demonstrated that the sensitization is governed by a radiative energy transfer conversion process; in other words, LRR(or radiative energy transfer, RET). As a result, tuneable UC emissions with wavelengths beyond those of RE^{3+}-doped NPs was realized via bandgap tailoring of PQDs. Short after, Dong et al. reported the design of UC nanoparticle-coupled

perovskite quantum dots that are full-colour tuneable under single NIR excitation (Figures 1.15c and d)[164]. Core-shell nanostructures of $NaYF_4$: Yb^{3+}/Tm^{3+}@$NaYF_4$ and $NaYF_4$: Yb^{3+}/Er^{3+}@$NaYF_4$ were synthesized and coupled with all-inorganic perovskite quantum dots (PQDs; $CsPbX_3$, X = Cl, Br, or I). Despite using only a simple mixing process, LRR sensitization between the two kinds of materials led to the convenient implementation of multicolour-emitting single-band emissions under NIR excitation.

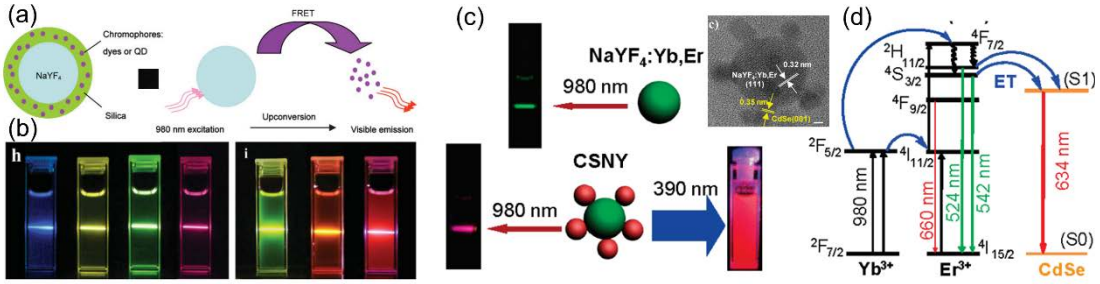

Figure 1.16 Schematic illustration of FRET-based RE^{3+}-doped core/shell $NaYF_4$@silica UCNPs (a); photographs of the UC luminescence of $NaYF_4$: Yb^{3+}/Tm^{3+}, $NaYF_4$: Yb^{3+}/Er^{3+}, $NaYF_4$: Yb^{3+}/Er^{3+} through green and red filters, and $NaYF_4$: Yb^{3+}/Tm^{3+}@FITC-doped silica, $NaYF_4$: Yb^{3+}/Er^{3+}@TRITC-doped silica, and $NaYF_4$: Yb^{3+}/Tm^{3+}@QD605-doped silica nanospheres (b, from left to right) [165]. Photographs of emission and TEM images from $NaYF_4$: Yb,Er nanoparticles and CdSe QDs attached to $NaYF_4$: Yb^{3+}/Er^{3+} NP heterostructures (c); schematic illustration of energy transfer in such a nanoheterostructure (d)[166]

Forster resonance energy transfer (FRET) is a mechanism of energy transfer from donor to acceptor through nonradiative dipole-dipole coupling. The difference between LRR and FRET is that the energy transfer process in LRR is radiative, whereas it is nonradiative in FRET[167-170]. For example, Chen et al. reported on the tuneable multicolour luminescence of $NaYF_4$: Yb,Er/Tm nanoparticles via FRET sensitization from UCNPs to organic dyes loaded in an amphiphilic polymer. Zhang et al. prepared core/shell-structured pure-hexagonal-phase $NaYF_4$: Yb,Er/Tm nanospheres with very thin and uniform silica coatings (Figure 1.16a)[165]. The nanospheres emit strong NIR-to-visible upconversion fluorescence (Figure 1.16b). Multicolour upconversion fluorescent nanospheres were produced by encapsulating organic dyes or QDs into the silica shells, and upconversion fluorescence was generated based on FRET, from the $NaYF_4$ core to the organic dyes or QDs. To generate effective FRET sensitization between two materials, the association and separation of donors and acceptors should be in the range of 1–10 nm[68]. Apart from mixing and conjunction approaches, hybrid heterostructures of two kinds of luminescent nanomaterials are particularly suitable for such FRET sensitization and can enable the tuning of emission colour. Yan et al. reported a synthesis of new

nanoheterostructures consisting of $NaYF_4$: Yb^{3+}/Er^{3+} nanoparticles dendritically decorated with CdSe QDs (Figures 1.16c and d)[166]. These materials combine up-converting and semiconducting properties, can up-convert NIR photons, and use the created excitons to generate charge carriers in CdSe, resulting in red emission by QDs under excitation of 980 nm.

Although organic dyes and quantum dots offer improved emission tuneability, FRET mechanisms have been utilized without sufficient understanding until now. For example, Morgan et al. suggested that radiative reabsorption might also contribute to energy transfer from RE^{3+} ions to dye or quantum dots, although it is generally believed that FRET mediates the optical interaction[27, 171]. There are many opportunities to tune UC emission by coupling UC mechanisms to other types of emitters through FRET. These may open totally new design paths for achieving wide tunability at high efficiency, and resolve the roles of radiative reabsorption and FRET.

1.6 Thesis aims and outline

Despite researchers having developed various strategies for fine-tuning the multicolour luminescence of UC materials over the past few years, one useful application remains to be developed: the controlled synthesis of UC materials with tuneable multicoloured emissions, high-throughput production, wide gamut and high performance. To enrich the multicolour properties, doped UC materials require elaborate control of the RE^{3+} dopants acting as the optical centres. Since RE^{3+} ions feature ladder-like-arranged energy levels that produce emission bands, the gamut of UC luminescence is limited because of the fixed characteristics of the emissions produced by level transitions. The range of upconverted emissions is unable to cover the full panchromatic range. To obtain excellent multicolour UC materials, especially UCNPs, repeated synthesis can be used to regulate the compositional arrangements of RE^{3+} ions in UC materials but is resource- and time-consuming. One has to perform a new set of reactions and have stringent control over a variety of experimental conditions, including the amount and concentration of dopant ions, the kinds of surfactants and solvent used, the reaction time and the temperature. These drawbacks may also raise safety and environmental concerns. Notably, the interaction between the optical centres that are spatially confined within a structure exerts a strong

influence on the emission profile of the material. Therefore, exploring the existence and distribution behaviour of doped ions in UC materials and understanding the energy transfer networks between sensitizer and activator ions within interior structures are prerequisites to achieving multicolour luminescence.

This thesis aims to 1) explore the distribution of doped RE^{3+} ions in UC materials and 2) achieve the controlled synthesis of UC materials with multicolour emissions, high-throughput production, wide gamut and high performance. The author will systematically introduce several strategies, including doping with various RE^{3+} ions, energy migration-mediated UC, and Forster resonance energy transfer (FRET), to fine-tune the multicolour luminescence produced. These studies will offer colourful luminescence for light-based applications, enabling a range of applications such as multiplexed biological labelling, anti-counterfeiting, and graphics imaging and display.

Specifically, the distribution of doped RE^{3+} ions in RE^{3+} (RE = Er, Ho, Tm)-doped alkaline indium oxide bulk materials and RE^{3+} (RE = Tm, Tb, Eu)-doped fluoride UC nanoparticles is explored to understand the multicolour luminescence produced by the network of energy transfer systems within their interior structures. Secondly, resource- and time-saving cation exchange methods are developed for fine-tuning the multicolour emission and strongly-luminescent properties of UC materials while preserving the original size, morphology and crystal phase of the nanoparticles. Based on the new cation exchange synthesis strategy, a hybrid heterostructure consisting of UCNPs and lead halide perovskite quantum dots (PQDs) is developed to fine-tune the multicolour luminescent gamut through FRET sensitization. Finally, a summary of the research presented in this thesis is presented. The results described in this thesis improve our knowledge of cation exchange strategies and heterostructure growth, and open up new opportunities for their synthesis.

1.7 References

1. Wisser, M. D.; Fischer, S.; Siefe, C.; Alivisatos, A. P.; Salleo, A.; Dionne, J. A., Improving Quantum Yield of Upconverting Nanoparticles in Aqueous Media via Emission Sensitization. *Nano Lett* **2018,** *18* (4), 2689-2695.

2. Tansil, N. C.; Li, Y.; Teng, C. P.; Zhang, S.; Win, K. Y.; Chen, X.; Liu, X. Y.; Han, M. Y., Intrinsically colored and luminescent silk. *Adv Mater* **2011,** *23* (12), 1463-6.

3. Shaner, N. C.; Campbell, R. E.; Steinbach, P. A.; Giepmans, B. N.; Palmer, A. E.; Tsien, R. Y., Improved monomeric red, orange and yellow fluorescent proteins derived from Discosoma sp. red fluorescent protein. *Nat Biotechnol* **2004,** *22* (12), 1567-72.

4. Kim, T.-H.; Cho, K.-S.; Lee, E. K.; Lee, S. J.; Chae, J.; Kim, J. W.; Kim, D. H.; Kwon, J.-Y.; Amaratunga, G.; Lee, S. Y.; Choi, B. L.; Kuk, Y.; Kim, J. M.; Kim, K., Full-colour quantum dot displays fabricated by transfer printing. *Nature Photonics* **2011,** *5* (3), 176-182.

5. Meinardi, F.; McDaniel, H.; Carulli, F.; Colombo, A.; Velizhanin, K. A.; Makarov, N. S.; Simonutti, R.; Klimov, V. I.; Brovelli, S., Highly efficient large-area colourless luminescent solar concentrators using heavy-metal-free colloidal quantum dots. *Nat Nanotechnol* **2015,** *10* (10), 878-85.

6. Dorokhin, D.; Tomczak, N.; Han, M.; Reinhoudt, D. N.; H., V. A.; Vancso, G. J., Reversible Phase Transfer of (CdSe/ZnS) Quantum Dots between Organic and Aqueous Solutions. *ACS Nano* **2009,** *3*, 661-667.

7. Pellet, N.; Teuscher, J.; Maier, J.; Grätzel, M., Transforming Hybrid Organic Inorganic Perovskites by Rapid Halide Exchange. *Chemistry of Materials* **2015,** *27* (6), 2181-2188.

8. Parobek, D.; Roman, B. J.; Dong, Y.; Jin, H.; Lee, E.; Sheldon, M.; Son, D. H., Exciton-to-Dopant Energy Transfer in Mn-Doped Cesium Lead Halide Perovskite Nanocrystals. *Nano Lett* **2016,** *16* (12), 7376-7380.

9. Makarov, N. S.; Guo, S.; Isaienko, O.; Liu, W.; Robel, I.; Klimov, V. I., Spectral and Dynamical Properties of Single Excitons, Biexcitons, and Trions in Cesium-Lead-Halide Perovskite Quantum Dots. *Nano Lett* **2016,** *16* (4), 2349-62.

10. Akkerman, Q. A.; D'Innocenzo, V.; Accornero, S.; Scarpellini, A.; Petrozza, A.; Prato, M.; Manna, L., Tuning the Optical Properties of Cesium Lead Halide Perovskite Nanocrystals by Anion Exchange Reactions. *J Am Chem Soc* **2015,** *137* (32), 10276-81.

11. Haase, M.; Schafer, H., Upconverting nanoparticles. *Angew Chem Int Ed* **2011,** *50* (26), 5808-29.

12. Xia, Z.; Wu, W., Preparation and luminescence properties of Ce^{3+} and Ce^{3+}/Tb^{3+}-activated $Y_4Si_2O_7N_2$ phosphors. *Dalton Trans* **2013,** *42* (36), 12989-97.

13. Zhuang, J.; Yang, X.; Fu, J.; Liang, C.; Wu, M.; Wang, J.; Su, Q., Monodispersed β-$NaYF_4$ Mesocrystals: In Situ Ion Exchange and Multicolor Up- and Down-Conversions. *Crystal Growth & Design* **2013,** *13* (6), 2292-2297.

14. Zhou, J.; Leano, J. L., Jr.; Liu, Z.; Jin, D.; Wong, K. L.; Liu, R. S.; Bunzli, J. G., Impact of Lanthanide Nanomaterials on Photonic Devices and Smart Applications. *Small* **2018,** *14* (40), e1801882.

15. Zheng, W.; Huang, P.; Tu, D.; Ma, E.; Zhu, H.; Chen, X., Lanthanide-doped upconversion nano-bioprobes: electronic structures, optical properties, and biodetection. *Chem Soc Rev* **2015,** *44* (6), 1379-415.

16. Wilhelm, S., Perspectives for Upconverting Nanoparticles. *ACS Nano* **2017,** *11* (11), 10644-10653.

17. Aharonovich, I.; Englund, D.; Toth, M., Solid-state single-photon emitters. *Nature Photonics* **2016,** *10* (10), 631-641.

18. Bailey, R. E.; Nie, S., Alloyed Semiconductor Quantum Dots: Tuning the Optical Properties without Changing the Particle Size. *J Am Chem Soc* **2003,** *125*, 7100-7106.

19. Jiang, K.; Sun, S.; Zhang, L.; Lu, Y.; Wu, A.; Cai, C.; Lin, H., Red, green, and blue luminescence by carbon dots: full-color emission tuning and multicolor cellular imaging. *Angew Chem Int Ed* **2015,** *54* (18), 5360-3.

20. Wang, X.; Qu, K.; Xu, B.; Ren, J.; Qu, X., Multicolor luminescent carbon nanoparticles: Synthesis, supramolecular assembly with porphyrin, intrinsic peroxidase-like catalytic activity and applications. *Nano Research* **2011,** *4* (9), 908-920.

21. Liu, D.; Xu, X.; Du, Y.; Qin, X.; Zhang, Y.; Ma, C.; Wen, S.; Ren, W.; Goldys, E. M.; Piper, J. A.; Dou, S.; Liu, X.; Jin, D., Three-dimensional controlled growth of monodisperse sub-50 nm heterogeneous nanocrystals. *Nat Commun* **2016,** *7*, 10254.

22. Zhou, B.; Shi, B.; Jin, D.; Liu, X., Controlling upconversion nanocrystals for emerging applications. *Nat Nanotechnol* **2015,** *10* (11), 924-36.

23. Wang, F.; Han, Y.; Lim, C. S.; Lu, Y.; Wang, J.; Xu, J.; Chen, H.; Zhang, C.; Hong, M.; Liu, X., Simultaneous phase and size control of upconversion nanocrystals through lanthanide doping. *Nature* **2010,** *463* (7284), 1061-5.

24. Dong, H.; Sun, L. D.; Wang, Y. F.; Ke, J.; Si, R.; Xiao, J. W.; Lyu, G. M.; Shi, S.; Yan, C. H., Efficient Tailoring of Upconversion Selectivity by Engineering Local Structure of Lanthanides in Na_xREF_{3+x} Nanocrystals. *J Am Chem Soc* **2015,** *137* (20), 6569-76.

25. Deng, R.; Qin, F.; Chen, R.; Huang, W.; Hong, M.; Liu, X., Temporal full-colour tuning through non-steady-state upconversion. *Nat Nanotechnol* **2015,** *10* (3), 237-42.

26. Yao, C.; Wang, P.; Li, X.; Hu, X.; Hou, J.; Wang, L.; Zhang, F., Near-Infrared-Triggered Azobenzene-Liposome/Upconversion Nanoparticle Hybrid Vesicles for Remotely Controlled Drug Delivery to Overcome Cancer Multidrug Resistance. *Adv Mater* **2016,** *28* (42), 9341-9348.

27. Wang, F.; Liu, X., Multicolor tuning of lanthanide-doped nanoparticles by single wavelength excitation. *Acc Chem Res* **2014,** *47* (4), 1378-85.

28. Gai, S.; Li, C.; Yang, P.; Lin, J., Recent progress in rare earth micro/nanocrystals: soft chemical synthesis, luminescent properties, and biomedical applications. *Chem Rev* **2014,** *114* (4), 2343-89.

29. Zhang, F.; Braun, G. B.; Pallaoro, A.; Zhang, Y.; Shi, Y.; Cui, D.; Moskovits, M.; Zhao, D.; Stucky, G. D., Mesoporous multifunctional upconversion luminescent and magnetic "nanorattle" materials for targeted chemotherapy. *Nano Lett* **2012,** *12* (1), 61-7.

30. Mader, H. S.; Kele, P.; Saleh, S. M.; Wolfbeis, O. S., Upconverting luminescent nanoparticles for use in bioconjugation and bioimaging. *Curr Opin Chem Biol* **2010,** *14* (5), 582-96.

31. Liu, Y.; Kang, N.; Lv, J.; Zhou, Z.; Zhao, Q.; Ma, L.; Chen, Z.; Ren, L.; Nie, L., Deep Photoacoustic/Luminescence/Magnetic Resonance Multimodal Imaging in Living Subjects Using High-Efficiency Upconversion Nanocomposites. *Adv Mater* **2016,** *28* (30), 6411-9.

32. He, H.; Howard, C. B.; Chen, Y.; Wen, S.; Lin, G.; Zhou, J.; Thurecht, K. J.; Jin, D., Bispecific Antibody-Functionalized Upconversion Nanoprobe. *Anal Chem* **2018,** *90* (5), 3024-3029.

33. Gai, S.; Yang, P.; Li, C.; Wang, W.; Dai, Y.; Niu, N.; Lin, J., Synthesis of Magnetic, Up-Conversion Luminescent, and Mesoporous Core-Shell-Structured Nanocomposites as Drug Carriers. *Advanced Functional Materials* **2010,** *20* (7), 1166-1172.

34. Huang, X.; Han, S.; Huang, W.; Liu, X., Enhancing solar cell efficiency: the search for luminescent materials as spectral converters. *Chem Soc Rev* **2013,** *42* (1), 173-201.

35. Liu, Y.; Lu, Y.; Yang, X.; Zheng, X.; Wen, S.; Wang, F.; Vidal, X.; Zhao, J.; Liu, D.; Zhou, Z.; Ma, C.; Zhou, J.; Piper, J. A.; Xi, P.; Jin, D., Amplified stimulated emission in upconversion nanoparticles for super-resolution nanoscopy. *Nature* **2017,** *543* (7644), 229-233.

36. Zhong, Y.; Ma, Z.; Zhu, S.; Yue, J.; Zhang, M.; Antaris, A. L.; Yuan, J.; Cui, R.; Wan, H.; Zhou, Y.; Wang, W.; Huang, N. F.; Luo, J.; Hu, Z.; Dai, H., Boosting the down-shifting luminescence of rare-earth nanocrystals for biological imaging beyond 1500 nm. *Nat Commun* **2017,** *8* (1), 737.

37. Yang, P.; Gai, S.; Lin, J., Functionalized mesoporous silica materials for controlled drug delivery. *Chem Soc Rev* **2012,** *41* (9), 3679-98.

38. Wang, L.; Li, Y., Green upconversion nanocrystals for DNA detection. *Chem Commun (Camb)* **2006,** (24), 2557-9.

39. Qian, H. S.; Guo, H. C.; Ho, P. C.; Mahendran, R.; Zhang, Y., Mesoporous-silica-coated up-conversion fluorescent nanoparticles for photodynamic therapy. *Small* **2009,** *5* (20), 2285-90.

40. Dou, Q.; Idris, N. M.; Zhang, Y., Sandwich-structured upconversion nanoparticles with tunable color for multiplexed cell labeling. *Biomaterials* **2013,** *34* (6), 1722-31.

41. Zhou, J.; Liu, Z.; Li, F., Upconversion nanophosphors for small-animal imaging. *Chem Soc Rev* **2012,** *41* (3), 1323-49.

42. Liu, Q.; Feng, W.; Li, F., Water-soluble lanthanide upconversion nanophosphors: Synthesis and bioimaging applications in vivo. *Coordination Chemistry Reviews* **2014,** *273-274*, 100-110.

43. McGuinness, L. P.; Yan, Y.; Stacey, A.; Simpson, D. A.; Hall, L. T.; Maclaurin, D.; Prawer, S.; Mulvaney, P.; Wrachtrup, J.; Caruso, F.; Scholten, R. E.; Hollenberg, L. C., Quantum measurement and orientation tracking of fluorescent nanodiamonds inside living cells. *Nat Nanotechnol* **2011,** *6* (6), 358-63.

44. Zhao, J.; Jin, D.; Schartner, E. P.; Lu, Y.; Liu, Y.; Zvyagin, A. V.; Zhang, L.; Dawes, J. M.; Xi, P.; Piper, J. A.; Goldys, E. M.; Monro, T. M., Single-nanocrystal sensitivity achieved by enhanced upconversion luminescence. *Nat Nanotechnol* **2013,** *8* (10), 729-34.

45. Zhang, Y.; Zhang, L.; Deng, R.; Tian, J.; Zong, Y.; Jin, D.; Liu, X., Multicolor barcoding in a single upconversion crystal. *J Am Chem Soc* **2014,** *136* (13), 4893-6.

46. Lu, Y.; Zhao, J.; Zhang, R.; Liu, Y.; Liu, D.; Goldys, E. M.; Yang, X.; Xi, P.; Sunna, A.; Lu, J.; Shi, Y.; Leif, R. C.; Huo, Y.; Shen, J.; Piper, J. A.; Robinson, J. P.; Jin, D., Tunable lifetime multiplexing using luminescent nanocrystals. *Nature Photonics* **2013,** *8* (1), 32-36.

47. Zhang, C.; Yang, L.; Zhao, J.; Liu, B.; Han, M. Y.; Zhang, Z., White-Light Emission from an Integrated Upconversion Nanostructure: Toward Multicolor Displays Modulated by Laser Power. *Angew Chem Int Ed* **2015,** *54* (39), 11531-5.

48. Xu, G.; Zeng, S.; Zhang, B.; Swihart, M. T.; Yong, K. T.; Prasad, P. N., New Generation Cadmium-Free Quantum Dots for Biophotonics and Nanomedicine. *Chem Rev* **2016,** *116* (19), 12234-12327.

49. Gargas, D. J.; Chan, E. M.; Ostrowski, A. D.; Aloni, S.; Altoe, M. V.; Barnard, E. S.; Sanii, B.; Urban, J. J.; Milliron, D. J.; Cohen, B. E.; Schuck, P. J., Engineering bright sub-10-nm upconverting nanocrystals for single-molecule imaging. *Nat Nanotechnol* **2014,** *9* (4), 300-5.

50. Liu, X.; Wang, Y.; Li, X.; Yi, Z.; Deng, R.; Liang, L.; Xie, X.; Loong, D. T. B.; Song, S.; Fan, D.; All, A. H.; Zhang, H.; Huang, L.; Liu, X., Binary temporal upconversion codes of Mn^{2+}-activated nanoparticles for multilevel anti-counterfeiting. *Nat Commun* **2017,** *8* (1), 899.

51. Zhou, J.; Jin, D., Triplet state brightens upconversion. *Nature Photonics* **2018,** *12*, 378-385.

52. Auzel, F., Upconversion and Anti-Stokes Processes with f and d Ions in Solids. *Chem Rev* **2004,** *104*, 139-173.

53. Wang, F.; Liu, X., Recent advances in the chemistry of lanthanide-doped upconversion nanocrystals. *Chem Soc Rev* **2009,** *38* (4), 976-89.

54. Wang, F.; Deng, R.; Wang, J.; Wang, Q.; Han, Y.; Zhu, H.; Chen, X.; Liu, X., Tuning upconversion through energy migration in core-shell nanoparticles. *Nat Mater* **2011,** *10* (12), 968-73.

55. Plohl, O.; Kraft, M.; Kovac, J.; Belec, B.; Ponikvar-Svet, M.; Wurth, C.; Lisjak, D.; Resch-Genger, U., Optically Detected Degradation of $NaYF_4$:Yb,Tm-Based Upconversion Nanoparticles in Phosphate Buffered Saline Solution. *Langmuir* **2017,** *33* (2), 553-560.

56. Wang, J.; Deng, R.; MacDonald, M. A.; Chen, B.; Yuan, J.; Wang, F.; Chi, D.; Hor, T. S.; Zhang, P.; Liu, G.; Han, Y.; Liu, X., Enhancing multiphoton upconversion through energy clustering at sublattice level. *Nat Mater* **2014,** *13* (2), 157-62.

57. Zhang, J.; Wang, Y.; Guo, L.; Dong, P., Up-conversion luminescence and near-infrared quantum cutting in $Y_6O_5F_8:RE^{3+}$ (RE = Yb, Er, and Ho) with controllable morphologies by hydrothermal synthesis. *Dalton Trans* **2013,** *42* (10), 3542-51.

58. Yu, X.; Liang, S.; Sun, Z.; Duan, Y.; Qin, Y.; Duan, L.; Xia, H.; Zhao, P.; Li, D., Microstructure and upconversion luminescence in Ho^{3+} and Yb^{3+} co-doped ZnO naocrystalline powders. *Optics Communications* **2014,** *313*, 90-93.

59. Matsuura, D., Red, green, and blue upconversion luminescence of trivalent-rare-earth ion-doped Y_2O_3 nanocrystals. *Applied Physics Letters* **2002,** *81* (24), 4526-4528.

60. Li, Q.; Lin, J.; Wu, J.; Lan, Z.; Wang, Y.; Peng, F.; Huang, M., Enhancing photovoltaic performance of dye-sensitized solar cell by rare-earth doped oxide of Lu_2O_3:(Tm^{3+}, Yb^{3+}). *Electrochimica Acta* **2011,** *56* (14), 4980-4984.

61. Fischer, S.; Martín-Rodríguez, R.; Fröhlich, B.; Krämer, K. W.; Meijerink, A.; Goldschmidt, J. C., Upconversion quantum yield of Er^{3+}-doped β-$NaYF_4$ and Gd_2O_2S: The effects of host lattice, Er^{3+} doping, and excitation spectrum bandwidth. *Journal of Luminescence* **2014,** *153*, 281-287.

62. Hou, X.; Zhou, S.; Jia, T.; Lin, H.; Teng, H., Investigation of up-conversion luminescence properties of RE/Yb co-doped Y_2O_3 transparent ceramic (RE=Er, Ho, Pr, and Tm). *Physica B: Condensed Matter* **2011,** *406* (20), 3931-3937.

63. Tian, Y.; Tian, B.; Cui, C. e.; Huang, P.; Wang, L.; Chen, B., Size-dependent upconversion luminescence and temperature sensing behavior of spherical $Gd_2O_3:Yb^{3+}/Er^{3+}$ phosphor. *RSC Advances* **2015,** *5* (19), 14123-14128.

64. Zong, L.; Xu, P.; Ding, Y.; Zhao, K.; Wang, Z.; Yan, X.; Yu, R.; Chen, J.; Xing, X., $Y_2O_3:Yb^{3+}/Er^{3+}$ Hollow Spheres with Controlled Inner Structures and Enhanced Upconverted Photoluminescence. *Small* **2015,** *11* (23), 2768-73.

65. Li, T.; Guo, C.-F.; Yang, Y.-M.; Li, L.; Zhang, N., Efficient green up-conversion emission in Yb^{3+}/Ho^{3+} co-doped $CaIn_2O_4$. *Acta Materialia* **2013,** *61* (19), 7481-7487.

66. Li, T.; Guo, C.; Li, L., Up-conversion luminescence of Er^{3+}-Yb^{3+} co-doped $CaIn_2O_4$. *Opt Express* **2013,** *21* (15), 18281-9.

67. Li, T.; Guo, C.; Jiao, H.; Li, L.; Agrawal, D. K., Infrared-to-visible up-conversion luminescence of $CaIn_2O_4$ co-doped with RE^{3+}/Yb^{3+} (RE=Tm, Pr, Nd). *Optics Communications* **2014,** *312*, 284-286.

68. Chen, G.; Qiu, H.; Prasad, P. N.; Chen, X., Upconversion nanoparticles: design, nanochemistry, and applications in theranostics. *Chem Rev* **2014,** *114* (10), 5161-214.

69. Shannon, R. D., Revised effective ionic radii and systematic studies of interatomic distances in halides and chalcogenides. *Acta Crystallographica Section A* **1976,** *32* (5), 751-767.

70. Yang, Z.; Tian, J.; Wang, S.; Yang, G.; Li, X.; Li, P., Combustion synthesis of $SrIn_2O_4:Eu^{3+}$ red-emitting phosphor for white light-emitting diodes. *Materials Letters* **2008,** *62* (8-9), 1369-1371.

71. Wang, H.; Tian, L., Luminescence properties of $SrIn_2O_4:Eu^{3+}$ incorporated with Gd^{3+} or Sm^{3+} ions. *Journal of Alloys and Compounds* **2011,** *509* (6), 2659-2662.

72. Orlova, A. I.; Pleskova, S. N.; Malanina, N. V.; Shushunov, A. N.; Gorshkova, E. N.; Pudovkina, E. E.; Gorshkov, O. N., $Ca_3(PO_4)_2:Er^{3+},Yb^{3+}$: An upconversion phosphor for in vivo imaging. *Inorganic Materials* **2013,** *49* (7), 696-700.

73. Ji, H.; Huang, Z.; Xia, Z.; Molokeev, M. S.; Jiang, X.; Lin, Z.; Atuchin, V. V., Comparative investigations of the crystal structure and photoluminescence property of eulytite-type $Ba_3Eu(PO_4)_3$ and $Sr_3Eu(PO_4)_3$. *Dalton Trans* **2015,** *44* (16), 7679-86.

74. Ji, H.; Huang, Z.; Xia, Z.; Molokeev, M. S.; Atuchin, V. V.; Fang, M.; Huang, S., New yellow-emitting Whitlockite-type structure $Sr_{1.75}Ca_{1.25}(PO_4)_2:Eu^{2+}$ phosphor for near-UV pumped white light-emitting devices. *Inorg Chem* **2014,** *53* (10), 5129-35.

75. Li, P.; Wang, Z.; Yang, Z.; Guo, Q., $SrIn_2O_4:Eu^{3+}$, Sm^{3+}: A Red Emitting Phosphor with a Broadened Near-Ultraviolet Absorption Band for Solid-State Lighting. *Journal of The Electrochemical Society* **2011,** *158* (12).

76. Baszczuk, A.; Jasiorski, M.; Nyk, M.; Hanuza, J.; Mączka, M.; Stręk, W., Luminescence properties of europium activated $SrIn_2O_4$. *Journal of Alloys and Compounds* **2005,** *394* (1-2), 88-92.

77. Grzechnik, A.; Bouvier, P.; Mezouar, M.; Mathews, M. D.; Tyagi, A. K.; Köhler, J., Hexagonal $Na_{1.5}Y_{1.5}F_6$ at High Pressures. *Journal of Solid State Chemistry* **2002,** *165* (1), 159-164.

78. Zhou, S.; Jiang, S.; Wei, X.; Chen, Y.; Duan, C.; Yin, M., Optical thermometry based on upconversion luminescence in Yb^{3+}/Ho^{3+} co-doped $NaLuF_4$. *Journal of Alloys and Compounds* **2014,** *588*, 654-657.

79. Martín-Rodríguez, R.; Meijerink, A., Infrared to near-infrared and visible upconversion mechanisms in $LiYF_4$: Yb^{3+}, Ho^{3+}. *Journal of Luminescence* **2014,** *147*, 147-154.

80. Lin, H.; Chen, D.; Yu, Y.; Shan, Z.; Huang, P.; Wang, Y.; Yuan, J., Nd^{3+}-sensitized upconversion white light emission of Tm^{3+}/Ho^{3+} bridged by Yb^{3+} in β-YF_3 nanocrystals embedded transparent glass ceramics. *Journal of Applied Physics* **2010,** *107* (10).

81. Song, E.-H.; Ding, S.; Wu, M.; Ye, S.; Xiao, F.; Dong, G.-P.; Zhang, Q.-Y., Temperature-tunable upconversion luminescence of perovskite nanocrystals $KZnF_3$:Yb^{3+},Mn^{2+}. *Journal of Materials Chemistry C* **2013,** *1* (27).

82. Wang, J.; Wang, F.; Xu, J.; Wang, Y.; Liu, Y.; Chen, X.; Chen, H.; Liu, X., Lanthanide-doped $LiYF_4$ nanoparticles: Synthesis and multicolor upconversion tuning. *Comptes Rendus Chimie* **2010,** *13* (6-7), 731-736.

83. Wu, M.; Song, E. H.; Chen, Z. T.; Ding, S.; Ye, S.; Zhou, J. J.; Xu, S. Q.; Zhang, Q. Y., Single-band red upconversion luminescence of Yb^{3+}–Er^{3+}via nonequivalent substitution in perovskite $KMgF_3$ nanocrystals. *Journal of Materials Chemistry C* **2016,** *4* (8), 1675-1684.

84. Chen, C.-W.; Lee, P.-H.; Chan, Y.-C.; Hsiao, M.; Chen, C.-H.; Wu, P. C.; Wu, P. R.; Tsai, D. P.; Tu, D.; Chen, X.; Liu, R.-S., Plasmon-induced hyperthermia: hybrid upconversion $NaYF_4$:Yb/Er and gold nanomaterials for oral cancer photothermal therapy. *Journal of Materials Chemistry B* **2015,** *3* (42), 8293-8302.

85. Zhu, X.; Zhou, J.; Chen, M.; Shi, M.; Feng, W.; Li, F., Core-shell Fe_3O_4@$NaLuF_4$:Yb,Er/Tm nanostructure for MRI, CT and upconversion luminescence tri-modality imaging. *Biomaterials* **2012,** *33* (18), 4618-27.

86. Zhao, J.; Lu, Z.; Yin, Y.; McRae, C.; Piper, J. A.; Dawes, J. M.; Jin, D.; Goldys, E. M., Upconversion luminescence with tunable lifetime in $NaYF_4$:Yb,Er nanocrystals: role of nanocrystal size. *Nanoscale* **2013,** *5* (3), 944-52.

87. Shen, J.; Chen, G.; Vu, A.-M.; Fan, W.; Bilsel, O. S.; Chang, C.-C.; Han, G., Engineering the Upconversion Nanoparticle Excitation Wavelength: Cascade Sensitization of Tri-doped Upconversion Colloidal Nanoparticles at 800 nm. *Advanced Optical Materials* **2013,** *1* (9), 644-650.

88. Wang, Z.-L.; Hao, J. H.; Chan, H. L. W., Down- and up-conversion photoluminescence, cathodoluminescence and paramagnetic properties of $NaGdF_4 : Yb^{3+}$,Er^{3+} submicron disks assembled from primary nanocrystals. *Journal of Materials Chemistry* **2010,** *20* (16).

89. Song, Y.; Liu, G.; Dong, X.; Wang, J.; Yu, W.; Li, J., Au Nanorods@$NaGdF_4$/Yb^{3+},Er^{3+} Multifunctional Hybrid Nanocomposites with Upconversion Luminescence, Magnetism, and Photothermal Property. *The Journal of Physical Chemistry C* **2015,** *119* (32), 18527-18536.

90. Berry, M. T.; May, P. S., Disputed Mechanism for NIR-to-Red Upconversion Luminescence in $NaYF_4$:Yb^{3+},Er^{3+}. *J Phys Chem A* **2015,** *119* (38), 9805-11.

91. Zeng, J. H.; Su, J.; Li, Z. H.; Yan, R. X.; Li, Y. D., Synthesis and Upconversion Luminescence of Hexagonal-Phase $NaYF_4$:Yb, Er^{3+} Phosphors of Controlled Size and Morphology. *Advanced Materials* **2005,** *17* (17), 2119-2123.

92. Xia, Z.; Li, J.; Luo, Y.; Liao, L.; Varela, J., Comparative Investigation of Green and Red Upconversion Luminescence in Er^{3+}Doped and Yb^{3+}/Er^{3+}Codoped LaOCl. *Journal of the American Ceramic Society* **2012,** *95* (10), 3229-3234.

93. Luo, Y.; Xia, Z.; Liao, L., Phase formation evolution and upconversion luminescence properties of LaOF:Yb^{3+}/Er^{3+} prepared via a two-step reaction. *Ceramics International* **2012,** *38* (8), 6907-6910.

94. Wen, S.; Zhou, J.; Zheng, K.; Bednarkiewicz, A.; Liu, X.; Jin, D., Advances in highly doped upconversion nanoparticles. *Nat Commun* **2018,** *9* (1), 2415.

95. Xia, Z.; Du, P.; Liao, L., Facile hydrothermal synthesis and upconversion luminescence of tetragonal Sr_2LnF_7:Yb^{3+}/Er^{3+}(Ln = Y, Gd) nanocrystals. *physica status solidi (a)* **2013**, n/a-n/a.

96. Wu, Z.; Lin, M.; Liang, S.; Liu, Y.; Zhang, H.; Yang, B., Hot-Injection Synthesis of Manganese-Ion-Doped $NaYF_4$:Yb,Er Nanocrystals with Red Up-Converting Emission and Tunable Diameter. *Particle & Particle Systems Characterization* **2013,** *30* (4), 311-315.

97. Wang, R.; Zhang, X.; Liu, F.; Xiao, L.; Chen, Y.; Liu, L., Upconversion mechanisms of Er^{3+}:$NaYF_4$ and thermal effects induced by incident photon on the green luminescence. *Journal of Luminescence* **2016,** *175*, 35-43.

98. Wang, R.; Zhang, W.; Xu, Y.; Xing, L., Upconversion emissions in $ZnNb_2O_6$:Ho^{3+}/Yb^{3+} ceramics. *Optics & Laser Technology* **2014,** *58*, 52-55.

99. Xu, X.; Wang, Z.; Lei, P.; Yu, Y.; Yao, S.; Song, S.; Liu, X.; Su, Y.; Dong, L.; Feng, J.; Zhang, H., alpha-NaYb(Mn)F_4:Er^{3+}/Tm^{3+}@$NaYF_4$ UCNPs as "Band-Shape" Luminescent Nanothermometers over a Wide Temperature Range. *ACS Appl Mater Interfaces* **2015,** *7* (37), 20813-9.

100. Xing, L.; Wang, R.; Xu, W.; Qian, Y.; Xu, Y.; Yang, C.; Liu, X., Upconversion white-light emission in $Ho^{3+}/Yb^{3+}/Tm^{3+}$ codoped $LiNbO_3$ polycrystals. *Journal of Luminescence* **2012,** *132* (6), 1568-1574.

101. Patra, A.; Saha, S.; Alencar, M. A. R. C.; Rakov, N.; Maciel, G. S., Blue upconversion emission of Tm^{3+}–Yb^{3+} in ZrO_2 nanocrystals: Role of Yb^{3+} ions. *Chemical Physics Letters* **2005,** *407* (4-6), 477-481.

102. Li, Y.; Hong, G.; Zhang, Y.; Yu, Y., Red and green upconversion luminescence of Gd_2O_3:Er^{3+}, Yb^{3+} nanoparticles. *Journal of Alloys and Compounds* **2008,** *456* (1-2), 247-250.

103. Li, D.; Wang, Y.; Zhang, X.; Yang, K.; Liu, L.; Song, Y., Optical temperature sensor through infrared excited blue upconversion emission in Tm^{3+}/Yb^{3+} codoped Y_2O_3. *Optics Communications* **2012,** *285* (7), 1925-1928.

104. Ma, C.; Xu, X.; Wang, F.; Zhou, Z.; Wen, S.; Liu, D.; Fang, J.; Lang, C. I.; Jin, D., Probing the Interior Crystal Quality in the Development of More Efficient and Smaller Upconversion Nanoparticles. *J Phys Chem Lett* **2016,** *7* (16), 3252-8.

105. Ma, C.; Xu, X.; Wang, F.; Zhou, Z.; Liu, D.; Zhao, J.; Guan, M.; Lang, C. I.; Jin, D., Optimal Sensitizer Concentration in Single Upconversion Nanocrystals. *Nano Lett* **2017,** *17* (5), 2858-2864.

106. Yang, Y.; Mi, C.; Yu, F.; Su, X.; Guo, C.; Li, G.; Zhang, J.; Liu, L.; Liu, Y.; Li, X., Optical thermometry based on the upconversion fluorescence from Yb^{3+}/Er^{3+} codoped La_2O_2S phosphor. *Ceramics International* **2014,** *40* (7), 9875-9880.

107. Xia, Z.; Zhou, W.; Du, H.; Sun, J., Synthesis and spectral analysis of $Yb^{3+}/Tm^{3+}/Ho^{3+}$-doped $Na_{0.5}Gd_{0.5}WO_4$ phosphor to achieve white upconversion luminescence. *Materials Research Bulletin* **2010,** *45* (9), 1199-1202.

108. Wang, Z.; Xia, Z.; Molokeev, M. S.; Atuchin, V. V.; Liu, Q., Blue-shift of Eu^{2+} emission in $(Ba,Sr)_3Lu(PO_4)_3:Eu^{2+}$ eulytite solid-solution phosphors resulting from release of neighbouring-cation-induced stress. *Dalton Trans* **2014,** *43* (44), 16800-4.

109. Lisjak, D.; Plohl, O.; Vidmar, J.; Majaron, B.; Ponikvar-Svet, M., Dissolution Mechanism of Upconverting AYF_4:Yb,Tm (A = Na or K) Nanoparticles in Aqueous Media. *Langmuir* **2016,** *32* (32), 8222-9.

110. Lisjak, D.; Plohl, O.; Ponikvar-Svet, M.; Majaron, B., Dissolution of upconverting fluoride nanoparticles in aqueous suspensions. *RSC Advances* **2015,** *5* (35), 27393-27397.

111. Yang, L. W.; Li, Y.; Li, Y. C.; Li, J. J.; Hao, J. H.; Zhong, J. X.; Chu, P. K., Quasi-seeded growth, phase transformation, and size tuning of multifunctional hexagonal $NaLnF_4$(Ln = Y, Gd, Yb) nanocrystalsvia in situcation-exchange reaction. *J. Mater. Chem.* **2012,** *22* (5), 2254-2262.

112. Vennerberg, D.; Lin, Z., Upconversion Nanocrystals: Synthesis, Properties, Assembly and Applications. *Science of Advanced Materials* **2011,** *3* (1), 26-40.

113. Li, D.; Lai, W.-Y.; Shao, Q.; Huang, W., A facile methodology for regulating the size of hexagonal $NaYF_4:Yb^{3+},Er^{3+}$ upconversion nanocrystals. *New J. Chem.* **2017,** *41* (20), 11521-11524.

114. Fischer, S.; Swabeck, J. K.; Alivisatos, A. P., Controlled Isotropic and Anisotropic Shell Growth in beta-$NaLnF_4$ Nanocrystals Induced by Precursor Injection Rate. *J Am Chem Soc* **2017,** *139* (35), 12325-12332.

115. Chen, G.; Agren, H.; Ohulchanskyy, T. Y.; Prasad, P. N., Light upconverting core-shell nanostructures: nanophotonic control for emerging applications. *Chem Soc Rev* **2015,** *44* (6), 1680-713.

116. Fan, S.; Wang, S.; Xu, W.; Li, M.; Sun, H.; Hu, L., Enormously enhanced upconversion emission in β-$NaYF_4$:20Yb,2Er microcrystals via Na^+ ion exchange. *Journal of Materials Science* **2016,** *52* (2), 869-877.

117. Deng, M.; Wang, L., Unexpected luminescence enhancement of upconverting nanocrystals by cation exchange with well retained small particle size. *Nano Research* **2014,** *7* (5), 782-793.

118. Zhang, F.; Shi, Y.; Sun, X.; Zhao, D.; Stucky, G. D., Formation of Hollow Upconversion Rare-Earth Fluoride Nanospheres: Nanoscale Kirkendall Effect During Ion Exchange. *Chemistry of Materials* **2009,** *21* (21), 5237-5243.

119. Rivest, J. B.; Jain, P. K., Cation exchange on the nanoscale: an emerging technique for new material synthesis, device fabrication, and chemical sensing. *Chem Soc Rev* **2013,** *42* (1), 89-96.

120. Yuan, J.-L.; Zeng, X.-Y.; Zhao, J.-T.; Zhang, Z.-J.; Chen, H.-H.; Yang, X.-X., Energy transfer mechanisms in Tb^{3+}, Yb^{3+}codoped Y_2O_3downconversion phosphor. *Journal of Physics D: Applied Physics* **2008,** *41* (10).

121. Yu, X.; Qin, Y.; Gao, M.; Duan, L.; Jiang, Z.; Gou, L.; Zhao, P.; Li, Z., Hydrothermal synthesis and upconversion luminescence of $NaGd(WO_4)2$ co-doped with Ho^{3+} and Yb^{3+}. *Journal of Luminescence* **2014,** *153*, 1-4.

122. Ding, Y.; Gu, J.; Ke, J.; Zhang, Y. W.; Yan, C. H., Sodium doping controlled synthesis of monodisperse lanthanide oxysulfide ultrathin nanoplates guided by density functional calculations. *Angew Chem Int Ed* **2011,** *50* (51), 12330-4.

123. Erdem, M.; Erguzel, O.; Ekmekci, M. K.; Orucu, H.; Cinkaya, H.; Genc, S.; Mergen, A.; Eryurek, G.; Di Bartolo, B., Bright white up-conversion emission from sol–gel derived $Yb^{3+}/Er^{3+}/Tm^{3+}$: Y_2SiO_5 nanocrystalline powders. *Ceramics International* **2015,** *41* (10), 12805-12810.

124. Wang, F.; Deng, R.; Liu, X., Preparation of core-shell $NaGdF_4$ nanoparticles doped with luminescent lanthanide ions to be used as upconversion-based probes. *Nat Protoc* **2014,** *9* (7), 1634-44.

125. Guanying Chen; Jie Shen; Tymish Y. Ohulchanskyy; Nayan J. Patel; Artem Kutikov; Zhipeng Li; Jie Song; Ravindra K. Pandey; Hans Agren; Paras N. Prasad; Han, G., (R-$NaYbF_4$:Tm^{3+})/CaF_2 Core/Shell Nanoparticles with Efficient Near-Infrared to Near-Infrared Upconversion for High-Contrast Deep Tissue Bioimaging. *ACS Nano* **2012,** *6* (9), 8280–8287.

126. Ren, W.; Zhou, Y.; Wen, S.; He, H.; Lin, G.; Liu, D.; Jin, D., DNA-mediated anisotropic silica coating of upconversion nanoparticles. *Chem Commun (Camb)* **2018,** *54* (52), 7183-7186.

127. Ren, W.; Wen, S.; Tawfik, S. A.; Su, Q. P.; Lin, G.; Ju, L. A.; Ford, M. J.; Ghodke, H.; van Oijen, A. M.; Jin, D., Anisotropic functionalization of upconversion nanoparticles. *Chem Sci* **2018,** *9* (18), 4352-4358.

128. Plohl, O.; Kralj, S.; Majaron, B.; Frohlich, E.; Ponikvar-Svet, M.; Makovec, D.; Lisjak, D., Amphiphilic coatings for the protection of upconverting nanoparticles against dissolution in aqueous media. *Dalton Trans* **2017,** *46* (21), 6975-6984.

129. Liu, J. N.; Bu, W. B.; Shi, J. L., Silica coated upconversion nanoparticles: a versatile platform for the development of efficient theranostics. *Acc Chem Res* **2015,** *48* (7), 1797-805.

130. Bogdan, N.; Vetrone, F.; Ozin, G. A.; Capobianco, J. A., Synthesis of ligand-free colloidally stable water dispersible brightly luminescent lanthanide-doped upconverting nanoparticles. *Nano Lett* **2011,** *11* (2), 835-40.

131. Lahtinen, S.; Lyytikäinen, A.; Päkkilä, H.; Hömppi, E.; Perälä, N.; Lastusaari, M.; Soukka, T., Disintegration of Hexagonal $NaYF_4$:Yb^{3+},Er^{3+} Upconverting Nanoparticles in Aqueous Media: The Role of Fluoride in Solubility Equilibrium. *The Journal of Physical Chemistry C* **2016,** *121* (1), 656-665.

132. Boyer, J. C.; Manseau, M. P.; Murray, J. I.; van Veggel, F. C., Surface modification of upconverting $NaYF_4$ nanoparticles with PEG-phosphate ligands for NIR (800 nm) biolabeling within the biological window. *Langmuir* **2010,** *26* (2), 1157-64.

133. Han, S.; Qin, X.; An, Z.; Zhu, Y.; Liang, L.; Han, Y.; Huang, W.; Liu, X., Multicolour synthesis in lanthanide-doped nanocrystals through cation exchange in water. *Nat Commun* **2016,** *7*, 13059.

134. Beberwyck, B. J.; Surendranath, Y.; Alivisatos, A. P., Cation Exchange: A Versatile Tool for Nanomaterials Synthesis. *The Journal of Physical Chemistry C* **2013,** *117* (39), 19759-19770.

135. Dong, C.; Korinek, A.; Blasiak, B.; Tomanek, B.; van Veggel, F. C. J. M., Cation Exchange: A Facile Method To Make $NaYF_4$:Yb,Tm-$NaGdF_4$ Core–Shell Nanoparticles with a Thin, Tunable, and Uniform Shell. *Chemistry of Materials* **2012,** *24* (7), 1297-1305.

136. Dong, H.; Sun, L. D.; Li, L. D.; Si, R.; Liu, R.; Yan, C. H., Selective Cation Exchange Enabled Growth of Lanthanide Core/Shell Nanoparticles with Dissimilar Structure. *J Am Chem Soc* **2017,** *139* (51), 18492-18495.

137. Zhou, B.; Tao, L.; Tsang, Y. H.; Jin, W., Core–shell nanoarchitecture: a strategy to significantly enhance white-light upconversion of lanthanide-doped nanoparticles. *Journal of Materials Chemistry C* **2013,** *1* (28).

138. Qian, H. S.; Zhang, Y., Synthesis of hexagonal-phase core-shell $NaYF_4$ nanocrystals with tunable upconversion fluorescence. *Langmuir* **2008,** *24* (21), 12123-5.

139. Liu, N.; Qin, W.; Qin, G.; Jiang, T.; Zhao, D., Highly plasmon-enhanced upconversion emissions from Au@beta-$NaYF_4$:Yb,Tm hybrid nanostructures. *Chem Commun (Camb)* **2011,** *47* (27), 7671-3.

140. Hinamoto, T.; Takashina, H.; Sugimoto, H.; Fujii, M., Controlling Surface Plasmon Resonance of Metal Nanocap for Upconversion Enhancement. *The Journal of Physical Chemistry C* **2017,** *121* (14), 8077-8083.

141. Zhang, Q.; Zhu, B.; Zhuang, Y.; Chen, G.; Liu, X.; Zhang, G.; Qiu, J.; Chen, D., Quantum Cutting in Tm^{3+}/Yb^{3+}-Codoped Lanthanum Aluminum Germanate Glasses. *Journal of the American Ceramic Society* **2010,** *93* (3), 654-657.

142. Li, Z.; Zhou, D.; Yang, Y.; Ren, P.; Qiu, J., Adjustable multicolor up-energy conversion in light-luminesce in $Tb^{3+}/Tm^{3+}/Yb^{3+}$ co-doped oxyfluorifFde glass-ceramics containing Ba2LaF7 nanocrystals. *Sci Rep* **2017,** *7* (1), 6518.

143. Ehlert, O.; Thomann, R.; Darbandi, M.; Nann, T., A Four-Color Colloidal Multiplexing Nanoparticle System. *ACS Nano* **2008,** *2* (1), 120-124.

144. Krishnan, R.; Thirumalai, J., Up/down conversion luminescence properties of $(Na_{0.5}Gd_{0.5})$MoO4:Ln^{3+}(Ln = Eu, Tb, Dy, Yb/Er, Yb/Tm, and Yb/Ho) microstructures: synthesis, morphology, structural and magnetic investigation. *New J. Chem.* **2014,** *38* (8), 3480-3491.

145. Heer, S.; Kampe, K.; Gudel, H.-U.; Haase, M., Highly Efficient Multicolour Upconversion Emission in Transparent Colloids of Lanthanide-Doped $NaYF_4$ Nanocrystals. *Adv Mater* **2004,** *16*, 23-24.

146. Boyer, J.-C.; Vetrone, F.; Cuccia, L. A.; Capobianco, J. A., Synthesis of Colloidal Upconverting $NaYF_4$ Nanocrystals Doped with Er^{3+}, Yb^{3+} and Tm^{3+}, Yb^{3+} via Thermal Decomposition of Lanthanide Trifluoroacetate Precursors. *J Am Chem Soc* **2006,** *128*, 7444-7445.

147. Chan, E. M.; Han, G.; Goldberg, J. D.; Gargas, D. J.; Ostrowski, A. D.; Schuck, P. J.; Cohen, B. E.; Milliron, D. J., Combinatorial discovery of lanthanide-doped nanocrystals with spectrally pure upconverted emission. *Nano Lett* **2012,** *12* (7), 3839-45.

148. Li, J. J.; Yang, L. W.; Zhang, Y. Y.; Zhong, J. X.; Sun, C. Q.; Chu, P. K., Pump-power tunable white upconversion emission in lanthanide-doped hexagonal $NaYF_4$ nanorods. *Optical Materials* **2011,** *33* (6), 882-887.

149. Chen, D.; Wang, Y.; Zheng, K.; Guo, T.; Yu, Y.; Huang, P., Bright upconversion white light emission in transparent glass ceramic embedding $Tm^{3+}/Er^{3+}/Yb^{3+}$:β-YF_3 nanocrystals. *Applied Physics Letters* **2007,** *91* (25).

150. Chen, D.; Wang, Y.; Yu, Y.; Huang, P.; Weng, F., Novel rare earth ions-doped oxyfluoride nano-composite with efficient upconversion white-light emission. *Journal of Solid State Chemistry* **2008,** *181* (10), 2763-2767.

151. Wang, F.; Liu, X., Upconversion Multicolor Fine-Tuning: Visible to Near-Infrared Emission from Lanthanide-Doped $NaYF_4$ Nanoparticles. *J Am Chem Soc* **2008,** *130*, 5642–5643.

152. Chen, G.; Qiu, H.; Fan, R.; Hao, S.; Tan, S.; Yang, C.; Han, G., Lanthanide-Doped Ultrasmall Yttrium Fluoride Nanoparticles with Enhanced Multicolor Upconversion Photoluminescence. *J. Mater. Chem.* **2012,** *22*.

153. Tian, G.; Gu, Z.; Zhou, L.; Yin, W.; Liu, X.; Yan, L.; Jin, S.; Ren, W.; Xing, G.; Li, S.; Zhao, Y., Mn^{2+} dopant-controlled synthesis of $NaYF_4$:Yb/Er upconversion nanoparticles for in vivo imaging and drug delivery. *Adv Mater* **2012,** *24* (9), 1226-31.

154. Zhong, Y.; Tian, G.; Gu, Z.; Yang, Y.; Gu, L.; Zhao, Y.; Ma, Y.; Yao, J., Elimination of photon quenching by a transition layer to fabricate a quenching-shield sandwich structure for 800 nm excited upconversion luminescence of Nd^{3+}-sensitized nanoparticles. *Adv Mater* **2014,** *26* (18), 2831-7.

155. Wen, H.; Zhu, H.; Chen, X.; Hung, T. F.; Wang, B.; Zhu, G.; Yu, S. F.; Wang, F., Upconverting near-infrared light through energy management in core-shell-shell nanoparticles. *Angew Chem Int Ed* **2013,** *52* (50), 13419-23.

156. Su, Q.; Han, S.; Xie, X.; Zhu, H.; Chen, H.; Chen, C. K.; Liu, R. S.; Chen, X.; Wang, F.; Liu, X., The effect of surface coating on energy migration-mediated upconversion. *J Am Chem Soc* **2012,** *134* (51), 20849-57.

157. Huang, X.; Lin, J., Active-core/active-shell nanostructured design: an effective strategy to enhance Nd^{3+}/Yb^{3+} cascade sensitized upconversion luminescence in lanthanide-doped nanoparticles. *Journal of Materials Chemistry C* **2015,** *3* (29), 7652-7657.

158. Ding, M.; Chen, D.; Wan, Z.; Zhou, Y.; Zhong, J.; Xi, J.; Ji, Z., Achieving efficient Tb^{3+} dual-mode luminescence via Gd-sublattice-mediated energy migration in a $NaGdF_4$ core–shell nanoarchitecture. *Journal of Materials Chemistry C* **2015,** *3* (21), 5372-5376.

159. Li, X.; Liu, X.; Chevrier, D. M.; Qin, X.; Xie, X.; Song, S.; Zhang, H.; Zhang, P.; Liu, X., Energy Migration Upconversion in Manganese(II)-Doped Nanoparticles. *Angew Chem Int Ed* **2015,** *54* (45), 13510-13515.

160. Jeong, S.; Won, N.; Lee, J.; Bang, J.; Yoo, J.; Kim, S. G.; Chang, J. A.; Kim, J.; Kim, S., Multiplexed near-infrared in vivo imaging complementarily using quantum dots and upconverting $NaYF_4$:Yb^{3+},Tm^{3+} nanoparticles. *Chem Commun (Camb)* **2011,** *47* (28), 8022-4.

161. Gorris, H. H.; Ali, R.; Saleh, S. M.; Wolfbeis, O. S., Tuning the dual emission of photon-upconverting nanoparticles for ratiometric multiplexed encoding. *Adv Mater* **2011,** *23* (14), 1652-5.

162. Chen, Y.; Duong, H. T. T.; Wen, S.; Mi, C.; Zhou, Y.; Shimoni, O.; Valenzuela, S. M.; Jin, D., Exonuclease III-Assisted Upconversion Resonance Energy Transfer in a Wash-Free Suspension DNA Assay. *Anal Chem* **2018,** *90* (1), 663-668.

163. Zheng, W.; Huang, P.; Gong, Z.; Tu, D.; Xu, J.; Zou, Q.; Li, R.; You, W.; Bunzli, J. G.; Chen, X., Near-infrared-triggered photon upconversion tuning in all-inorganic cesium lead halide perovskite quantum dots. *Nat Commun* **2018,** *9* (1), 3462.

164. Rao, M.; Fu, J.; Wen, X.; Sun, B.; Wu, J.; Liu, X.; Dong, X., Near-infrared-excitable perovskite quantum dots via coupling with upconversion nanoparticles for dual-model anti-counterfeiting. *New Journal of Chemistry* **2018,** *42* (15), 12353-12356.

165. Li, Z.; Zhang, Y.; Jiang, S., Multicolor Core/Shell-Structured Upconversion Fluorescent Nanoparticles. *Adv. Mater* **2008,** *20*, 4765–4769.

166. Yan, C.; Dadvand, A.; Rosei, F.; Perepichka, D. F., Near-IR Photoresponse in New Up-Converting CdSe/$NaYF_4$:Yb,Er Nanoheterostructures. *J Am Chem Soc* **2010,** *132*, 8868–8869.

167. Yao, L.; Zhou, J.; Liu, J.; Feng, W.; Li, F., Iridium-Complex-Modifi ed Upconversion Nanophosphors for Effective LRET Detection of Cyanide Anions in Pure Water. *Adv. Funct. Mater.* **2012,** *22*, 2667–2672.

168. Wang, L.; Yan, R.; Huo, Z.; Wang, L.; Zeng, J.; Bao, J.; Wang, X.; Peng, Q.; Li, Y., Fluorescence resonant energy transfer biosensor based on upconversion-luminescent nanoparticles. *Angew Chem Int Ed* **2005,** *44* (37), 6054-7.

169. Marin, R.; Labrador-Paéz, L.; Skripka, A.; Haro-González, P.; Benayas, A.; Canton, P.; Jaque, D.; Vetrone, F., Upconverting Nanoparticle to Quantum Dot Förster Resonance Energy Transfer: Increasing the Efficiency through Donor Design. *ACS Photonics* **2018,** *5* (6), 2261-2270.

170. Cheng, L.; Yang, K.; Shao, M.; Lee, S.-T.; Liu, Z., Multicolor In Vivo Imaging of Upconversion Nanoparticles with Emissions Tuned by Luminescence Resonance Energy Transfer. *J. Phys. Chem. C* **2011,** *115*, 2686–2692.

171. Morgan, C. G.; Dad, S.; Mitchell, A. C., Present status of, and future prospects for, upconverting phosphors in proximity-based bioassay. *Journal of Alloys and Compounds* **2008,** *451* (1-2), 526-529.

CHAPTER 2

Multicolour Luminescence of RE^{3+} (RE = Er, Ho, Tm) Ions in Bulk Alkaline Indium Oxide

2.1 Introduction

Direct doping with various rare-earth ions (RE^{3+}) is one of the most effective methods of producing multicolour luminescence in upconversion (UC) materials. RE^{3+} dopant ions are activators that accumulate energy from sensitizer ions and then emit high-energy photons. RE^{3+} ions feature ladder-like-arranged energy levels; therefore, various RE^{3+} ions show different emission colours[1-2].

To generate practical multicolour properties, RE^{3+}-doped UC materials require an elaborate selection of RE^{3+} activators[3-4]. The ions Er^{3+}, Tm^{3+} and Ho^{3+} are frequently used as activators for their characteristic spectral emissions[5-10]. Er^{3+} ion has abundant energy levels. Acting as the luminescent centre, Er^{3+} can emit intense green and red light. The Ho^{3+} ion provides both a red emission (from $^5F_5$ by an ESA process) and a faint green emission (from the $^5S_2$ level). Tm^{3+} is an activator that produces the most efficient UC blue light. Yb^{3+} only has two energy states: $^2F_{7/2}$ and $^2F_{5/2}$. The $^2F_{5/2}$ energy level of the Yb^{3+} ion can be resonant with the f–f transitions of other RE^{3+} activators, so co-doping of Yb^{3+} and other RE^{3+} activators is supposed to greatly enhance UC efficiency through an energy transfer process. By co-doping of Yb^{3+} with Er^{3+}, Tm^{3+} or Ho^{3+} ions, the emission spectra of these ions cover almost the entire visible light spectrum, from blue to red.

Though one of the most important directions in UC research focuses on fluoride hosts due to their low phonon energy[11-14], developing new oxide UC matrix materials and improving their UC efficiency are also critical. Oxides exhibit high chemical stability and are always easy to synthesize. These oxide host materials have relatively low phonon energy and can also show excellent luminescent properties after doping by sensitizers and

activators. Some oxide-based UC phosphors with relatively low phonon energy, such as Y_2O_3 and Gd_2O_3, have been widely studied[15-20]. Li reported that the oxide of $CaIn_2O_4$ has a low phonon energy (~475 cm^{-1}), which is much lower than those of other typical oxide hosts such as ZrO_2 (~500 cm^{-1}), Y_2O_3 (~550 cm^{-1}), GdOCl (~500 cm^{-1})[21-24]. Therefore, RE^{3+} ion-doped $CaIn_2O_4$ phosphors show very efficient UC luminescence. Indium (In) belongs to the same group as boron, aluminium and gallium, and In^{3+} is a trivalent ion with a similar ionic size as RE^{3+} ions. Materials containing In^{3+} ions are suggested to be excellent host lattices for UC luminescence. Research has shown that alkaline indium oxides have stable physical and chemical properties and are good ultraviolet-excited fluorescent host materials for certain RE^{3+} ions, such as Eu^{3+} and Tb^{3+} [25-29]. In the crystal structure of (Ca/Sr)In_2O_4 (orthorhombic, Pnma, ICSD #16241), two kinds of distorted InO6 octahedra are connected to form a network, and alkaline (Ca/Sr) ions located in the middle of the formed pentagonal prism tunnel. Alkaline earth ions (Ca^{2+}/Sr^{2+}) in this structure also exhibit close ionic size to RE^{3+} ions (Table 2.1)[30-31]. Because the radii of RE^{3+} ions are between those of In^{3+} and Ca^{2+} (or Sr^{2+}) ions, there are two atomic sites where In^{3+} and Ca^{2+} (or Sr^{2+}) show the potential to be replaced by RE^{3+} ions. Therefore, *where* the doped RE^{3+} ions are distributed in the crystal structure and *how* they influence the UC properties are mysteries worthy of study. Doing research on alkaline indium oxide also helps researchers to explore new host materials for UC luminescence.

Table 2.1 Radii of In^{3+}, typical upconverted RE^{3+}, and $Ca^{2+}$and Sr^{2+} ions under corresponding coordinates

Name of ions	Coordinate (CN)	Radius（Å）
In^{3+}	6 / 8	0.80 / 0.92
Yb^{3+}	6 / 8	0.868 / 0.985
Er^{3+}	6 / 8	0.89 / 1.004
Ho^{3+}	6 / 8	0.901 / 1.015
Tm^{3+}	6 / 8	0.88 / 0.994
Ca^{2+}	6 / 8	1.00 / 1.12
Sr^{2+}	6 / 8	1.18 / 1.26

In this work, we prepared and studied Yb^{3+}/Ho^{3+}- and Yb^{3+}/Er^{3+}- pair co-doped (Ca/Sr)In_2O_4 continuous solid solution. The crystal structure evolution and distribution of RE^{3+} ions, such as their atomic occupancy in the crystal structure, were finely modified

using Rietveld refinement of X-ray powder diffraction. After that, multicolour luminescent $SrIn_2O_4$ UC bulk materials were prepared by doping of Yb^{3+}/Er^{3+}, Yb^{3+}/Ho^{3+} and Yb^{3+}/Tm^{3+} ions, and their multicolour luminescent properties are discussed in detail.

2.2 Experimental section

2.2.1 Reagents and equipment

The chemicals and reagents described in this chapter are listed in Table 2.2. All the chemicals were used without further purification or modification unless stated otherwise.

Table 2.2 Main experimental reagents, specifications and manufacturer

Chemical	Specification	Manufacturer
$CaCO_3$	A.R.	China National Medicines Corporation Ltd.
$SrCO_3$	A.R.	
In_2O_3	99.995%	
Tm_2O_3	99.995%	
Ho_2O_3	99.995%	
Er_2O_3	99.995%	
Yb_2O_3	99.995%	
Ethanol	96%	

The commercial instruments and equipment used for specimen synthesis in this chapter are listed in Table 2.3.

Table 2.3 Main experimental equipment, specific indicators and manufacturer

Equipment	Specification	Manufacturer
Analytical balance	ME-204	Mettler Toledo (Switzerland)
Muffle furnace	KSL-1100X-S	Hefei Kejing (China)
Air-dry oven	DHG-9003	Shanghai Yiheng (China)
Agate mortar	15 cm diameter	Beijing Chemical Glass
Corundum crucible	1.5 cm diameter	Beijing Chemical Glass
Power-tunable semiconductor laser, 980 nm	VA-I-DC-980	Viasho Technology (China)

2.2.2 Synthesis of materials

All samples were synthesized by a solid-state reaction method. In a typical procedure, starting materials of $CaCO_3$, $SrCO_3$, In_2O_3, Yb_2O_3, Ho_2O_3, and Yb_2O_3 were weighed according to stoichiometric ratios. Then, all materials were mixed and ground thoroughly in an agate mortar, placed into alumina crucibles and then sintered at 1300–1400 °C for 3 hours under an air atmosphere at a heating rate of 5 °C/min. The samples were then allowed to cool to room temperature. Finally, all samples were washed three times with deionized water and dried for subsequent measurement.

2.2.3 Characterization

XRD characterization: X-ray diffraction (XRD, D8 Advance diffractometer, Bruker Corporation, Germany, with Cu-Kα and linear VANTEC detector, λ = 0.15406 nm, 40 kV, 30 mA) was used to examine the phase composition and for structural refinement. The powder diffraction data for Rietveld analysis were collected in the 2θ range of 5–100° with a step size of 0.02° and counting time of 2–3 s per step[32]. Rietveld refinement was performed using TOPAS 4.2 software[33].

SEM characterization: The morphology of samples was characterized by field emission scanning electron microscopy (FESEM, JSM-7001F, Japan).

Photoluminescence spectra by spectrofluorometer: The UC luminescent spectra were recorded on a spectrophotometer (F-4600, Hitachi, Japan) equipped with an external power-controllable 980 nm semiconductor laser (Beijing Viasho Technology Company, China) as the excitation source.

Diffuse reflection spectra: Diffuse reflection spectra were measured on a UV-vis-NIR spectrophotometer (Shimadzu UV-3600, Japan) attached to an integral sphere, with $BaSO_4$ used as a reference standard.

Fourier transform infrared spectroscopy: Fourier transform infrared spectra (FT-IR) were recorded with a PerkinElmer Spectrum 100 spectroscope (USA). All measurements were carried out at room temperature.

2.3 Results and discussion

2.3.1 Distribution of RE^{3+} in $(Ca/Sr)In_2O_4$

Yb^{3+}/Ho^{3+}-co-doped $(Ca/Sr)In_2O_4$ UC compounds were prepared first. XRD and Rietveld refinement were employed to characterize the crystal structures evolution of all samples and explore the distribution of RE^{3+} ions in the crystal structures.

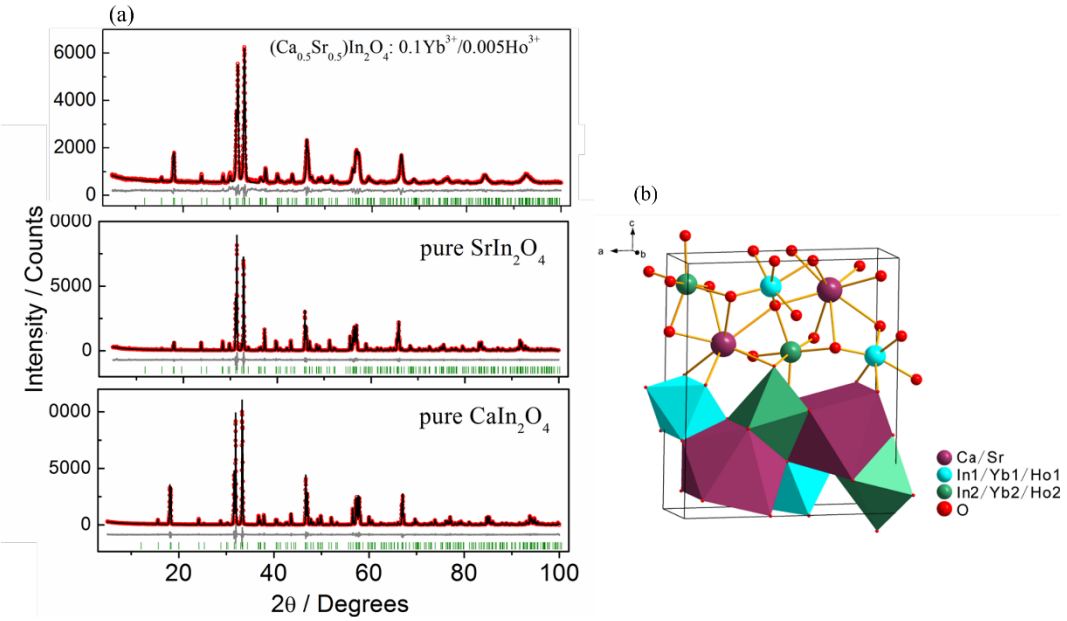

Figure 2.1 Observed (red), calculated (black), and difference (gray) XRD patterns for the refinement of $(Ca_{0.5}Sr_{0.5})In_2O_4$: 0.1$Yb^{3+}$/0.005$Ho^{3+}$, and pure $CaIn_2O_4$ and $SrIn_2O_4$ samples (a). Crystal structure of the $(Ca_{1-x}Sr_x)In_2O_4$: Yb^{3+}/Ho^{3+} sample (b)

All peaks of the compounds were indexed by orthorhombic cells (*Pnma*) with parameters close to those earlier reported for $SrIn_2O_4$ [34]. Therefore, the crystal structure of $SrIn_2O_4$ was taken as a starting model for Rietveld refinement. In the crystal structure, there is only one position which can be occupied by Sr and Ca, and this position is multiplied by four positions by symmetry elements (Figure 2.1). The occupations of Sr/Ca ions were fixed during refinement. Also, Yb^{3+} and Ho^{3+} ions were dissolved in the lattice and partly substituted for In^{3+} ions, and their occupancies were fixed. The refinement of all the samples of $(Ca_{1-x}Sr_x)In_2O_4$: Yb^{3+}/Ho^{3+}, pure $CaIn_2O_4$ and $SrIn_2O_4$ were stable, and ended with low R-factors. $(Ca/Sr)O_8$ square antiprism and $(In/Yb/Ho)O6$ octahedra existed simultaneously in the crystal structure. Figure 2.1a shows selected XRD patterns and the crystal structure of the $(Ca_{0.5}Sr_{0.5})In_2O_4$: Yb^{3+}/Ho^{3+} sample, as well as those of pure $CaIn_2O_4$ and $SrIn_2O_4$. Figure 2.1b shows the detailed crystal structure of the $(Ca_{1-}$

$_x$Sr$_x$)In$_2$O$_4$: 0.1Yb^{3+}/0.005Ho^{3+} sample. Table 2.4 presents the main processing and refinement parameters of these samples.

Table 2.4 Main processing and refinement parameters of (Ca$_{1-x}$Sr$_x$)In$_2$O$_4$:0.1Yb^{3+}/0.005Ho^{3+}, pure CaIn$_2$O$_4$ and SrIn$_2$O$_4$ samples

Compound	Space	*a*, Å	*b*, Å	*c*, Å	*V*, Å^3	*Rwp*, %
CaIn$_2$O$_4$	*Pnma*	9.64847	3.21443(3)	11.29593	350.336	11.14
CaIn$_2$O$_4$:0.1Yb^{3+},0.005Ho^{3+}	*Pnma*	9.6543 (2)	3.21652(8)	11.3034	351.007	12.29
(Ca$_{0.9}$Sr$_{0.1}$)In$_2$O$_4$:0.1Yb^{3+},0.005Ho^{3+}	*Pnma*	9.6768 (4)	3.22542(13)	11.3307	353.65	11.65
(Ca$_{0.7}$Sr$_{0.3}$)In$_2$O$_4$:0.1Yb^{3+},0.005Ho^{3+}	*Pnma*	9.7180 (5)	3.24012(16)	11.3826	358.41	9.96
(Ca$_{0.5}$Sr$_{0.5}$)In$_2$O$_4$:0.1Yb^{3+},0.005Ho^{3+}	*Pnma*	9.7613 (5)	3.25218(17)	11.4253	362.70	10.17
(Ca$_{0.3}$Sr$_{0.7}$)In$_2$O$_4$:0.1Yb^{3+},0.005Ho^{3+}	*Pnma*	9.7967 (4)	3.25980(12)	11.4624	366.06	9.33
(Ca$_{0.1}$Sr$_{0.9}$)In$_2$O$_4$:0.1Yb^{3+},0.005Ho^{3+}	*Pnma*	9.8266 (3)	3.26668(10)	11.4917	368.886	11.05
SrIn$_2$O$_4$:0.1Yb^{3+},0.005Ho^{3+}	*Pnma*	9.8519 (4)	3.27340(6)	11.5178	371.443	9.08
SrIn$_2$O$_4$	*Pnma*	9.83188 (9)	3.26563(3)	11.49003	368.914	10.14

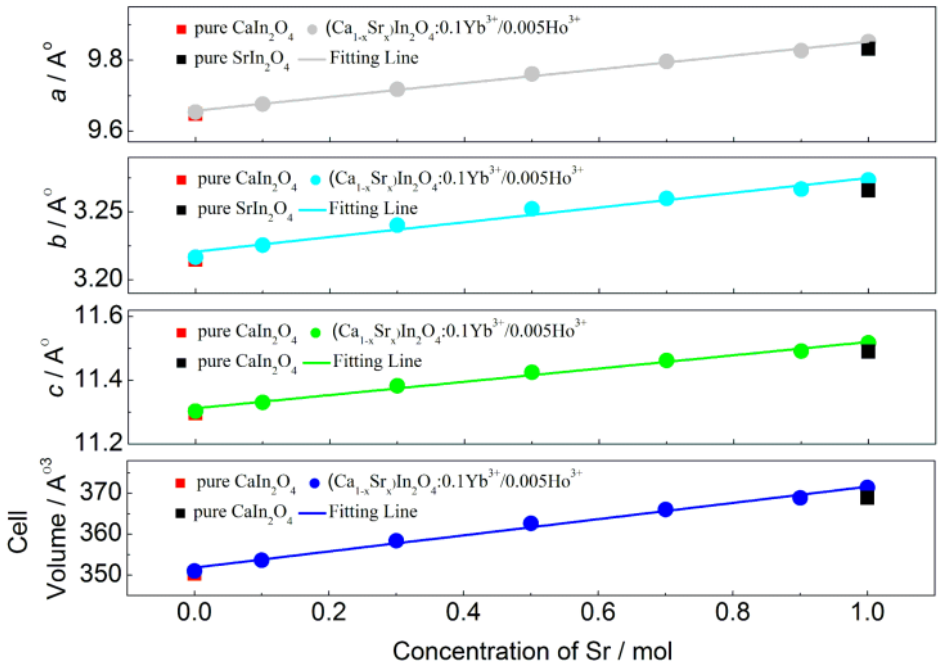

Figure 2.2 Refined lattice parameters a, b, c, and unit cell volume (V) showed a linear increase as functions of x values in (Ca$_{1-x}$Sr$_x$)In$_2$O$_4$: Yb^{3+}/Ho^{3+} UC materials

Figure 2.2 shows the refined lattice parameters of *a*, *b*, *c*, and unit cell volume (*V*) as functions of *x* values in (Ca$_{1-x}$Sr$_x$)In$_2$O$_4$:Yb^{3+}/Ho^{3+} (*x* = 0, 0.1, 0.3, 0.5, 0.7, 0.9, 1.0) samples, and individual *a*, *b*, *c*, and *V* values in pure CaIn$_2$O$_4$ or SrIn$_2$O$_4$. Since Ca/Sr in

eight coordination, and the ionic radii IR (Ca^{2+}, CN = 8) = 1.12Å, IR (Sr^{2+},= 1.26Å) [35], the lattice parameters *a*, *b*, *c* and *V* of these samples showed a linear increase with increasing Sr content, indicating that $(Ca_{1-x}Sr_x)In_2O_4$ formed a continuous solid solution. Moreover, pure $CaIn_2O_4$ and $SrIn_2O_4$ had smaller lattice parameters and cell volumes than Yb^{3+}/Ho^{3+}-co-doped $CaIn_2O_4$ and $SrIn_2O_4$, respectively. This is because In/Yb/Ho in six coordination, and IR (Yb^{3+}, CN = 6) = 0.868Å, IR (Ho^{3+}, CN = 6) = 0.901Å, IR (In^{3+}, CN = 6) = 0.8Å. Yb^{3+}/Ho^{3+} dopants in $CaIn_2O_4$ or $SrIn_2O_4$ enlarged the unit cells due to their larger IR than In^{3+}, testifying that Yb^{3+} and Ho^{3+} ions occupied the In^{3+} ion sites.

2.3.2 Luminescence upon phonon energy in $(Ca/Sr)In_2O_4$

As known, the phonon energy of the host has an important influence on the UC luminescent efficiency. Therefore, FT-IR spectra of pure $SrIn_2O_4$ and $CaIn_2O_4$ were determined (Figure 2.3). Compared with $CaIn_2O_4$ (489, 637 cm^{-1}), the strong absorption bands of $SrIn_2O_4$ (467, 598 cm^{-1}) shifted to smaller wavenumbers, suggesting that the phonon energy of $SrIn_2O_4$ (467 cm^{-1}) was lower than that of $CaIn_2O_4$. Moreover, because of the difference between Sr^{2+} and Ca^{2+} ions, RE^{3+} doped $SrIn_2O_4$ may show better luminescent properties than RE^{3+} -doped $CaIn_2O_4$, which was confirmed by doping Yb^{3+}/Er^{3+} and Yb^{3+}/Ho^{3+} ions in the $(Ca/Sr)In_2O_4$ host.

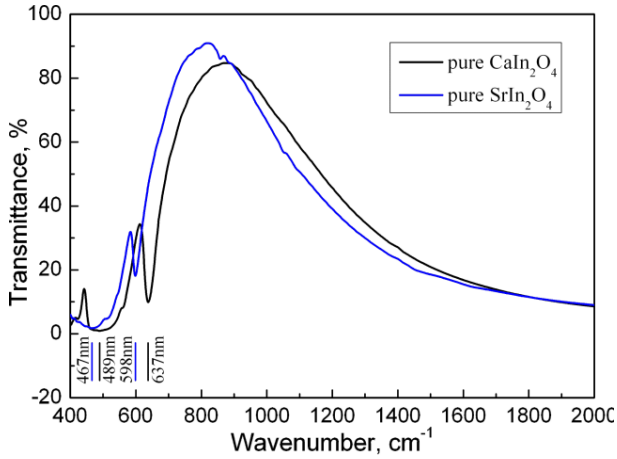

Figure 2.3 FT-IR spectra of pure $SrIn_2O_4$ and $CaIn_2O_4$ showing that the phonon energy of $SrIn_2O_4$ (467 cm^{-1}) is lower than that of $CaIn_2O_4$ (489 cm^{-1})

In the Yb^{3+}/Er^{3+}-doped $(Ca/Sr)In_2O_4$ UC compounds, the amount of RE^{3+} ions was determined as $0.1Yb^{3+}/xEr^{3+}$ (x = 0.005, 0.01, 0.03). The UC luminescence spectra of these samples are shown in Figure 2.4. Obvious visible emissions at around 550 and 663 nm were observed, which indicates that Yb^{3+}/Er^{3+}-doped $SrIn_2O_4$ compounds with

excellent UC luminescent properties were prepared successfully. From the inset of Figure 2.4, one can see that the luminescent intensities of $SrIn_2O_4$ and $CaIn_2O_4$ increased with increases in Er^{3+} (from 0.005 to 0.03). However, the intensities of Yb^{3+}/Er^{3+}-co-doped $SrIn_2O_4$ were higher than that of $CaIn_2O_4$, regardless of the doping concentration.

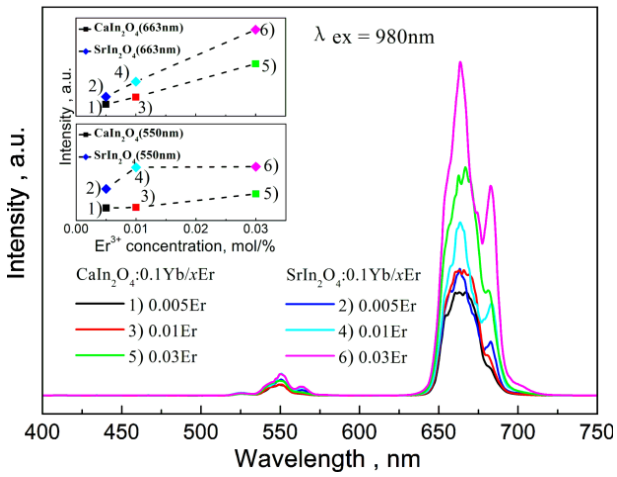

Figure 2.4 Comparison of UC luminescence spectra of $0.1Yb^{3+}/xEr^{3+}$ (x = 0.005, 0.01, 0.03) co-doped $SrIn_2O_4$ and $CaIn_2O_4$

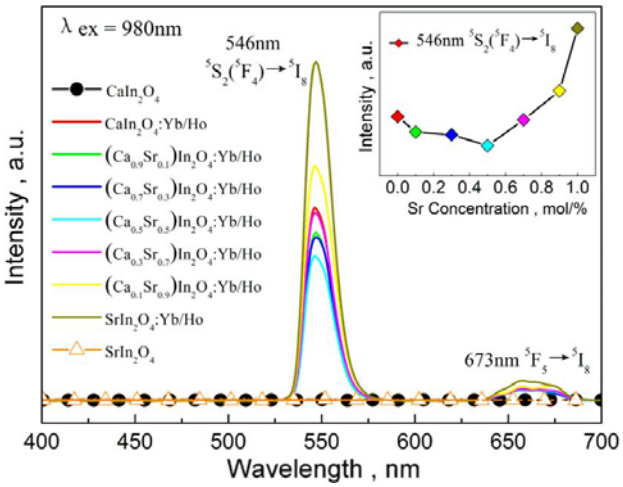

Figure 2.5 UC emission spectra of pure $CaIn_2O_4$, $(Ca_{1-x}Sr_x)In_2O_4$: $0.1Yb^{3+}/0.005Ho^{3+}$ (x = 0, 0.1, 0.3, 0.5, 0.7, 0.9, 1.0), and $SrIn_2O_4$ upon 980 nm laser excitation. The inset shows the variation in UC emission intensity

For the Yb^{3+}/Ho^{3+}-doped $(Ca/Sr)In_2O_4$ UC compounds, Figure 2.5 presents the UC emission spectra of pure $CaIn_2O_4$, $(Ca_{1-x}Sr_x)In_2O_4$: $0.1Yb^{3+}/0.005Ho^{3+}$ (x = 0, 0.1, 0.3, 0.5, 0.7, 0.9, 1.0), and pure $SrIn_2O_4$ upon 980 nm laser excitation. For the samples of $(Ca_{1-x}Sr_x)In_2O_4$: Yb^{3+}/Ho^{3+}, strong green emission, with the strongest peak at 546 nm, was obtained, which was associated with the characteristic energy level transition of $^5S_2(^5F_4)\rightarrow{}^5I_8$ of Ho^{3+} [6, 21, 36]. $SrIn_2O_4$: Yb^{3+}/Ho^{3+} showed the strongest UC luminescence

among all the samples, also suggesting that $SrIn_2O_4$ is a better UC host material.

2.3.3 Luminescence upon structures in (Ca/Sr)In_2O_4

In the Yb^{3+}/Ho^{3+}-doped (Ca/Sr)In_2O_4 UC compounds, it can be seen that the majority of Ca/Sr-ratio-substituted samples had lower UC luminescent intensities than the $CaIn_2O_4$: Yb^{3+}/Ho^{3+} and $SrIn_2O_4$: Yb^{3+}/Ho^{3+} samples. In order to explain the UC emission intensity differences in Ca/Sr-ratio-substituted samples, the detailed crystal structures and polyhedrons of some samples were analysed. The (Ca/Sr)O_8 polyhedral distortion index, D, can be calculated as followed:

$$D = \frac{1}{n}\sum_{i=1}^{n}\frac{|l_i - l_{av}|}{l_{av}} \quad (1),$$

where l_i is the distance between the central atom and the i^{th} coordinating atom, and l_{av} is the mean bond length.[37-38]

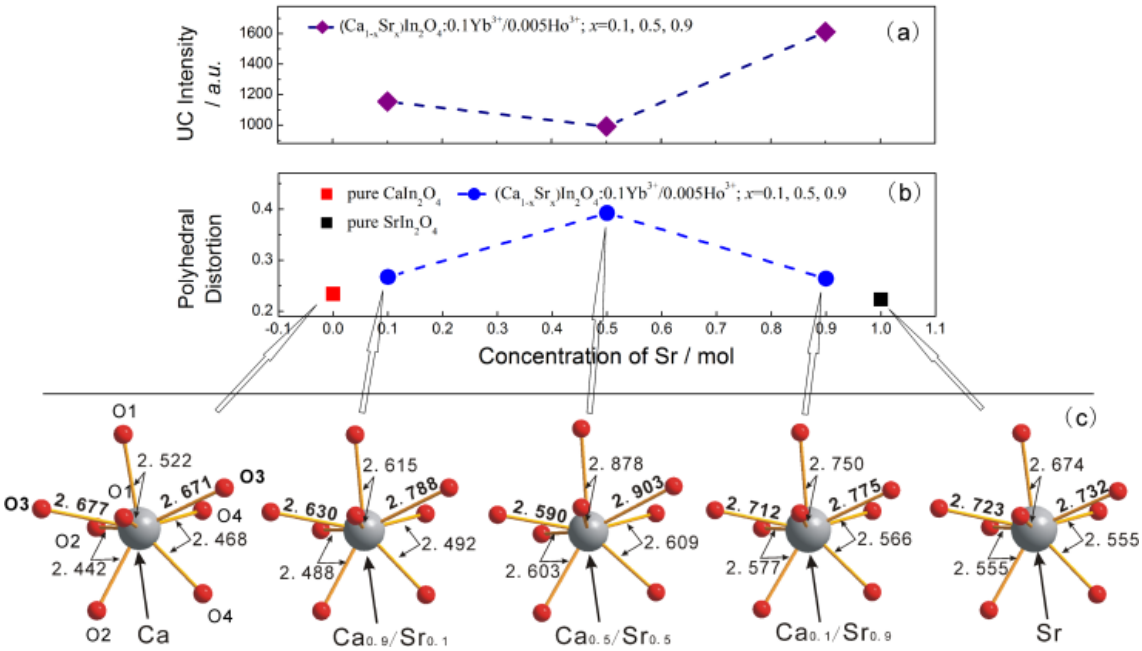

Figure 2.6 UC emission intensities at 546 nm of $(Ca_{1-x}Sr_x)In_2O_4$: $0.1Yb^{3+}/0.005Ho^{3+}$ (x = 0.1, 0.5, 0.9) (a). Calculated distortion indexes of (Ca/Sr)O_8 polyhedron in pure $CaIn_2O_4$, $(Ca_{1-x}Sr_x)In_2O_4$: $0.1Yb^{3+}/0.005Ho^{3+}$ (x = 0.1, 0.5, 0.9), and pure $SrIn_2O_4$ (b); (Ca/Sr)O_8 polyhedron of pure $CaIn_2O_4$, $Ca_{1-x}Sr_xIn_2O_4$: $0.1Yb^{3+}/0.005Ho^{3+}$ (x = 0.1, 0.5, 0.9), and pure $SrIn_2O_4$ (c)

The calculated distortions of pure $CaIn_2O_4$, $(Ca_{1-x}Sr_x)In_2O_4$: Yb^{3+}/Ho^{3+} ($x = 0.1, 0.5, 0.9$), and pure $SrIn_2O_4$ were determined as 0.234, 0.267, 0.392, 0.264, and 0.223, respectively. With the increased Sr substituting for Ca, the UC emission intensities of $(Ca_{1-x}Sr_x)In_2O_4$: Yb^{3+}/Ho^{3+} decreased first and then increased, as shown in Figure 2.6a. Meanwhile, the

crystal structures of $(Ca_{1-x}Sr_x)In_2O_4:Yb^{3+}/Ho^{3+}$ became distorted with the substitution between Ca/Sr, and these distortions first increased and then decreased, as shown in Figure 2.6b. In Figure 2.6c, distortions also can be observed from the variations in Ca-O_3 bond distances, which were 2.677 and 2.671 in pure $CaIn_2O_4$, 2.590 and 2.903 in $(Ca_{0.5}Sr_{0.5})In_2O_4$: Yb^{3+}/Ho^{3+}, and 2.723 and 2.732 in pure $SrIn_2O_4$. Accordingly, a new model was proposed, where the distortion (D) of the (Ca/Sr)O_8 polyhedron has a negative relationship with UC luminescent intensity (I) in $(Ca_{1-x}Sr_x)In_2O_4$: Yb^{3+}/Ho^{3+} samples:

$$I \propto \frac{1}{D} \quad (2),$$

The lattice expansion and increased distortion caused by partial substitution for Ca/Sr changed the crystal field acting on the Ho^{3+} or Yb^{3+}/Ho^{3+} ions, leading to variation in the UC luminescent properties of the Yb^{3+}/Ho^{3+} co-doped $(Ca_{1-x}Sr_x)In_2O_4$ continuous solid solution phosphors. This result also indicates that $SrIn_2O_4$ is a better UC host material.

2.3.4 Upconversion emission colour of Er^{3+} in $SrIn_2O_4$

Figure 2.7 displays the UC luminescence spectra of as-prepared $SrIn_2O_4$: $0.1Yb^{3+}/xEr^{3+}$ and $SrIn_2O_4$: $0.01Er^{3+}$ phosphors upon 980 nm laser excitation. The insets show the variation in UC emission intensities (Er^{3+}, at 663 nm and 550 nm) of these corresponding samples. For $SrIn_2O_4$: $0.1Yb^{3+}/xEr^{3+}$, strong green and red UC emissions with peaks at 525, 550, and 663 nm were observed, which were assigned to the characteristic Er^{3+} ion transitions of $^2H_{11/2}\rightarrow{}^4I_{15/2}$, $^4S_{3/2}\rightarrow{}^4I_{15/2}$, and $^4F_{9/2}\rightarrow{}^4I_{15/2}$, respectively[39].

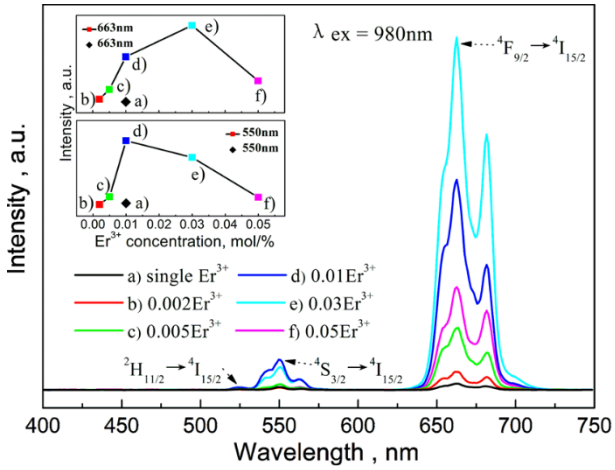

Figure 2.7 UC luminescence spectra of $SrIn_2O_4$: $0.1Yb^{3+}/xEr^{3+}$ and $SrIn_2O_4$: $0.01Er^{3+}$ samples

Compared with $SrIn_2O_4$: $0.01Er^{3+}$, the luminescent intensity of $SrIn_2O_4$: $0.1Yb^{3+}/0.01Er^{3+}$ increased greatly, indicating that the addition of Yb^{3+} ions improved the UC properties of

these materials. UC emission intensities of red (663 nm) and green emissions (550 nm) reached maximums in $SrIn_2O_4$: $0.1Yb^{3+}/0.03Er^{3+}$ and $SrIn_2O_4$: $0.1Yb^{3+}/0.01Er^{3+}$, respectively. The luminescent intensities of $SrIn_2O_4$: $0.1Yb^{3+}/xEr^{3+}$ increased first and then decreased at either 663 nm or 550 nm with increasing Er^{3+} concentration, suggesting that concentration quenching occurred. The over-doped Er^{3+} ions led to a decreased distance between Er^{3+} and Yb^{3+} (or Er^{3+}) ions, which limited the energy transfer (ET) of $Yb^{3+} \rightarrow Er^{3+}$, followed by decreasing the luminescent intensity of Er^{3+} ions.

The UC emission intensity (I_{em}) depends on the pumping laser power (P_{pump}) which follows the relation:

$$I_{em} \propto (P_{pump})^n \quad (3),$$

where n is the number of pump photons required for the transition from the ground state to the upper emitting state. The value of n can be obtained from the slope of a straight line fitted to log I_{em} versus log P_{pump} [40]. Figure 2.8a shows the UC emission spectra of $SrIn_2O_4$: $0.1Yb^{3+}/0.01Er^{3+}$ with different pumping powers, and the inset shows the dependence of green and red UC emission intensities upon pumping power. The calculated slopes were 2.09 ± 0.07 for the red emission (663 nm: $^4F_{9/2} \rightarrow {}^4I_{15/2}$) and 1.81 ± 0.06 for the green emission (550 nm: $^4S_{3/2} \rightarrow {}^4I_{15/2}$), indicating that UC luminescence in Yb^{3+}/Er^{3+} co-doped $SrIn_2O_4$ is mainly a two-photon process. According to the above-mentioned photon process, an energy level diagram of Er^{3+} and Yb^{3+} ions and the proposed UC luminescent mechanism that produces green and red emissions is provided in Figure 2.8b. First of all, infrared photons near the 980 nm wavelength are absorbed by Yb^{3+} ions, elevating them from the $^2F_{7/2}$ to the $^2F_{5/2}$ energy level. Then, the energy is transferred to the Er^{3+} ions, because the non-radiative energy transition (ET) from $^2F_{5/2}$ of Yb^{3+} to $^4I_{11/2}$ of Er^{3+} is resonant or near resonant and, thus, very efficient. The first ET promotes an Er^{3+} ion from the $^4I_{15/2}$ to the $^4I_{11/2}$ level, and the second ET elevates the Er^{3+} ion from the $^4I_{11/2}$ to the $^4F_{7/2}$ level if $^4I_{11/2}$ is already populated. The Er^{3+} ions in the $^4F_{7/2}$ state decay non-radiatively to the slightly lower energy states of $^2H_{11/2}$ and $^4S_{3/2}$, so that green light of 525 nm and 550 nm is emitted by the Er^{3+} transition from the $^2H_{11/2}$ to $^4I_{15/2}$ and $^4S_{3/2}$ to $^4I_{15/2}$ states, respectively. At the same time, Er^{3+} can decay to the $^4F_{9/2}$ level via a non-radiative relaxation process, and then red light (663 nm) was observed through the radiative transition from $^4F_{9/2}$ to $^4I_{15/2}$. Moreover, Er^{3+} in the $^4I_{11/2}$ level can relax non-radiatively to the less-excited state of $^4I_{13/2}$; thus, the second ET can also take place from

the $^4I_{13/2}$ level and promote Er^{3+} to the $^4I_{9/2}$ level. The relative UC intensity of red light is larger than that of green light, indicating that the population of the $^4F_{9/2}$ level was greater than that of the $^2H_{11/2}$ and $^4S_{3/2}$ levels.

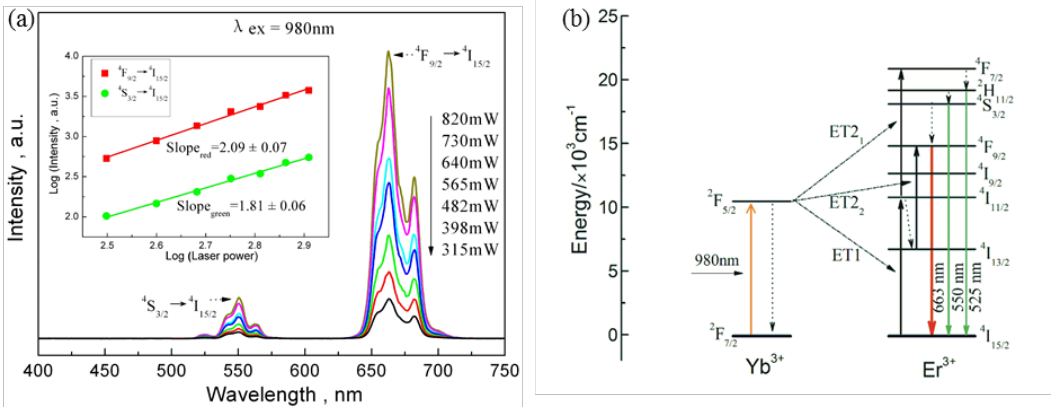

Figure 2.8 UC emission spectra of $SrIn_2O_4$: Yb^{3+}/Er^{3+} with different pumping powers, and the dependence of green and red UC emission intensities upon pumping power (a). Proposed UC luminescence mechanism in $SrIn_2O_4$: Yb^{3+}/Er^{3+} phosphors (b)

2.3.5 Upconversion emission colour of Ho^{3+} in $SrIn_2O_4$

Figure 2.9 presents the UC emission spectra of Yb^{3+}/Ho^{3+}-doped $SrIn_2O_4$ samples upon 980 nm near-infrared laser excitation. In the UC spectra, a strong green emission band with a peak at 546 nm and slight red luminescence around 673 nm were observed, which are assigned to the characteristic level transitions of $^5S_2(^5F_4)\rightarrow{}^5I_8$ and $^5F_5\rightarrow{}^5I_8$ of Ho^{3+}, respectively. With increasing Ho^{3+} concentration, the luminescent intensity of these samples first increases and then decreases, as shown in the inset. This result was attributed to the concentration quenching effect, which can be explained by the energy transfer (ET) of $Yb^{3+}\rightarrow Ho^{3+}$: increasing the content of Ho^{3+} leads to a decreased distance between Ho^{3+} and Yb^{3+}(or Ho^{3+}) ions, which promotes non-radiative ET and decreases the luminescent intensity of Ho^{3+} ions. The optimum Ho^{3+}/Yb^{3+} content was determined to be 0.75%/10% according to the strongest luminescence intensity.

Figure 2.10a depicts the UC emission spectra of $SrIn_2O_4$: 0.75%Ho^{3+}/10%Yb^{3+} upon 980 nm excitation with various pumping powers. As shown in the inset, the slopes of $SrIn_2O_4$: 0.75%Ho^{3+}/10%Yb^{3+} were determined to be 1.99 for the green emission ($^5S_2(^5F_4)\rightarrow{}^5I_8$) and 1.87 for the red emission ($^5F_5\rightarrow{}^5I_8$), indicating that a two-photon process took place in the UC luminescence of Ho^{3+}/Yb^{3+} co-doped $SrIn_2O_4$. Figure 2.10b proposes the UC luminescence mechanism of these Yb^{3+}/Ho^{3+} co-doped phosphors. In the present system,

energy from the $^2F_{7/2} \rightarrow {}^2F_{5/2}$ transition of Yb^{3+} is transferred to the neighbouring Ho^{3+} ion by ET, followed by a level transition from ground state $^5I_8$ to the intermediate excited state $^5I_6$ of Ho^{3+}. Then, a second energy transfer from the Yb^{3+} ion excites the same Ho^{3+} ion from the $^5I_6$ level to the $^5S_2(^5F_4)$ level. Consequently, bright green emission at 546 nm was observed because of the radiative decay of $^5S_2(^5F_4) \rightarrow {}^5I_8$. In contrast, the red emission of Ho^{3+} is due to the $^5F_5 \rightarrow {}^5I_8$ transition, which can be generated in two possible ways: 1) Ho^{3+} in the excited state $^5S_2(^5F_4)$ relaxes non-radiatively to the $^5F_5$ state, and 2) Ho^{3+} is promoted to the $^5F_5$ state after relaxing from $^5I_6$ to $^5I_7$ by non-radiative relaxation. Finally, it decays radiatively and emits red light at 673 nm by $^5F_5 \rightarrow {}^5I_8$ transition.

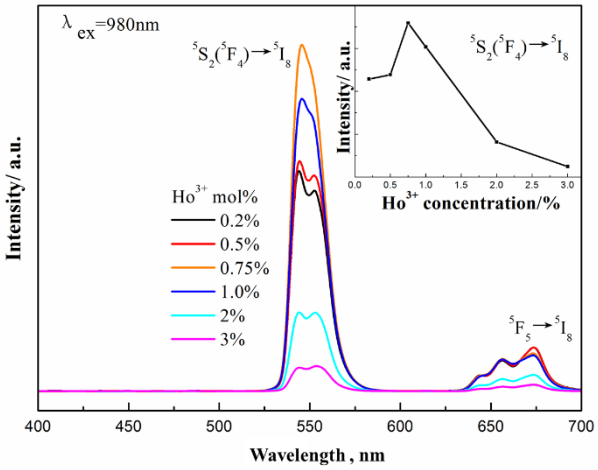

Figure 2.9 UC luminescence spectra of the different concentrations of Ho^{3+}-doped $SrIn_2O_4$ samples upon 980 nm laser excitation. The inset shows the variation in luminescence intensity dependent on Ho^{3+} concentration

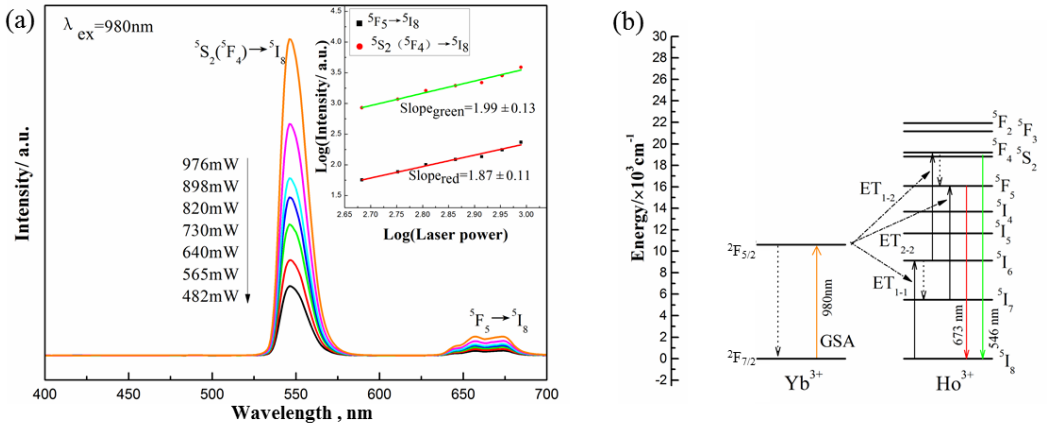

Figure 2.10 UC emission spectra of $SrIn_2O_4$: Yb^{3+}/Ho^{3+} at different pumping powers. The inset shows the pump power dependence of green and red UC emissions (a). Proposed UC luminescence mechanisms in Yb^{3+}/Ho^{3+}-doped $(Ca_{1-x}Sr_x)In_2O_4$ phosphors (b)

2.3.6 Upconversion emission colour of Tm^{3+} in $SrIn_2O_4$

Figure 2.11a depicts the Yb^{3+}/Tm^{3+}-doped $SrIn_2O_4$ samples upon 980 nm near-infrared laser excitation. The amount of RE^{3+} ions was determined as 0.75%Tm^{3+}/10%Yb^{3+}. Upon 980 nm excitation with different pumping powers, the phosphor showed bright luminescence: a blue emission band at 486 nm and a weak red emission at 657 nm, which were associated with the characteristic ion level transitions of $^1G_4 \rightarrow {}^3H_6$ and $^1G_4 \rightarrow {}^3F_4$ of Tm^{3+}, respectively[41]. From the inset, it can be seen that the slopes (*n* values) obtained were 2.36 for blue emission ($^1G_4 \rightarrow {}^3H_6$) and 1.23 for red emission ($^1G_4 \rightarrow {}^3F_4$). This reveals that UC luminescence in $SrIn_2O_4$: Tm^{3+}/Yb^{3+} is mainly ascribed to a three-photon process. The number of pump photons involved in the Tm^{3+} red emission was less than two, which is due to the exchange interactions between neighbouring activator ions and the large excited ground absorption.

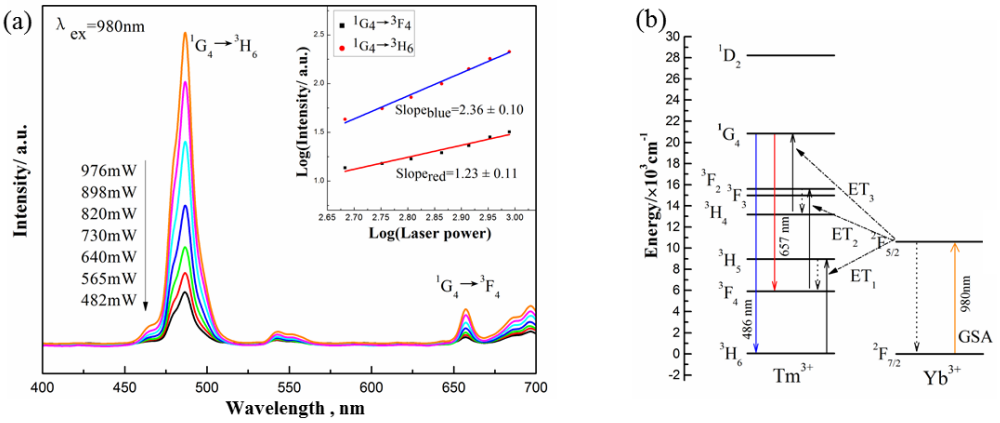

Figure 2.11 UC emission spectra of $SrIn_2O_4$: Yb^{3+}/Tm^{3+} with different pumping powers. The inset shows the pump power dependence of blue and red UC emissions (a). Energy level diagrams of Yb^{3+}/Tm^{3+} ions and the proposed UC luminescence mechanism that produces blue emission (b)

Figure 2.11b shows the proposed UC emission mechanism. As we know, UC luminescence in Tm^{3+}/Yb^{3+} co-doped $SrIn_2O_4$ is a three-photon process. Firstly, the Yb^{3+} absorbs one 980 nm photon with a ground state absorption (GSA) from the $^2F_{5/2}$ to $^2F_{7/2}$ state. Then, Yb^{3+} transfers energy to a neighbouring Tm^{3+} ion, leading to a transition from the $^3H_6$ ground state to the $^3H_5$ level of Tm^{3+}, followed by a non-radiative relaxation to the $^3F_4$ level of Tm^{3+}. Secondly, Tm^{3+} at the $^3F_4$ level can be excited to the $^3F_2$ level by a second ET process from the transition of Yb^{3+}, and then back to $^3H_4$ by non-radiative relaxation. Thirdly, energy from Yb^{3+} can be absorbed by the Tm^{3+} ions that stay at the $^3H_4$ level, resulting in the $^1G_4$ excited state of Tm^{3+} being populated. From the $^1G_4$ level,

Tm^{3+} will decay radiatively to the $^3H_6$ ground state and $^3F_4$ metastable state, generating blue and red emissions at around 486 nm and 657 nm.

2.3.7 Multicolour and CIE chromaticity

RE^{3+}-ion doping makes it possible to obtain blue, green and red UC emissions in a single $SrIn_2O_4$ host, which is a feasible route to realizing multicolour emission under excitation by 980 nm NIR light. The CIE chromaticity coordinates (*x,y*) of some typical samples were calculated through its UC luminescent spectrum, which is shown in Figure 2.12.

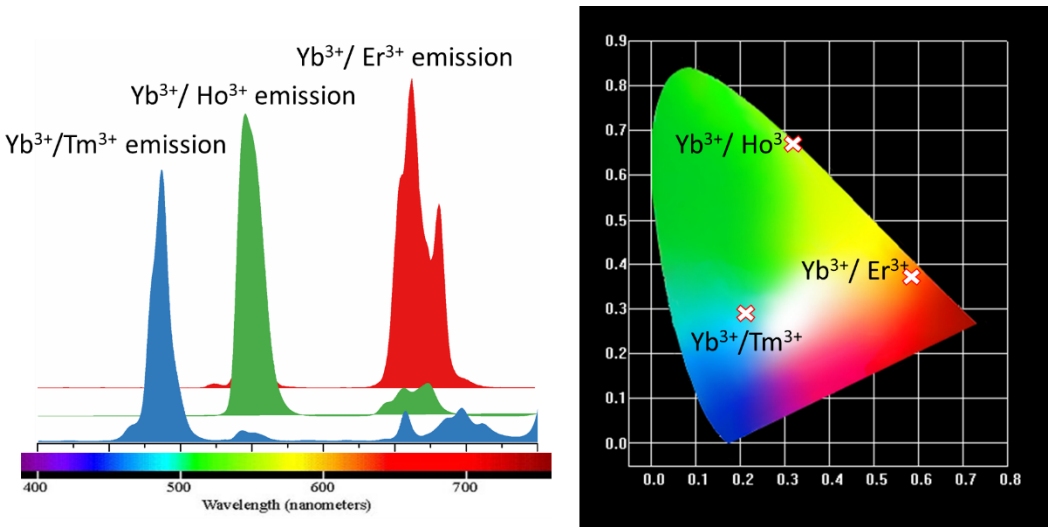

Figure 2.12 UC spectra and CIE chromaticity coordinates (x,y) of Yb^{3+}/Er^{3+}, Yb^{3+}/Ho^{3+} and Yb^{3+}/Tm^{3+} doped $SrIn_2O_4$ UC phosphors upon 980 nm excitation

Yb^{3+}/Er^{3+}-doped $SrIn_2O_4$ UC phosphors showed the strong emission, mainly at 663 nm, which is located in the region of red light (0.57, 0.37). Yb^{3+}/Ho^{3+}-doped $SrIn_2O_4$ UC phosphors presented a strong green emission (0.22, 0.29) with the dominant peak at 546 nm. In Yb^{3+}/Tm^{3+}-doped $SrIn_2O_4$ UC phosphors, the emission centred at 486 nm belongs to the blue light region (0.32, 0.67). Thus, UC emissions in a large colour gamut were obtained by doping various RE^{3+} ions in alkaline indium oxide bulks.

2.4 Conclusions

In this chapter, Yb^{3+}/Er^{3+}-, Yb^{3+}/Ho^{3+}- and Yb^{3+}/Tm^{3+}-doped alkaline indium oxide UC materials were prepared. Then, the distribution of RE^{3+} ions in the crystal structure and their UC luminescent spectra were characterized in detail. It was found that the $SrIn_2O_4$ host has great potential to serve as a multicolour UC-emitting phosphor that can produce

blue, green and red emissions. Although the radius of the RE^{3+} ion is located between those of In^{3+} and Ca^{2+} (Sr^{2+}) ions, Rietveld refinement showed that doped RE^{3+} ions occupied the In^{3+} sites, which helps to understand the network of energy transfer systems. Yb^{3+}/Er^{3+}-doped $SrIn_2O_4$ UC phosphors showed strong red emission and Yb^{3+}/Ho^{3+}-doped $SrIn_2O_4$ emitted green light, while Yb^{3+}/Tm^{3+}-doped $SrIn_2O_4$ showed blue light. Thus, through the strategy of doping with various RE^{3+} ions, multicolour luminescence in a large colour gamut was fulfilled in oxide bulk UC materials using activators such as Er^{3+}, Tm^{3+} and Ho^{3+}.

2.5 References

1. Zhang, C.; Yang, L.; Zhao, J.; Liu, B.; Han, M. Y.; Zhang, Z., White-Light Emission from an Integrated Upconversion Nanostructure: Toward Multicolor Displays Modulated by Laser Power. *Angew Chem Int Ed* **2015,** *54* (39), 11531-5.
2. Xia, Z.; Wu, W., Preparation and luminescence properties of Ce^{3+} and Ce^{3+}/Tb^{3+}-activated $Y_4Si_2O_7N_2$ phosphors. *Dalton Trans* **2013,** *42* (36), 12989-97.
3. Haase, M.; Schafer, H., Upconverting nanoparticles. *Angew Chem Int Ed* **2011,** *50* (26), 5808-29.
4. Zhou, B.; Shi, B.; Jin, D.; Liu, X., Controlling upconversion nanocrystals for emerging applications. *Nat Nanotechnol* **2015,** *10* (11), 924-36.
5. Zhang, Q.; Zhu, B.; Zhuang, Y.; Chen, G.; Liu, X.; Zhang, G.; Qiu, J.; Chen, D., Quantum Cutting in Tm^{3+}/Yb^{3+}-Codoped Lanthanum Aluminum Germanate Glasses. *Journal of the American Ceramic Society* **2010,** *93* (3), 654-657.
6. Zhou, S.; Jiang, S.; Wei, X.; Chen, Y.; Duan, C.; Yin, M., Optical thermometry based on upconversion luminescence in Yb^{3+}/Ho^{3+} co-doped $NaLuF_4$. *Journal of Alloys and Compounds* **2014,** *588*, 654-657.
7. Zeng, J. H.; Su, J.; Li, Z. H.; Yan, R. X.; Li, Y. D., Synthesis and Upconversion Luminescence of Hexagonal-Phase $NaYF_4$:Yb, Er^{3+} Phosphors of Controlled Size and Morphology. *Advanced Materials* **2005,** *17* (17), 2119-2123.
8. Wang, Z.-L.; Hao, J. H.; Chan, H. L. W., Down- and up-conversion photoluminescence, cathodoluminescence and paramagnetic properties of $NaGdF_4 : Yb^{3+},Er^{3+}$ submicron disks assembled from primary nanocrystals. *Journal of Materials Chemistry* **2010,** *20* (16).

9. Luo, Y.; Xia, Z.; Liao, L., Phase formation evolution and upconversion luminescence properties of LaOF:Yb^{3+}/Er^{3+} prepared via a two-step reaction. *Ceramics International* **2012,** *38* (8), 6907-6910.

10. Martín-Rodríguez, R.; Meijerink, A., Infrared to near-infrared and visible upconversion mechanisms in $LiYF_4$: Yb^{3+}, Ho^{3+}. *Journal of Luminescence* **2014,** *147*, 147-154.

11. Wang, F.; Liu, X., Recent advances in the chemistry of lanthanide-doped upconversion nanocrystals. *Chem Soc Rev* **2009,** *38* (4), 976-89.

12. Zheng, W.; Huang, P.; Tu, D.; Ma, E.; Zhu, H.; Chen, X., Lanthanide-doped upconversion nano-bioprobes: electronic structures, optical properties, and biodetection. *Chem Soc Rev* **2015,** *44* (6), 1379-415.

13. Xu, G.; Zeng, S.; Zhang, B.; Swihart, M. T.; Yong, K. T.; Prasad, P. N., New Generation Cadmium-Free Quantum Dots for Biophotonics and Nanomedicine. *Chem Rev* **2016,** *116* (19), 12234-12327.

14. Gai, S.; Li, C.; Yang, P.; Lin, J., Recent progress in rare earth micro/nanocrystals: soft chemical synthesis, luminescent properties, and biomedical applications. *Chem Rev* **2014,** *114* (4), 2343-89.

15. Zhang, J.; Wang, Y.; Guo, L.; Dong, P., Up-conversion luminescence and near-infrared quantum cutting in $Y_6O_5F_8$:RE^{3+} (RE = Yb, Er, and Ho) with controllable morphologies by hydrothermal synthesis. *Dalton Trans* **2013,** *42* (10), 3542-51.

16. Yu, X.; Liang, S.; Sun, Z.; Duan, Y.; Qin, Y.; Duan, L.; Xia, H.; Zhao, P.; Li, D., Microstructure and upconversion luminescence in Ho^{3+} and Yb^{3+} co-doped ZnO naocrystalline powders. *Optics Communications* **2014,** *313*, 90-93.

17. Xia, Z.; Li, J.; Luo, Y.; Liao, L.; Varela, J., Comparative Investigation of Green and Red Upconversion Luminescence in Er^{3+}Doped and Yb^{3+}/Er^{3+}Codoped LaOCl. *Journal of the American Ceramic Society* **2012,** *95* (10), 3229-3234.

18. Li, Q.; Lin, J.; Wu, J.; Lan, Z.; Wang, Y.; Peng, F.; Huang, M., Enhancing photovoltaic performance of dye-sensitized solar cell by rare-earth doped oxide of Lu_2O_3:(Tm^{3+}, Yb^{3+}). *Electrochimica Acta* **2011,** *56* (14), 4980-4984.

19. Fischer, S.; Martín-Rodríguez, R.; Fröhlich, B.; Krämer, K. W.; Meijerink, A.; Goldschmidt, J. C., Upconversion quantum yield of Er^{3+}-doped β-$NaYF_4$ and Gd_2O_2S: The effects of host lattice, Er^{3+} doping, and excitation spectrum bandwidth. *Journal of Luminescence* **2014,** *153*, 281-287.

20. Hou, X.; Zhou, S.; Jia, T.; Lin, H.; Teng, H., Investigation of up-conversion luminescence properties of RE/Yb co-doped Y_2O_3 transparent ceramic (RE=Er, Ho, Pr, and Tm). *Physica B: Condensed Matter* **2011,** *406* (20), 3931-3937.

21. Li, T.; Guo, C.-F.; Yang, Y.-M.; Li, L.; Zhang, N., Efficient green up-conversion emission in Yb^{3+}/Ho^{3+} co-doped $CaIn_2O_4$. *Acta Materialia* **2013,** *61* (19), 7481-7487.

22. Li, T.; Guo, C.; Li, L., Up-conversion luminescence of Er^{3+}-Yb^{3+} co-doped $CaIn_2O_4$. *Opt Express* **2013,** *21* (15), 18281-9.

23. Li, T.; Guo, C.; Jiao, H.; Li, L.; Agrawal, D. K., Infrared-to-visible up-conversion luminescence of $CaIn_2O_4$ co-doped with RE^{3+}/Yb^{3+} (RE=Tm, Pr, Nd). *Optics Communications* **2014,** *312*, 284-286.

24. Chen, G.; Qiu, H.; Prasad, P. N.; Chen, X., Upconversion nanoparticles: design, nanochemistry, and applications in theranostics. *Chem Rev* **2014,** *114* (10), 5161-214.

25. Yang, Z.; Tian, J.; Wang, S.; Yang, G.; Li, X.; Li, P., Combustion synthesis of $SrIn_2O_4:Eu^{3+}$ red-emitting phosphor for white light-emitting diodes. *Materials Letters* **2008,** *62* (8-9), 1369-1371.

26. Wang, H.; Tian, L., Luminescence properties of $SrIn_2O_4:Eu^{3+}$ incorporated with Gd^{3+} or Sm^{3+} ions. *Journal of Alloys and Compounds* **2011,** *509* (6), 2659-2662.

27. Rodríguez-García, C. E.; Perea-López, N.; Hirata, G. A.; DenBaars, S. P., Red-emitting $SrIn_2O_4 : Eu^{3+}$ phosphor powders for applications in solid state white lamps. *Journal of Physics D: Applied Physics* **2008,** *41* (9).

28. Li, P.; Wang, Z.; Yang, Z.; Guo, Q., $SrIn_2O_4:Eu^{3+}$, Sm^{3+}: A Red Emitting Phosphor with a Broadened Near-Ultraviolet Absorption Band for Solid-State Lighting. *Journal of The Electrochemical Society* **2011,** *158* (12).

29. Baszczuk, A.; Jasiorski, M.; Nyk, M.; Hanuza, J.; Mączka, M.; Stręk, W., Luminescence properties of europium activated $SrIn_2O_4$. *Journal of Alloys and Compounds* **2005,** *394* (1-2), 88-92.

30. Shannon, R. D., Revised effective ionic radii and systematic studies of interatomic distances in halides and chalcogenides. *Acta Crystallographica Section A* **1976,** *32* (5), 751-767.

31. Orlova, A. I.; Pleskova, S. N.; Malanina, N. V.; Shushunov, A. N.; Gorshkova, E. N.; Pudovkina, E. E.; Gorshkov, O. N., $Ca_3(PO_4)_2:Er^{3+},Yb^{3+}$: An upconversion phosphor for in vivo imaging. *Inorganic Materials* **2013,** *49* (7), 696-700.

32. Molokeev, M. S.; Bogdanov, E. V.; Misyul, S. V.; Tressaud, A.; Flerov, I. N., Crystal structure and phase transition mechanisms in $CsFe_2F_6$. *Journal of Solid State Chemistry* **2013,** *200*, 157-164.

33. V4, B. A. T., General Profile and Structure Analysis Software for Powder Diffraction Data. *User's Manual. Bruker AXS, Karlsruhe, Germany* **2008**.

34. Tang, J.; Zou, Z.; Ye, J., Effects of Substituting Sr^{2+} and Ba^{2+} for Ca^{2+} on theStructural roperties and Photocatalytic Behaviors of $CaIn_2O_4$. *Chem. Mater.* **2004,** *16*, 1644-1649.

35. Shannon, R. D., Revised Effective Ionic Radii and Systematic Studies of Interatomic Distances in Halides and Chalcogenides. *Acta Cryst. A* **1976,** *32*, 751-767.

36. Liu, Q.; Feng, W.; Li, F., Water-soluble lanthanide upconversion nanophosphors: Synthesis and bioimaging applications in vivo. *Coordination Chemistry Reviews* **2014,** *273-274*, 100-110.

37. Denault, K. A.; Brgoch, J.; Gaultois, M. W.; Mikhailovsky, A.; Petry, R.; Winkler, H.; DenBaars, S. P.; Seshadri, R., Consequences of Optimal Bond Valence on Structural Rigidity and Improved Luminescence Properties in $Sr_xBa_{2-x}SiO_4:Eu^{2+}$ Orthosilicate Phosphors. *Chemistry of Materials* **2014,** *26* (7), 2275-2282.

38. Atuchin, V. V.; Aleksandrovsky, A. S.; Chimitova, O. D.; Gavrilova, T. A.; Krylov, A. S.; Molokeev, M. S.; Oreshonkov, A. S.; Bazarov, B. G.; Bazarova, J. G., Synthesis and Spectroscopic Properties of Monoclinic α-$Eu_2(MoO_4)_3$. *The Journal of Physical Chemistry C* **2014,** *118* (28), 15404-15411.

39. Berry, M. T.; May, P. S., Disputed Mechanism for NIR-to-Red Upconversion Luminescence in $NaYF_4:Yb^{3+},Er^{3+}$. *J Phys Chem A* **2015,** *119* (38), 9805-11.

40. Xia, Z.; Du, P.; Liao, L., Facile hydrothermal synthesis and upconversion luminescence of tetragonal $Sr_2LnF_7:Yb^{3+}/Er^{3+}$(Ln = Y, Gd) nanocrystals. *physica status solidi (a)* **2013**, n/a-n/a.

41. Zhao, J.; Jin, D.; Schartner, E. P.; Lu, Y.; Liu, Y.; Zvyagin, A. V.; Zhang, L.; Dawes, J. M.; Xi, P.; Piper, J. A.; Goldys, E. M.; Monro, T. M., Single-nanocrystal sensitivity achieved by enhanced upconversion luminescence. *Nat Nanotechnol* **2013,** *8* (10), 729-34.

CHAPTER 3

Multicolour Luminescence of RE^{3+} (RE = Tm, Tb, Eu) ions in Fluoride Nanoparticles

3.1 Introduction

Direct doping with various RE^{3+} ions is the key to producing multicolour luminescence in fluoride upconversion nanoparticles (UCNPs). With the improvement of synthesis technology in recent years, RE^{3+} ion-doped fluoride UC materials have become widely studied at the nanoscopic level, where UCNPs can be well controlled in terms of particle size, phase, dimension and doping level[1-5]. With these advances, UCNPs with multicolour luminescence have been used in a wide range of applications such as 3D volumetric displays [6-7], sensing [8-10], bio-imaging and fluorescent probes[11-13], drug delivery [14-15], photovoltaic devices [16] and anti-counterfeiting technology [17-19].

In typical RE^{3+} ion-doped fluoride UCNP systems, $NaYF_4$ and $NaGdF_4$ are considered ideal host materials for UC luminescence due to their very low phonon energies. By introducing thousands of photon sensitizers (i.e., Yb^{3+} ions) and activator ions (i.e., Tm^{3+} and Er^{3+}) to form an energy-transfer network in a single nanoparticle, $NaREF_4$ UCNPs can up-convert low energy near-infrared (NIR) photons into high-energy visible emissions with many unique properties, including tunable multicolour emission capability, high signal-to-noise ratio, low cytotoxicity and high chemical and photoluminescent stability[20-21]. These properties originate from intro-configuration 4fn electron transitions between the RE^{3+} doped ions[22]. In order to tune and improve the multicolour luminescent properties of UCNPs, it is critical to understand their crystal structures, the distribution of RE^{3+} ions within them, and their internal energy transfer networks.

However, very little attention has been paid to dopant ion distributions in $NaREF_4$ host crystals. It has been often assumed that the dopants of sensitizer and activator ions are uniformly distributed because these ions have similar chemical properties to the trivalent RE^{3+} host ions. However, minor differences in ionic radius and electronic polarity could cause different local distributions, so doped ions can show different local distributions across a single nanoparticle. Van Veggel et al. found that due to cation exchange, using a procedure intended for an alloy structure that does not have a true alloy structure means that the dopant ions are not statistically distributed in the nanoparticle. They employed synchrotron-based high-resolution X-ray photoelectron spectroscopy (XPS) to analyse RE^{3+}-doped and undoped $NaREF_4$ nanocrystals. The results showed non-uniform distributions of Y^{3+}, Nd^{3+} and Tb^{3+} in a $NaGdF_4$ matrix, due to the differences in the ionic radii of the dopants compared to that of Gd^{3+} [23]. Additionally, they were able to identify two distinct chemical environments of Y at the surface and interior of the $NaYF_4$ nanoparticles [24], and also provided evidence for the core-shell structure of $NaYF_4/NaGdF_4$ [25] and LaF_3/GdF_3 [26] (Figure 3.1a). Zhang et al. also reported heterogeneous distributions of Yb^{3+} and Er^{3+} ions in $NaGdF_4$ nanoparticles at different stages of the spontaneous growth process (Figure 3.1b) using energy dispersive X-ray spectroscopy (EDX) and inductively coupled plasma mass/atomic emission spectrometry (ICP-MS/AES)[27]. Yan and co-workers found that the lattice parameters, as well as the coordination number and local symmetry of rare earth ions within NaY/GdF_4: Yb^{3+}/Er^{3+} nanoparticles, changed with the molar ratio of [F]/[RE] [28].

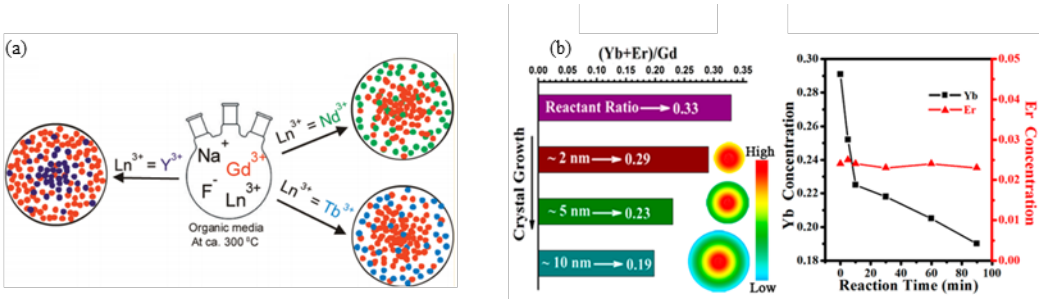

Figure 3.1 The phenomenon of non-uniform distributions of Y^{3+}, Nd^{3+} and Tb^{3+} ions in a $NaGdF_4$ host (a)[23]. Heterogeneous distribution of Yb^{3+} in $NaGdF_4$ UCNPs: the total doping concentrations of Yb^{3+} and Er^{3+} ions at different growth stages, and the evolutions of Yb^{3+} and Er^{3+} doping concentrations during the spontaneous growth process (b)[27]

These examples illustrate that systematic characterization of the dopant distribution in host $NaREF_4$ nanoparticles will lead to a better understanding of the UC luminescence

mechanism. Because of the different nucleation energies of RE^{3+} ions, some ions may tend to be concentrated in the centre of the nanoparticles and exhibit a radially-decreasing concentration gradient towards the surface, forming a core-shell-like nanostructure. The core-shell-like distribution of doped RE^{3+} ions across nanoparticles plays a potential role in optimizing and improving the properties of multicolour luminescence.

In this work, by employing synchrotron-based XPS measurements, we conducted a systematic analysis of the distributions of RE^{3+} ions within typical $NaYF_4$: Yb^{3+}, Tm^{3+} and $NaYF_4$: Gd^{3+}, Tm^{3+} UCNP systems. Then, the UC luminescent properties of $NaGdF_4$ UCNPs by doping with Yb^{3+}/Tm^{3+} ions were studied. Under the guidance of the distribution of RE^{3+} ions within the UCNPs, Yb^{3+}/Tm^{3+}/Tb^{3+} and Yb^{3+}/Tm^{3+}/Eu^{3+}-ion co-doped $NaGdF_4$ UCNPs were prepared using a cation exchange method in water, and we systematically correlated the structure with its multicolour luminescence.

3.2 Experimental section

3.2.1 Reagents and equipment

The chemicals and reagents described in this chapter are listed in Table 3.1. All the chemicals were used without further purification or modification unless otherwise stated.

Table 3.1 Main experimental reagents, specifications and manufacturer

Chemicals	Specification	Manufacturer
$YCl_3 \cdot 6H_2O$	99.99%	Sigma-Aldrich (Australia)
$GdCl_3 \cdot 6H_2O$	99.99%	
$YbCl_3 \cdot 6H_2O$	99.99%	
$TmCl_3 \cdot 6H_2O$	99.99%.	
$ErCl_3 \cdot 6H_2O$	99.99%.	
$TbCl_3 \cdot 6H_2O$	99.99%.	
$EuCl_3 \cdot 6H_2O$	99.99%.	
NaOH	99.99%	
NH_4F	≥99.99%	
NaF	99.99%	
Oleic Acid (OA)	90%	
1-Octadecene (ODE)	90%	

Oleylamine (OM)	90%	
Ethanol	100%	
Methanol	≥99.9%	
Toluene	≥99.9%	Chem-Supply (Australia)
Cyclohexane	≥99.9%	
Tetrahydrofuran (THF)	≥99.9%	
Hydrochoride (HCl)	37%	Sigma-Aldrich (Australia)

The instruments and equipment used for specimen synthesis in this chapter are listed in Table 3.2.

Table 3.2 Main experimental equipment, specific indicators and manufacturer

Equipment	**Specification**	**Manufacturer**
Analytical balance	SJF2104 (0.1 mg)	Eppendorf (Germany)
Ultrasonic cleaner	Benchtop Cleaners (FXP) 2.7 Litre	Unisonics (Australia)
Vortex mixer	LSE	Corning (Australia)
Centrifuge	Centrifuge 5424 and 5804	Eppendorf (Germany)
Magnetic stirrer	Model: RO 10	IKA (Australia)
Heating mantle	Temperature range: up to 400 °C	Labquip Technologies
Temperature controller	Temperature range: up to 400 °C	Labquip Technologies
Three-neck round-bottom	50 mL, 100 mL	Synthware (China)
Thermometer	Range: 0 to 330 °C	RS Components PTY Ltd.
Rare earth extra power stir	TPFE-coated, elliptical	Sigma-Aldrich (Australia)
Pipettes	Eppendorf Reference® 2, whole set	Eppendorf (Germany)
Pipette tips	epT.I.P.S.® Motion, full range	Eppendorf (Germany)
Centrifuge tubes	SSUbio 1260-00 and 1310-00	Scientific Specialties, Inc.
Glass slide	25 × 57 mm	Hurst Scientific Pty. Ltd.
Cover slip	22 × 22 mm	Muraban Laboratories

3.2.2 Synthesis of materials

The coprecipitation method was used to produce monodispersed core UCNPs for testing in this chapter[29].

Synthesis of $NaYF_4$: 20%Yb^{3+}, 4%Tm^{3+} UCNPs: β-20%Yb^{3+}, 4%Tm^{3+} UCNPs were prepared according to previous reports[30-31]. Typically, a methanol solution of 0.04 mmol

$TmCl_3$, 0.2 mmol $YbCl_3$, and 0.76 mmol YCl_3 was mixed with 6 ml OA and 15 ml ODE in a 50 ml round-bottom flask. The mixture was degassed under an Ar flow and then heated at 150 °C under stirring for 30 min until the solution became clear. After cooling to 50 °C, a methanol solution containing 4.0 mmol NH_4F and 2.5 mmol NaOH was added and stirred vigorously for more than 30 min. Then, the mixed solution was heated to 110 °C to evaporate the methanol and then to 150 °C to evaporate the residual water. Finally, the solution was heated to 300 °C with different heating profiles by using heating durations of 21 mins, 17 mins, 12 mins, 9.3 mins and 8 mins. After reaction and cooling to room temperature, the synthesized nanocrystals were washed with cyclohexane/ethanol several times and dispersed in toluene (or cyclohexane) for use. By adjusting the mole ratio of NH_4F and NaOH, different sizes of UCNPs could be synthesized. The $NaYF_4$: 45%Gd^{3+}, 4%Tm^{3+} material was also synthesized using this method.

Synthesis of $NaGdF_4$: 49%Yb^{3+}, 1%Tm^{3+} UCNPs: The same method as above was adopted, except for some minor changes: the methanol solution contained NH_4F (3.3 mmol) and NaOH (2.5 mmol), and the heating temperature was 290 °C.

Preparation of $Yb^{3+}/Tm^{3+}/Tb^{3+}$ and $Yb^{3+}/Tm^{3+}/Eu^{3+}$ co-doped $NaGdF_4$ UCNPs: Corresponding samples were prepared using a cation exchange method in water according to a previous report [32]. In a typical process, the as-prepared oleic acid-capped nanoparticles were dispersed in a mixed solution of ethanol (1 mL) and HCl (0.2 M; 1 mL). The mixture was sonicated for 5 min and collected by centrifugation. Subsequently, the resulting products were washed with ethanol/H_2O several times and re-dispersed in H_2O. After that, a stock solution (1 mL) of the as-prepared ligand-free $NaGdF_4$: Yb^{3+}/Tm^{3+} nanoparticles was mixed with an aqueous solution of $RECl_3$ (RE = Tb^{3+}, Eu^{3+}). The resulting mixture was shaken thoroughly and heated at room temperature for 30 min. Subsequently, the products were collected by centrifugation, washed with H_2O several times, and re-dispersed in H_2O for testing.

3.2.3 Characterization

TEM Characterization: The morphology of the synthesized nanocrystals was characterized using transmission electron microscopy (TEM; Philips CM10 TEM) at an operating voltage of 100 kV. The samples were prepared by placing a drop of a dilute

suspension of nanocrystals onto formvar-coated copper grids (300 mesh) and allowing it to dry in a desiccator at room temperature.

XRD Characterization: X-ray diffraction (XRD) patterns were recorded on a D8 Advance X-ray powder diffractometer (Bruker Corporation, Germany) using Cu-Kα1 radiation (40 kV, 25 mA, λ = 0.15418 nm) in the 2θ range from 5° to 100°. Scan steps were 0.02° with a 4 s duration at each step. Rietveld refinement was performed using TOPAS 4.2 software[33]. The XRD samples were prepared by placing several drops of nanocrystal dispersion in a toluene cast on a glass wafer.

Photoluminescence Spectra by Spectrofluorometer: The UC luminescence spectra were obtained using of a Fluorolog-Tau3 spectrofluorometer (JobinYvon-Horiba) equipped with an external 980 nm CW diode laser with a pump power density of 500 W/cm^2. The UC nanocrystals were prepared to a concentration of 1 mg/ml by the subtractive weighting method for the entire specimen. The dispersion was transferred to quartz cuvettes with 10 mm path lengths, and three measurements were conducted for each sample.

X-ray Photoelectron Spectroscopy (XPS) with Variable Excitation Energy: X-ray photoelectron spectroscopy (XPS) with variable photon energy was performed on the Soft X-ray Spectroscopy beamline at the Australian Synchrotron. UCNPs dispersed in cyclohexane were drop-cast onto clean test-grade silicon wafers (<1 ohm/cm) and allowed to dry in air before being loaded into the analysis chamber at ultrahigh vacuum (~10^{-10} mbar) for data acquisition. Spectra calibrated to a polycrystalline gold reference were collected at varying X-ray photon energies with an energy step size of 0.1 eV in the regions of the Y 3d core level, the Yb 4d core level and the Gd 4d core level (200–140 eV). A background fit was applied to each spectrum and the integrated area of each intensity determined with the area ratios of Y and Yb (Gd) plotted against photoelectron kinetic energy. The inelastic electron mean free path of the photoelectrons was calculated using QUASES-IMFP-TPP2M Ver. 3.0 software.

3.3 Results and discussion

3.3.1 Morphology of $NaYF_4$: Yb^{3+}, Tm^{3+} UCNPs

The doping concentration of Tm^{3+} in the $NaYF_4$: Yb^{3+}, Tm^{3+} nanoparticles was kept at 4% for all samples so, in this work, the samples will be denoted as $NaYF_4$: Yb^{3+}. Figure 3.2 shows the morphology of the $NaYF_4$: Yb^{3+}, Tm^{3+} nanoparticles with different sizes induced by controlling the heating rate during the formation of UCNPs [34], or by varying the doping concentration of Yb^{3+} [35]. Figure 3.2 (a-e) shows the $NaYF_4$: 20%Yb^{3+} UCNPs with sizes of 13.0 nm, 26.2 nm, 31.1 nm, 36.6 nm and 43.0 nm. Figure 3.2 (f-i) shows the $NaYF_4$: *x*%Yb^{3+} UCNPs with sizes of 21.9 nm, 26.1 nm, 35.9 nm and 51.3 nm, with x = 20%, 30%, 45% and 60% Yb^{3+}, respectively.

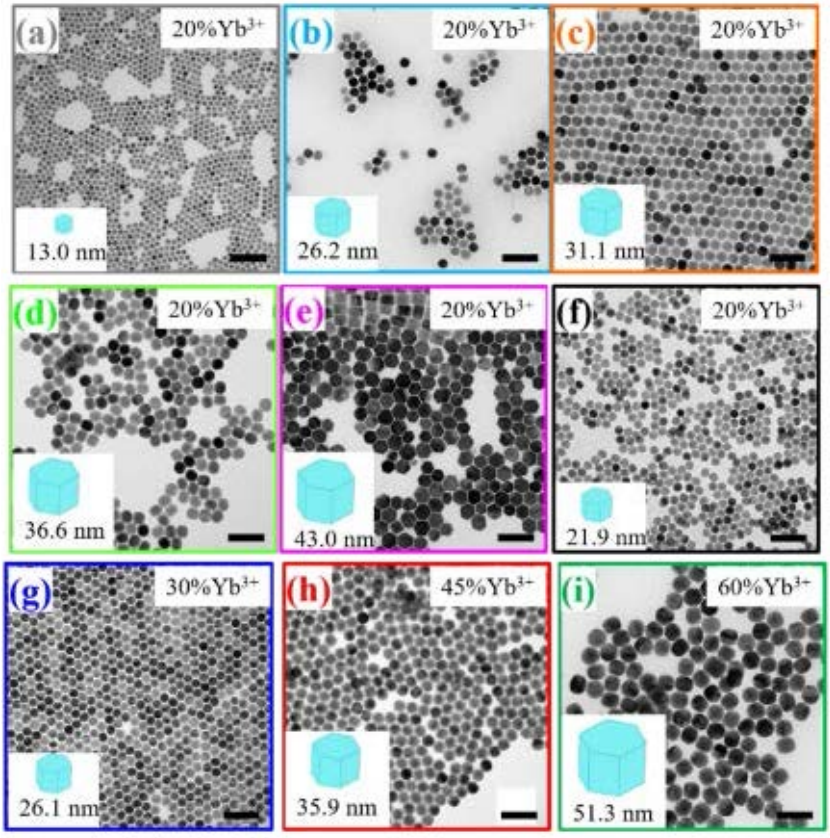

Figure 3.2 TEM images of as-synthesized UCNPs with different sizes and Yb^{3+} doping concentrations

3.3.2 Distribution of RE^{3+} in Lattice

Typical $NaYF_4$:20%Yb^{3+}/4%Tm^{3+} nanoparticles with a diameter of about 26.2 nm were selected for phase and crystal structure characterization. The collected XRD patterns and Rietveld refinement plots are shown in Figure 3.3a. Rietveld refinement showed a good

result, in that all peaks of the UCNPs were indexed by hexagonal cells (P63/m) with parameters close to those reported earlier for $NaYF_4$. Therefore, the crystal structure of $NaYF_4$ was taken as a starting model for Rietveld refinement. The real chemical formula should be $Na_{1.5}RE_{1.5}F_6$. In the crystal structure of β-$NaYF_4$: Yb^{3+}/Tm^{3+} UCNPs, there are two types of cationic sites in the unit cell model for $Na_{1.5}RE_{1.5}F_6$: a nine-fold coordinated position occupied randomly by $1/2Na^+$ and $1/2RE^{3+}$, and a six-fold coordinated one occupied by Na^+ [36]. The polyhedra about the first positions are tricapped trigonal prisms, and those about the second positions are irregular octahedra. With the doping of Yb^{3+} and Tm^{3+} ions, these ions replace the Y-occupation in the unit cell structure, thus forming a random $Na/Y/Yb^{3+}/Tm^{3+}$ in the same position in the crystal lattice. The final crystal structure of Yb^{3+}/Tm^{3+}-doped $NaYF_4$ is shown in Figure 3.3b.

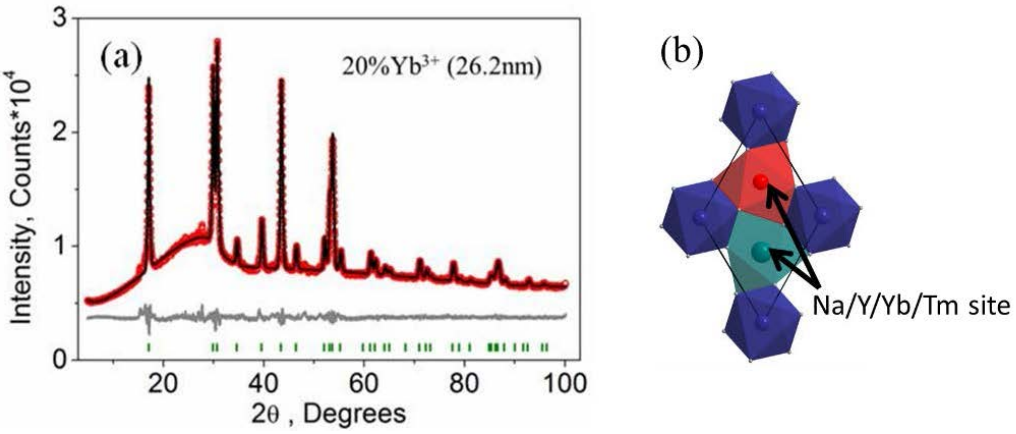

Figure 3.3 XRD pattern for the refinement of 26.2 nm $NaYF_4$: 20%Yb^{3+}/4%Tm^{3+} UCNPs (a). Crystal structure of Yb^{3+}/Tm^{3+}-doped $NaYF_4$ (b)

3.3.3 Distribution of RE^{3+} within $NaYF_4$: Yb^{3+}/Tm^{3+} nanoparticles

Since the RE^{3+} ions distribute randomly in one site in the lattice cell, it is not known how the RE^{3+} ions distribute across a single UCNP particle. Therefore, synchrotron-based XPS measurements were made to conduct a systematic analysis of the distributions of RE^{3+} ions within typical $NaYF_4$: Yb^{3+}, Tm^{3+} and $NaYF_4$: Gd^{3+}, Tm^{3+} UCNP systems. First of all, the XPS survey patterns of three samples of $NaYF_4$: Yb^{3+}/Tm^{3+} under a photon excitation of 1486 eV were measured (Figure 3.4). These three samples showed similar patterns, and all the peaks could be identified as characteristic peaks of the Na, Y, Yb and F elements in the UCNPs.

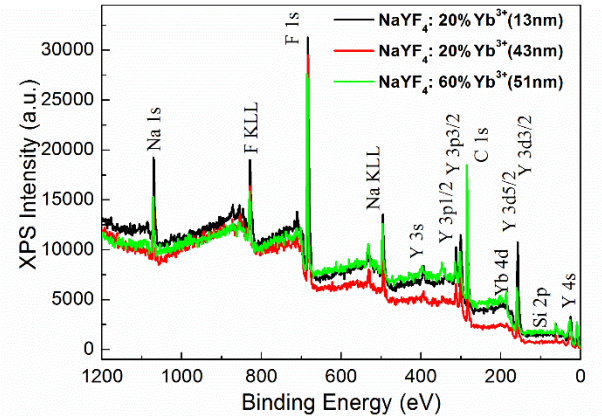

Figure 3.4 XPS survey spectra for the $NaYF_4$ UCNPs acquired at a photon energy of 1486 eV. All the peaks are identified as elements in the UCNPs

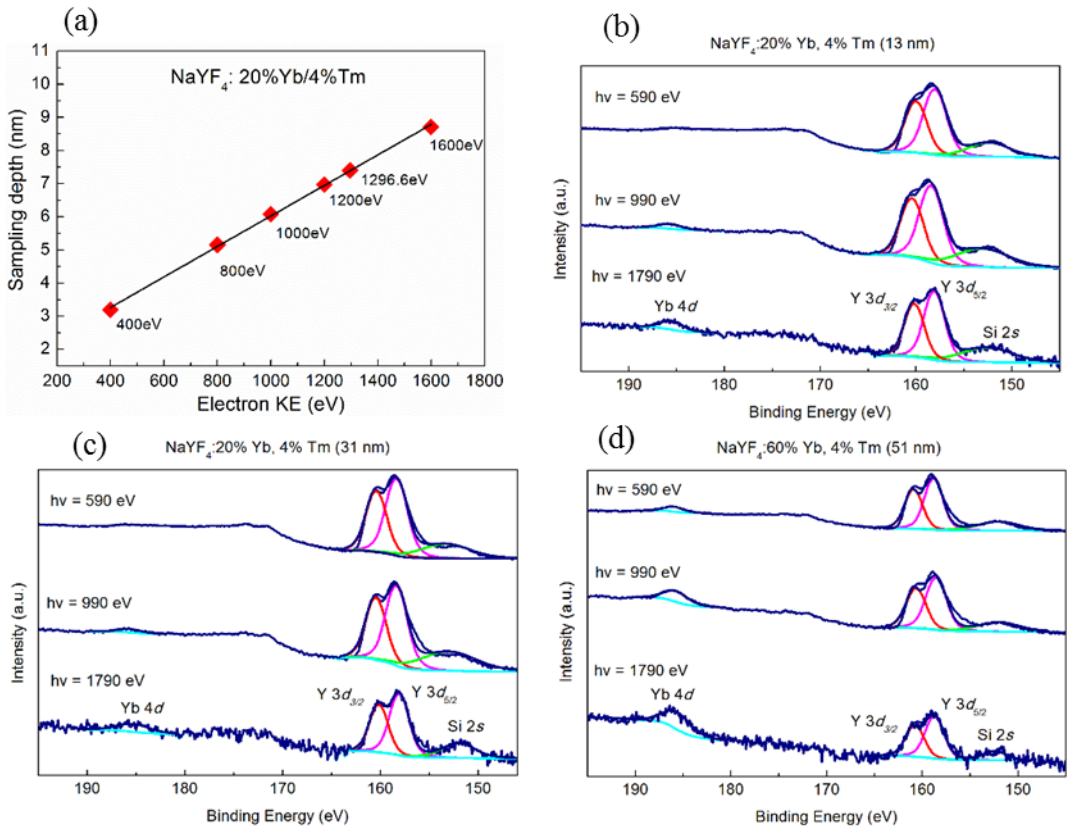

Figure 3.5 XPS sampling depth in $NaYF_4$ as a function of photoelectron kinetic energy (KE) (a). Fitted variable photon energy XPS spectra of three typical UCNPs with different sizes and Yb^{3+} concentrations, showing the consistent increase in Yb/Y ratio as the photon energy increases (b, c, d)

Synchrotron-based XPS measurements use variable photoelectron kinetic energy as excitation, which makes it possible to adjust the sampling depth to determine the elemental gradient with depth in a material. Under a certain range of photoelectron energy, increasing the photoelectron energy leads to an increase in the kinetic energy of the

emitted photoelectrons and, hence, the electron inelastic mean free path (IMFP). Hence, the XPS sampling depth (taken as 3 × IMFP) in $NaYF_4$ is a function of photoelectron kinetic energy (KE), which is plotted in Figure 3.5a. The XPS sampling depth based on synchrotron radiation is approximately 2–10 nm under the surface of the nanoparticle. Because most of the $NaYF_4$ UCNPs we prepared had a size distribution of 20–40 nm, this sampling depth is very suitable for studying the elemental distribution of UCNPs from surface to interior. For example, at hν = 400 eV, the sampling depth in $NaYF_4$: $20\%Yb^{3+}/4\%Tm^{3+}$ was about 3.2 nm, and at 1600 eV, it was about 8.7 nm.

Figures 3.5b, c, d show the depth-resolved XPS spectra of Y 3*d*, Yb 4*d* and Si 2*s* core levels collected from UCNPs of $NaYF_4$: $20\%Yb^{3+}$ (13.0 nm), $NaYF_4$: $20\%Yb^{3+}$ (31.1 nm), and $NaYF_4$: $60\%Yb^{3+}$ (51.3 nm) at photon energies of 590 eV, 990 eV and 1790 eV. The photoelectron data for Yb^{3+} and Y^{3+} were collected within the same photoelectron energy window under identical acquisition conditions. The variations in the relative intensities of Yb^{3+} and Y^{3+} with increasing sampling depth are associated with the inhomogeneous distributions of these elements. Each spectrum had a Shirley background removed and the peak intensities were extracted using Gaussian peak fitting. As shown in the figures, the binding energies of the doublet peaks of the Y 3*d* split spin-orbital core level match the reported values of ~159 eV and ~161 eV, respectively, for the Y 3*d*5/2 and Y 3*d*3/2 peaks [23-24]. The binding energy of the Yb 4*d* core level also matches the reported value of ~185 eV [37]. The Si 2*s* peak at around ~153 eV belongs to the silicon wafer used as the substrate for the experiment. At the lowest photon energy used, 590 eV and, thus, at the shallowest sampling depth, the Yb 4*d* peak was undetectable; however, as the photon energy was increased to 990 eV and, finally, to 1790 eV, the relative ratio of the intensity of the Yb 4*d* peak to the Y 3*d* doublet increased. The XPS peak of the Yb^{3+} dopant increased significantly compared with that of the host Y^{3+} as the photon energy was increased from 590 eV to 1790 eV, corresponding to the sampling depth range of 3.2–8.7 nm. This indicates that the nanoparticles are more heavily doped with Yb^{3+} at the crystal core.

To determine the distribution of the dopant ions in $NaYF_4$ matrix nanoparticles, the intensity ratio of the Yb 4*d* and Y 3*d* core levels was calculated and plotted as a function of the electron kinetic energy and effective sampling depth after correction by the relevant photoionization cross-sections [38] in Figure 3.6. Figure 3.6a shows the intensity ratios of

Yb 4*d* and Y 3*d* for $NaYF_4$: 20%Yb^{3+} nanoparticles of various sizes. The ascending trends in Yb 4*d*/Y 3*d* ratio are quite similar for all 20%Yb^{3+}-doped $NaYF_4$ nanoparticles, although their size varies from 13.0 nm to 43.0 nm, indicating that 20% Yb^{3+} is more concentrated in the crystal interior and gradually decreases from the centre to the surface. Figure 3.6b shows the intensity ratios of Yb 4*d*/Y 3*d* of $NaYF_4$ nanoparticles with 20%, 30%, 45% and 60% Yb^{3+}. The general trends in these ratios for nanoparticles with different Yb^{3+} concentrations increase with sampling depth, also indicating that Yb^{3+} is concentrated in the central area and that the doping level decreases towards the surface. The positive and uniform linear increases in the Yb 4*d*/Y 3*d* ratios with sampling depth indicates that the distribution of Yb^{3+} in the $NaYF_4$ nanoparticles decreases radially from the centre to the surface with a constant gradient. The results indicate that the distributions of sensitizer ions within the host nanoparticles are not uniform, but the heterogeneous distribution gradient is the same for every UCNP regardless of its size or sensitizer concentration.

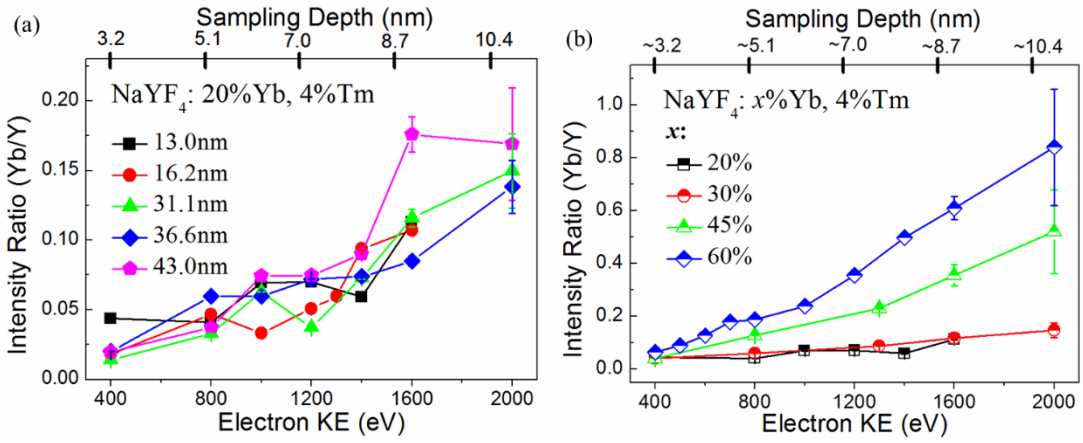

Figure 3.6 Increasing Yb^{3+}/Y^{3+} atomic ratio within UCNPs with increasing photon energy/sampling depth in $NaYF_4$: 20%Yb^{3+} nanoparticles with sizes of 13.0 nm, 26.2 nm, 31.1 nm, 36.6 nm and 43.0 nm (a), and in $NaYF_4$ nanoparticles containing 20% Yb^{3+}, 30%Yb^{3+}, 45%Yb^{3+}, and 60%Yb^{3+} with sizes of 21.9 nm, 26.1 nm. 35.9 nm and 51.3 nm, respectively (b)

3.3.4 Distribution of RE^{3+} ions within $NaYF_4$:Gd^{3+}/Tm^{3+} nanoparticles

A similar phenomenon has been observed in $NaYF_4$:45%Gd, 4%Tm nanoparticles. In this work, these samples will be denoted as $NaYF_4$: Gd^{3+}. The distributions of Gd^{3+} and Y^{3+} ions in single nanoparticles are also non-uniform, and there is a radical gradient in Gd^{3+} distribution from the surface to the core of each nanoparticle. Figure 3.7a shows the depth-resolved XPS spectra of the Y 3d, Gd 4d and Si 2s core levels collected from

UCNPs of $NaYF_4$:45%Gd at a photon energy of 1790 eV. Photoelectron data for Gd^{3+} and Y^{3+} were also collected within the same photoelectron energy window under identical acquisition conditions.

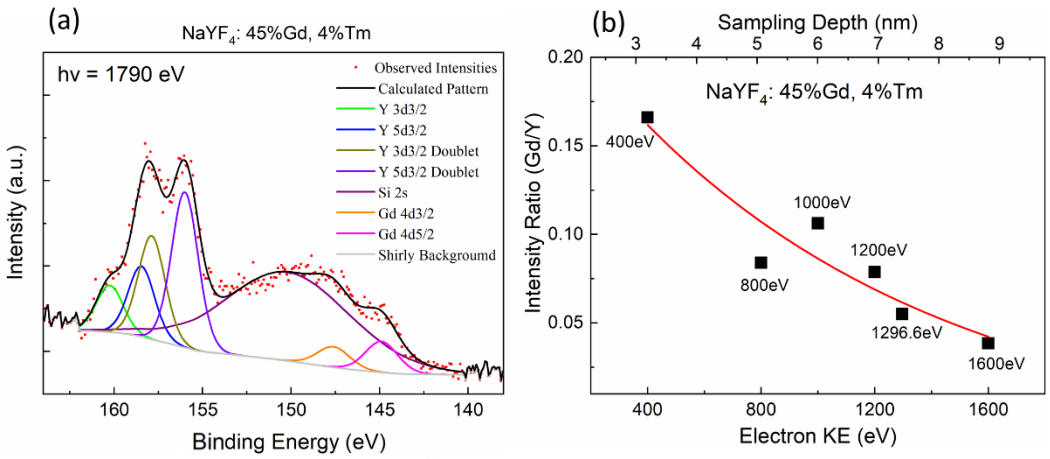

Figure 3.7 Fitted variable photon energy XPS spectra of $NaYF_4$:45%Gd nanoparticles at a photon energy of 1790 eV (a); Decreasing Gd^{3+}/Y^{3+} atomic ratio within $NaYF_4$:45%Gd UCNPs with increasing photon energy and sampling depth (b)

As shown in the figures, the binding energies of the doublet peaks of the Y 3*d* split spin-orbital core level match the reported values of ~159 eV and ~161 eV for the Y 3*d*5/2 and Y 3*d*3/2 peaks, respectively [23-24]. The binding energy of the Gd 4*d* core level also matches the reported values of ~144 eV and ~148 eV for the Gd 4*d*5/2 and Gd 4*d*3/2 peaks, respectively. The Si 2*s* peak at around ~153 eV belongs to the silicon wafer used as the substrate in the experiment. The photon energy was increased from 590 eV to 1790 eV to determine the distribution of Gd dopant ions in $NaYF_4$ matrix nanoparticles. The intensity ratios of the Gd 4*d* and Y 3*d* core levels were calculated and plotted as a function of the electron kinetic energy and effective sampling depth after correction by the relevant photoionization cross-sections in Figure 3.7b. The descending trends of the Gd 4*d*/Y 3*d* ratios indicate that the 45% Gd^{3+} ions are more concentrated at the nanoparticle surface, and their concentration gradually decreases from the surface to the centre.

3.3.5 Core-shell-like distribution of RE^{3+} Ions

Table 3.3 shows the radii of four kinds of RE^{3+} ions (Gd^{3+}, Y^{3+}, Tm^{3+} and Yb^{3+}, listed in order of decreasing radius) under 9-fold coordinate[39]. It was found that the radius of Gd^{3+} was bigger than that of Y^{3+}, which was bigger than that of Yb^{3+}. According to previous reports[40], and as illustrated in Figure 3.8, we conclude that RE^{3+} ions with larger radii

tend to be concentrated at the surface of UCNPs and exhibit a radially decreasing gradient in concentration towards the centre. Therefore, they form a core-shell-like nanostructure within UCNPs. This may be because different RE^{3+} ions have different nucleation energies during synthesis. The RE^{3+} ion distribution revealed in the present work demonstrates the formation of Y^{3+}-rich and Yb^{3+}-depleted shells in $NaYF_4$: Yb, Tm, while Gd^{3+}-rich and Y^{3+}-depleted shells were also observed in $NaYF_4$: Gd, Tm UCNPs. Due to the core-shell-like nanostructures of $NaYF_4$: Gd, Tm and $NaYF_4$: Yb, Tm, we propose that $NaGdF_4$: Yb^{3+}/Tm^{3+} UCNPs will also form core-shell-like nanostructures during synthesis. Furthermore, Gd^{3+} ions should be more concentrated at the nanoparticle surface and gradually decrease in concentration towards the centre. Therefore, a Gd^{3+}-rich shell would form at the surfaces of UCNPs.

Table 3.3 Radii of four types of RE^{3+} ions under their corresponding coordinate

Ion	Coordinate (CN)	Radius（Å）
Gd^{3+}	9	1.107
Y^{3+}	9	1.075
Tm^{3+}	9	1.052
Yb^{3+}	9	1.042

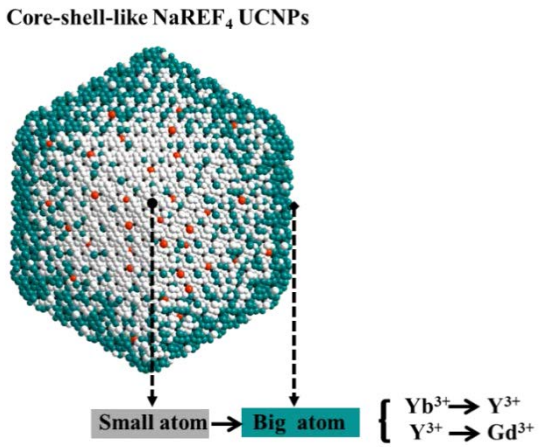

Figure 3.8 Diagram of the proposed RE^{3+} distribution within a single $NaREF_4$ nanoparticle: small radius ions occupy the centre while large ones occupy the surface

3.3.6 Cation exchange on core-shell-like UCNPs

These core-shell-like structures are expected to influence the multicolour luminescent properties of UCNPs. Natural Gd^{3+}-rich shells can effectively bridge the energy transfer gap from sensitizers to activators through long-range energy migration in the sub-lattice,

such that the real core-shell structure of $NaGdF_4$: Yb^{3+}/Tm^{3+}@$NaGdF_4$ is not necessary anymore. Therefore, the multicolour luminescence properties of the core-shell-like $NaGdF_4$: Yb^{3+}/Tm^{3+} nanoparticles can be directly tuned by adding different kinds of new activator ions, such as Tb^{3+} and Eu^{3+}. The combination of cation exchange and EMU in core-shell-like $NaGdF_4$: Yb^{3+}/Tm^{3+} nanocrystals enables us to obtain luminescence in the colours of interest. In this study, Tb^{3+}-exchanged nanocrystals were taken as an example to study the process of multicolour luminescence. $Yb^{3+}/Tm^{3+}/Tb^{3+}$ co-doped $NaGdF_4$ UCNPs were prepared by a cation exchange method according to a previous report[32]. In the procedure, UCNPs of $NaGdF_4$: 49%Yb^{3+}, 1%Tm^{3+} were prepared first. Subsequently, the oleic acid capped on the surfaces of UCNPs was removed using HCl acid. After that, cation exchange was introduced for mixing an aqueous solution containing a $TbCl_3$ (or $EuCl_3$) precursor and the as-prepared ligand-free $NaGdF_4$: Yb^{3+}/Tm^{3+} nanoparticles under ambient conditions. A schematic illustration of the cation exchange involved in the preparation of $Yb^{3+}/Tm^{3+}/Tb^{3+}$ (Eu^{3+}) co-doped core-shell-like $NaGdF_4$ UCNPs is shown in Figure 3.9a. It also shows TEM images of typical core-shell-like $NaGdF_4$: Yb^{3+}/Tm^{3+} UCNPs before and after cation-exchange with Tb^{3+}ions. Under the premise of retaining surface ligands, the $NaGdF_4$: Yb^{3+}/Tm^{3+} UCNPs were dispersed very well in non-polar solvents. After the post-synthetic treatment by HCl and cation exchange in water, these particles showed no obvious change in particle size.

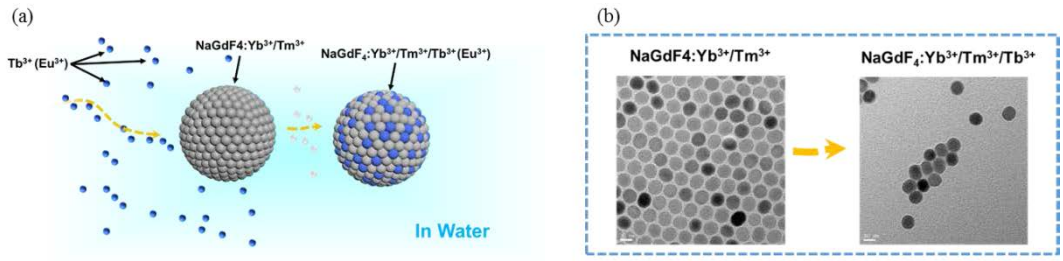

Figure 3.9 Schematic illustration of cation exchange in the preparation of $Yb^{3+}/Tm^{3+}/Tb^{3+}$ (Eu^{3+}) co-doped core-shell-like $NaGdF_4$ UCNPs (a); TEM images of typical $NaGdF_4$: Yb^{3+}/Tm^{3+} UCNPs before and after cation-exchange with Tb^{3+}ions in water (left), and formed $NaGdF_4$: $Yb^{3+}/Tm^{3+}/Tb^{3+}$ UCNPs (right) (b)

3.3.7 UC luminescence of Core-shell-like $NaGdF_4$: Yb^{3+}/Tm^{3+} UCNPs

Figure 3.10 depicts the UC luminescence spectra of Yb^{3+}/Tm^{3+}-doped core-shell-like $NaGdF_4$ UCNPs, as well as a digital photograph showing their light emission upon 980 nm near-infrared laser excitation. The amounts of RE^{3+} ions were determined to be 49%Yb^{3+}/1%Tm^{3+}. The colloidal solution containing UCNPs showed weak

luminescence because of the quenching effect of water. Blue emission bands at 448 nm and 476 nm, and a weak red emission at 644 nm were observed, which were associated with the characteristic ion level transitions $^1D_2 \rightarrow {}^3F_4$, $^1G_4 \rightarrow {}^3H_6$ and $^1D_2 \rightarrow {}^3H_4$ of Tm^{3+}, respectively. A TEM image of the Yb^{3+}/Tm^{3+} doped core-shell-like $NaGdF_4$ UCNPs is shown in the inset.

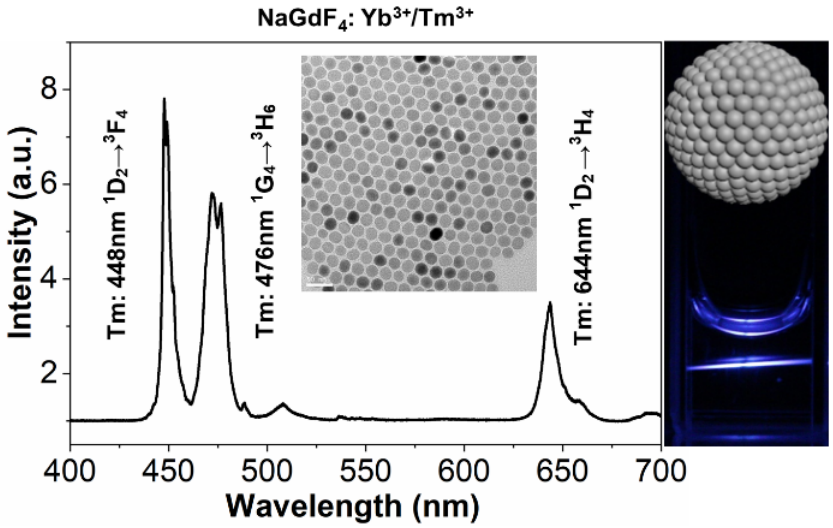

Figure 3.10 UC luminescence spectra of Yb^{3+}/Tm^{3+}-doped core-shell-like $NaGdF_4$ UCNPs (left), and a photograph of the light emission upon 980 nm near-infrared laser excitation (right)

3.3.8 UC luminescence of core-shell-like $NaGdF_4$: $Yb^{3+}/Tm^{3+}/Tb^{3+}$ UCNPs

Figure 3.11 depicts the UC luminescence spectra of $Yb^{3+}/Tm^{3+}/Tb^{3+}$-doped core-shell-like $NaGdF_4$ UCNPs and a photograph of their emitted light (from the sample with the strongest intensity) upon 980 nm near-infrared laser excitation. Five Tb^{3+} contents were adopted for tuning the UC luminescent intensities. From the figure, it is clear that the emissions at 448 nm, 476 nm, and 644 nm are characteristic emissions of Tm^{3+}. However, new emission peaks at 540 nm, 582 nm and 618 nm originated from the characteristic ion level transitions $^5D_4 \rightarrow {}^7F_5$, $^5D_4 \rightarrow {}^7F_5$ and $^5D_4 \rightarrow {}^7F_3$ of Tb^{3+}, respectively. Due to quenching effects, the luminescence spectra of the samples measured at room temperature showed a decrease in Tb^{3+} emission intensity with increasing concentrations of exchange ions. The optimal concentration of Tb^{3+} ions for obtaining the strongest Tb characteristic emissions in mixed solvents was found to be 0.05 μM.

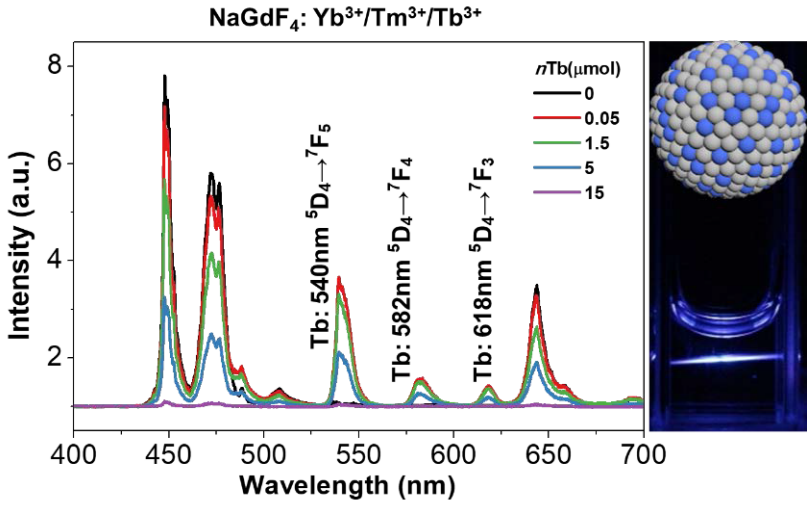

Figure 3.11 UC luminescence spectra of $Yb^{3+}/Tm^{3+}/Tb^{3+}$-doped core-shell-like $NaGdF_4$ UCNPs, and photograph showing their light emission (from the sample with strongest intensity) upon 980 nm near-infrared laser excitation

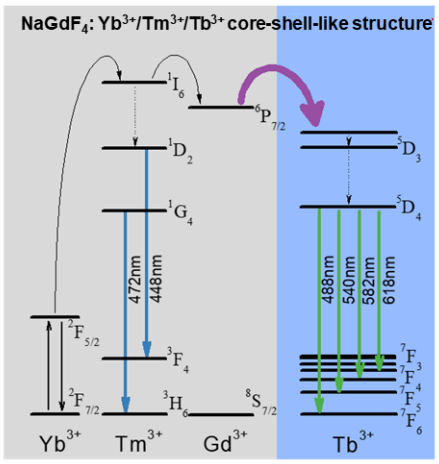

Figure 3.12 Level diagram and proposed mediated energy migration from Tm^{3+}/Yb^{3+} to Tb^{3+} layer through a Gd^{3+}-rich shell

The emission of Tb^{3+} ions indicates a successful mediated energy migration in $NaGdF_4$: Yb^{3+}/Tm^{3+} UCNPs. This is consistent with our hypothesis for core-shell-like $NaGdF_4$: Yb^{3+}/Tm^{3+} UCNPs: that Gd^{3+} ions are concentrated at the nanoparticle surface and form a natural Gd^{3+}-rich shell. This means that without the real core-shell structure of $NaGdF_4$: Yb^{3+}/Tm^{3+}@$NaGdF_4$, the naturally-formed Gd^{3+}-rich shell also can effectively bridge the energy transfer gap from sensitizers to activators through long-range energy migration in the sub-lattice. Therefore, the multicolour luminescent properties of the core-shell-like $NaGdF_4$: Yb^{3+}/Tm^{3+} nanoparticles can be directly tuned by adding new activator ions such as Tb^{3+}. In the tridoped system, Tb^{3+} upconverted emissions are produced by capturing the energy populated at the excited states of Tm^{3+} (1I6) through Yb^{3+}

sensitization and Gd^{3+} bridge-like energy migration upon 980 nm laser excitation (Figure 3.12)[41-42]. The natural Gd^{3+}-rich shell in the core-shell-like structure of $NaGdF_4$: Yb^{3+}/Tm^{3+} provides a new way to obtain coloured emissions with $NaGdF_4$: Yb^{3+}/Tm^{3+} UCNPs without real core-shell structures.

3.3.9 UC luminescence of core-shell-like $NaGdF_4$: $Yb^{3+}/Tm^{3+}/Eu^{3+}$ UCNPs

Figure 3.13 depicts the UC luminescence spectra of $Yb^{3+}/Tm^{3+}/Eu^{3+}$-doped core-shell-like $NaGdF_4$ UCNPs, and a photograph of their emitted light (from the sample with strongest intensity) upon 980 nm near-infrared laser excitation. Similarly, five different Eu^{3+} contents were adopted for tuning the UC luminescent intensities. The emissions at 448 nm, 476 nm, and 644 nm in the figure belong to the characteristic emissions of Tm^{3+}. New emission peaks at 592 nm and 613 nm correspond to the characteristic ion level transitions $^5D_0 \rightarrow {}^7F_1$ and $^5D_0 \rightarrow {}^7F_2$ of Eu^{3+}, respectively. The quenching effect is also evident with increasing concentrations of exchange ions. The optimal concentration of Eu^{3+} ions for obtaining the strongest Eu characteristic emissions in mixed solvents was determined as 0.05 μM. The emissions of Eu^{3+} ions demonstrate the successful mediated energy migration in the natural core-shell-like $NaGdF_4$ UCNPs[43]. The naturally-formed Gd^{3+}-rich shell can also effectively bridge the energy transfer gap from sensitizers to activators through long-range energy migration in the sub-lattice. Therefore, the multicolour luminescence properties of the core-shell-like $NaGdF_4$:Yb^{3+}/Tm^{3+} nanoparticles can be directly tuned by adding new activator ions such as Eu^{3+}.

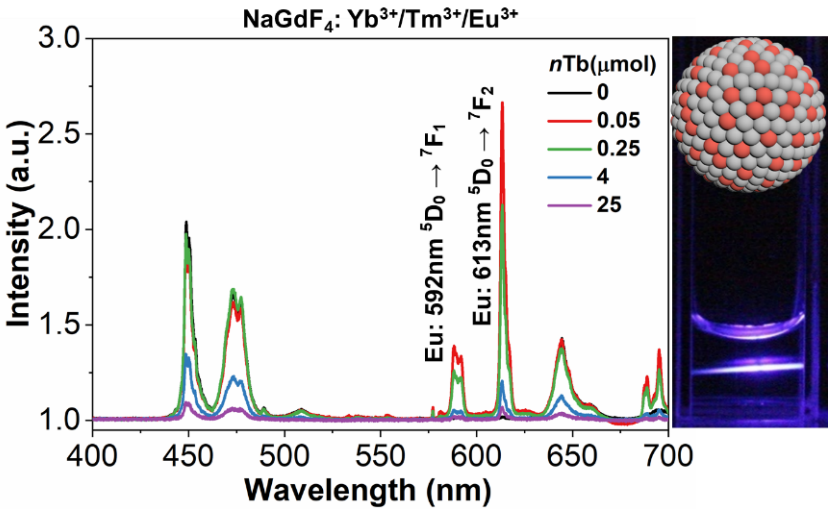

Figure 3.13 UC luminescence spectra of $Yb^{3+}/Tm^{3+}/Eu^{3+}$-doped core-shell-like $NaGdF_4$ UCNPs, and photograph showing their light emission (from the sample with strongest intensity) upon 980 nm near-infrared laser excitation

3.3.9 Multicolour and CIE chromaticity

CIE chromaticity coordinates (*x,y*) of typical samples were calculated through their UC luminescent spectra, which are shown in Figure 3.14. Yb^{3+}/Tm^{3+}-doped core-shell-like $NaGdF_4$ UCNPs only showed the characteristic emissions of Tm^{3+} ions, which are close to the blue light region (0.27, 0.24). $Yb^{3+}/Tm^{3+}/Tb^{3+}$-doped core-shell-like $NaGdF_4$ UCNPs presented Tm^{3+} and Tb^{3+} emissions, with colours located in the region of white light (0.29, 0.28). In $Yb^{3+}/Tm^{3+}/Eu^{3+}$-doped core-shell-like $NaGdF_4$ UCNPs, the emissions combining Tm^{3+} and Eu^{3+} were near the red light region (0.33, 0.31). Thus, multicolour luminescence was obtained by cation exchange based on the natural core-shell-like structure of $NaGdF_4$: Yb^{3+}/Tm^{3+} nanoparticles.

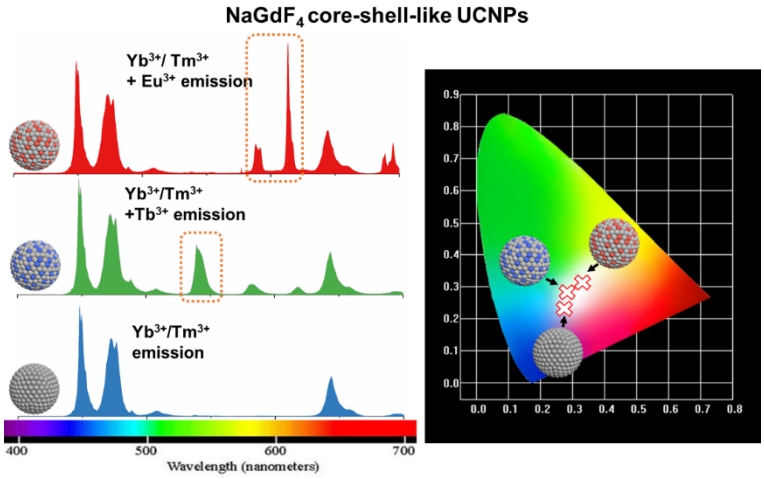

Figure 3.14 CIE chromaticity coordinates (x,y) of Yb^{3+}/Er^{3+}, Yb^{3+}/Ho^{3+} and Yb^{3+}/Tm^{3+}-doped $SrIn_2O_4$ UC phosphors upon 980 nm excitation

3.4 Conclusions

In this chapter, Yb^{3+}/Tm^{3+}- and Gd^{3+}/Tm^{3+}-doped $NaYF_4$ fluoride UC nanoparticles (UCNPs) were prepared, and the distribution of RE^{3+} ions within a single particle was characterized by depth-resolved XPS. The results show that Gd ions with large radii tend to occupy the surfaces of $NaYF_4$: Gd^{3+} UCNPs, while small-radius ions of Yb tend to be concentrated at the cores of $NaYF_4$: Yb^{3+} UCNPs. According to these results, the presence of a Gd^{3+}-rich shells on the surfaces of Yb^{3+}/Tm^{3+}-doped $NaGdF_4$ nanoparticles is proposed. Multicolour UC luminescence was observed by adding various new activators, such as Tb^{3+} and Eu^{3+}, via a cation exchange method. The natural Gd^{3+}-rich shells in the

core-shell-like $NaGdF_4$: Yb^{3+}/Tm^{3+} nanoparticles minimize the surface quenching effect and, more importantly, effectively bridge the energy transfer gap between sensitizers and activators through long-range energy migration in the sub-lattice. The core-shell-like distribution feature of UCNPs opens a new energy pathway that can be exploited to tune and improve the multicolour luminescent properties of UCNPs.

3.5 References

1. Wang, F.; Liu, X., Recent advances in the chemistry of lanthanide-doped upconversion nanocrystals. *Chem Soc Rev* **2009,** *38* (4), 976-89.

2. Makarov, N. S.; Guo, S.; Isaienko, O.; Liu, W.; Robel, I.; Klimov, V. I., Spectral and Dynamical Properties of Single Excitons, Biexcitons, and Trions in Cesium-Lead-Halide Perovskite Quantum Dots. *Nano Lett* **2016,** *16* (4), 2349-62.

3. Wang, F.; Han, Y.; Lim, C. S.; Lu, Y.; Wang, J.; Xu, J.; Chen, H.; Zhang, C.; Hong, M.; Liu, X., Simultaneous phase and size control of upconversion nanocrystals through lanthanide doping. *Nature* **2010,** *463* (7284), 1061-5.

4. Gai, S.; Li, C.; Yang, P.; Lin, J., Recent progress in rare earth micro/nanocrystals: soft chemical synthesis, luminescent properties, and biomedical applications. *Chem Rev* **2014,** *114* (4), 2343-89.

5. Cozzoli, P. D.; Pellegrino, T.; Manna, L., Synthesis, properties and perspectives of hybrid nanocrystal structures. *Chem Soc Rev* **2006,** *35* (11), 1195-208.

6. Wang, F.; Wang, J.; Liu, X., Direct evidence of a surface quenching effect on size-dependent luminescence of upconversion nanoparticles. *Angew Chem Int Ed* **2010,** *49* (41), 7456-60.

7. Deng, R.; Qin, F.; Chen, R.; Huang, W.; Hong, M.; Liu, X., Temporal full-colour tuning through non-steady-state upconversion. *Nat Nano* **2015,** *10* (3), 237-242.

8. Wang, L.; Yan, R.; Huo, Z.; Wang, L.; Zeng, J.; Bao, J.; Wang, X.; Peng, Q.; Li, Y., Fluorescence Resonant Energy Transfer Biosensor Based on Upconversion-Luminescent Nanoparticles. *Angewandte Chemie International Edition* **2005,** *44* (37), 6054-6057.

9. Park, Y. I.; Kim, J. H.; Lee, K. T.; Jeon, K.-S.; Na, H. B.; Yu, J. H.; Kim, H. M.; Lee, N.; Choi, S. H.; Baik, S.-I.; Kim, H.; Park, S. P.; Park, B.-J.; Kim, Y. W.; Lee, S. H.; Yoon, S.-Y.; Song, I. C.; Moon, W. K.; Suh, Y. D.; Hyeon, T., Nonblinking and Nonbleaching Upconverting Nanoparticles as an Optical Imaging Nanoprobe and T1 Magnetic Resonance Imaging Contrast Agent. *Advanced Materials* **2009,** *21* (44), 4467-4471.

10. Wu, S.; Han, G.; Milliron, D. J.; Aloni, S.; Altoe, V.; Talapin, D. V.; Cohen, B. E.; Schuck, P. J., Non-blinking and photostable upconverted luminescence from single lanthanide-doped nanocrystals. *Proceedings of the National Academy of Sciences* **2009,** *106* (27), 10917-10921.

11. Nyk, M.; Kumar, R.; Ohulchanskyy, T. Y.; Bergey, E. J.; Prasad, P. N., High Contrast in Vitro and in Vivo Photoluminescence Bioimaging Using Near Infrared to Near Infrared Up-Conversion in Tm^{3+} and Yb^{3+} Doped Fluoride Nanophosphors. *Nano Letters* **2008,** *8* (11), 3834-3838.

12. Cheng, L.; Yang, K.; Li, Y.; Zeng, X.; Shao, M.; Lee, S.-T.; Liu, Z., Multifunctional nanoparticles for upconversion luminescence/MR multimodal imaging and magnetically targeted photothermal therapy. *Biomaterials* **2012,** *33* (7), 2215-2222.

13. Liu, Q.; Feng, W.; Li, F., Water-soluble lanthanide upconversion nanophosphors: Synthesis and bioimaging applications in vivo. *Coordination Chemistry Reviews* **2014,** *273-274*, 100-110.

14. Wang, C.; Cheng, L.; Liu, Z., Drug delivery with upconversion nanoparticles for multi-functional targeted cancer cell imaging and therapy. *Biomaterials* **2011,** *32* (4), 1110-1120.

15. Tian, G.; Gu, Z.; Zhou, L.; Yin, W.; Liu, X.; Yan, L.; Jin, S.; Ren, W.; Xing, G.; Li, S.; Zhao, Y., Mn^{2+} Dopant-Controlled Synthesis of $NaYF_4$:Yb/Er Upconversion Nanoparticles for in vivo Imaging and Drug Delivery. *Advanced Materials* **2012,** *24* (9), 1226-1231.

16. Liu, X.; Yan, C.-H.; Capobianco, J. A., Photon upconversion nanomaterials. *Chemical Society Reviews* **2015,** *44* (6), 1299-1301.

17. Lu, Y.; Zhao, J.; Zhang, R.; Liu, Y.; Liu, D.; Goldys, E. M.; Yang, X.; Xi, P.; Sunna, A.; Lu, J.; Shi, Y.; Leif, R. C.; Huo, Y.; Shen, J.; Piper, J. A.; Robinson, J. P.; Jin, D., Tunable lifetime multiplexing using luminescent nanocrystals. *Nat Photon* **2014,** *8* (1), 32-36.

18. Zhao, J.; Jin, D.; Schartner, E. P.; Lu, Y.; Liu, Y.; Zvyagin, A. V.; Zhang, L.; Dawes, J. M.; Xi, P.; Piper, J. A.; Goldys, E. M.; Monro, T. M., Single-nanocrystal sensitivity achieved by enhanced upconversion luminescence. *Nat Nano* **2013,** *8* (10), 729-734.

19. Zhao, J.; Jin, D.; Schartner, E. P.; Lu, Y.; Liu, Y.; Zvyagin, A. V.; Zhang, L.; Dawes, J. M.; Xi, P.; Piper, J. A.; Goldys, E. M.; Monro, T. M., Single-nanocrystal sensitivity achieved by enhanced upconversion luminescence. *Nat Nanotechnol* **2013,** *8* (10), 729-34.

20. Chen, G.; Qiu, H.; Prasad, P. N.; Chen, X., Upconversion Nanoparticles: Design, Nanochemistry, and Applications in Theranostics. *Chemical Reviews* **2014,** *114* (10), 5161-5214.

21. Zhou, B.; Shi, B.; Jin, D.; Liu, X., Controlling upconversion nanocrystals for emerging applications. *Nat Nano* **2015,** *10* (11), 924-936.

22. Gai, S.; Li, C.; Yang, P.; Lin, J., Recent Progress in Rare Earth Micro/Nanocrystals: Soft Chemical Synthesis, Luminescent Properties, and Biomedical Applications. *Chemical Reviews* **2014,** *114* (4), 2343-2389.

23. Dong, C.; Pichaandi, J.; Regier, T.; van Veggel, F. C. J. M., Nonstatistical Dopant Distribution of Ln^{3+}-Doped $NaGdF_4$ Nanoparticles. *The Journal of Physical Chemistry C* **2011,** *115* (32), 15950-15958.

24. Pichaandi, J.; Das, G. K.; Johnson, N. J. J.; Regier, T.; van Veggel, F. C. J. M., Probing the Structure of $NaYF_4$ Nanocrystals using Synchrotron-Based Energy-Dependent X-ray Photoelectron Spectroscopy. *The Journal of Physical Chemistry C* **2014,** *118* (37), 21639-21646.

25. Abel, K. A.; Boyer, J.-C.; Veggel, F. C. J. M. v., Hard Proof of the $NaYF_4$/$NaGdF_4$ Nanocrystal Core/Shell Structure. *Journal of the American Chemical Society* **2009,** *131* (41), 14644-14645.

26. Dong, C.; Pichaandi, J.; Regier, T.; van Veggel, F. C. J. M., The unexpected structures of "core-shell" and "alloy" LnF_3 nanoparticles as examined by variable energy X-ray photo-electron spectroscopy. *Nanoscale* **2011,** *3* (8), 3376-3384.

27. Li, X.; Wang, R.; Zhang, F.; Zhao, D., Engineering homogeneous doping in single nanoparticle to enhance upconversion efficiency. *Nano Lett* **2014,** *14* (6), 3634-9.

28. Dong, H.; Sun, L.-D.; Wang, Y.-F.; Ke, J.; Si, R.; Xiao, J.-W.; Lyu, G.-M.; Shi, S.; Yan, C.-H., Efficient Tailoring of Upconversion Selectivity by Engineering Local Structure of Lanthanides in Na_xREF_{3+x} Nanocrystals. *Journal of the American Chemical Society* **2015,** *137* (20), 6569-6576.

29. Wang, F.; Deng, R.; Liu, X., Preparation of core-shell $NaGdF_4$ nanoparticles doped with luminescent lanthanide ions to be used as upconversion-based probes. *Nature Protocols* **2014,** *9*, 1634.

30. Wang, F.; Deng, R.; Liu, X., Preparation of core-shell $NaGdF_4$ nanoparticles doped with luminescent lanthanide ions to be used as upconversion-based probes. *Nat Protoc* **2014,** *9* (7), 1634-44.

31. Liu, D.; Xu, X.; Du, Y.; Qin, X.; Zhang, Y.; Ma, C.; Wen, S.; Ren, W.; Goldys, E. M.; Piper, J. A.; Dou, S.; Liu, X.; Jin, D., Three-dimensional controlled growth of monodisperse sub-50 nm heterogeneous nanocrystals. *Nat Commun* **2016,** *7*, 10254.

32. Han, S.; Qin, X.; An, Z.; Zhu, Y.; Liang, L.; Han, Y.; Huang, W.; Liu, X., Multicolour synthesis in lanthanide-doped nanocrystals through cation exchange in water. *Nat Commun* **2016,** *7*, 13059.

33. V4, B. A. T., General Profile and Structure Analysis Software for Powder Diffraction Data. *User's Manual. Bruker AXS, Karlsruhe, Germany* **2008**.

34. Ma, C.; Xu, X.; Wang, F.; Zhou, Z.; Wen, S.; Liu, D.; Fang, J.; Lang, C. I.; Jin, D., Probing the Interior Crystal Quality in the Development of More Efficient and Smaller Upconversion Nanoparticles. *The Journal of Physical Chemistry Letters* **2016,** *7* (16), 3252-3258.

35. Chenshuo Ma, X. X., Fan Wang, £, Zhiguang Zhou, Deming Liu, Jiangbo Zhao, Candace I Lang, and Dayong Jin, Optimal Sensitizer Concentration in Single Upconversion Nanocrystals. *Nano Letters* **2016,** *Submitted*.

36. Grzechnik, A.; Bouvier, P.; Mezouar, M.; Mathews, M. D.; Tyagi, A. K.; Köhler, J., Hexagonal $Na_{1.5}Y_{1.5}F_6$ at High Pressures. *Journal of Solid State Chemistry* **2002,** *165* (1), 159-164.

37. Lang, W. C.; Padalia, B. D.; Watson, L. M.; Fabian, D. J.; Norris, P. R., Multiplet structure in X-ray photoelectron spectra of rare earth elements and their surface oxides. *Faraday Discussions of the Chemical Society* **1975,** *60* (0), 37-43.

38. Yeh, J. J.; Lindau, I., Atomic subshell photoionization cross sections and asymmetry parameters: $1 \leqslant Z \leqslant 103$. *Atomic Data and Nuclear Data Tables* **1985,** *32* (1), 1-155.

39. Shannon, R. D., Revised effective ionic radii and systematic studies of interatomic distances in halides and chalcogenides. *Acta Crystallographica Section A* **1976,** *32* (5), 751-767.

40. Li, X.; Wang, R.; Zhang, F.; Zhao, D., Engineering Homogeneous Doping in Single Nanoparticle To Enhance Upconversion Efficiency. *Nano Letters* **2014,** *14* (6), 3634-3639.

41. Li, X.; Liu, X.; Chevrier, D. M.; Qin, X.; Xie, X.; Song, S.; Zhang, H.; Zhang, P.; Liu, X., Energy Migration Upconversion in Manganese(II)-Doped Nanoparticles. *Angew Chem Int Ed* **2015,** *54* (45), 13510-13515.

42. Wang, F.; Deng, R.; Wang, J.; Wang, Q.; Han, Y.; Zhu, H.; Chen, X.; Liu, X., Tuning upconversion through energy migration in core-shell nanoparticles. *Nat Mater* **2011,** *10* (12), 968-73.

43. Zhang, C.; Yang, L.; Zhao, J.; Liu, B.; Han, M. Y.; Zhang, Z., White-Light Emission from an Integrated Upconversion Nanostructure: Toward Multicolor Displays Modulated by Laser Power. *Angew Chem Int Ed* **2015,** *54* (39), 11531-5

CHAPTER 4

Direct Cation Exchange of Surface Ligand Capped Up-conversion Nanoparticles to Produce Strong Multicolor Luminescence

4.1 Introduction

Controlled synthesis plays a fundamental role in the production of multicolour luminescence in lanthanide-doped upconversion nanoparticles (UCNPs, or UCNCs). Since the nanotechnology era began in 1960 [1], controlled synthesis has created diverse artificial nanomaterials, including quantum dots[2-5], metal nanoparticles[6-7], defects/elements-doped nanoparticles[8-9], and 2D nanomaterials[10-11]. Most of them show colourful fluorescence and have light-based functionality beyond the size/morphology advantages, giving them enormous application potential in the fields of life sciences, electronic displays, energy harvesting and quantum engineering[12-19]. To enrich the fluorescence colour, nano semiconductors rely on the tuning of bandgaps[20], while doped nano-insulators require elaborate control of the dopants[21-24]. Repeated synthesis is able to regulate these compositional arrangements but is resource- and time-consuming.

Cation exchange strategies make it possible to tune multicolour luminescence properties of large classes of UCNPs expeditiously[25]. Currently, the main approaches for preparing UCNPs are co-precipitation, thermal decomposition and hydrothermal reaction. To obtain excellent UC luminescent properties such as multicolour emissions and strong intensities, one has to perform a new set of reactions and have stringent control over a variety of experimental conditions, including the amount and concentration of dopant ions, the kinds of surfactants and solvents used, and the reaction time and temperature[26-27]. All of these drawbacks may raise some safety and environmental concerns. Alternatively, cation exchange allows high-throughput production of multicolour-emitting nanoparticles while

preserving the original size, morphology and crystal phase of the nanoparticles[28-29]. As a facile method, a simplified procedure suitable for the as-synthesized UCNPs is the key attractiveness to make the cation exchange be extensively adopted. A recent strategy of cation exchange in water has enabled researchers to precisely tailor luminescence to colours of interest[8, 25]. With $NaGdF_4:Yb^{3+}/Tm^{3+}$@ $NaGdF_4$ core-shell structures, the $NaGdF_4$ long-range energy migration layer bridges the energy transfer gap between sensitizers and activators in the sub-lattice. The luminescent properties of the nanoparticles can be easily tuned by adding different kinds of new activator ions, making it possible to achieve UC luminescence with new colour regimes (Figure 4.1).

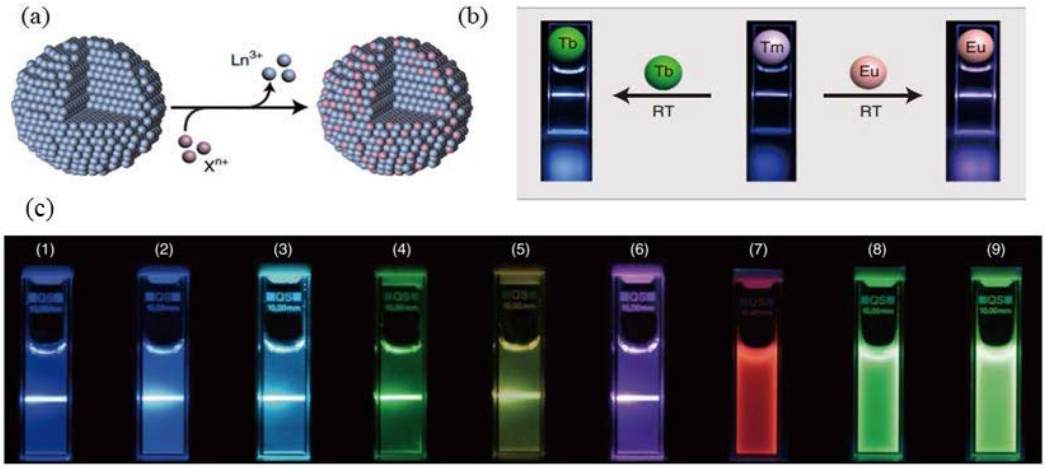

Figure 4.1 Cation exchange in water strategy for UCNPs: Schematic representation of the cation exchange process in water (a); Photoluminescence images showing the change in the emitted colours of $NaGdF_4$: Yb^{3+}/Tm^{3+}@$NaGdF_4$ colloidal solutions upon addition of Tb^{3+} or Eu^{3+} ions (b); Multicolour luminescence in lanthanide-doped nanocrystals through cation exchange in water (c)[8]

As is well known that the wet-chemical route to UCNP growth produces hydrophobic nanoparticles with monodispersity and stable fluorescence in non-polar solvents because of the surface ligands, e.g., oleic acid (OA). This cation exchange in water strategy has some drawbacks. First of all, it is still time- and labour-consuming to use hydrochloric acid (HCl) to remove the OA ligand layer coated on the surface of UCNPs, which is done so that particles can be dispersed into water to complete cation exchange synthesis. The tedious pre-treatment of as-synthesized UCNPs may damage the peripheral lattices[23, 30-31]. Furthermore, this practice wastes particles in the processes of washing and centrifuging. Particle aggregation and degradation inevitably occur in such water circumstances, as has recently been observed[31-35]. Most importantly, cation exchange in water has the inherent

disadvantages of low UC intensity due to the quenching effect of naked particles without protecting ligand layers and the absorption of excitation laser energy by the water[36-37]. These drawbacks limit their development and application; thus, it is fundamentally necessary and important to explore new cation exchange methods for UCNPs.

Here, we report a novel cation exchange method for as-synthesized RE^{3+}-doped UCNPs, which are emerging as promising light carriers in different fields[23, 38-43]. Our method can directly exchange cations when the surfaces of the as-synthesized nanocrystals are capped with ligands. Under the premise of retaining surface ligands, we are able to complete cation exchange within seconds by simply dripping the cation-containing solution into the nanocrystal colloid. This novel cation exchange method allows the high-throughput production of RE^{3+}-doped UCNPs with a myriad of different colour spaces.

4.2 Experimental section

4.2.1 Reagents and equipment

Most chemicals and reagents used in this chapter have already been described in Chapter 3. Additional chemicals are listed in Table 4.1. All chemicals were used as received without further purification or modification unless otherwise described.

Table 4.1 Main experimental reagents, specifications and manufacturer

Chemical	Specification	Manufacturer
Toluene	≥99.9%	Chem-Supply (Australia)
Hexane	≥99.9%	
Acetone	≥99.9%	
Acetonitrile	≥99.9%	
Tetrahydrofuran (THF)	≥99.9%	
N,N-dimethylformamide (DMF)	99.5%	
Dimethylsulfoxide (DMSO)	99.5%	

Most instruments and equipment used in this chapter were also described in Chapter 3, and additional instruments used for specimen synthesis in this chapter are listed in Table 4.2.

Table 4.2 Main experimental equipment, specifications and manufacturer

Equipment	Specification	Manufacturer
Glass slide	25 × 57 mm	Hurst Scientific Pty. Ltd.
Coverslip	22 × 22 mm	Muraban Laboratories

4.2.2 Synthesis of materials

Synthesis of $NaGdF_4$: Yb^{3+}/Tm^{3+} (49%/1%) UCNPs: Core-only $NaGdF_4$: Yb^{3+}/Tm^{3+} (49%/1%) nanoparticles were prepared according to the method described in Chapter 3. Typically, a methanol solution of 0.5 mmol $GdCl_3$, 0.49 mmol $YbCl_3$, and 0.01 mmol $TmCl_3$ was mixed with 10 ml OA and 15 ml ODE in a 50 mL flask. The mixture was heated at 150 °C under stirring for 30 min until the solution became clear. After cooling to 50 °C, a methanol solution containing NH_4F (3.3 mmol) and NaOH (2.5 mmol) was added with vigorous stirring for more than 1 h. Then, the mixed solution was heated to 90 °C to evaporate the methanol and then to 150 °C to evaporate all the residual water. Finally, the solution was heated to 290 °C and kept there for 1.5 h under a flow of argon. After reaction and cooling to room temperature, the synthesized nanoparticles were washed with cyclohexane/ethanol several times and dispersed in toluene for use. By adjusting the mole ratio of NH_4F and NaOH, different sizes of UCNPs could be synthesized.

***Synthesis of $NaGdF_4$: Yb^{3+}/Tm^{3+}@$NaGdF_4$ core-shell UCNPs*:** A modified hot-injection method was used for growing core-shell-structured UCNPs. Some 0.2 mmol of $NaGdF_4$: Yb^{3+}/Tm^{3+} nanoparticles were dispersed in cyclohexane and mixed with OA (8 mL) and ODE (12 mL) in a 50 mL three-neck flask. The mixture was degassed under an Ar flow and kept at 100 °C for 30 min to completely remove the cyclohexane. Then, it was heated to 150 °C and kept at this temperature for 30 min to remove any remaining water. The mixture was then quickly heated to 290 °C and a certain amount of pure $NaGdF_4$ source solution was injected into the core nanoparticle mixture solution using a syringe at a rate of 0.05 ml/2 min. After the reaction, the precipitate was washed with cyclohexane/ethanol several times and dispersed in toluene for use. To synthesize pure $NaGdF_4$ shell precursors, typically, a methanol solution of 1 mmol $GdCl_3$ was mixed with 10 ml OA and 15 ml ODE in a 50 mL flask. The mixture was heated at 150 °C under stirring for 30 min until the solution became clear. After cooling to 50 °C, a methanol solution containing NH_4F (3.3 mmol) and NaOH (2.5 mmol) was added with vigorous stirring for

at least 1 h. Then, the mixed solution was heated to 90 °C to evaporate the methanol and to 150 °C to evaporate any residual water. After reaction and cooling to room temperature, pure $NaGdF_4$ precursor was obtained.

Cation exchange in organic solvent: To obtain the optimal emission intensity, we prepared a series of UCNPs by cation exchange in organic solvent (OSCE) with different amounts of activators (Tb^{3+} and Eu^{3+}). In a typical experiment, a stock toluene solution (666 μL) of the 0.05 mmol as-prepared UCNPs ($NaGdF_4$: Yb^{3+}/Tm^{3+} or $NaGdF_4$: Yb^{3+}/Tm^{3+}@$NaGdF_4$) was mixed with an ethanol solution (333 μl) of $RECl_3$ (RE = Tb^{3+}, Eu^{3+}). The resulting mixture was shaken thoroughly at room temperature for 10 min. Subsequently, the products were collected by centrifugation, washed with toluene/ethanol (2:1) several times, and re-dispersed in toluene. When using methanol, DMF or DMSO for dissolving $RECl_3$, the corresponding molar ratio of toluene and organic solution should be optimised. Corresponding samples by WACE were prepared according to previous reports[8].

4.2.3 Characterization

TEM and XRD Characterization: TEM and XRD characterization were described in Chapter 3.

High-resolution transmission electron microscopy (HRTEM) and energy-dispersive X-ray spectroscopy (EDS): Element mapping images were collected by aberration-corrected analytical transmission electron microscopy (TEM, JEOL ARM-200F) equipped with a Centurio SSD energy-dispersive X-ray spectroscopy (EDS) detector set at 77 K. The TEM was operated at 80 kV. The line profiles were processed with the LOWESS smoothing algorithm as implemented in OriginPro software.

Photoluminescence spectra by spectrofluorometer: The UC luminescence spectra were obtained using a Fluorolog-Tau3 spectrofluorometer (Jobin Yvon-Horiba) equipped with an external 980 nm CW diode laser with a pump power density of 500 W/cm^2. The upconversion nanoparticles were dispersed in toluene and prepared to a concentration of 1 mg/ml by the subtractive weighting method for the entire specimen. Corresponding samples by WACE were also prepared to a concentration of 1 mg/ml. The dispersion was transferred to quartz cuvettes with 10 mm path lengths, and three measurements were conducted for each sample.

Photoluminescence characterization for single UCNPs: We used a modified laser scanning confocal microscope for the intensity measurement of single UCNPs. The excitation source was a 976 nm single mode polarized laser (power density of 30 MW cm^{-2}), which was focused onto the sample through a 100× objective lens (NA 1.4). A single photon counting avalanche diode (SPAD) detector was connected to the collecting optical fibre to detect the emission intensity. Scanning was achieved by moving the 3D piezo stage. The layout of the laser scanning confocal microscope built by our research group is illustrated in Figure 4.2.

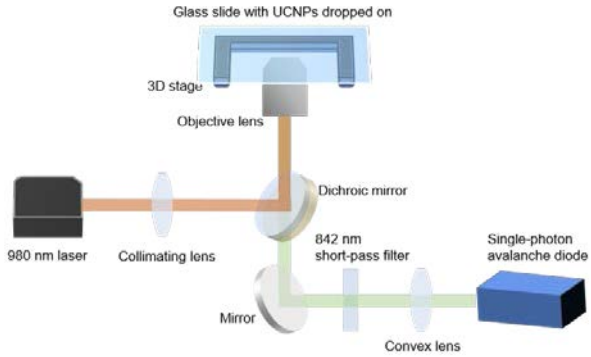

Figure 4.2 Laser scanning confocal microscope for the intensity measurement of single UCNPs[44-45]

Monodispersed single UCNP samples were prepared first. The slide samples were prepared as follows [46]: (1) The coverslip was cleaned by sonication in pure ethanol and left to dry at room temperature. (2) A 50 µL drop of poly-L-lysine solution (at 0.1% w/v concentration in water) was added to the coverslip and left to stand for 30 min; afterwards, the poly-L-lysine was washed off by distilled water and left to dry at room temperature. (3) UCNPs were diluted with cyclohexane or with water at 0.1 $mg \cdot mL^{-1}$, then 20 µL was dropped onto the treated surface of the glass slide and the coverslip was flushed carefully with cyclohexane or water and left to dry. (4) The coverslip and glass slide were sealed using an embedding medium and air bubbles were removed by squeezing. Before measurement, the slide-mounted samples were incubated at room temperature for 24 h to ensure complete dryness. (5) Embedding medium was used as it provided a refraction index larger than air. A protocol for its use is as follows. Briefly, 2.4 g of Mowiol 4-88 was mixed with 6 g of glycerol in a 50 ml centrifuge tube. After stirring on a magnetic stirrer for 1 h, 6 ml of distilled water was added, followed by 2 h of stirring. Then, 12 ml of Tris-HCl buffer (set at 0.2 M and pH 8.5) was added. The solution was then placed in

a water bath at 50 °C and agitated until the Mowiol dissolved. Any remaining precipitate was removed by centrifuging.

4.3 Results and discussion

4.3.1 Cation exchange in organic solvent

As illustrated in Figure 4.3, we used solvent X to dissolve rare-earth salts and form rare-earth cations in solution, while we used toluene to disperse oleic acid-capped $NaGdF_4$ UCNPs. Typically, solvent X dissolves $TbCl_3$, and toluene disperses the as-synthesized UCNPs, followed by a cation exchange reaction caused by mixing these two kinds of solutions at appropriate volume ratios at room temperature. Tb^{3+} ions partially replace the rare-earth sites in the crystal structure of $NaGdF_4$: Tm^{3+},Yb^{3+}, forming new $NaGdF_4$: Tm^{3+},Yb^{3+},Tb^{3+} compositions on the surfaces of the UCNPs. Our method directly exchanges the cations when the surfaces of the as-synthesized nanocrystals are capped with ligands. Under the premise of retaining surface ligands, we can complete cation exchange within seconds by simply dripping the cation-containing solution into the nanocrystal colloid.

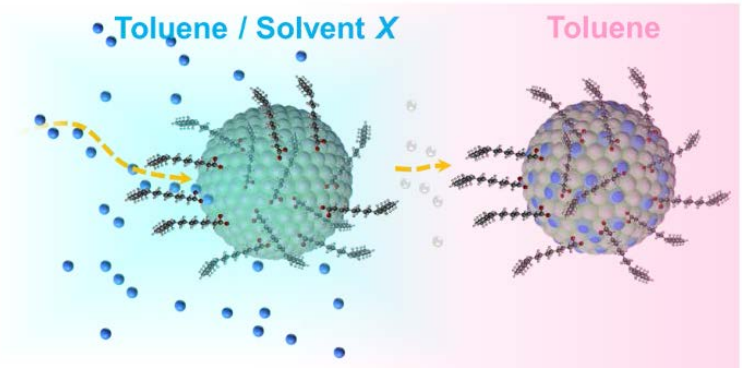

Figure 4.3 Schematic illustration of the cation exchange in organic solvent (OSCE) procedure

In a typical cation exchange in organic solvent (OSCE) process with $TbCl_3$ and UCNPs, a new tridoped system formed by cation exchange produces Tb^{3+} upconverted emissions by capturing the energy populated at the excited states of Tm^{3+} ($^1I_6$) through Yb^{3+} sensitization and Gd^{3+} bridge-like energy migration upon 980 nm laser excitation. The characteristic emission peaks of Tb^{3+} at 540 nm, 582 nm and 618 nm (green segments highlighted in Figure 4.4) originated from the characteristic ion level transitions $^5D_4 \rightarrow {}^7F_5$, $^5D_4 \rightarrow {}^7F_5$ and $^5D_4 \rightarrow {}^7F_3$ of Tb^{3+} ions, respectively. This result indicates that Tb^{3+}

successfully entered the $NaGdF_4$ crystal sites. We first proved that the OSCE method is applicable to different solvents, for example, methanol, ethanol, dimethylformamide (DMF), and dimethylsulfoxide (DMSO; listed in increasing order of their polarity indexes, 5.1, 5.2, 6.4, and 7.2, respectively). Tb^{3+} emissions appeared in all mixed solutions of toluene/ethanol, toluene/methanol, toluene/DMF, and toluene/DMSO, indicating that once UCNPs and free ions meet in an organic solvent, cation exchange takes place (Figure 4.4). However, the increased polarity of solvent *X* leads to decreased UC emission intensities due to weaker intersolubility with non-polar toluene.

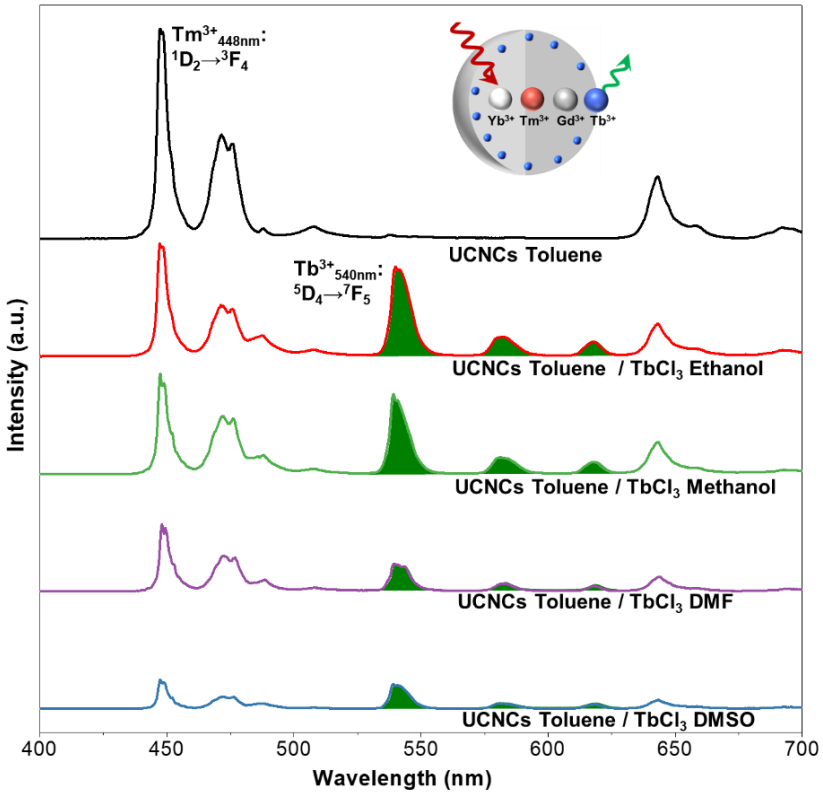

Figure 4.4 Nanostructure of core-only $NaGdF_4$: Yb^{3+}/Tm^{3+} UCNPs for OSCE, and UC emission spectra of the UCNPs before and after exchange in toluene/ethanol, toluene/methanol, toluene/DMF, toluene/DMSO, respectively

Taking toluene/ethanol-supported OSCE as an example for systematic study, the best volume ratio of toluene and ethanol was 2:1 (see Figure 4.5 a), and the exchange occurred within 5 s, while the balance time for exchanging 0.5 μM Tb^{3+} was 4 mins (Figure 4.5 b). The emission intensity of Tb^{3+} (monitored at 540 nm) was enhanced by slightly increasing the concentration of the exchange ions, and the optimal concentration of Tb^{3+} in mixed solvents was 0.5 μM (Figure 4.5 c). At the same time, the UC intensity of Tm^{3+} (monitored at 448 nm) deceased monotonically due to the population redistribution

among excited states when extra Tb^{3+} ions appeared in the nanocrystal, opening a new energy pathway from Tm^{3+}: $^1I_6$ to Tb^{3+}: $^5D_4$ through the Gd^{3+}: $^6P_{7/2}$ state.

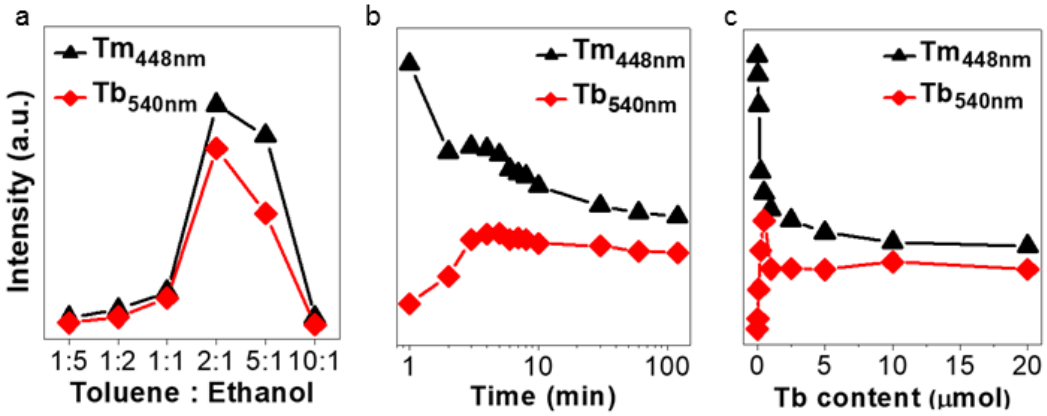

Figure 4.5 Emission intensity as a function of toluene/ethanol ratio (a), exchange time (b), and Tb^{3+} concentration (c). All emission spectra were recorded under irradiation by a 980 nm laser at a power density of 500 mW cm^{-2}

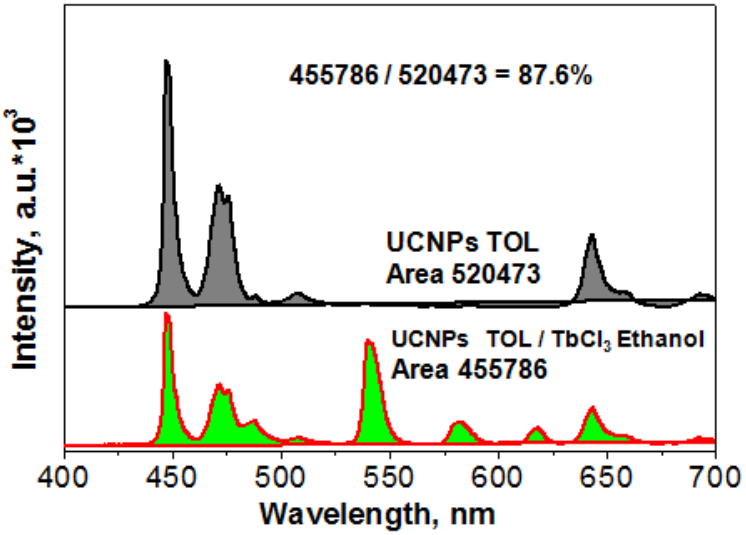

Figure 4.6 Upconversion emission intensity areas of initial UCNP template and UCNPs after OSCE. The integrated UC emission intensity areas of $NaGdF_4$: $Tm^{3+}/Yb^{3+}/Tb^{3+}$ (UCNPs TOL / $TbCl_3$ ethanol) was about 87.6% of the initial $NaGdF_4$: Tm^{3+}/Yb^{3+} UCNP template (UCNPs TOL)

Under the optimized OSCE conditions, the upconversion luminescent intensities before and after OSCE (obtained by calculating the area of luminescent patterns), were compared to study the cation exchange efficiency. The sample with the 0.5 μM Tb^{3+} concentration showed the strongest upconversion luminescence. Though the peak areas of the Tm^{3+} ions showed a decreasing trend, the new peak areas of Tb^{3+} ions produced by cation exchange compensate the integrated upconversion luminescent spectrum. In the 0.5 μM Tb^{3+} concentration exchange condition, the integrated UC emission intensity areas of $NaGdF_4$:

$Tm^{3+}/Yb^{3+}/Tb^{3+}$ were about 87.6% that of the $NaGdF_4$: Tm^{3+}/Yb^{3+} UCNP template (455,786 / 520,473 = 87.6%), as shown in Figure 4.6.

This OSCE method is also applicable to other rare-earth precursor salts, e.g., rare-earth acetate. In Figure 4.7, $Tb(CH_3COO)_3$ acetate instead of $TbCl_3$ chloride was dissolved in ethanol and subject to a cation exchange reaction at the appropriate volume ratio with a UCNP-toluene solution at room temperature. Tb^{3+} ions could still partially replace the rare-earth sites in the crystal structure of $NaGdF_4$: Tm^{3+},Yb^{3+}, forming new $NaGdF_4$: Tm^{3+},Yb^{3+},Tb^{3+} compositions. These showed obvious emission peaks at 540 nm, 582 nm and 618 nm, originating from the characteristic Tb^{3+} ion level transitions $^5D_4 \rightarrow {}^7F_5$, $^5D_4 \rightarrow {}^7F_5$ and $^5D_4 \rightarrow {}^7F_3$, respectively.

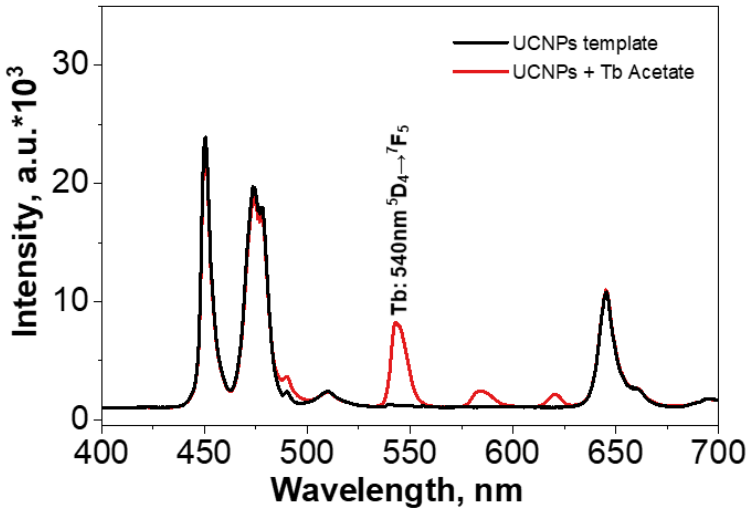

Figure 4.7 $Tb(CH_3COO)_3$ (Tb Acetate) substituted for $TbCl_3$ for OSCE in $NaGdF_4$: Tm^{3+}/Yb^{3+} UCNPs: Tb emissions prove that $Tb(CH_3COO)_3$ can also be used for cation exchange

Some other exchange ions, such as Eu^{3+}, can also be doped into the lattice of UCNPs by OSCE. In Figure 4.8, $EuCl_3$ chloride was dissolved in ethanol and then subject to a cation exchange reaction by mixing with a UCNP-toluene solution at the appropriate volume ratio at room temperature. Eu^{3+} ions can also partially replace the rare-earth sites in the crystal structure of $NaGdF_4$: Tm^{3+},Yb^{3+}, forming new $NaGdF_4$: Tm^{3+},Yb^{3+},Eu^{3+} compositions. These showed new emission peaks at 592 nm and 613 nm, which correspond to the characteristic Eu^{3+}ion level transitions of $^5D_0 \rightarrow {}^7F_1$ and $^5D_0 \rightarrow {}^7F_2$, respectively.

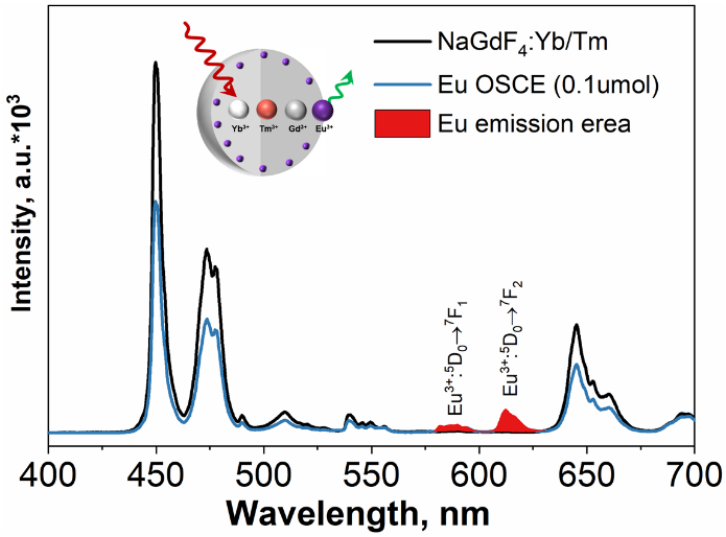

Figure 4.8 Eu^{3+} ions for OSCE in core-only $NaGdF_4$: Tm^{3+}/Yb^{3+} UCNPs: the emission peaks of 589 ($^5D_0 \rightarrow {}^7F_1$) and 611 nm ($^5D_0 \rightarrow {}^7F_2$) belong to Eu^{3+} ions

4.3.2 Exchange ion characterization

To confirm the introduction of exchange ions into the lattice, we performed a structural analysis of the nanocrystals. Transmission electron microscope (TEM) images revealed the particle size and morphology of UCNPs before and after OSCE with 0.5 μM Tb^{3+} ions. Before cation exchange, the size of the initial $NaGdF_4$: Yb^{3+},Tm^{3+} UCNP template was about 23 nm (Figure 4.9 a). After cation exchange in toluene/ethanol under ambient conditions for 10 min, the exchanged particles showed no obvious changes in terms of particle size (23.1 nm) and morphology (Figure 4.9 b).

We then employed high-resolution transmission electron microscopy (HRTEM) imaging and energy-dispersive X-ray spectroscopy (EDS) to confirm the existence of Tb^{3+} ions (Figure 4.9c-f). Combined with the linear profile for a single particle (Figure 4.9c), we found that Tb^{3+} ions only appeared on the surface, while Gd^{3+} ions existed in the centre of the particles, indicating the enrichment of Tb^{3+} at the surface of UCNPs. We also used the X-ray diffraction (XRD) and Rietveld refinement to characterize the structural evolution in terms of cell parameters and cell volumes. Both of the X-ray patterns were in line with the hexagonal cell (P63/m), with parameters close to the standard model of ICSD #5192039[47]. Therefore, the crystal structure was taken as a starting model for Rietveld refinement. The results indicate that OSCE did not induce variation in particle phase. In the structure of $NaGdF_4$: Yb^{3+},Tm^{3+} UCNPs, Yb^{3+}, Tm^{3+}, and Gd^{3+} ions occupy the same position and have ionic radii of 1.042, 1.052, and 1.107 Å (9 coordination),

respectively[48]. Refinements showed that the initial UCNP template had a unit cell volume of 111.532 Å^3 (Figure 4.9g, h). After OSCE with 0.5 μM Tb^{3+} ions (r = 1.095 Å, 9 coordination), the cell volume of the $NaGdF_4$: Yb^{3+},Tm^{3+},Tb^{3+} UCNPs decreased to 111.236 Å^3, which implies that the small Tb^{3+} ions mostly replaced the larger Gd^{3+} ions in the lattice.

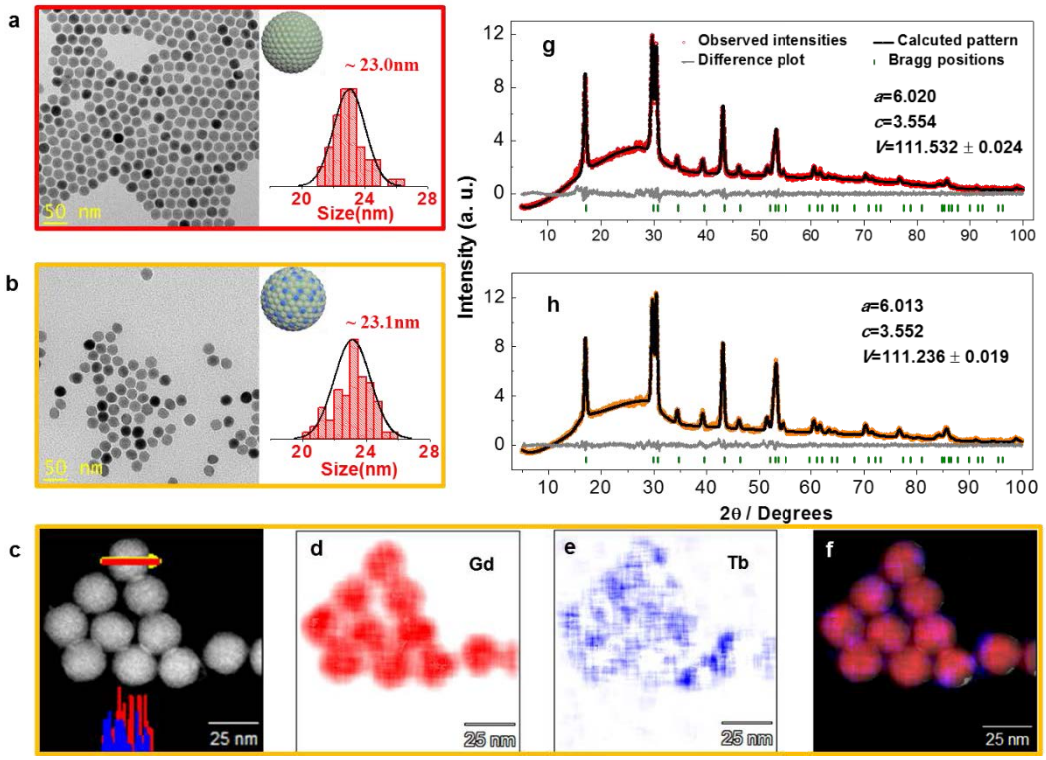

Figure 4.9 TEM images and size distributions of $NaGdF_4$: Yb^{3+},Tm^{3+} nanocrystals before and after OSCE (with 0.5 μM Tb^{3+}) (a-b). HRTEM and EDS images of $NaGdF_4$: Yb^{3+},Tm^{3+} after OSCE (c-f). Note that the elemental maps of Gd and Tb ions (d-f) reveal that Tb penetrated into the outer layer of the $NaGdF_4$: Yb^{3+},Tm^{3+} UCNPs. XRD patterns and calculated cell parameters and volumes of $NaGdF_4$: Yb^{3+},Tm^{3+} before and after OSCE with Tb^{3+} ions (g-h)

4.3.3 UC luminescence of Tb^{3+} by OSCE

To visualize the advantages of the OSCE method in retaining the emission intensity of UCNPs, we compared the colloidal luminescent intensity/colour and spectroscopic properties of the exchanged UCNPs with those of samples produced using the WACE method. In a typical procedure, $NaGdF_4$: Yb^{3+}/Tm^{3+} core nanocrystals about 16 nm in size were firstly synthesized by a co-precipitation process. Upon coating with a $NaGdF_4$ shell via a hot-injection procedure, the average size of the $NaGdF_4$: Yb^{3+},Tm^{3+}@$NaGdF_4$ core-shell nanocrystals increased to around 23 nm (Figure 4.10).

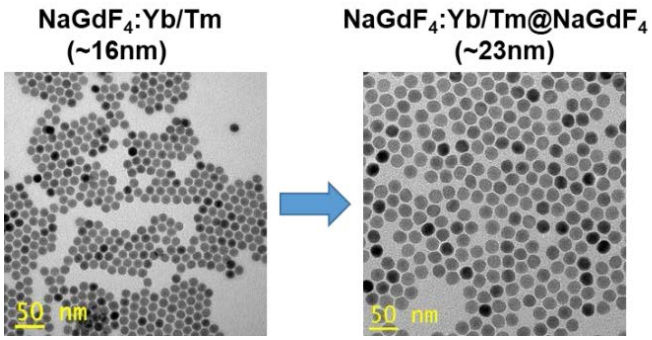

Figure 4.10 *TEM images of core-shell UCNPs for cation exchange. Firstly, core-only $NaGdF_4$: Yb^{3+}/Tm^{3+} nanoparticles about 16 nm in size were prepared. Then, $NaGdF_4$: Yb^{3+}/Tm^{3+}@$NaGdF_4$ core-shell structures about 23 nm in size were prepared by hot-injection*

As shown in Figure 4.11a, core-shell $NaGdF_4$: Yb^{3+}/Tm^{3+}@$NaGdF_4$ nanoparticles were adopted as a template for WACE and OSCE. Then, the upconversion luminescent spectra and digital images were collected. The photos clearly show that under excitation at 980 nm using a continuous-wave (CW) laser, the emission intensity of UCNPs after Tb^{3+} exchange by OSCE was much stronger than that done by WACE in parallel. Moreover, the hybrid emitted light from Tb^{3+} and Tm^{3+} produced by the OSCE method tended to be whiter. Specifically, five Tb^{3+} concentrations, 1, 5, 15, and 50 mM, were selected for cation exchange, and a comparison of the spectra is provided in Figure 4.11b. The characteristic Tb^{3+} emission peaks at 540 nm, 582 nm and 618 nm originated from the characteristic Tb^{3+} ion level transitions of $^5D_4 \rightarrow {}^7F_5$, $^5D_4 \rightarrow {}^7F_5$ and $^5D_4 \rightarrow {}^7F_3$, respectively. The comparison of spectroscopic properties (Figures 4.11c and d) shows that much stronger emission peaks were obtained by the OSCE method, regardless of the Tb^{3+} concentration used for cation exchange. The emission intensities of the typical Tm^{3+} (448 nm) and Tb^{3+} (540 nm) peaks decreased with increases in Tb^{3+} concentration from 1 to 50 μM (Figure 4.11d). Furthermore, the intensity ratio of Tb^{3+}/Tm^{3+} by OSCE was greater than 1, while the ratio of Tb^{3+}/Tm^{3+} by WACE was less than 1 (Figure 4.11e), implying that the UC emissions of Tb^{3+} ions in the UCNPs produced by OSCE were more efficient. This may be because the OSCE took place in an organic solvent, which avoids damage to peripheral lattices and degradation of the nanocrystals. Since nanocrystals are under the premise of retaining surface ligands, the efficiency of Tb^{3+} ions via OSCE tend to be higher. The level diagram and proposed energy transfer mechanism for the core-shell $NaGdF_4$: Yb^{3+},Tm^{3+}@$NaGdF_4$ UCNPs' cation exchange with the Tb^{3+} layer are shown in Figure 4.12.

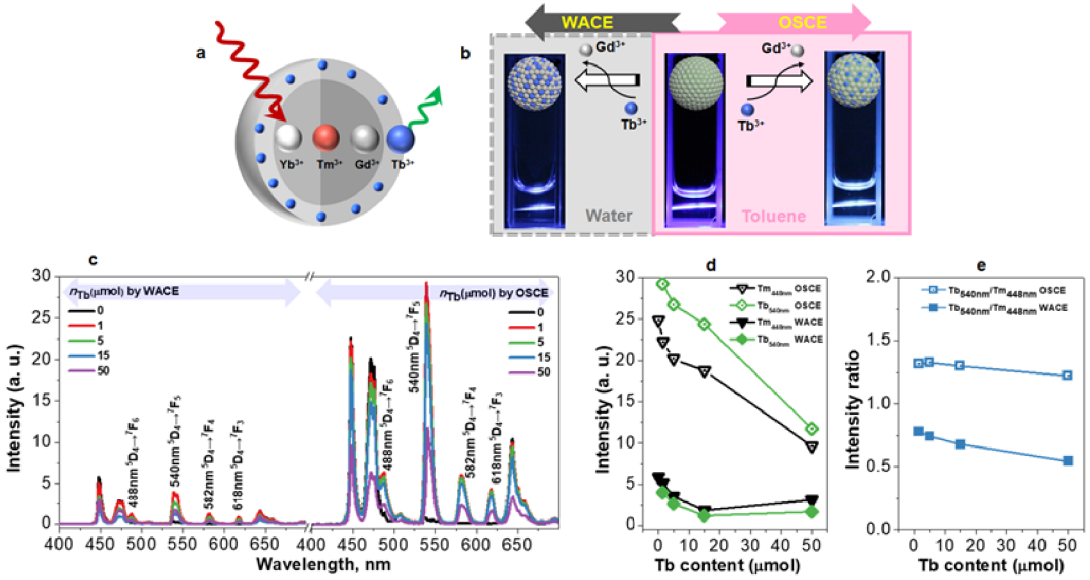

Figure 4.11 Nanostructure of core-shell $NaGdF_4$: Yb^{3+},Tm^{3+}@$NaGdF_4$ UCNPs for cation exchange (a); Luminescent photos of UCNPs by WACE, initial UCNP template, UCNPs by OSCE under irradiation by a 980 nm laser (b); Upconversion emission spectra after cation exchange by WACE and OSCE, respectively (five Tb^{3+} contents), the concentrations of all samples were 1 mg mL^{-1} (c); Intensities of Tm^{3+} and Tb^{3+} emissions as a function of Tb^{3+} content (d); Intensity ratio of Tb^{3+}/Tm^{3+} emissions as a function of Tb^{3+} content (e). All spectra were recorded under 980 nm excitation at a power density of 500 mW cm^{-2}

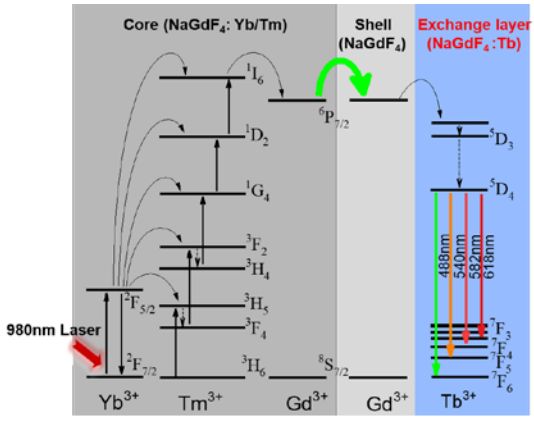

Figure 4.12 Level diagram and proposed energy transfer mechanism between core-shell $NaGdF_4$: Yb^{3+},Tm^{3+}@$NaGdF_4$ UCNPs and a cation-exchanged Tb^{3+} layer

To quantify the luminescence properties and enhancement, the integrated intensity of typical samples (UCNPs produced by WACE, initial UCNP template, UCNPs by OSCE in a 1 μM $TbCl_3$ solution) were calculated. We found that the intensity of UCNPs was enhanced 1.68-fold after OSCE, whereas the intensity decreased to 27% of the initial template after WACE (Figure 4.13). The brightness of colloidal UCNPs after Tb^{3+}- OSCE was about 6.2-fold stronger than that of the UCNPs after Tb^{3+}- WACE.

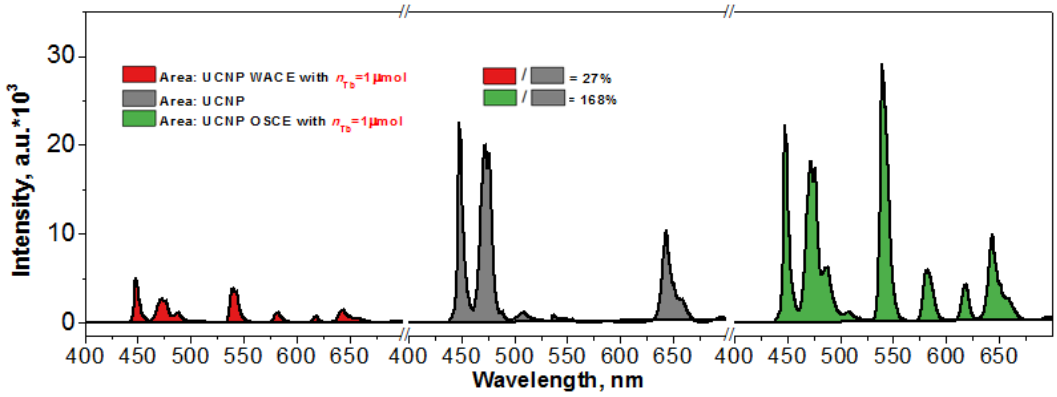

Figure 4.13 Upconversion emission intensity areas of core-shell UCNPs produced by WACE, initial core-shell UCNP template, and core-shell UCNPs by OSCE (1 µmol Tb content): the intensity of UCNPs showed a 1.68-fold enhancement after OSCE, while the intensity decreased to 27% of the initial template after WACE

In addition, when the other solvents were used to support the OSCE process, similar phenomena were observed. Figure 4.14 shows OSCE using DMF as the solvent to dissolve $TbCl_3$. First of all, the optimum ratio of toluene/DMF was determined to be 10:1 (Figure 4.14a). Using two Tb concentrations, the integrated UC luminescent intensities of all samples produced by OSCE (using DMF as solvent), and the corresponding ones by WACE, were collected and compared. Under excitation at 980 nm using a CW laser, it is clearly shown in the spectra that the characteristic emissions of both Tm^{3+} and Tb^{3+} ions in the UCNPs produced by OSCE (using DMF) were very strong. In contrast, the emission intensities of Tm^{3+} and Tb^{3+} ions in the UCNPs produced by WACE were comparatively weak. Regardless of the Tb^{3+} concentration used for cation exchange, the UC luminescent intensities of UCNPs produced by OSCE were always obviously higher than those produced by WACE (Figure 4.14 b).

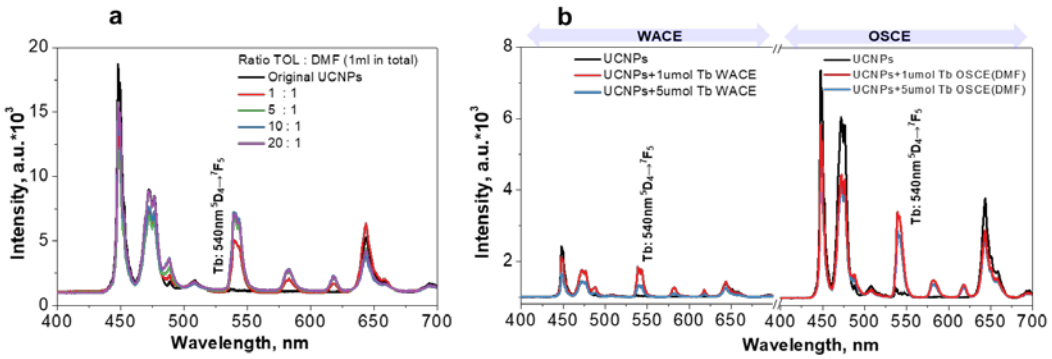

Figure 4.14 OSCE using DMF as a solvent to dissolve $TbCl_3$: the optimum ratio of toluene/DMF was 10:1 (a); the integrated UC luminescent intensities of all samples by OSCE (using DMF as solvent) were much stronger than those by WACE (with two Tb concentrations) (b)

4.3.4 UC luminescence of Eu^{3+} by OSCE

A similar phenomenon occurs when Eu^{3+} ions work as the exchange ions. Figure 4.15 shows the nanostructure of core-shell $NaGdF_4$: Yb^{3+},Tm^{3+}@$NaGdF_4$ UCNPs used for cation exchange with Eu^{3+} ions, as well as the upconversion luminescent spectra and digital images by WACE and OSCE, respectively.

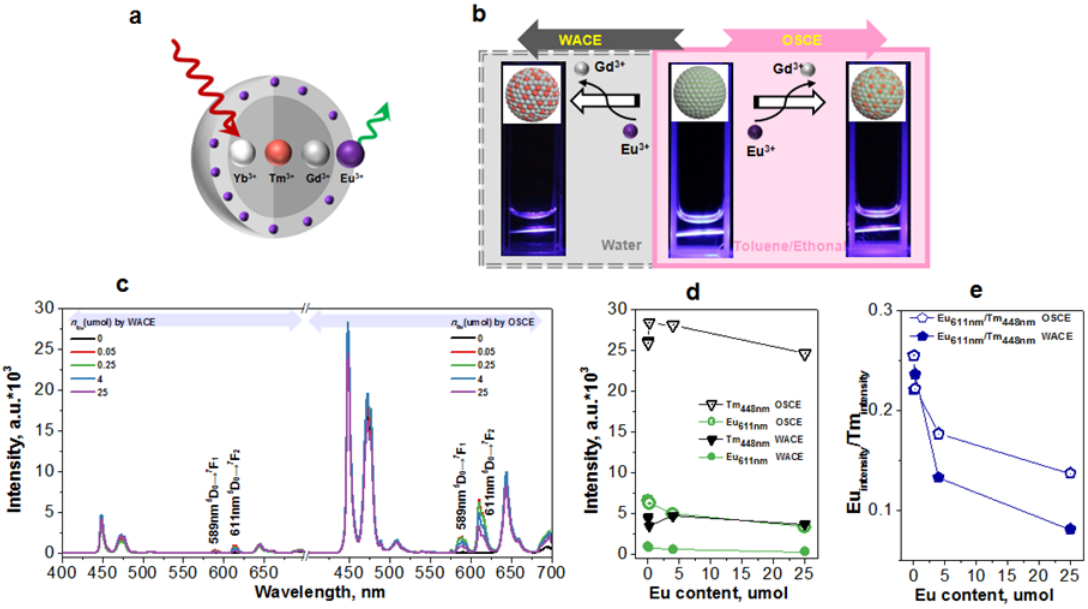

Figure 4.15 Eu^{3+} ions working as exchange ions: Nanostructure of core-shell $NaGdF_4$: Yb^{3+},Tm^{3+}@$NaGdF_4$ UCNPs used for cation exchange with Eu^{3+} ions (a); Luminescent photos of UCNPs produced by WACE, initial UCNP template, UCNPs produced by OSCE under irradiation by a 980 nm laser (b); Upconversion emission spectra after cation exchange through WACE and OSCE, respectively (5 Eu^{3+} concentrations), and all samples are 1 mg/mL (c); Intensities of Tm^{3+} and Eu^{3+} emissions as a function of Eu^{3+} content (d); Intensity ratio of Eu^{3+}/Tm^{3+} emissions as a function of Eu^{3+} content ***(e)****. All spectra were recorded under 980 nm excitation at a power density of 500 W cm^{-2}*

Under excitation at 980 nm using a CW laser, it is apparent in the digital photos that the emission intensity of UCNPs after Eu^{3+} exchange by OSCE was much stronger than in those produced in parallel by WACE. (Figure 4.15b). The emission peaks at 592 nm and 613 nm correspond to the characteristic ion level transitions of $^5D_0 \rightarrow {}^7F_1$ and $^5D_0 \rightarrow {}^7F_2$ of Eu^{3+} ions, respectively[49]. The colour of the new nanoparticles formed by OSCE tended to be red because of the characteristic UC emission peaks of Eu^{3+} ions. Five Eu^{3+} concentrations, 0.05, 0.25, 4, and 25 μM, were chosen for cation exchange. Under excitation at 980 nm using a CW laser, it is clearly shown in the spectra that the characteristic emissions of Eu^{3+} and Tm^{3+} ions in UCNPs produced by OSCE were very strong. In contrast, those produced by WACE were comparatively weak. Regardless of

the Eu^{3+} concentration used for the cation exchange, the UC luminescent intensities of the Eu^{3+}-doped UCNPs produced by the OSCE process were always obviously higher than those produced by WACE (Figures 4.15c and d).

4.3.5 UC luminescence at the single particle level

We used a home-made confocal microscope to quantify the emission intensities of the core-shell nanocrystals after Tb^{3+} exchange through OSCE and WACE at the single particle level. To achieve high signal-to-noise ratios with the confocal microscope for accurate single-nanocrystal analysis, we made large-sized core-shell $NaGdF_4$: Yb^{3+},Tm^{3+}@$NaGdF_4$ UCNPs (~37 nm core, ~44 nm core-shell, Figure 4.16) for luminescence testing at the single particle level.

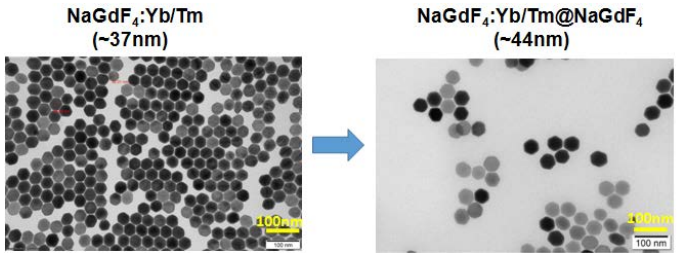

Figure 4.16 TEM images of core-shell UCNPs used for single-particles tests: firstly, core-only $NaGdF_4$: Yb^{3+}/Tm^{3+} nanoparticles about 37 nm in size were prepared, and then $NaGdF_4$: Yb^{3+}/Tm^{3+}@$NaGdF_4$ core-shell structures of about 44 nm were prepared by hot injection

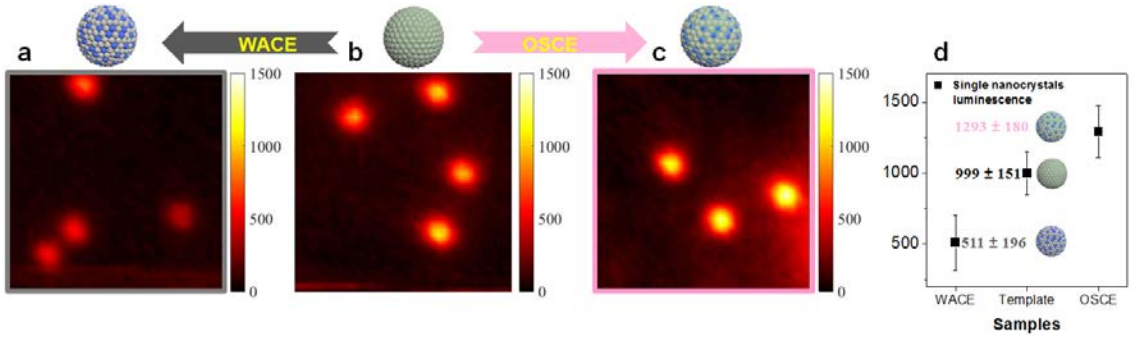

Figure 4.17 Confocal scanning images and averaged brightness of core-shell $NaGdF_4$: Yb^{3+},Tm^{3+}@$NaGdF_4$ single nanoparticles: confocal images of UCNPs by WACE, initial UCNP template, and UCNPs by OSCE, respectively, and all samples were produced by 1 μM Tb^{3+} ion exchange (a-c); Brightness statistics of the single UCNPs corresponding to a−c. All optical images were recorded with a 842 nm short-pass filter under irradiation of a 980 nm single-mode laser (30 MW cm^{-2}) (d)

The average brightness of single core-shell UCNPs after Tb^{3+}-WACE was about 511 photon counts after background subtraction, which is half as much as the brightness of the initial core-shell UCNP template (999 photon counts; Figures 4.17a, b, d). For the

core-shell UCNPs after Tb^{3+}-OSCE, the average brightness of single particles (1293 photon counts) was about 1.3-fold stronger than that of initial core-shell UCNP templates (Figure 4.17 b, c, d). The brightness of single UCNPs after Tb^{3+}- OSCE was about 2.5-fold stronger than that of UCNPs after Tb^{3+}-WACE. These results are consistent with the spectroscopic properties tested in colloidal solutions using a spectrofluorometer, demonstrating that multicolour-emitting nanoparticles with high luminescent performance were obtained by the developed OSCE synthesis strategy, which is facile and rapid.

4.3.6 Multicolour by OSCE and CIE chromaticity

CIE chromaticity coordinates (*x,y*) of typical samples were calculated throughout their upconversion luminescent spectra, as shown in Figure 4.18. The core-shell $NaGdF_4$: Yb^{3+},Tm^{3+}@$NaGdF_4$ UCNPs only showed the characteristic emission of Tm^{3+} ions, which is close to the blue light region (0.28, 0.26). After OSCE by Tb^{3+} ions, the core-shell $NaGdF_4$: Yb^{3+},Tm^{3+}@$NaGdF_4$ UCNPs presented Tm^{3+} and Tb^{3+} emissions, with a colour located in the white light region (0.3, 0.32). After OSCE by Eu^{3+} ions, the core-shell-like $NaGdF_4$ UCNPs showed emissions of Tm^{3+} and Eu^{3+}, which are in the red light region (0.27, 0.18). The results indicate that multicolour luminescence, as well as high performance, were realized in the as-synthesized UCNPs by using our OSCE synthesis strategy. Particularly, the formed Yb^{3+}/Tm^{3+}/Tb^{3+} co-doped $NaGdF_4$: Yb^{3+},Tm^{3+}@$NaGdF_4$ UCNPs showed strong colour output located in the centre of the white region.

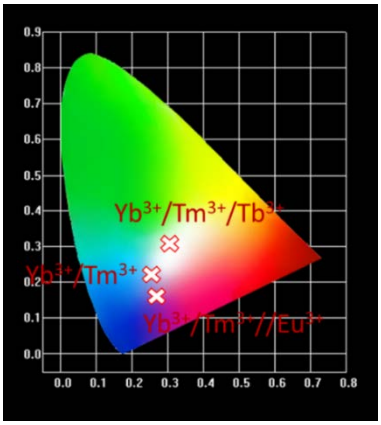

Figure 4.18 CIE chromaticity coordinates (x,y) of core-shell $NaGdF_4$: Yb^{3+},Tm^{3+}@$NaGdF_4$ UCNPs; the UCNPs after OSCE by Tb^{3+} ions; and the UCNPs after OSCE by Eu^{3+} ions upon 980 nm excitation

4.4 Conclusions

In this chapter, we developed a rapid and facile cation exchange method for UCNPs, without needing to remove surface ligands in an organic solvent. This cation exchange strategy makes it possible to produce multicolour luminescence in RE^{3+}-doped upconversion nanoparticles expeditiously. Using typical Tb^{3+} and Eu^{3+} ions for cation exchange, we have quantitatively compared the UC emissions of cation-exchanged UCNPs prepared by the OSCE and conventional WACE methods, we found that OSCE is featured by strong emissions of exchanged activators. The WACE method had a significant quenching effect on the fluorescence intensity of UCNPs, whereas the OSCE method gives UCNPs higher intensity in both colloidal and single-particle states. This facile and rapid OSCE synthesis strategy provides a new way to create UCNPs with high luminescent performance at high rates of production. Furthermore, with the preservation of surface ligands, UCNPs can be re-dispersed into an oleic acid environment. These techniques show great potential for growing new heterogeneously structured nanomaterials.

4.5 References

1. Feynman, R., There's plenty of room at the bottom: An invitation to enter a new field of physics. *Caltech Eng Sci* **1960,** *23*, 22-36.

2. Huang, G.; Wang, C.; Xu, S.; Zong, S.; Lu, J.; Wang, Z.; Lu, C.; Cui, Y., Postsynthetic Doping of $MnCl_2$ Molecules into Preformed $CsPbBr_3$ Perovskite Nanocrystals via a Halide Exchange-Driven Cation Exchange. *Adv Mater* **2017,** *29* (29).

3. Beberwyck, B. J.; Surendranath, Y.; Alivisatos, A. P., Cation Exchange: A Versatile Tool for Nanomaterials Synthesis. *The Journal of Physical Chemistry C* **2013,** *117* (39), 19759-19770.

4. Koscher, B. A.; Bronstein, N. D.; Olshansky, J. H.; Bekenstein, Y.; Alivisatos, A. P., Surface- vs Diffusion-Limited Mechanisms of Anion Exchange in $CsPbBr_3$ Nanocrystal Cubes Revealed through Kinetic Studies. *J Am Chem Soc* **2016,** *138* (37), 12065-8.

5. Dorokhin, D.; Tomczak, N.; Han, M.; Reinhoudt, D. N.; H., V. A.; Vancso, G. J., Reversible Phase Transfer of (CdSe/ZnS) Quantum Dots between Organic and Aqueous Solutions. *ACS Nano* **2009,** *3*, 661-667.

6. Langlois, C.; Benzo, P.; Arenal, R.; Benoit, M.; Nicolai, J.; Combe, N.; Ponchet, A.; Casanove, M. J., Fully Crystalline Faceted Fe-Au Core-Shell Nanoparticles. *Nano Lett* **2015,** *15* (8), 5075-80.

7. Gilroy, K. D.; Hughes, R. A.; Neretina, S., Kinetically controlled nucleation of silver on surfactant-free gold seeds. *J Am Chem Soc* **2014,** *136* (43), 15337-45.

8. Han, S.; Qin, X.; An, Z.; Zhu, Y.; Liang, L.; Han, Y.; Huang, W.; Liu, X., Multicolour synthesis in lanthanide-doped nanocrystals through cation exchange in water. *Nat Commun* **2016,** *7*, 13059.

9. Vlasov, II; Shiryaev, A. A.; Rendler, T.; Steinert, S.; Lee, S. Y.; Antonov, D.; Voros, M.; Jelezko, F.; Fisenko, A. V.; Semjonova, L. F.; Biskupek, J.; Kaiser, U.; Lebedev, O. I.; Sildos, I.; Hemmer, P. R.; Konov, V. I.; Gali, A.; Wrachtrup, J., Molecular-sized fluorescent nanodiamonds. *Nat Nanotechnol* **2014,** *9* (1), 54-8.

10. Wu, X. J.; Chen, J.; Tan, C.; Zhu, Y.; Han, Y.; Zhang, H., Controlled growth of high-density CdS and CdSe nanorod arrays on selective facets of two-dimensional semiconductor nanoplates. *Nat Chem* **2016,** *8* (5), 470-5.

11. Tan, C.; Zhang, H., Epitaxial growth of hetero-nanostructures based on ultrathin two-dimensional nanosheets. *J Am Chem Soc* **2015,** *137* (38), 12162-74.

12. Huang, X.; Han, S.; Huang, W.; Liu, X., Enhancing solar cell efficiency: the search for luminescent materials as spectral converters. *Chem Soc Rev* **2013,** *42* (1), 173-201.

13. Berry, M. T.; May, P. S., Disputed Mechanism for NIR-to-Red Upconversion Luminescence in $NaYF_4:Yb^{3+},Er^{3+}$. *J Phys Chem A* **2015,** *119* (38), 9805-11.

14. Liu, Q.; Feng, W.; Li, F., Water-soluble lanthanide upconversion nanophosphors: Synthesis and bioimaging applications in vivo. *Coordination Chemistry Reviews* **2014,** *273-274*, 100-110.

15. Liu, Y.; Lu, Y.; Yang, X.; Zheng, X.; Wen, S.; Wang, F.; Vidal, X.; Zhao, J.; Liu, D.; Zhou, Z.; Ma, C.; Zhou, J.; Piper, J. A.; Xi, P.; Jin, D., Amplified stimulated emission in upconversion nanoparticles for super-resolution nanoscopy. *Nature* **2017,** *543* (7644), 229-233.

16. Kim, T.-H.; Cho, K.-S.; Lee, E. K.; Lee, S. J.; Chae, J.; Kim, J. W.; Kim, D. H.; Kwon, J.-Y.; Amaratunga, G.; Lee, S. Y.; Choi, B. L.; Kuk, Y.; Kim, J. M.; Kim, K., Full-colour quantum dot displays fabricated by transfer printing. *Nature Photonics* **2011,** *5* (3), 176-182.

17. Aharonovich, I.; Englund, D.; Toth, M., Solid-state single-photon emitters. *Nature Photonics* **2016,** *10* (10), 631-641.

18. Meinardi, F.; McDaniel, H.; Carulli, F.; Colombo, A.; Velizhanin, K. A.; Makarov, N. S.; Simonutti, R.; Klimov, V. I.; Brovelli, S., Highly efficient large-area colourless luminescent solar concentrators using heavy-metal-free colloidal quantum dots. *Nat Nanotechnol* **2015,** *10* (10), 878-85.

19. McGuinness, L. P.; Yan, Y.; Stacey, A.; Simpson, D. A.; Hall, L. T.; Maclaurin, D.; Prawer, S.; Mulvaney, P.; Wrachtrup, J.; Caruso, F.; Scholten, R. E.; Hollenberg, L. C., Quantum measurement and orientation tracking of fluorescent nanodiamonds inside living cells. *Nat Nanotechnol* **2011,** *6* (6), 358-63.

20. Bailey, R. E.; Nie, S., Alloyed Semiconductor Quantum Dots: Tuning the Optical Properties without Changing the Particle Size. *J Am Chem Soc* **2003,** *125*, 7100-7106.

21. Liu, D.; Xu, X.; Du, Y.; Qin, X.; Zhang, Y.; Ma, C.; Wen, S.; Ren, W.; Goldys, E. M.; Piper, J. A.; Dou, S.; Liu, X.; Jin, D., Three-dimensional controlled growth of monodisperse sub-50 nm heterogeneous nanocrystals. *Nat Commun* **2016,** *7*, 10254.

22. Wang, F.; Deng, R.; Wang, J.; Wang, Q.; Han, Y.; Zhu, H.; Chen, X.; Liu, X., Tuning upconversion through energy migration in core-shell nanoparticles. *Nat Mater* **2011,** *10* (12), 968-73.

23. Zhou, B.; Shi, B.; Jin, D.; Liu, X., Controlling upconversion nanocrystals for emerging applications. *Nat Nanotechnol* **2015,** *10* (11), 924-36.

24. Wang, F.; Han, Y.; Lim, C. S.; Lu, Y.; Wang, J.; Xu, J.; Chen, H.; Zhang, C.; Hong, M.; Liu, X., Simultaneous phase and size control of upconversion nanocrystals through lanthanide doping. *Nature* **2010,** *463* (7284), 1061-5.

25. Dong, C.; Korinek, A.; Blasiak, B.; Tomanek, B.; van Veggel, F. C. J. M., Cation Exchange: A Facile Method To Make $NaYF_4$:Yb,Tm-$NaGdF_4$ Core–Shell Nanoparticles with a Thin, Tunable, and Uniform Shell. *Chemistry of Materials* **2012,** *24* (7), 1297-1305.

26. Fischer, S.; Swabeck, J. K.; Alivisatos, A. P., Controlled Isotropic and Anisotropic Shell Growth in beta-$NaLnF_4$ Nanocrystals Induced by Precursor Injection Rate. *J Am Chem Soc* **2017,** *139* (35), 12325-12332.

27. Chen, G.; Agren, H.; Ohulchanskyy, T. Y.; Prasad, P. N., Light upconverting core-shell nanostructures: nanophotonic control for emerging applications. *Chem Soc Rev* **2015,** *44* (6), 1680-713.

28. Zhang, F.; Shi, Y.; Sun, X.; Zhao, D.; Stucky, G. D., Formation of Hollow Upconversion Rare-Earth Fluoride Nanospheres: Nanoscale Kirkendall Effect During Ion Exchange. *Chemistry of Materials* **2009,** *21* (21), 5237-5243.

29. Rivest, J. B.; Jain, P. K., Cation exchange on the nanoscale: an emerging technique for new material synthesis, device fabrication, and chemical sensing. *Chem Soc Rev* **2013,** *42* (1), 89-96.

30. Makarov, N. S.; Guo, S.; Isaienko, O.; Liu, W.; Robel, I.; Klimov, V. I., Spectral and Dynamical Properties of Single Excitons, Biexcitons, and Trions in Cesium-Lead-Halide Perovskite Quantum Dots. *Nano Lett* **2016,** *16* (4), 2349-62.

31. Lahtinen, S.; Lyytikäinen, A.; Päkkilä, H.; Hömppi, E.; Perälä, N.; Lastusaari, M.; Soukka, T., Disintegration of Hexagonal $NaYF_4$:Yb^{3+},Er^{3+} Upconverting Nanoparticles in Aqueous Media: The Role of Fluoride in Solubility Equilibrium. *The Journal of Physical Chemistry C* **2016,** *121* (1), 656-665.

32. Plohl, O.; Kralj, S.; Majaron, B.; Frohlich, E.; Ponikvar-Svet, M.; Makovec, D.; Lisjak, D., Amphiphilic coatings for the protection of upconverting nanoparticles against dissolution in aqueous media. *Dalton Trans* **2017,** *46* (21), 6975-6984.

33. Lisjak, D.; Plohl, O.; Ponikvar-Svet, M.; Majaron, B., Dissolution of upconverting fluoride nanoparticles in aqueous suspensions. *RSC Advances* **2015,** *5* (35), 27393-27397.

34. Plohl, O.; Kraft, M.; Kovac, J.; Belec, B.; Ponikvar-Svet, M.; Wurth, C.; Lisjak, D.; Resch-Genger, U., Optically Detected Degradation of $NaYF_4$:Yb,Tm-Based Upconversion Nanoparticles in Phosphate Buffered Saline Solution. *Langmuir* **2017,** *33* (2), 553-560.

35. Lisjak, D.; Plohl, O.; Vidmar, J.; Majaron, B.; Ponikvar-Svet, M., Dissolution Mechanism of Upconverting AYF_4:Yb,Tm (A = Na or K) Nanoparticles in Aqueous Media. *Langmuir* **2016,** *32* (32), 8222-9.

36. Wang, F.; Wang, J.; Liu, X., Direct evidence of a surface quenching effect on size-dependent luminescence of upconversion nanoparticles. *Angew Chem Int Ed* **2010,** *49* (41), 7456-60.

37. Bogdan, N.; Vetrone, F.; Ozin, G. A.; Capobianco, J. A., Synthesis of ligand-free colloidally stable water dispersible brightly luminescent lanthanide-doped upconverting nanoparticles. *Nano Lett* **2011,** *11* (2), 835-40.

38. Suo, H.; Hu, F.; Zhao, X.; Zhang, Z.; Li, T.; Duan, C.; Yin, M.; Guo, C., All-in-one thermometer-heater up-converting platform YF_3:Yb^{3+},Tm^{3+} operating in the first biological window. *Journal of Materials Chemistry C* **2017,** *5* (6), 1501-1507.

39. Haase, M.; Schafer, H., Upconverting nanoparticles. *Angew Chem Int Ed* **2011,** *50* (26), 5808-29.

40. Chan, E. M.; Han, G.; Goldberg, J. D.; Gargas, D. J.; Ostrowski, A. D.; Schuck, P. J.; Cohen, B. E.; Milliron, D. J., Combinatorial discovery of lanthanide-doped nanocrystals with spectrally pure upconverted emission. *Nano Lett* **2012,** *12* (7), 3839-45.

41. Zhao, J.; Jin, D.; Schartner, E. P.; Lu, Y.; Liu, Y.; Zvyagin, A. V.; Zhang, L.; Dawes, J. M.; Xi, P.; Piper, J. A.; Goldys, E. M.; Monro, T. M., Single-nanocrystal sensitivity achieved by enhanced upconversion luminescence. *Nat Nanotechnol* **2013,** *8* (10), 729-34.

42. Liu, X.; Wang, Y.; Li, X.; Yi, Z.; Deng, R.; Liang, L.; Xie, X.; Loong, D. T. B.; Song, S.; Fan, D.; All, A. H.; Zhang, H.; Huang, L.; Liu, X., Binary temporal upconversion codes of Mn^{2+}-activated nanoparticles for multilevel anti-counterfeiting. *Nat Commun* **2017,** *8* (1), 899.

43. Zhou, J.; Wen, S.; Liao, J.; Clarke, C.; Tawfik, S. A.; Ren, W.; Mi, C.; Wang, F.; Jin, D., Activation of the surface dark-layer to enhance upconversion in a thermal field. *Nature Photonics* **2018,** *12* (3), 154-158.

44. Ren, W.; Zhou, Y.; Wen, S.; He, H.; Lin, G.; Liu, D.; Jin, D., DNA-mediated anisotropic silica coating of upconversion nanoparticles. *Chem Commun (Camb)* **2018,** *54* (52), 7183-7186.

45. Ren, W.; Wen, S.; Tawfik, S. A.; Su, Q. P.; Lin, G.; Ju, L. A.; Ford, M. J.; Ghodke, H.; van Oijen, A. M.; Jin, D., Anisotropic functionalization of upconversion nanoparticles. *Chem Sci* **2018,** *9* (18), 4352-4358.

46. Ma, C.; Xu, X.; Wang, F.; Zhou, Z.; Liu, D.; Zhao, J.; Guan, M.; Lang, C. I.; Jin, D., Optimal Sensitizer Concentration in Single Upconversion Nanocrystals. *Nano Letters* **2017,** *17* (5), 2858-2864.

47. Grzechnik, A.; Bouvier, P.; Mezouar, M.; Mathews, M. D.; Tyagi, A. K.; Köhler, J., Hexagonal $Na_{1.5}Y_{1.5}F_6$ at High Pressures. *Journal of Solid State Chemistry* **2002,** *165* (1), 159-164.

48. Shannon, R. D., Revised effective ionic radii and systematic studies of interatomic distances in halides and chalcogenides. *Acta Crystallographica Section A* **1976,** *32* (5), 751-767.

49. Zhang, C.; Yang, L.; Zhao, J.; Liu, B.; Han, M. Y.; Zhang, Z., White-Light Emission from an Integrated Upconversion Nanostructure: Toward Multicolor Displays Modulated by Laser Power. *Angew Chem Int Ed* **2015,** *54* (39), 11531-5.

CHAPTER 5

Cation Exchange for the Hybrid Growth of Multicolour Luminescent Upconversion Nanoparticles

5.1 Introduction

Though many methods have been used for tuning the multicolour properties of upconversion nanoparticles (UCNPs), the colour gamut of UC luminescence remains limited because of the fixed characteristic emissions produced by the level transitions of rare-earth (RE^{3+}) ions[1-4]. Synthesizing hybrid nanocrystals containing two or more nanoscale components is a promising strategy for widening the colour gamut and enhancing the efficiency of UC multicolour luminescence[1, 5-11]. This is critical to meeting the growing demands of many potential applications.

Lead halide perovskite quantum dots (PQDs) have a very wide gamut (~140%) which exceeds that of commercially available OLEDs[12-14]. Their tunable bandgap and PL emissions can be precisely controlled by varying the halide composition (Figure 5.1)[15-18]. Besides, PQDs also show narrow emission bandwidths (12–40 nm), high photoluminescence quantum yields and facile fabrication[19-21]. Therefore, they have attracted much attention in a wide array of research fields[22]. The PQDs are downconversion materials, which always absorb high-energy photons of violet to green. Notably, the UC emission bands of UCNPs are located in the same region as the photon absorption of PQDs[23-26]. By combining UCNPs and PQDs in one system, UCNPs can act as energy donors, while PQDs can act as acceptors. Therefore, energy transfer could take place in such a hybrid system under NIR excitation. There are two ways of completing such energy transfer: 1) luminescence radiative reabsorption (LRR, also called radiative energy transfer, RET), and 2) the non-radiative dipole-dipole coupling of Forster

resonance energy transfer (FRET). Dong et al. reported an approach to fine-tuning the multicolour UC luminescence of $CsPbX_3$ PQDs through sensitization by RE^{3+}-doped NPs[27]. The sensitization is governed by an LRR upconversion process. Chen et al. also reported a similar phenomenon using an LRR process[28].

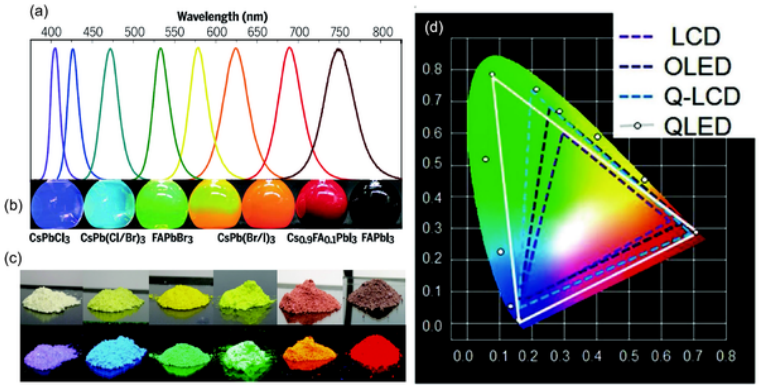

Figure 5.1 PL spectra of lead halide perovskite quantum dots with different components (a) and corresponding photographs under UV and daylight irradiation (b)[29]; Photographs of $CsPbX_3$-SiO2 (X = Cl, Br, I) composites under daylight (upper) and UV (lower) irradiation (c)[30]; CIE coordinates and corresponding colour gamuts of liquid crystal displays (LCD), organic light emitting diodes (OLED), quantum dot-type liquid crystal displays (QD-LCD), and perovskite quantum dot light emitting diodes (QLED) (d)[31]

However, the LRR process leads to energy loss because it is radiative reabsorption instinct instead of the direct energy transfer of FRET[32-37]. To generate sensitive luminescent signals by FRET, the association and separation of donors and acceptors should be precisely controlled in the range of 1–10 nm[5, 38-40]. Thereby, developing a hybrid structure of UCNPs and PQDs is the most direct method of realizing the FRET and widening the colour gamut of UC luminescence. Besides, hybrid heterojunctions of UCNPs and PQDs are also expected to reduce surface defects, improve the stability and quantum efficiency of UCNPs and PQDs through surface growth[41], dual-band (UV and NIR) excitation and polychromatic luminescence regulation, as well as enhance the luminescence intensities under single excitation through energy transfer of nonradiative dipole–dipole coupling.

The cation exchange in organic solvent strategy (OSCE) for UCNPs encourages us to develop a hybrid of UCNPs and other materials. Lattice matching is vital for hybrid growth; however, cation exchange may remediate the dissimilar structures of UCNPs and PQDs. Through a cation exchange strategy, one can try to penetrate transition-metal ions onto the surfaces of UCNPs. Then, these transition metals would show great potential to

form heterostructures of modified UCNPs and new PQDs. Both UCNPs and PQDs are always synthesized in the oleic acid environment. The OSCE method, which preserves the surface ligands of UCNPs, is particularly suited to the re-dispersion of modified UCNPs into an oleic acid environment for further hybrid growth.

In this chapter, transition-metal ions such as Pb^{2+} and Mn^{2+} ions are applied to the surfaces of UCNPs using our developed cation exchange strategy, which are then re-dispersed into an oleic acid environment. As the exchanged transition-metal ions can remediate the dissimilar structures of UCNPs and PQDs, a hybrid heterostructure is attempted to produce multicolour emissions and fine-tune them through FRET sensitization.

5.2 Experimental section

5.2.1 Reagents and equipment

Most chemicals and reagents used in this chapter were described in Chapters 3 and 4. Additional chemicals are listed in Table 5.1. All chemicals were used as received without further purification or modification unless otherwise described.

Table 5.1 Main experimental reagents, specifications and manufacturer

Chemical	Specification	Manufacturer
Tm_2O_3	≥99.9%	Sigma-Aldrich (Australia)
Yb_2O_3	≥99.9%	
Y_2O_3	≥99.9%	
Gd_2O_3	≥99.9%	
Trifluoroacetic acid	99%	
Sodium trifluoroacetate	98%	
Cs_2CO_3	≥99.9%	
$PbCl_2$	≥99.9%	
$PbBr_2$	≥99.9%	
PbI_2	≥99.9%	
$MnCl_2$	≥99.9%	
$Ni(acac)_2$	≥99.9%	
Trioctylphosphine (TOP)	99.5%	
n-Octylamine	99.5%	

Acetone	99.5%	Chem-Supply (Australia)
Ethanoic acid	30%	

Most instruments and equipment used in this chapter were described in Chapters 3 and 4, and additional instruments used for specimen synthesis in this chapter are listed in Table 5.2.

Table 5.2 Main experimental equipment, specific indicators and manufacturer

Equipment	Specification	Manufacturer
Fluorescence analysis cabinet	CM-10A	Grace Discovery Sciences
Spectro fluorophotometer	RF-6000	Shimadzu (Japan)

5.2.2 Synthesis of materials

Synthesis of β-*$NaYF_4$: Yb^{3+}/Tm^{3+} and* β-*$NaGdF_4$: Yb^{3+}/Tm^{3+} UCNPs*: The method used to prepare β-$NaYF_4$: Yb^{3+}/Tm^{3+} and β-$NaGdF_4$: Yb^{3+}/Tm^{3+} UCNPs was described in Chapters 3 and 4.

Synthesis of α-*$NaYF_4$: Yb^{3+}/Tm^{3+} and* α-*$NaGdF_4$: Yb^{3+}/Tm^{3+} UCNPs:* To obtain uniform UCNPs with an α phase, the thermal decomposition method was adopted for the synthesis[41]. Note that all decomposition processes should be carried out in a well-ventilated fume hood. First of all, a certain amount of Tm_2O_3 was dissolved in 50% aqueous trifluoroacetic acid at 80 °C. The residual water and acid were then slowly evaporated at 50 °C, then $Tm(CF_3CF_2CO)_3$ was obtained. The $Yb(CF_3CF_2CO)_3$, $Y(CF_3CF_2CO)_3$ and $Gd(CF_3CF_2CO)_3$ were also prepared by this method. After that, in the case of the $NaGdF_4$: Yb^{3+}/Tm^{3+} (20%/1%) codoped UCNPs, 0.79 mmol $Gd(CF_3CF_2CO)_3$, 0.20 mmol $Yb(CF_3CF_2CO)_3$, 0.01 mmol $Tm(CF_3CF_2CO)_3$, as well as 2.5 mmol of sodium trifluoroacetate (98%) were weighed and mixed with 8 ml OA, 8 ml oleylamine and 15 ml ODE in a 50 mL flask. The resulting solution was slowly heated to 100 °C under vacuum with magnetic stirring for 30 min to remove residual water and oxygen. Finally, the solution was heated to 300 °C and kept there for 1 h under a flow of argon. After reaction and cooling to room temperature, the synthesized nanoparticles were washed with cyclohexane/ethanol several times and dispersed in toluene for use.

Cation exchange (OSCE) by transition-metal ions: Mn^{2+}, Pb^{2+}, and Ni^{2+} were trialled in an attempt to penetrate the lattice of UCNPs by cation exchange in organic solvent. In a typical experiment, a stock toluene solution (6.66 ml) of the 1 mmol as-prepared UCNPs

($NaGdF_4$: Yb^{3+}/Tm^{3+}) was mixed with an ethanol solution (3.33 ml) of $MnCl_2$ (or $PbCl_2$, $Ni(acac)_2$) in a 25 ml flask. The resulting solution was slowly heated to 100 °C in an argon atmosphere with magnetic stirring for 30 min under reflux condensation. Subsequently, the products were collected by centrifugation, washed with toluene/ethanol (2:1) several times, and the modified UCNPs were re-dispersed in toluene for further use. DMF can also be used for dissolving transition metal chemicals to finish the cation exchange process.

Synthesis of UCNP and $CsPbX_3$ PQD hybrid structures: A modification of a previously published synthesis method was used[16, 42]. First of all, Cs-oleate was prepared. Cs_2CO_3 (0.814 g, 99.9%) was loaded into a 100 mL three-necked flask along with octadecene (40 mL) and oleic acid (2.5 mL, OA), dried for 1 h at 120 °C, and then heated under N_2 to 150 °C until all Cs_2CO_3 had reacted with OA. Since Cs-oleate precipitates out of ODE at room temperature, it had to be pre-heated to 100 °C before injection. After that, a certain amount of UCNPs that had been modified by cation exchange with Pb^{2+} ions, and oleylamine (5 mL, OLA) and dried OA (5 mL), were added into a 25 mL three-necked flask. The resulting solution was slowly heated to 150 °C under vacuum with magnetic stirring for 30 min to remove residual water and oxygen, and then cooled to 50 °C. In another three-necked flask, ODE (5 mL) and PbX_2 (0.188 mmol), such as PbI_2 (0.087g), $PbBr_2$ (0.069g), $PbCl_2$ (0.052g) or their mixtures were loaded into 25 mL three-necked flasks and dried under vacuum for 1 h at 120 °C. After complete solubilisation of a PbX_2 salt, 1 ml of the mixture of oleylamine, OA and modified UCNPs was injected at 120 °C under argon, then the temperature was raised to about 150 °C and 0.4 mL Cs-oleate solution was quickly injected; then, 5 s later, the reaction mixture was cooled in an ice-water bath. Finally, the crude solution was cooled with a water bath and aggregated NCs were separated by centrifuging. After centrifugation, the particles were redispersed in toluene or hexane, forming long-term colloidally-stable solutions for further testing.

Synthesis of a UCNP and Ni_2P hybrid structure: To determine whether the cation exchange process can remediate dissimilar structures and form hybrid heterostructures of UCNPs and other materials, we conducted hybrid growth of $NaGdF_4$ and Ni_2P nanoparticles. We modified the synthesis method according to previous literature[43-44]. In a typical synthesis, a certain amount of UCNPs that were modified by cation exchange of Ni^{2+} ions was added with 1-octadecene (4.5 mL, 14.1 mmol) and oleylamine (6.4 mL,

19.5 mmol) into a 50 mL three-necked flask. The resulting solution was slowly heated to 100 °C under vacuum with magnetic stirring for 30 min to remove residual water and oxygen. After cooling to 50 °C, $Ni(acac)_2$ (25 mg, 0.098 mmol) and trinoctylphosphine (0.2 mL, 0.44 mmol) were added to the flask and stirred vigorously for about 30 mins. Note that the flask was also equipped with a Liebig condenser. After that, the reaction mixture was heated to 120 °C for 1 h under vacuum to remove water and other low-boiling impurities. Finally, the solution was placed under Ar and heated to 320 °C with a holding time of 2 h. After reaction and cooling down to room temperature, the synthesized nanoparticles were centrifuged and washed using 1:3 (*v:v*) hexane:ethanol several times. The resulting compounds, consisting of UCNPs and Ni_2P nanoparticles, were re-dispersed in hexane for further testing.

5.2.3 Characterization

The synthesized materials were characterised by TEM, XRD, high-resolution transmission electron microscopy (HRTEM) and energy-dispersive X-ray spectroscopy (EDS), which were described in Chapters 3 and 4.

Photoluminescence spectra by spectrofluorometer: The down-conversion emission and excitation spectra of the PQDs were recorded on a spectrofluorophotometer (RF-6000, SHIMADZU, Japan) with a 150 W Xe lamp for excitation. The upconversion luminescence spectra were obtained using a Fluorolog-Tau3 spectrofluorometer (Jobin Yvon-Horiba) equipped with an external 980 nm CW diode laser with a pump power density of 500 W/cm^2.

5.3 Results and discussion

5.3.1 Lattice calculation and luminescence of PQDs

First of all, high-quality lead halide perovskite quantum dots (PQDs, $CsPbX_3$) were synthesized, including $CsPbCl_3$, $CsPb(Cl_{0.5}Br_{0.5})3$, $CsPbBr_3$, $CsPb(Br_{0.5}I_{0.5})3$, and $CsPbI_3$ PQDs,. X-ray diffraction (XRD) and Rietveld refinement were employed to characterize the space groups, and to calculate the cell parameters of this series of PQDs. These cell parameters were used as guidance for further hybrid growth with UCNPs.

The as-synthesized PQDs were cubic (Pm-3m) and highly crystallized. Figure 5.2 shows

the TEM images, XRD patterns and calculated cell parameters of this series of PQDs. The particle sizes of $CsPbX_3$ showed a decreasing trend as the halide composition changed from Cl^- to I^- (Figures 5.2 a, c, e, g, i). In contrast, the lattice parameters *a* (*a*=*b*=*c* in cubic structure) and *V* of these PQDs showed an obvious increase (Figures 5.2 b, d, f, h, j), because I^- (with larger radii) replaced the Br^- or Cl^- ions (with small radii). Therefore, the unit cells were enlarged as the halide composition changed from Cl^- to I^-. The calculated cell parameters and cell volume (*a, V*) of these $CsPbCl_3$, $CsPb(Cl_{0.5}Br_{0.5})_3$, $CsPbBr_3$, $CsPb(Br_{0.5}I_{0.5})_3$, and $CsPbI_3$ PQDs were determined as (5.61, 176.6), (5.74, 189.3), (5.89, 204.1), (6.00, 215.3) and (6.23, 242.1), respectively.

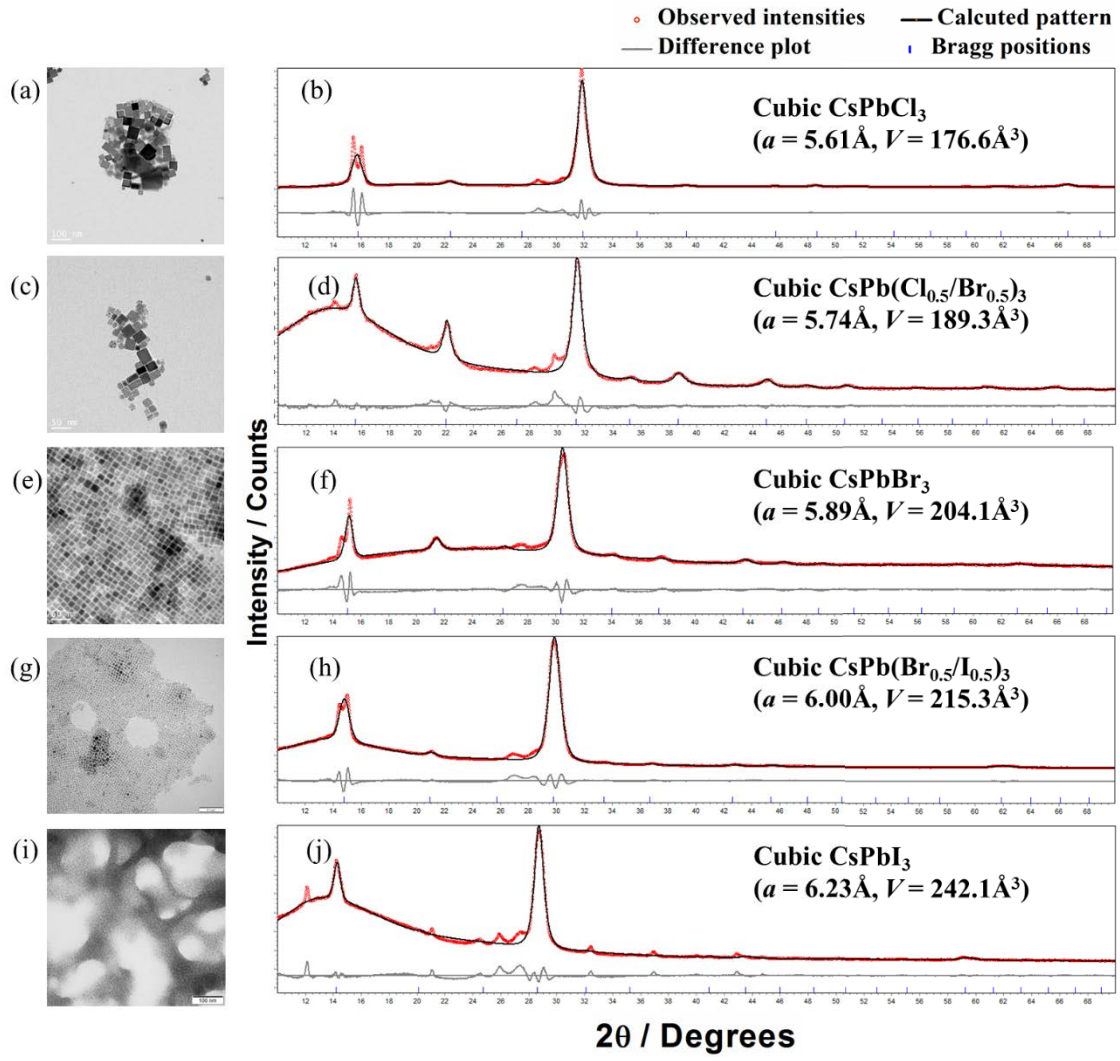

Figure 5.2 TEM images, XRD patterns, and calculated cell parameters and volumes using Rietveld refinement of typical $CsPbCl_3$ (a, b), $CsPb(Cl_{0.5}Br_{0.5})3$ (c, d), $CsPbBr_3$ (e, f), $CsPb(Br_{0.5}I_{0.5})3$ (g, h), and $CsPbI_3$ PQDs (i, j); the lattice parameters and V values of these samples showed an obvious increase as the halide composition changed from Cl^- to I^- (b, d, f, h, j)

Under excitation by 365 nm ultraviolet light, the PQDs of $CsPbCl_3$, $CsPb(Cl_{0.5}Br_{0.5})_3$, $CsPbBr_3$, $CsPb(Br_{0.5}I_{0.5})_3$, and $CsPbI_3$ displayed remarkably bright multicolour photoluminescent emissions with full gamuts from violet to green and deep red (Figure 5.3). The visible spectral region of this series of PQDs shifted from ~410 nm to ~700 nm as the halide composition changed from Cl^- to I^-. Due to the bandgap tailoring of PQDs achieved by adjusting the halide composition, the luminescent spectra of these PQDs exhibited tuneable multicolour emission bands.

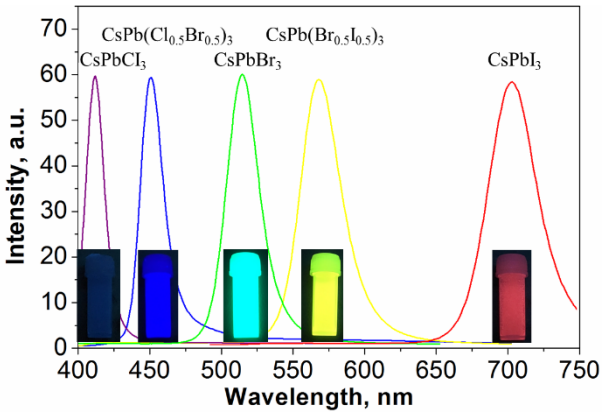

Figure 5.3 PQDs of $CsPbCl_3$, $CsPb(Cl_{0.5}Br_{0.5})_3$, $CsPbBr_3$, $CsPb(Br_{0.5}I_{0.5})_3$, and $CsPbI_3$ displayed bright multicolour luminescent emissions with full gamuts from violet to red (410 nm to 700 nm)

5.3.2 Lattice calculation and selection of UCNPs

Considering that α-UCNPs have a cubic structure (Fm-3m), and also have similar cell parameters as cubic PQDs, hybrid growth between α-UCNPs and PQDs seems most promising. Therefore, α-UCNPs were used to synthesize heterostructured materials with $CsPbX_3$ PQDs. As we know, lattice matching is the key for epitaxial growth. To minimize the lattice mismatching between α-UCNPs and PQDs, the cell parameters of α-UCNPs can be adjusted by doping different RE^{3+} ions, while the counterpart of $CsPbX_3$ PQDs can be adjusted by changing the halide composition.

UCNPs of α-$NaYF_4$ and α-$NaGdF_4$ were synthesized by the thermal decomposition method. The doping concentration of Yb^{3+}/Tm^{3+} was kept the same at 20%/2% for all the samples so, in this work, the samples will be denoted as α-$NaYF_4$ and α-$NaGdF_4$. Figure 5.4 shows the TEM images, XRD patterns and calculated cell parameters of these uniform α-$NaYF_4$ and α-$NaGdF_4$ UCNPs. The as-synthesized UCNPs were highly crystallized. Under 980 nm excitation, these UCNPs displayed strong blue UC luminescence from Tm^{3+} ions. Calculated using Rietveld refinement, the cell parameters and cell volume (*a,*

V) of the α-$NaYF_4$ and α-$NaGdF_4$ UCNPs were determined as (5.54, 170.77), and (5.57, 173.00), respectively.

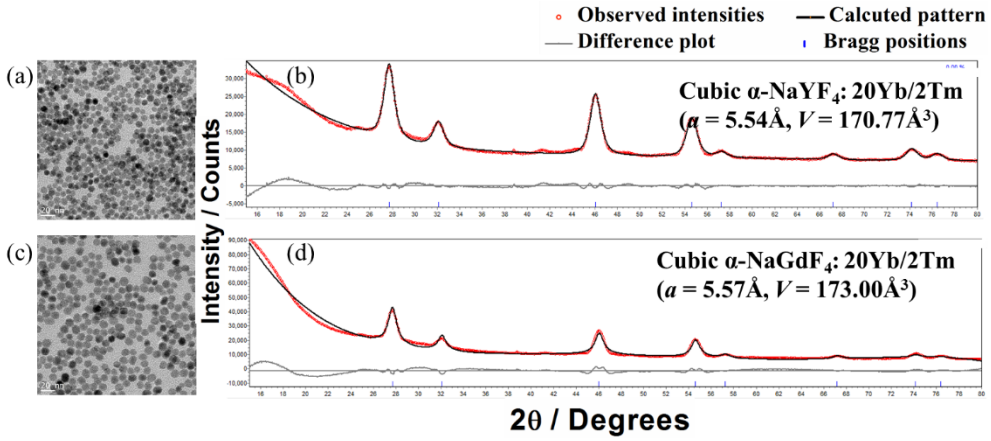

Figure 5.4 TEM images, XRD patterns and calculated cell parameters and volumes (by Rietveld refinement) of the as-synthesized α-$NaYF_4$ (a, b) and α-$NaGdF_4$ UCNPs (c, d)

UCNPs of β-$NaYF_4$ and β-$NaGdF_4$ were also synthesized by the coprecipitation method. The doping concentration of Yb^{3+}/Tm^{3+} was kept the same at 20%/2% for all the samples so, in this work, the samples will be denoted as β-$NaYF_4$ and β-$NaGdF_4$. Figure 5.5 shows the TEM images, XRD patterns and calculated cell parameters of these uniform UCNPs. The as-synthesized β-UCNPs had a hexagonal phase and were highly crystallized. Calculated by using Rietveld refinement, the cell parameters and cell volumes (*a, c, V*) of the β-$NaYF_4$ and β-$NaGdF_4$ samples were determined as (5.97, 3.51, 108.29) and (6.00, 3.53, 110.33), respectively.

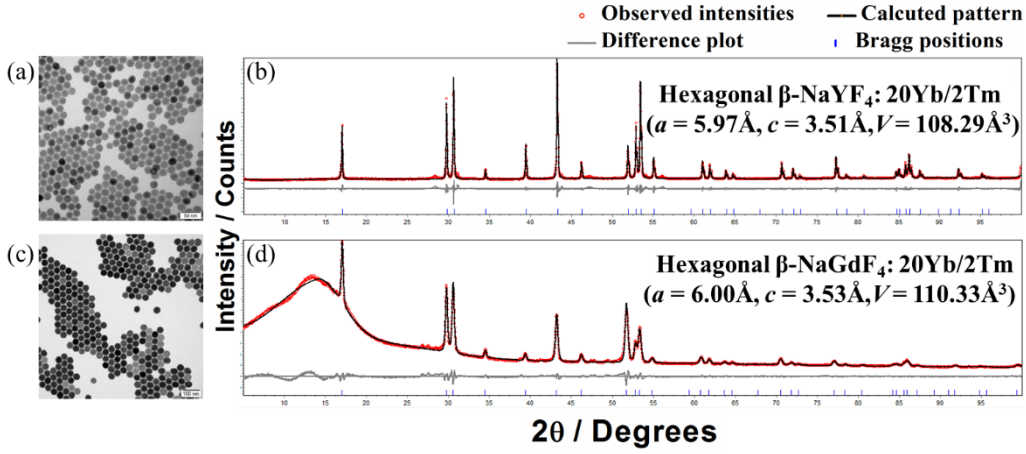

Figure 5.5 TEM images, XRD patterns and calculated cell parameters and volumes (by Rietveld refinement) of the as-synthesized β-$NaYF_4$ (a, b) and β-$NaGdF_4$ UCNPs (c, d)

According to the calculated cell parameters, we plotted the linear increase in the lattice

parameters of $CsPbX_3$ PQDs by changing the halide composition from Cl^- to I^-, as shown in Figure 5.6. The cell parameters of the α- and β-UCNPs are also illustrated in the figure. It is clear that the cell parameters of the α-UCNPs were very close to those of the $CsPbCl_3$ PQDs. Generally, typical α-UCNP unit shell is slightly smaller than the PQDs of $CsPbCl_3$. For the RE^{3+} ions that are usually used for UCNPs, Gd^{3+} (1.053, coordinate of 8) has a relatively large radius. Therefore, it better to use α-$NaGdF_4$ UCNPs and select the smallest $CsPbCl_3$ PQDs for hybrid growth. It should be noted that although the β-UCNPs have a hexagonal structure (P63/m), Dong et al. discovered that preferential cation exchange can trigger surface hexagonal-to-cubic structural evolution in the hexagonal phase of $NaREF_4$ [45]. Thereby, β-UCNPs still show great potential to form hybrid structures with PQDs.

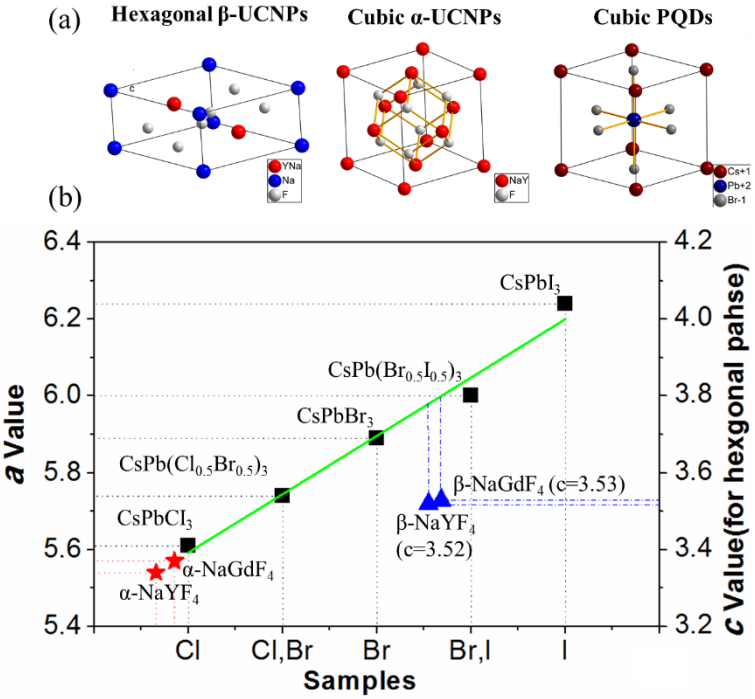

Figure 5.6 Crystal structures of β-UCNPs, α-UCNPs and PQDs (a); Refined lattice parameters of $CsPbX_3$ PQDs show a linear increase by changing the halide composition from Cl^- to I^-, as well as the cell parameters of α- and β-UCNPs

5.3.3 Luminescence radiative reabsorption between UCNPs and PQDs

$NaREF_4$ UCNPs and $CsPbBr_3$ PQDs were selected for mixing in a colloid solution to study the luminescence radiative reabsorption (LRR) of UCNPs and PQDs. Figure 5.7 shows the UC luminescent spectra of the mixture of UCNPs and PQDs under 980 nm NIR laser excitation. The inset of Figure 5.7a shows that the colour of the pure UCNPs is blue, and the green colour in the mixed sample can be attributed to $CsPbBr_3$ PQDs. From

the spectra, the pure β-UCNPs show characteristic UC emission peaks from the Tm^{3+} ions. The mixture showed a green emission peak around 530 nm, which corresponds to the PQDs, whereas the emissions of Tm^{3+} from the UCNPs (shorter than 500 nm) were quenched in accordance with the absorption of PQDs. Because pure PQDs cannot trigger UC emissions, the emission of PQDs was attributed to the NPs, indicating that UCNPs can function as an internal UV or blue lamp to illuminate the PQDs by utilizing their intense UC luminescence. This result confirms the existence of LRR sensitization from the UCNPs to PQDs. However, compared with the emission areas of Tm^{3+} below 500 nm, the emission area of PQDs around 530 nm is very small. A similar phenomenon was also observed by mixing the α-UCNPs and $CsPbBr_3$ PQDs (Figure 5.7b). This means a lot of energy was wasted by the LRR process because of its mechanism of radiative reabsorption, rather than direct energy transfer (such as FRET). Thereby, it is essential to develop UCNP-PQD hybrid structures to realize multicolour luminescence through FRET sensitization.

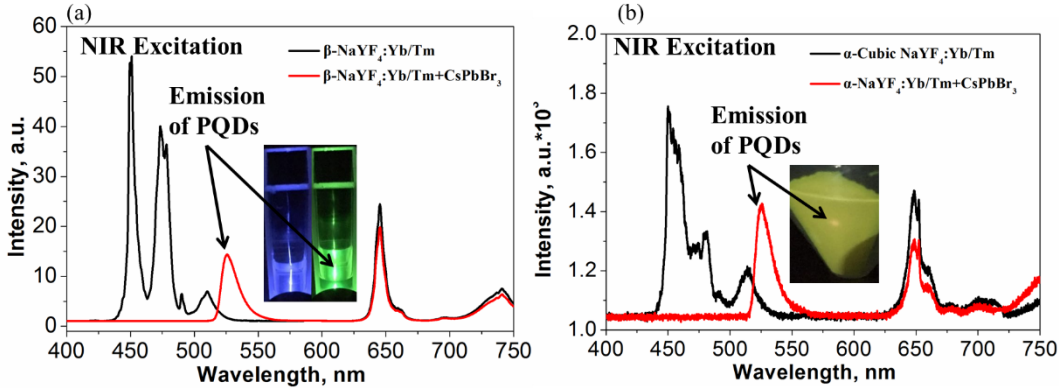

Figure 5.7 UC luminescent spectra of pure β-UCNPs and the mixture of β-UCNPs and PQDs under 980 nm NIR laser excitation (a); the same, but for α-UCNPs and their mixture with PQDs (b)

5.3.4 Attempting cation exchange with transition metal ions

In order to synthesize hybrid composites, Pb^{2+}, Mn^{2+} and Ni^{2+} ions with 2+ valence were used for cation exchange to test the feasibility of penetrating transition-metal ions into the surface of UCNPs. Figure 5.8 illustrates a schematic showing the typical cation exchange process between RE^{3+} and transition metal ions in a colloid solution of $NaYF_4$ UCNPs (Figure 5.8a), and TEM images of UCNPs before and after cation exchange with Pb^{2+}, Mn^{2+} and Ni^{2+} (Figure 5.8b). In terms of morphology, one can see that the UCNPs

did not change much after cation exchange, indicating that cation exchange by transition metal ions preserves the original size, morphology and crystal phase of the UCNPs.

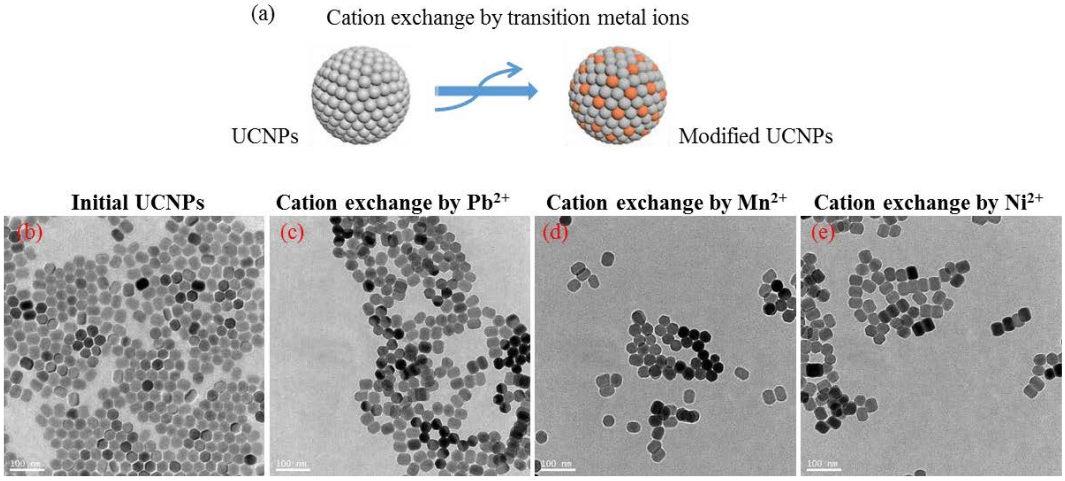

Figure 5.8 Schematic showing the typical cation exchange process between RE^{3+} and transition metal ions in a colloid solution of $NaYF_4$ UCNPs (a); and the TEM images of UCNPs before and after cation exchange with Pb^{2+}, Mn^{2+} and Ni^{2+}, respectively (b)

Since Pb^{2+} and Ni^{2+} ions cannot act as activators in the lattice of a UC host, the luminescent properties did not show any changes after cation exchange with these ions. Therefore, it is necessary to use Mn^{2+} ions, whose characteristic UC emissions have been proven to be in the green light region, for the characterization of the cation exchange process.

XRD and Rietveld refinement were employed to characterize the structural evolution of the Mn^{2+}-modified $NaYF_4$ UCNPs. In this case, two concentrations of Mn^{2+} ions, 5 μmol and 50 μmol, were tested (Figure 5.9a). Figure 5.9b shows the XRD patterns for the refinements of the initial $NaYF_4$ UCNPs and those modified by different concentrations of Mn^{2+}. Both of the X-ray patterns are in line with the hexagonal cell (P63/m), with parameters close to those of the starting model of $NaYF_4$, indicating that the particle phase did not change after cation exchange. The refined lattice parameters *a*, *c*, and *V* showed obvious decreasing trends with increasing concentrations of Mn^{2+} (Figure 5.9b). In the lattice of β-$NaYF_4$ UCNPs, the RE^{3+} ion coordinate is nine (Figure 5.9c). Note that the maximum coordinate of Mn^{2+} is eight. It is clear that the radius of the Mn^{2+} ion is smaller than that of the RE^{3+} ions of Y, Tm and Yb (Table 5.3)[46]. Replacement of the larger Y^{3+} ions in the lattice with smaller Mn^{2+} ions would constrain the unit cells of the UCNPs.

Therefore, the decreased unit cell parameters and volume confirm the existence of a Mn^{2+} cation exchange process in the lattice of $NaYF_4$ UCNPs.

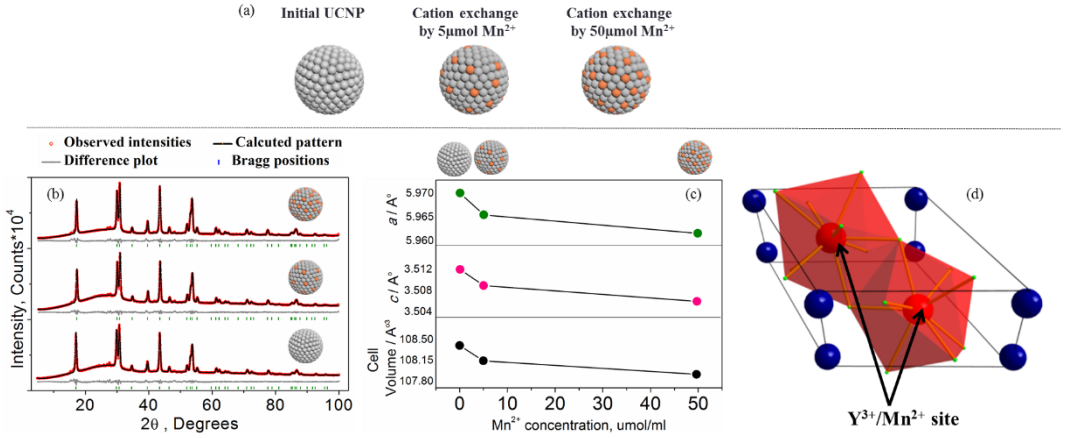

Figure 5.9 Schematics of two concentrations of Mn^{2+} ions (5 μmol and 50 μmol) used for cation exchange in a colloid solution of $NaYF_4$ UCNPs (a); Observed (red), calculated (black), and difference (grey) XRD patterns for the refinement of initial $NaYF_4$ UCNPs and Mn^{2+}-modified UCNPs (b); Refined lattice parameters of a, c, and unit cell volume (V) show obvious decreases with increasing Mn^{2+} concentration, indicating that Mn was doped into the lattice (c); Crystal structure of Mn^{2+}-exchanged $NaYF_4$ UCNPs (c)

Table 5.3 Radii of several ions and corresponding coordinates

Ion	Coordinate (CN)	Radius (Å)
Y^{3+}	9	1.075
Tm^{3+}	9	1.052
Yb^{3+}	9	1.042
Mn^{2+}	(Maximum 8)	0.96

Furthermore, the enhanced red/green (652/535) ratio in Mn^{2+}-modified $NaYF_4$: Yb^{3+}/Er^{3+} UCNPs is also evidence of successful cation exchange[47-50]. Two kinds of UCNPs (without shells, and ~2.5 nm inert shells) were prepared for cation exchange and red/green tests (Figures 5.10a, e). All the Yb^{3+}/Er^{3+} co-doped $NaYF_4$ samples showed a bright green emission (around 537 nm) along with a dark red emission (around 652 nm). Without the inert shell, the doping of Mn^{2+} ions into $NaYF_4$: Yb^{3+}/Er^{3+} changed the transition possibilities of Er^{3+} and promoted red emission, resulting in the red to green intensity ratio (652/537 nm) gradually increasing from 2.66 to 3.00 (or 2.93) with increasing Mn^{2+} concentration (Figure 5.10b). The existence of Mn^{2+} ions disturbs the transition possibilities between the green and red emissions of Er^{3+} and facilitates red emission

(Figure 5.10d), indicating that cation exchange between transition metal ions and Mn^{2+} UCNPs was successful. In contrast, with a 2.5 nm shell, the red to green intensity ratio no longer showed an increasing trend, because Mn^{2+} cannot influence the Er^{3+} activator due to its thick inert shell (Figure 5.10f, g).

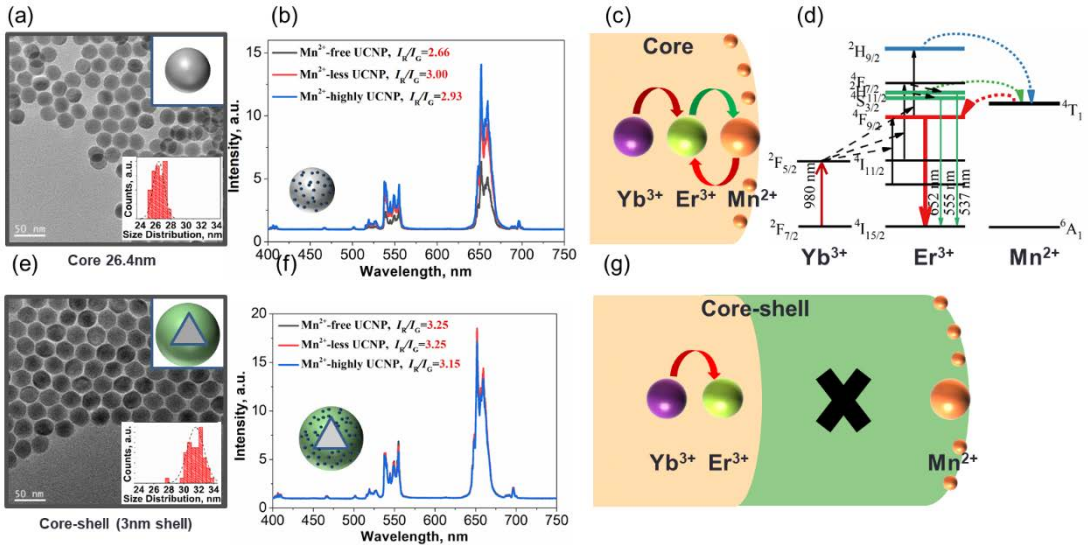

Figure 5.10 TEM image and size distribution chart of core-only $NaYF_4$:Yb,Er UCNPs (a); UC spectra and enhanced red-to-green luminescent intensity ratio with the increasing Mn^{2+} doping in core-only UCNPs (b); Schematic and energy level diagram showing that Mn^{2+} ions disturbed the transition possibilities and facilitated red emission of Er^{3+} in Mn^{2+} doped core-only UCNPs (c, d) ; TEM image and size distribution chart of core-shell $NaYF_4$:Yb,Er@ $NaYF_4$ UCNPs with 2.5nm inert shell (e); UC spectra showing no any red/green ratio enhancement in Mn^{2+} doped core-shell UCNPs (f); Schematic showing that Mn^{2+} cannot influence the Er^{3+} activator due to the 2.5nm thick inert shell in the core-shell UCNPs (g)

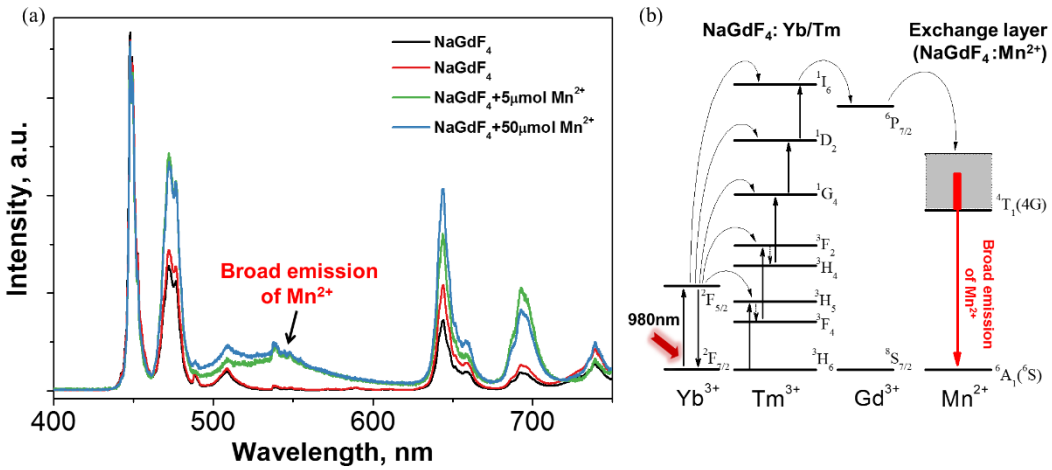

Figure 5.11 UC luminescent spectra of modified $NaGdF_4$ UCNPs after cation exchange by Mn^{2+} ions (a); Proposed energy transfer mechanism of the Mn^{2+}-activated $NaGdF_4$ UC nanoparticles, which occurs through the Yb-Tm-Gd-Mn pathway (b)

In addition, cation exchange between Mn^{2+} and the $NaGdF_4$: Yb^{3+}/Tm^{3+} UCNPs was also proven. The UC luminescent spectra are shown in Figure 5.11a. There is a clear, characteristically broad emission band of Mn^{2+} ions at around 540 nm. This is because the Gd^{3+}-mediated energy migration layer bridged the Tm^{3+} ion donor and Mn^{2+} ion acceptor[51-52]. By taking advantage of energy transfer through Yb-Tm-Gd-Mn in the nanoparticles, the UC emission of Mn^{2+} was realized (Figure 5.11b), which confirms that Mn^{2+} ions were doped into the host lattices by cation exchange. In conclusion, our investigations illustrate that transition metal ions such as Mn^{2+} can indeed penetrate the surface of UCNPs.

5.3.5 Attempting to grow a UCNP-PQD hybrid

Encouraged by the successful cation exchange by transition metal ions, PQDs and UCNPs were used next in an attempt to construct a new hybrid structure that can produce full-gamut UC luminescence. We hoped that Pb^{2+} ions would penetrate the lattice of UCNPs by cation exchange, and then bridge PQDs and UCNPs to form hybrid composites. To maximize the possibility of hybrid growth between PQDs and UCNPs, both α- and β-UCNPs (including $NaYF_4$ and $NaGdF_4$) and PQDs with halide compositions from Cl^- to I^- (including $CsPbCl_3$, $CsPb(Cl_{0.5}Br_{0.5})3$, $CsPbBr_3$, $CsPb(Br_{0.5}I_{0.5})3$, and $CsPbI_3$) were selected for the hybrid growth attempts.

These as-synthesized UCNPs were reacted with Pb^{2+} ions by cation exchange, then the modified UCNPs were used as seeds for the next hybrid growth attempt with different kinds of $CsPbX_3$ PQDs. We chose different kinds of combinations of UCNPs and PQDs, as well as different kinds of reaction solvent (and combinations). In addition, we modified many reaction conditions, such as temperature, holding time, atmosphere, UCNP:PQD concentration ratio, and amount ratio of reaction solvent. Though many syntheses were attempted, no matter which UCNPs (α- or β-phase, $NaYF_4$ or $NaGdF_4$) and PQDs ($CsPbCl_3$, $CsPb(Cl_{0.5}Br_{0.5})3$, $CsPbBr_3$, $CsPb(Br_{0.5}I_{0.5})3$, or $CsPbI_3$) were selected, they could not form hybrid composites. Morphological characterization by TEM showed that hybrid growth of UCNPs and PQDs remains a great challenge. Some TEM images are shown in Figure 5.12.

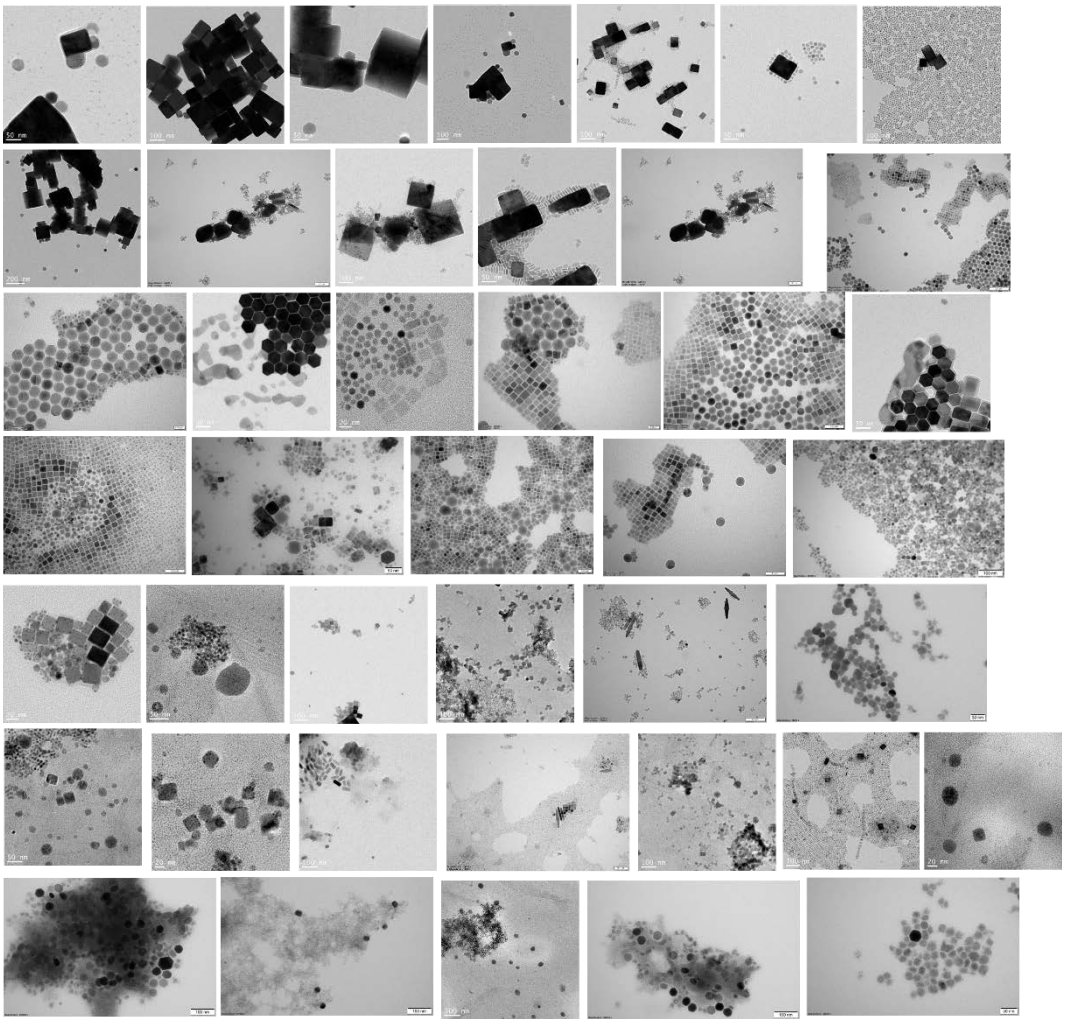

Figure 5.12 TEM images of some of the samples produced in the hybrid growth attempts

5.3.6 Hybrid growth between UCNP and Ni_2P nanoparticles

However, we tried a hybrid heterostructures growth between UCNPs and Ni_2P nanoparticles. The reason why Ni_2P was selected is that it has the same hexagonal phase (but different space groups) and similar cell parameters as UCNPs[43-44].

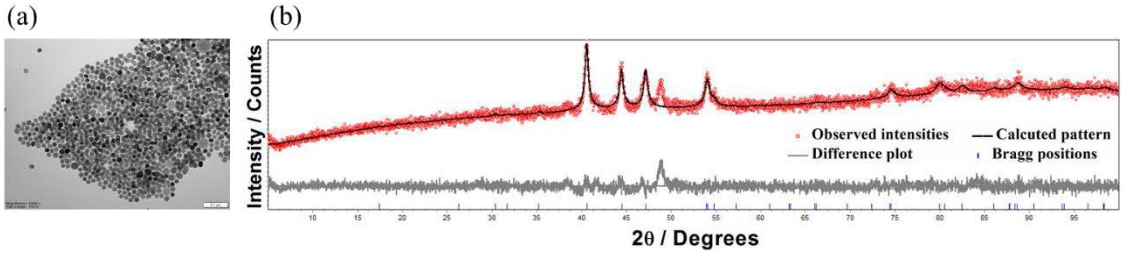

Figure 5.13 TEM images of the synthesized Ni_2P nanoparticles (a); XRD pattern for the refinement of the synthesized Ni_2P nanoparticles (b)

Figure 5.13a shows TEM images of synthesized, pure Ni_2P nanoparticles. The Rietveld refinement and calculation results show a hexagonal phase with accurate parameters (a = 5.88 Å, b = 3.39 Å) and volume (101.50 $Å^3$; Figure 5.13b). Note the β-$NaREF_4$ also has similar cell parameters (always a = ~5.9 Å, and c = ~3.5 Å, as shown before in Section 5.3.2).

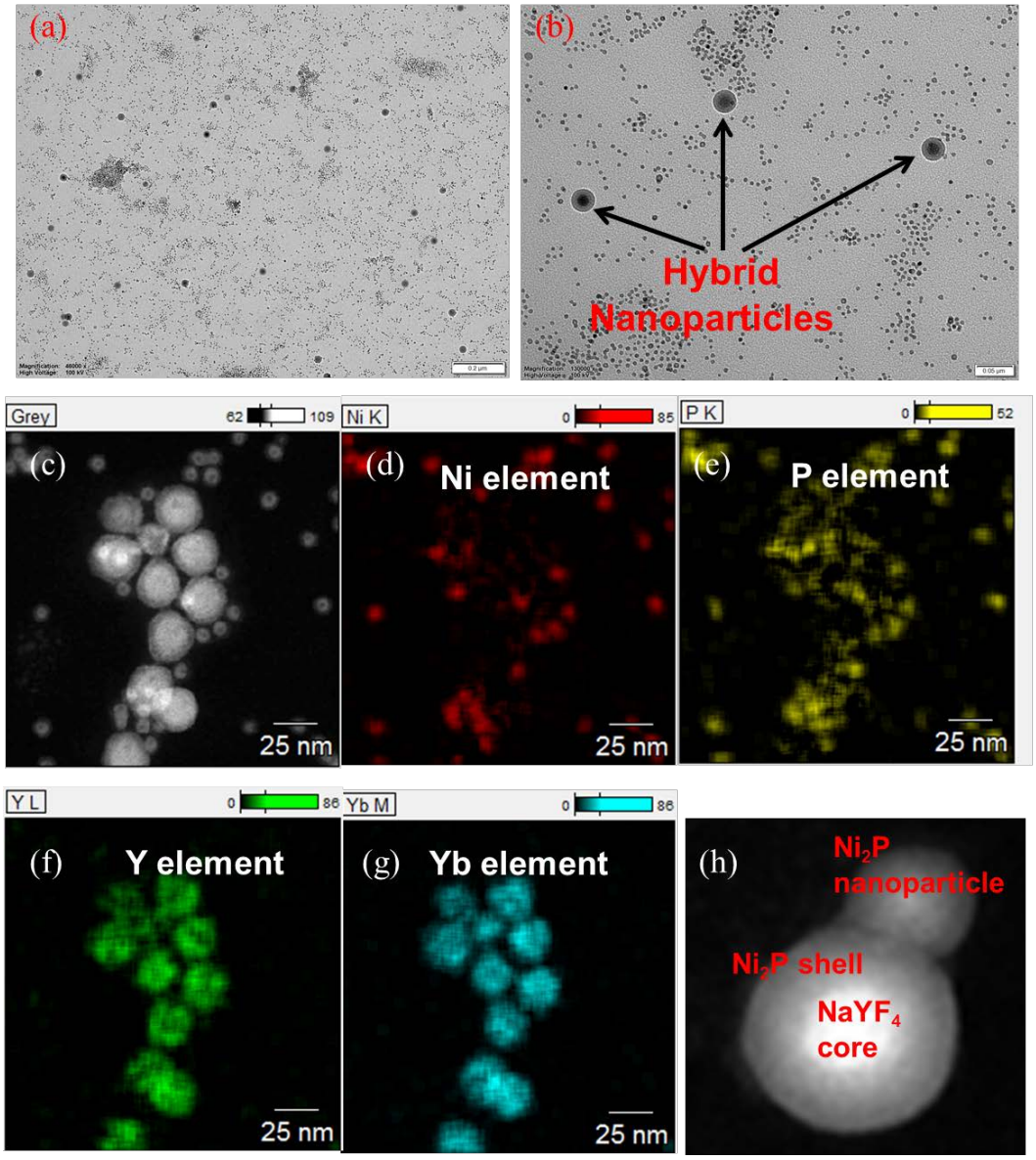

Figure 5.14 TEM images of $NaYF_4$ and Ni_2P compounds, note that the large particles are core-shell structures of UCNP and Ni_2P (a, b); HRTEM image of the hybrid structure of $NaYF_4$ and Ni_2P (c), Elemental maps of Ni (d), P (e), Y (f) and Yb (g); illustration of hybrid core-shell structure of UCNP and Ni_2P (h)

After that, we conducted hybrid growth of β-$NaYF_4$ and Ni_2P nanoparticles. We modified the UCNPs by cation exchange with Ni^{2+} ions and then used the modified UCNPs to synthesize Ni_2P. The resulting compounds are shown in Figure 5.14. Notably, the large

particles in Figures 5.14a and b clearly show a core-shell structure. Comparing the morphologies of the initial UCNPs and pure Ni_2P nanoparticles, we confirmed that the cores of large particles are modified UCNPs, while the shells of large particles are Ni_2P layers. We further conducted high-resolution transmission electron microscopy (HRTEM) imaging and energy-dispersive X-ray spectroscopy (EDS) to confirm the hybrid structure of $NaYF_4$ and Ni_2P nanoparticles. HRTEM images and elemental mapping of the heavy atoms of the compounds are shown in Figures 5.14c-h. From the large particles with core-shell structures, it can be seen that Ni^{2+} and P^{4-} ions are distributed on the surface (Figures 5.14d and e), while Yb^{3+} and Y^{3+} ions are concentrated in the central areas of the particles (Figures 5.14f and g). This distribution tendency within the large particles confirms that the cores consist of modified UCNPs, while the shells are Ni_2P layers.

Because Ni_2P nanoparticles are black, which greatly quenches the UC luminescence of UCNPs, this as-synthesized hybrid nanomaterial is not suitable for tuning multicolour luminescence. Nevertheless, this observed hybrid heterostructures from UCNPs and Ni_2P supports the hypothesis proposed before: that the cation exchange strategy can remediate the dissimilar structures of two materials, particularly in terms of different space groups. This finding will help us to continue the UCNP-QD hybrid growth in the future.

5.4 Conclusions

In summary, the development of hybrid syntheses of UCNPs and PQDs was investigated for the purposes of realizing multicolour luminescence. We observed green UC luminescence under the process of LRR sensitization in the mixture of UCNPs and $CsPbBr_3$ PQDs under excitation by a 980 nm near-infrared laser, in which the UCNPs functioned as an internal UV or blue lamp to illuminate the PQDs. The investigations illustrate that transition metal ions such as Mn^{2+} can indeed penetrate the surface of UCNPs by the cation exchange strategy. UCNPs and PQDs were used to construct new hybrid heterostructures. However, regardless of whether α- or β-phase UCNPs were employed, the results indicate that hybrid growth of UCNPs and PQDs remains a great challenge. Nevertheless, we successfully synthesized hybrid heterostructures of modified UCNPs and Ni_2P nanoparticles, which supports the hypothesis that cation exchange strategy can remediate the dissimilar structures. The modified UCNPs can be re-dispersed

into an oleic acid environment to form hybrid heterostructures. We hope this the cation exchange strategy may help to achieve heteroepitaxial UCNP-PQD growth in the future.

5.5 Reference

1. Zhou, B.; Shi, B.; Jin, D.; Liu, X., Controlling upconversion nanocrystals for emerging applications. *Nat Nanotechnol* **2015,** *10* (11), 924-36.

2. Zheng, W.; Huang, P.; Tu, D.; Ma, E.; Zhu, H.; Chen, X., Lanthanide-doped upconversion nano-bioprobes: electronic structures, optical properties, and biodetection. *Chem Soc Rev* **2015,** *44* (6), 1379-415.

3. Xu, G.; Zeng, S.; Zhang, B.; Swihart, M. T.; Yong, K. T.; Prasad, P. N., New Generation Cadmium-Free Quantum Dots for Biophotonics and Nanomedicine. *Chem Rev* **2016,** *116* (19), 12234-12327.

4. Wilhelm, S., Perspectives for Upconverting Nanoparticles. *ACS Nano* **2017,** *11* (11), 10644-10653.

5. Chen, G.; Qiu, H.; Prasad, P. N.; Chen, X., Upconversion nanoparticles: design, nanochemistry, and applications in theranostics. *Chem Rev* **2014,** *114* (10), 5161-214.

6. Li, Z.; Zhang, Y.; Jiang, S., Multicolor Core/Shell-Structured Upconversion Fluorescent Nanoparticles. *Adv. Mater* **2008,** *20*, 4765–4769.

7. Xia, A.; Gao, Y.; Zhou, J.; Li, C.; Yang, T.; Wu, D.; Wu, L.; Li, F., Core-shell $NaYF_4$:Yb^{3+},Tm^{3+}@FexOy nanocrystals for dual-modality T2-enhanced magnetic resonance and NIR-to-NIR upconversion luminescent imaging of small-animal lymphatic node. *Biomaterials* **2011,** *32* (29), 7200-8.

8. Wang, L.; Ren, L.; Mitchell, D.; Casillas-Garcia, G.; Ren, W.; Ma, C.; Xu, X. X.; Wen, S.; Wang, F.; Zhou, J.; Xu, X.; Hao, W.; Dou, S. X.; Du, Y., Enhanced energy transfer in heterogeneous nanocrystals for near infrared upconversion photocurrent generation. *Nanoscale* **2017,** *9* (47), 18661-18667.

9. Dou, Q. Q.; Rengaramchandran, A.; Selvan, S. T.; Paulmurugan, R.; Zhang, Y., Core-shell upconversion nanoparticle - semiconductor heterostructures for photodynamic therapy. *Sci Rep* **2015,** *5*, 8252.

10. Costi, R.; Saunders, A. E.; Banin, U., Colloidal hybrid nanostructures: a new type of functional materials. *Angew Chem Int Ed* **2010,** *49* (29), 4878-97.

11. Banin, U.; Ben-Shahar, Y.; Vinokurov, K., Hybrid Semiconductor–Metal Nanoparticles: From Architecture to Function. *Chemistry of Materials* **2013,** *26* (1), 97-110.

12. Ramasamy, P.; Lim, D. H.; Kim, B.; Lee, S. H.; Lee, M. S.; Lee, J. S., All-inorganic cesium lead halide perovskite nanocrystals for photodetector applications. *Chem Commun (Camb)* **2016,** *52* (10), 2067-70.

13. Huang, H.; Polavarapu, L.; Sichert, J. A.; Susha, A. S.; Urban, A. S.; Rogach, A. L., Colloidal lead halide perovskite nanocrystals: synthesis, optical properties and applications. *NPG Asia Materials* **2016,** *8* (11), e328-e328.

14. Fu, Y.; Zhu, H.; Stoumpos, C. C.; Ding, Q.; Wang, J.; Kanatzidis, M. G.; Zhu, X.; Jin, S., Broad Wavelength Tunable Robust Lasing from Single-Crystal Nanowires of Cesium Lead Halide Perovskites (CsPbX3, X = Cl, Br, I). *ACS Nano* **2016,** *10* (8), 7963-72.

15. Koscher, B. A.; Bronstein, N. D.; Olshansky, J. H.; Bekenstein, Y.; Alivisatos, A. P., Surface- vs Diffusion-Limited Mechanisms of Anion Exchange in $CsPbBr_3$ Nanocrystal Cubes Revealed through Kinetic Studies. *J Am Chem Soc* **2016,** *138* (37), 12065-8.

16. Makarov, N. S.; Guo, S.; Isaienko, O.; Liu, W.; Robel, I.; Klimov, V. I., Spectral and Dynamical Properties of Single Excitons, Biexcitons, and Trions in Cesium-Lead-Halide Perovskite Quantum Dots. *Nano Lett* **2016,** *16* (4), 2349-62.

17. Pellet, N.; Teuscher, J.; Maier, J.; Grätzel, M., Transforming Hybrid Organic Inorganic Perovskites by Rapid Halide Exchange. *Chemistry of Materials* **2015,** *27* (6), 2181-2188.

18. Akkerman, Q. A.; D'Innocenzo, V.; Accornero, S.; Scarpellini, A.; Petrozza, A.; Prato, M.; Manna, L., Tuning the Optical Properties of Cesium Lead Halide Perovskite Nanocrystals by Anion Exchange Reactions. *J Am Chem Soc* **2015,** *137* (32), 10276-81.

19. Huang, G.; Wang, C.; Xu, S.; Zong, S.; Lu, J.; Wang, Z.; Lu, C.; Cui, Y., Postsynthetic Doping of $MnCl_2$ Molecules into Preformed $CsPbBr_3$ Perovskite Nanocrystals via a Halide Exchange-Driven Cation Exchange. *Adv Mater* **2017,** *29* (29).

20. Zhang, D.; Yang, Y.; Bekenstein, Y.; Yu, Y.; Gibson, N. A.; Wong, A. B.; Eaton, S. W.; Kornienko, N.; Kong, Q.; Lai, M.; Alivisatos, A. P.; Leone, S. R.; Yang, P., Synthesis of Composition Tunable and Highly Luminescent Cesium Lead Halide Nanowires through Anion-Exchange Reactions. *J Am Chem Soc* **2016,** *138* (23), 7236-9.

21. Saidaminov, M. I.; Haque, M. A.; Almutlaq, J.; Sarmah, S.; Miao, X.-H.; Begum, R.; Zhumekenov, A. A.; Dursun, I.; Cho, N.; Murali, B.; Mohammed, O. F.; Wu, T.; Bakr, O. M., Inorganic Lead Halide Perovskite Single Crystals: Phase-Selective Low-Temperature Growth, Carrier Transport Properties, and Self-Powered Photodetection. *Advanced Optical Materials* **2017,** *5* (2).

22. Wang, H. C.; Lin, S. Y.; Tang, A. C.; Singh, B. P.; Tong, H. C.; Chen, C. Y.; Lee, Y. C.; Tsai, T. L.; Liu, R. S., Mesoporous Silica Particles Integrated with All-Inorganic $CsPbBr_3$ Perovskite Quantum-Dot Nanocomposites (MP-PQDs) with High Stability and Wide Color Gamut Used for Backlight Display. *Angew Chem Int Ed* **2016,** *55* (28), 7924-9.

23. Yan, C.; Dadvand, A.; Rosei, F.; Perepichka, D. F., Near-IR Photoresponse in New Up-Converting CdSe/$NaYF_4$:Yb,Er Nanoheterostructures. *J Am Chem Soc* **2010,** *132*, 8868–8869.

24. Boyer, J.-C.; Vetrone, F.; Cuccia, L. A.; Capobianco, J. A., Synthesis of Colloidal Upconverting $NaYF_4$ Nanocrystals Doped with Er^{3+}, Yb^{3+} and Tm^{3+}, Yb^{3+} via Thermal Decomposition of Lanthanide Trifluoroacetate Precursors. *J Am Chem Soc* **2006,** *128*, 7444-7445.

25. Ning, Z.; Gong, X.; Comin, R.; Walters, G.; Fan, F.; Voznyy, O.; Yassitepe, E.; Buin, A.; Hoogland, S.; Sargent, E. H., Quantum-dot-in-perovskite solids. *Nature* **2015,** *523* (7560), 324-8.

26. Chen, J.; Zidek, K.; Chabera, P.; Liu, D.; Cheng, P.; Nuuttila, L.; Al-Marri, M. J.; Lehtivuori, H.; Messing, M. E.; Han, K.; Zheng, K.; Pullerits, T., Size- and Wavelength-Dependent Two-Photon Absorption Cross-Section of $CsPbBr_3$ Perovskite Quantum Dots. *J Phys Chem Lett* **2017,** *8* (10), 2316-2321.

27. Rao, M.; Fu, J.; Wen, X.; Sun, B.; Wu, J.; Liu, X.; Dong, X., Near-infrared-excitable perovskite quantum dots via coupling with upconversion nanoparticles for dual-model anti-counterfeiting. *New Journal of Chemistry* **2018,** *42* (15), 12353-12356.

28. Zheng, W.; Huang, P.; Gong, Z.; Tu, D.; Xu, J.; Zou, Q.; Li, R.; You, W.; Bunzli, J. G.; Chen, X., Near-infrared-triggered photon upconversion tuning in all-inorganic cesium lead halide perovskite quantum dots. *Nat Commun* **2018,** *9* (1), 3462.

29. Kovalenko, M. V.; Protesescu, L.; Bodnarchuk, M. I., Properties and potential optoelectronic applications of lead halide perovskite nanocrystals. *Science* **2017,** *358*, 745–750.

30. Li, X.; Wang, Y.; Sun, H.; Zeng, H., Amino-Mediated Anchoring Perovskite Quantum Dots for Stable and Low-Threshold Random Lasing. *Adv Mater* **2017,** *29* (36).

31. Dai, X.; Deng, Y.; Peng, X.; Jin, Y., Quantum-Dot Light-Emitting Diodes for Large-Area Displays: Towards the Dawn of Commercialization. *Adv Mater* **2017,** *29* (14).

32. Chen, Y.; Duong, H. T. T.; Wen, S.; Mi, C.; Zhou, Y.; Shimoni, O.; Valenzuela, S. M.; Jin, D., Exonuclease III-Assisted Upconversion Resonance Energy Transfer in a Wash-Free Suspension DNA Assay. *Anal Chem* **2018,** *90* (1), 663-668.

33. Yao, L.; Zhou, J.; Liu, J.; Feng, W.; Li, F., Iridium-Complex-Modifi ed Upconversion Nanophosphors for Effective LRET Detection of Cyanide Anions in Pure Water. *Adv. Funct. Mater.* **2012,** *22*, 2667–2672.

34. Wang, L.; Yan, R.; Huo, Z.; Wang, L.; Zeng, J.; Bao, J.; Wang, X.; Peng, Q.; Li, Y., Fluorescence resonant energy transfer biosensor based on upconversion-luminescent nanoparticles. *Angew Chem Int Ed* **2005,** *44* (37), 6054-7.

35. Wang, F.; Liu, X., Multicolor tuning of lanthanide-doped nanoparticles by single wavelength excitation. *Acc Chem Res* **2014,** *47* (4), 1378-85.

36. Marin, R.; Labrador-Paéz, L.; Skripka, A.; Haro-González, P.; Benayas, A.; Canton, P.; Jaque, D.; Vetrone, F., Upconverting Nanoparticle to Quantum Dot Förster Resonance Energy Transfer: Increasing the Efficiency through Donor Design. *ACS Photonics* **2018,** *5* (6), 2261-2270.

37. Broadband dye-sensitized upconversion of near-infrared light. **2012**.

38. Jeong, S.; Won, N.; Lee, J.; Bang, J.; Yoo, J.; Kim, S. G.; Chang, J. A.; Kim, J.; Kim, S., Multiplexed near-infrared in vivo imaging complementarily using quantum dots and upconverting $NaYF_4$:Yb^{3+},Tm^{3+} nanoparticles. *Chem Commun (Camb)* **2011,** *47* (28), 8022-4.

39. Cheng, L.; Yang, K.; Shao, M.; Lee, S.-T.; Liu, Z., Multicolor In Vivo Imaging of Upconversion Nanoparticles with Emissions Tuned by Luminescence Resonance Energy Transfer. *J. Phys. Chem. C* **2011,** *115*, 2686–2692.

40. Gorris, H. H.; Ali, R.; Saleh, S. M.; Wolfbeis, O. S., Tuning the dual emission of photon-upconverting nanoparticles for ratiometric multiplexed encoding. *Adv Mater* **2011,** *23* (14), 1652-5.

41. Guanying Chen; Jie Shen; Tymish Y. Ohulchanskyy; Nayan J. Patel; Artem Kutikov; Zhipeng Li; Jie Song; Ravindra K. Pandey; Hans Agren; Paras N. Prasad; Han, G., (R-$NaYbF_4$:Tm^{3+})/CaF_2 Core/Shell Nanoparticles with Efficient Near-Infrared to Near-Infrared Upconversion for High-Contrast Deep Tissue Bioimaging. *ACS Nano* **2012,** *6* (9), 8280–8287.

42. Parobek, D.; Roman, B. J.; Dong, Y.; Jin, H.; Lee, E.; Sheldon, M.; Son, D. H., Exciton-to-Dopant Energy Transfer in Mn-Doped Cesium Lead Halide Perovskite Nanocrystals. *Nano Lett* **2016,** *16* (12), 7376-7380.

43. Popczun, E. J.; McKone, J. R.; Read, C. G.; Biacchi, A. J.; Wiltrout, A. M.; Lewis, N. S.; Schaak, R. E., Nanostructured nickel phosphide as an electrocatalyst for the hydrogen evolution reaction. *J Am Chem Soc* **2013,** *135* (25), 9267-70.

44. Chen, T.; Liu, D.; Lu, W.; Wang, K.; Du, G.; Asiri, A. M.; Sun, X., Three-Dimensional Ni_2P Nanoarray: An Efficient Catalyst Electrode for Sensitive and Selective Nonenzymatic Glucose Sensing with High Specificity. *Anal Chem* **2016,** *88* (16), 7885-9.

45. Dong, H.; Sun, L. D.; Li, L. D.; Si, R.; Liu, R.; Yan, C. H., Selective Cation Exchange Enabled Growth of Lanthanide Core/Shell Nanoparticles with Dissimilar Structure. *J Am Chem Soc* **2017,** *139* (51), 18492-18495.

46. Shannon, R. D., Revised effective ionic radii and systematic studies of interatomic distances in halides and chalcogenides. *Acta Crystallographica Section A* **1976,** *32* (5), 751-767.

47. Berry, M. T.; May, P. S., Disputed Mechanism for NIR-to-Red Upconversion Luminescence in $NaYF_4$:Yb^{3+},Er^{3+}. *J Phys Chem A* **2015,** *119* (38), 9805-11.

48. Tian, G.; Gu, Z.; Zhou, L.; Yin, W.; Liu, X.; Yan, L.; Jin, S.; Ren, W.; Xing, G.; Li, S.; Zhao, Y., Mn^{2+} dopant-controlled synthesis of $NaYF_4$:Yb/Er upconversion nanoparticles for in vivo imaging and drug delivery. *Adv Mater* **2012,** *24* (9), 1226-31.

49. Xu, X.; Wang, Z.; Lei, P.; Yu, Y.; Yao, S.; Song, S.; Liu, X.; Su, Y.; Dong, L.; Feng, J.; Zhang, H., alpha-NaYb(Mn)F_4:Er^{3+}/Tm^{3+}@$NaYF_4$ UCNPs as "Band-Shape" Luminescent Nanothermometers over a Wide Temperature Range. *ACS Appl Mater Interfaces* **2015,** *7* (37), 20813-9.

50. Wu, Z.; Lin, M.; Liang, S.; Liu, Y.; Zhang, H.; Yang, B., Hot-Injection Synthesis of Manganese-Ion-Doped $NaYF_4$:Yb,Er Nanocrystals with Red Up-Converting Emission and Tunable Diameter. *Particle & Particle Systems Characterization* **2013,** *30* (4), 311-315.

51. Liu, X.; Wang, Y.; Li, X.; Yi, Z.; Deng, R.; Liang, L.; Xie, X.; Loong, D. T. B.; Song, S.; Fan, D.; All, A. H.; Zhang, H.; Huang, L.; Liu, X., Binary temporal upconversion codes of Mn^{2+}-activated nanoparticles for multilevel anti-counterfeiting. *Nat Commun* **2017,** *8* (1), 899.

52. Li, X.; Liu, X.; Chevrier, D. M.; Qin, X.; Xie, X.; Song, S.; Zhang, H.; Zhang, P.; Liu, X., Energy Migration Upconversion in Manganese(II)-Doped Nanoparticles. *Angew Chem Int Ed* **2015,** *54* (45), 13510-13515.

CHAPTER 6

Conclusions and Perspectives

6.1 Conclusions

This thesis has explored the controlled synthesis of upconversion (UC) materials with wide-gamut multicolour luminescence that can be produced with high-throughput. Several strategies were employed to produce and fine-tune the multicolour luminescent properties, including doping with various rare-earth (RE^{3+}) ions, energy migration-mediated upconversion (EMU) and Forster resonance energy transfer (FRET).

First studied were the distribution and multicolour luminescence of doped RE^{3+} ions within UC materials, including alkaline indium oxide bulk UC materials and fluoride upconversion nanoparticles (UCNPs). According to observations of the core-shell-like distribution of RE^{3+} ions within UCNPs, multicolour luminescence was realized via EMU with cation exchange. Secondly, a novel direct cation exchange method was developed to prepare multicolour UCNPs expeditiously in an organic solvent. Transition-metal ions were exchanged onto the surface of UCNPs using this method, and the modified UCNPs were re-dispersed into oleic acid for further growth. Finally, attempts were made to develop hybrid heterostructures of UCNPs and lead halide perovskite quantum dots (PQDs) to fine-tune multicolour luminescence via FRET sensitization.

The main achievements of this thesis are summarised as follows.

(1) Doping with various RE^{3+} ions is a simple and feasible route to producing materials with multicolour UC emissions. In alkaline indium oxide UC materials such as (Ca/Sr)In_2O_4, Rietveld refinement showed that doped RE^{3+} ions occupied the In^{3+} sites, which helps us to understand the network of energy transfer systems within such materials. The structural evolution had a strong influence on the emission profile; however, $SrIn_2O_4$ serves as an excellent multicolour UC host. Through the strategy of doping with various RE^{3+} ions, large-gamut multicolour luminescence in activators such as Er^{3+}, Tm^{3+} and Ho^{3+} was achieved in

oxide bulk UC materials.

(2) The gradient distribution of RE^{3+} ions within fluoride UCNPs can induce multicolour luminescence via the addition of various new activators by cation exchange. The synchrotron-based X-ray photoelectron spectroscopy (XPS) measurements demonstrated that Gd ions (with a large radius) occupied the surface areas of $NaYF_4$: Gd^{3+} UCNPs, while small-radius Yb ions were concentrated at the core areas of $NaYF_4$: Yb^{3+} UCNPs. A Gd^{3+}-rich shell was proposed to the surfaces of Yb^{3+}/Tm^{3+}-doped $NaGdF_4$ nanoparticles, which produced multicolour UC luminescence with the addition of various new activators such as Tb^{3+} and Eu^{3+} via cation exchange.

(3) A method of direct cation exchange on surface-ligand capped $NaGdF_4$: Yb^{3+}/Tm^{3+} UCNPs was developed. This as-synthesized UCNPs presented strong multicolour luminescence via EMU pathways. This method took place in organic solvent to avoid the requirement for tedious pre-treatment, and the luminescent intensities of UCNPs produced by this new method were much stronger than those produced by conventional cation exchange in water. This facile and rapid cation exchange synthesis strategy provides a new method for the expeditious, high-throughput synthesis of multicolour-emitting nanoparticles with high luminescent performance.

(4) Transition-metal ions, such as Mn^{2+} ions, were penetrated into the surfaces of UCNPs using the cation exchange strategy. The modified UCNPs were able to re-dispersed into oleic acid for further hybrid growth. Multicolour UC luminescence was expected to be achieved in the heterostructures of UCNPs and PQDs via FRET sensitization. However, such hybrid heterostructural growth of UCNPs and PQDs was not successful and remains a big challenge. Nevertheless, we successfully synthesized hybrid heterostructures of UCNPs and Ni_2P nanoparticles, which supports the hypothesis that cation exchange strategy can remediate the dissimilar structures to form hybrid heterostructures.

6.2 Perspectives

By exploring the distributions of RE^{3+} ions in UNCPs and their resulting multicolour luminescence as produced by different synthesis strategies, this PhD thesis has opened a new research path into the controlled synthesis of high-quality, multicolour, luminescent UC materials. This creates many future opportunities in the theoretical study of UC materials and their applications.

First of all, the gradient in RE^{3+}-ion distribution with UCNPs aids precision in doping during synthesis, which helps optimize their optical properties. For example, the hot-injection method, rather than co-precipitation or thermal decomposition, is advantageous in producing elaborate, multilayered, doped nanostructures. Epitaxial growth of multiple layers onto core nanoparticles will allow control of the spatial distributions of sensitizers and activators in UCNPs.

Furthermore, the cation exchange strategy allows expeditious, high-throughput production of multicolour-emitting nanoparticles while preserving their original sizes, morphologies and crystal phases. This advanced material fabrication method and resulting multicolour nanoparticles will help develop applications in optical multiplexing, complex data analysis, information storage, optoelectronic devices, and graphics imaging and display.

Finally, although the hybrid heterostructural growth of UCNPs and PQDs was unsuccessful and remains a great challenge, there are still many future opportunities for tuning multicolour emissions by coupling UC mechanisms to PQD emitters. Future work by the author will attempt to synthesize a UCNP-PQD nanocomposite to achieve multicolour emissions via FRET; for example, by using mesoporous silica to cap UCNPs and PQDs simultaneously. Or, by using (3-aminopropyl) triethoxysilane (APTES) to form a cross-linked matrix by embedding PQDs onto silica-coated UCNPs. These potential UCNP-PQD nanocomposites are expected to possess excellent multicolour luminescent properties and stability, which may clarify the FRET mechanism and allow wider colour tunability at higher efficiency.